Electroproduction of η' mesons at backward angles

by

TAKERU AKIYAMA

TOHOKU
UNIVERSITY

A dissertation submitted in partial fulfillment of
the requirements for the degree of
Doctor of Science

Department of Physics, Graduate School of Science,
Tohoku University

2024

Abstract

One of the goals of nuclear physics is to understand the physical characteristics of hadrons and their interaction based on the picture of quarks. The three lightest quarks of u, d, and s and their antiquarks form a spin-0 meson nonet under the flavor $SU(3)$ symmetry. In this classification, the η' meson is an isoscalar meson that has a large mass of 958 MeV/c^2 due to the quantum anomaly of QCD. In recent years, the mass acquisition mechanism of it in finite nuclear density has been studied through the search for bound states with atomic nuclei. It has become more interesting subject to research.

Real- and virtual-photoinduced meson productions off a nucleon have been studied in various reaction channels. Meson production by electromagnetic interaction near the energy threshold is strongly affected by the couplings with nucleon excited states in the s-channel. The $\eta' p$ final state can only be coupled to the N^* resonances due to isospin conservation. Its higher energy threshold exposes a lot of candidates for resonances that have not yet been experimentally established. Also, the angular dependence of extreme forward and backward angles with respect to the beam particles reveals contributions from resonances with higher spins. The present study reports for the first time the differential cross section of the η' production by electron scattering. The latest setup of hypernuclear spectroscopy allows the measurements of virtual-photoproduction of η' mesons at ultra-backward angles.

A series of experiments was conducted in Hall-A of Thomas Jefferson National Accelerator Labratory (JLab) in the United States from October to November 2018 as JLab E12-17-003. A 4.326 GeV electron beam was irradiated onto a 40 K cryogenic hydrogen target to generate η' with the $^1\mathrm{H}(e, e'p)\eta'$ reaction. The momenta of $p_p \sim 1.8$ GeV/c and $p_{e'} \sim 2.1$ GeV/c were measured simultaneously using two arms of magnetic spectrometers, HRS-R and -L that have the QQDQ magnetic components, at the angles of $\theta_p = \theta_{e'} = 13.2$ deg. A peak of η' was identified to count the number of the events on the missing mass distribution. The total charge of the beam was 4.6 C.

The number of observed η' was found to be 467 ± 85 counts by fitting the missing mass spectrum of the $^1\mathrm{H}(e, e'p)X$ reaction. The differential cross section of the $^1\mathrm{H}(\gamma^*, p)\eta'$reaction was derived as follows based on the number of η' given by the data and the acceptance estimated by a Monte Carlo simulation dedicated to JLab Hall-A setup,

$$\left(\frac{\mathrm{d}\sigma_{\gamma^* p\to\eta' p}}{\mathrm{d}\Omega_{\eta'}}\right)^{\mathrm{CM}} = 4.4 \pm 0.8 \ \ (\mathrm{stat.}) \pm 0.4 \ \ (\mathrm{sys.}) \ \ [\mathrm{nb/sr}]\,.$$

In order to consider this result, an isobar model calculation was developed to explain the electroproduction together with the photoproduction of η' mesons. It takes into account the lowest order perturbation of tree-level diagrams, and adopt the couplings with the N^* resonances,

ρ and ω meson couplings in the t-channel, and the ground state couplings called Born terms in the s- and u-channels. Fitting the experimental database of photoproduction has been successfully performed to determine the effective coupling constants, and the calculation has reproduced the present data of electroproduction consistently. The present study verifies the theoretical framework for the meson electroproduction, and also is expected to add new constraint on analysis of nucleon resonances.

"Philosophy will clip an Angel's wings,
Concuer all mysteries by rule and line,
Empty the haunted air, and gnomed mine—
Unweave a rainbow, as it erewhile made
The tender-person'd Lamia melt into a shade."

— *Lamia*; II, by John Keats

"No, no, no, no! Come, let's away to prison:
We two alone will sing like birds i' the cage:
When thou dost ask me blessing, I'll kneel down,
And ask of thee forgiveness: so we'll live,
And pray, and sing, and tell old tales, and laugh
At gilded butterflies, and hear poor rogues
Talk of court news; and we'll talk with them too,
Who loses and who wins; who's in, who's out;
And take upon's the mystery of things,
As if we were God's spies: and we'll wear out,
In a wall'd prison, packs and sects of great ones,
That ebb and flow by the moon."

— *King Lear*; Act 5, Scene 3, by William Shakespeare

Contents

Chapter 1

Introduction

1.1 Nuclear Physics

Nuclear physics focuses on compact quantum many-body systems governed by strong interactions, and also attempts to describe astrophysical phenomena, such as element synthesis in the universe and the internal structure of neutron stars, based on a microscopic understanding. This compact quantum many-body system consists, on one hand, of particles formed by quarks bound by gluons—these are baryons and mesons, collectively known as hadrons. On the other hand, it also includes clusters of nucleons bound together by nuclear forces, known as atomic nuclei. Therefore, one of the major goals in nuclear physics, particularly when focusing on the former, is to understand the physical properties of various hadrons—their masses, lifetimes, spins, parities, radii, production probabilities, and interactions—through the depiction of quarks.

In the modern era, renowned physicists established the Standard Model, which describes interactions between particles based on quantum field theory. In the Standard Model, elementary particles are categorized into three generations of six flavors of quarks and leptons that make up matter, gauge bosons that mediate interactions, and the Higgs boson, which provides "bare" mass to the particles. With the discovery of the Higgs boson at CERN's LHC in 2012 [1, 2], all 17 elementary particles in the Standard Model have now been verified experimentally.

The Standard Model encompasses Quantum Chromodynamics (QCD), which is the first-principle theory describing strong interactions. In QCD, quarks (and antiquarks) with color charge couple with gluons, which also carry color, to form color-neutral hadrons. This coupling has an important property: as energy increases, the coupling constant weakens (a phenomenon known as asymptotic freedom), whereas in the low-energy region, the coupling constant exceeds 1 and grows, making it impossible to isolate quarks individually. It creates a theoretical problem; while quantum perturbative calculations are available for dynamic properties like high-energy hadron production, they are no longer applicable for static properties such as hadron masses or nuclear forces. In recent years, lattice QCD calculations, which were pioneered by M. Creutz [3] based on the lattice gauge theory proposed by K. Wilson [4], have been actively studied using massive computational resources to simulate the static properties of hadrons based on first

principles (for example refs. [5–8]). Yet, this approach remains in a developmental stage, and descriptions of hadrons in low-energy regions still rely on effective field approximations. Therefore, it is crucial to provide precise data through experiments to clarify the model dependence inherent in these approximate and effective theoretical calculations, and to substantiate the validity of these theories. Thus, we hold in our heart an unsatisfied desire to understand, in a unified and consistent manner, how hadrons acquire their mass and how interactions between colorless hadrons occur.

1.2 The $\eta'(958)$ meson

The η' meson is a type of meson, which is a color-neutral composite particle formed by a pair of quark and antiquark. It is known to have a mass of $m_{\eta'} = 957.78$ MeV/c^2, a spin of $J = 0$, parity of $P = -1$, and an isospin of $I = 0$ [9].

Here, it is essential to introduce isospin, one of the important properties of hadrons. Isospin is a quantum number introduced based on the fact that protons (composed of uud quarks) and neutrons (composed of udd quarks), which form atomic nuclei, exhibit very similar properties aside from their electric charge. By analogy with the spin-up and spin-down states of an electron, isospin is introduced with the idea that these particles are two different states of the same particle, the "nucleon." In other words, the magnitude of isospin for nucleons is $\frac{1}{2}$, and the z component is given by

$$\hat{I}_z \left|p\right\rangle = +\frac{1}{2} \left|p\right\rangle \tag{1.1}$$

$$\hat{I}_z \left|n\right\rangle = -\frac{1}{2} \left|n\right\rangle . \tag{1.2}$$

One can discribe other hadrons in terms of isospin, too, by extending this concept. For example, π mesons exist in three forms— π^+, π^0 and π^- depending on their electrical charge and are represented as particles with an isospin $I = 1$. The z components of π mesons' isospin are expressed as

$$\hat{I}_z \left|\pi^+\right\rangle = + \left|\pi^+\right\rangle \tag{1.3}$$

$$\hat{I}_z \left|\pi^0\right\rangle = 0 \tag{1.4}$$

$$\hat{I}_z \left|\pi^-\right\rangle = - \left|\pi^-\right\rangle . \tag{1.5}$$

In the quark model established later, isospin is understood in terms of the flavor $SU(2)$ group at the quark level, represented by the two components of the u and d quarks. The crucial point is that isospin is always conserved in strong interactions, making it a particularly useful quantum number for classifying hadrons.

Then, by adding the next lightest quark, the s-quark, the quark model was extended to $SU(3)$ symmetry, as proposed by M. Gell-Mann [10–12]. His model successfully classified many baryons

and mesons that had been discovered up to that time. Furthermore, its validity was confirmed in 1964 by the discovery of the Ω^- baryon, which had a strangeness of $S = -3$ [13].

Now, consider the composition of mesons as described by the quark model. Each quark and antiquark has a spin of $J = \frac{1}{2}$, and a pair of these can form either a spin-0 or spin-1 state. When one considers the case where the relative orbital angular momentum $L = 0$ between the quark and antiquark, one finds that the spin-parity of the meson can be either 0^- or 1^+. The former is known as a pseudoscalar meson, which includes the ground states of mesons such as the π, K, η and η' mesons. On the other hand, the latter is known as a vector meson, which includes mesons such as the ρ, ω and ϕ. The tensor product of the quark-antiquark pair, expressed by the fundamental representation of $SU(3)$ symmetry, decomposes as follows:

$$3 \otimes \bar{3} = 8 + 1. \tag{1.6}$$

The weight diagram in the following Fig. 1.1 and Fig. 1.2 plots the pseudoscalar and vector meson $8+1$ multiplets in the I_z-Y plane (Y represents hypercharge $Y = B+S$. For mesons, the baryon number is always 0, so the hypercharge Y always matches the strangeness S.). For each case, there are three overlapping states with $I_z = 0$ and $Y = 0$. Focusing on the pseudoscalar mesons, one of these three states has a total isospin $I = 1$ and is distinguished from the other two. This is the previously mentioned π^0 meson, whose quark composition is:

$$\pi^0 = \frac{1}{\sqrt{2}} \left(d\bar{d} - u\bar{u} \right). \tag{1.7}$$

The remaining two states both have total isospin $I = 0$, and are labeled as η_1 and η_8 depending on whether they belong to the octet or singlet of $q\bar{q}$ combinations:

$$\eta_8 = \frac{1}{\sqrt{6}} \left(u\bar{u} + d\bar{d} - 2s\bar{s} \right) \tag{1.8}$$

$$\eta_1 = \frac{1}{\sqrt{3}} \left(u\bar{u} + d\bar{d} + s\bar{s} \right). \tag{1.9}$$

These η_1 and η_8 states are distinguished as independent states in a theory where flavor $SU(3)$ symmetry holds completely. However, in reality, this flavor $SU(3)$ symmetry is broken due to differences in the intrinsic masses of the quarks, causing mixing between η_1 and η_8. As a result, the two eigenstates of mass, η and η', can be expressed in terms of η_1, η_8, and the mixing angle θ as follows:

$$\begin{bmatrix} \eta \\ \eta' \end{bmatrix} = \begin{bmatrix} \cos\theta & -\sin\theta \\ \sin\theta & \cos\theta \end{bmatrix} \begin{bmatrix} \eta_8 \\ \eta_1 \end{bmatrix} \tag{1.10}$$

And this η' meson is the protagonist of the present thesis. The mixing angle θ here has been discussed by various theoretical and experimental research groups. According to the latest summary from the PDG [9], this angle is relatively small, approximately between -20 and -10 degrees. Therefore, η and η' are essentially composed mostly of the contributions from the octet component η_8 and the singlet component η_1, respectively.

The η' meson was independently discovered in 1964 (the same year as the discovery of the Ω^- baryon!) by G.R. Kalbfleisch *et al.* [14] and M. Goldberg *et al.* [15], in a hydrogen bubble

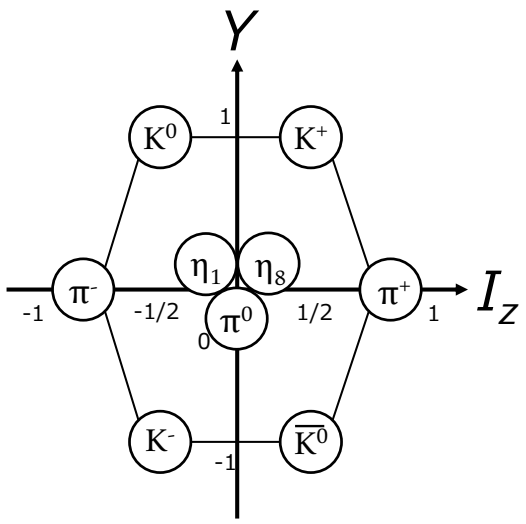

Fig. 1.1: The classification of pseudoscalar mesons on the weight diagram.

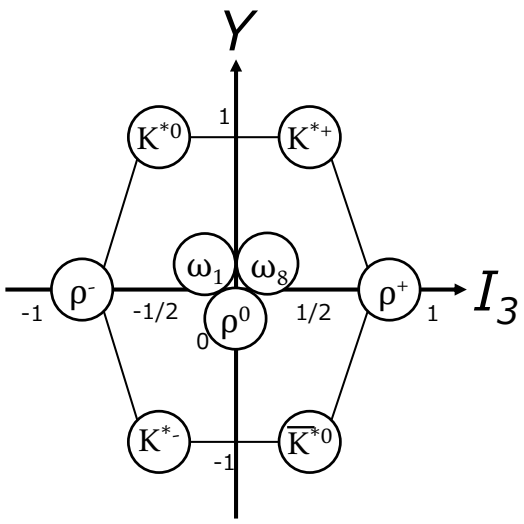

Fig. 1.2: The classification of vector mesons on the weight diagram.

chamber exposed to a K^- beam. The author speculates that the reason for this discovery's historical delay compared to other mesons and baryons, including scalar mesons, was solely due to the difficulty arising from its large mass. The unique mass of η' has attracted the attention of physicists for many years, and efforts have been made to understand it. As mentioned earlier, the mass of η' is $m_{\eta'} = 957.78$ MeV/c^2, which is exceptionally heavy compared to its brothers and sisters ($m_\pi \approx 140$ MeV/c^2, $m_K \approx m_\eta \approx 500$ MeV/c^2). The mechanism by which η' acquires this large mass is closely related to the symmetrical structure of QCD and is currently thought to be caused by the explicit breaking of the axial U_A (1) symmetry in the Lagrangian [16–19]. Recently, the mass of η' has become a topic of more active discussion. This renewed interest originated from several theoretical groups suggesting that, in a finite density medium, partial restoration of chiral symmetry breaking could lead to a reduction in the η' mass. The mass reduction of the η' meson at nuclear density could be interpreted as an attraction between the nucleus and η' [20–23]. Furthermore, numerical simulations conducted by multiple groups have led to the intriguing conclusion that this attraction is strong enough to form bound states between η' and nuclei, namely, η'-mesic nuclei. Attempts to experimentally observe this interesting state, have been conducted since the beginning of this century at GSI in Germany [24] and SPring-8 in Japan [25]. So far, these experiments have not succeeded in discovering a definitive peak indicating the existence of such a bound state. However, both collaborations have planned upgrades to improve experimental data and acquire additional data. In this way, the latest developments in research on the mass of η' have generated great anticipation, as they could potentially lead to a deeper understanding of the mass acquisition mechanism of hadrons.

1.3 Elementary process of the η' meson production off a nucleon

1.3.1 Overview

In the 1950s, R. Hofstadter *et al.* conducted elastic scattering experiments off protons and atomic nuclei using an electron beam [26, 27]. This series of experiments achieved two major accomplishments: first, it measured the Wood-Saxon-form charge distribution of various nuclear targets, leading to the discovery of the saturation of nuclear density. Second, it revealed that the proton itself has a finite charge distribution with a radius of approximately 0.8 fm, suggesting that the proton is a composite particle formed by intrinsic particles. This marked the beginning of hadron physics research using electron scattering.

Then, with the remarkable advances in accelerator technology scince the late 1960s, it became possible to perform inelastic scattering from protons, namely the $e + p \to e + p + X$ reaction, using GeV-order electron beams. The reaction probability for the inelastic scattering, *i.e.*, the cross section, was found to exhibit different behaviors depending on energy levels. Just above the energy threshold and in regions relatively close to it, the cross section forms several peaks with specific widths at certain energy values. Each of these peaks corresponds to short-lived nucleon excited states (known as Δ and N^* baryon resonances) that appear in the intermediate state of the reaction. In other words, a proton receives energy from electron scattering and changes into a nucleon resonance which promptly decays into a final-state proton and meson. Thus, one can understand the energy spectrum of baryon resonances by measuring the cross section, and can determine their spin and parity by measuring its angular distributions (this is true not only for reactions using electron scattering but also for experiments using photon and hadron beams). On the other hand, as the energy transferred to the proton increases, the peak structure of the cross section disappears, leaving only a smooth distribution. This non-resonant behavior can be understood, from the perspective of hadron excitation, as an overlap of many states with much shorter lifetimes. However, at the same time, it was found that as the four-momentum transfer $Q^2 = -(p_e - p_{e'})^2$ from electron scattering reaches regions above several GeV, the cross section asymptotically approaches quasi-free scattering with point-like particles—known as partons inside the proton. In other words, by increasing the energy of the electron beam, the scattering target becomes not the nucleon itself but more microscopic particles, such as quarks and gluons. This scattering phenomenon is known as Deep Inelastic Scattering (DIS) of the proton, and provided direct evidence for the quark model. The three physicists, J.I. Friedman, H.W. Kendall, and R.E. Taylor, who made significant contributions to establishing this experiment, were awarded the Nobel Prize in Physics in 1990 [28, 29].

The electroproduction of mesons near threshold energy using an electron beam closely resembles the production using a photon beam, *i.e.,* photoproduction. This resemblance arises not only because both processes involve electromagnetic interactions mediated by QED but also because, in the low Q^2 region of electroproduction, the One-Photon-Exchange Approximation (OPEA)—in which only a single virtual photon is exchanged between the electron and the target proton—holds sufficiently well. In other words, electroproduction in the relatively low-

energy region can essentially be described as virtual-photoproduction, and this description takes a mathematical form very similar to that of real-photoproduction. The kinematic description using OPEA, which is necessary for the present thesis, is presented in Sec. 2.1 and, in more detail, in Appendix A. Here, the author wishes to emphasize that both photoproduction and electroproduction of mesons in the resonant region serve as valuable probes for exploring the excited states of nucleons coupled to the reaction vertex. In particular, not all resonances predicted by the quark model have been experimentally verified. Such undiscovered states are referred to as "missing resonances." Experimental searches for these states are ongoing, and theoretical discussions are also being conducted based on the framework of couplings between hadrons and real- or virtual-photons to identify the resonances necessary to explain the obtained data. For the author, taking an experimental perspective, the mission of providing reliable data covering various reaction channels, angular dependencies, and energy ranges is crucial for uncovering the energy structure of nucleons, which are composed of quarks and gluons.

In the present thesis, the author discusses the electroproduction experiment of the η' meson. The final state consisting of $\eta' + p$ measured in the experiment exhibits several unique characteristics. First and needless to say, due to the significantly large mass of η' compared to other pseudoscalar mesons, the energy threshold is high at $E_{\rm th} = 1986$ MeV. Consequently, the experiment is sensitive to higher energy resonances, specifically those around 1900 to 2200 MeV, among which there are several resonances whose existence remains under discussion. Additionally, focusing on the isospin of the $\eta' + p$ final state, the proton has an isospin of $I_p = \frac{1}{2}$, and η' has an isospin of $I_{\eta'} = 0$, resulting in a total isospin of $I_{\rm total} = \frac{1}{2}$. This constrains the isospin of the intermediate state in the reaction to $I_{\rm res} = \frac{1}{2}$. In other words, Δ resonances with isospin $I_\Delta = \frac{3}{2}$ are excluded from coupling with the $\eta' + p$ final state, and only N^* resonances with isospin $I_{N^*} = \frac{1}{2}$ can decay into the $\eta' + p$ final state. This important property reduces the number of resonances that need to be investigated, simplifying the analysis of the experimental results by decreasing the number of free parameters in theoretical calculations. (This property of isospin applies equally to the $\eta + p$ reaction channel because η and η' possess identical quantum numbers. However, it is distinguished from the production of isovector π mesons.)

To date, while multiple experimental datasets exist for the photoproduction of η' mesons, there are no reported datasets for the cross section of η' electroproduction. The author speculates that this lack of experimental data might be attributed to the technical demands of simultaneously measuring high-energy scattered electrons and protons, as well as the significant background events inherent in high-energy reactions. Furthermore, likely due to the absence of experimental data, there are no theoretical calculations describing η' electroproduction. On the other hand, a large collection of research exists for η' photoproduction in both theory and experiment. Since electroproduction and photoproduction are reactions with considerable similarities in their descriptions, examining the behavior of η' photoproduction serves as a valuable reference for understanding the expected results of η' electroproduction in the preset study. In Fig. 1.3, a summary from the EtaMAID theoretical group compares the photoproduction databases of (a)

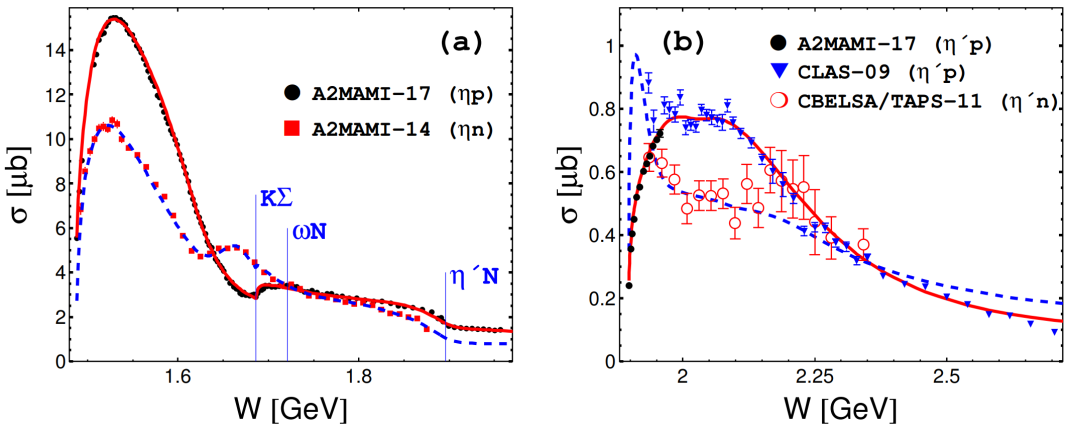

Fig. 1.3: The W dependence of the total cross-section of ηN (a) and $\eta' N$ (b) photoproduction measured so far [30]. The red-solid and blue-dashed lines represent the calculations by the calculations with the EtaMAID model for $\eta p/\eta' p$ and $\eta n/\eta' n$ channels, respectively.

η mesons and (b) η' mesons with the theoretical calculation using the model EtaMAID2018 [30]. In the graphs, the horizontal axis represents the energy W in the center-of-mass (CM) frame of the final state, and the vertical axis shows the total cross section σ. Additionally, Fig. 1.3 includes data and theoretical calculations for $\eta + p$ and $\eta' + p$ production using a hydrogen target, as well as $\eta + n$ and $\eta' + n$ production using a deuterium target. Looking first at η photoproduction, a characteristic energy dependence is observed, beginning just above the threshold $E_{\mathrm{th}} = 1486$ MeV with a prominent peak around 1500 MeV. This dominant peak, primarily formed by the presence of the nuclear resonance $N\,(1535)\,\frac{1}{2}^{-}$ (formerly denoted as $S_{11}\,(1535)$), located 49 MeV above the threshold, has been explained by theoretical partial-wave analysis and strongly supports the existence of this resonance. In contrast, η' photoproduction lacks such a dominant peak structure, instead showing a more gradual, hill-like pattern (though data on $\eta' + n$ production remains sparse and uncertain). This is because the high energy threshold allows for a larger number of N^* resonances to couple and overlap. Thus, referencing past experimental data and calculations (although in photoproduction) underscores the importance, at a point of view of experiment, of accurately measuring the elementary process of η' meson production, which may contain information on uncertain resonances. Specifically, it is crucial to obtain angular dependence data to identify the spin-parity of these candidates.

1.3.2 Past experiments with the real photon beam

Here, the author introduce a more detailed summary of individual experiments on η' production with a real photon beam conducted so far. In these experiments, the real photon beam—also referred to as a γ beam—is generated by inducing bremsstrahlung or backward Compton scattering on electrons accelerated by an accelerator, and it is then directed at a stationary proton target within the laboratory. Although the methods for measuring the final states vary across these experiments, they all capture the decay products from the η'.

The earliest measurements of the $\eta' p$ final state were performed by analyzing the trajectory of particles. As previously mentioned, the discovery of the η' meson itself was made in 1964 by G.R. Kalbfleisch *et al.* [14] and M. Goldberg *et al.* [15] with the hadronic reactions. Just four years later, in 1968, R. Erbe *et al.* (ABBHHM collaboration) conducted a measurement of the η' meson using a photon beam, and reported 11 events of η' production [31]. This was the first experiment to measure the cross section of the $\gamma p \to \eta' p$ reaction. In 1976, W. Struczinski *et al.* (AHHM collaboration) reported 7 events of η' photoproduction using a streamer chamber [32]. In this experiment, photon beams were tagged for each event by capturing the electrons after the scattering.

The first measurement of η' photoproduction with advanced accelerator and counter techniques was reported in 1998 by R. Plötzke *et al.* (SAPHIR collaboration) [33]. This experiment was conducted at the Electron Stretcher Accelerator (ELSA facility) at the University of Bonn. They irradiated a liquid hydrogen target with a γ beam generated by bremsstrahlung and used a magnetic spectrometer SAPPHIR covering a solid angle of 4π to detect five charged particles in the decay chain of $\gamma p \to p\eta' \to p\pi^+\pi^-\eta \to p\pi^+\pi^+\pi^-\pi^-\pi^0$. As a result, an η' peak of 330 events was successfully observed on the proton missing mass spectrum. They reported for the first time the differential cross section in which the energy range 1.44 GeV $< E_\gamma <$ 2.64 GeV was divided into 7 bins and the angular range $-1.0 < \cos\theta^{\mathrm{CM}}_{\gamma\eta'} < 1.0$ was divided into 5 bins (see Fig. 1.4). It was found by this experiment that the $\cos\theta^{\mathrm{CM}}_{\gamma\eta'}$ dependence with cross section monotonically increases toward the forward angles. They applied linear functions for the data fitting and then discussed the possibility of coherent generation of S_{11} and P_{11} partial waves based on this behavior.

In the 21st century, the CLAS collaboration reported experimental results with significantly higher precision twice, in 2006 and 2009 [34, 35]. In the present thesis, these two experimental datasets are labeled as "CLAS06" and "CLAS09" to distinguish them. The CEBAF Large Acceptance Spectrometer (CLAS) is an experimental collaboration conducted at the Thomas Jefferson National Accelerator Facility (JLab) Hall-B, and it is also the name of the detector system used in the experiment. A photon beam was extracted by bremsstrahlung from a continuous electron beam and then irradiated onto a liquid hydrogen target to induce a reaction. Charged particles in their final state were detected using a group of particle detectors installed in a toroidal magnetic field. In CLAS06 and CLAS09, 2×10^5 and more events of η' were measured. This large statistical data provides the measurement of angle-dependent cross section with significantly improved statistical errors. The solid angle of the CLAS detector is in the range $-0.8 < \cos\theta^{\mathrm{CM}}_{\gamma\eta'} < 0.8$, but they also report the total cross section, which was obtained by applying acceptance correction based on simulation. Another advantage of the measurements is the wide energy range of 1.505 GeV $< E_\gamma <$ 3.694 GeV in CLAS09 (which corresponds to 1.925 GeV $< W <$ 2.795 GeV). This is why the author states that the CLAS collaboration provides highly reliable data about η' photoproduction. In 2017, they also reported measurements of the photon beam asymmetry Σ using a linear polarized photon beam [36].

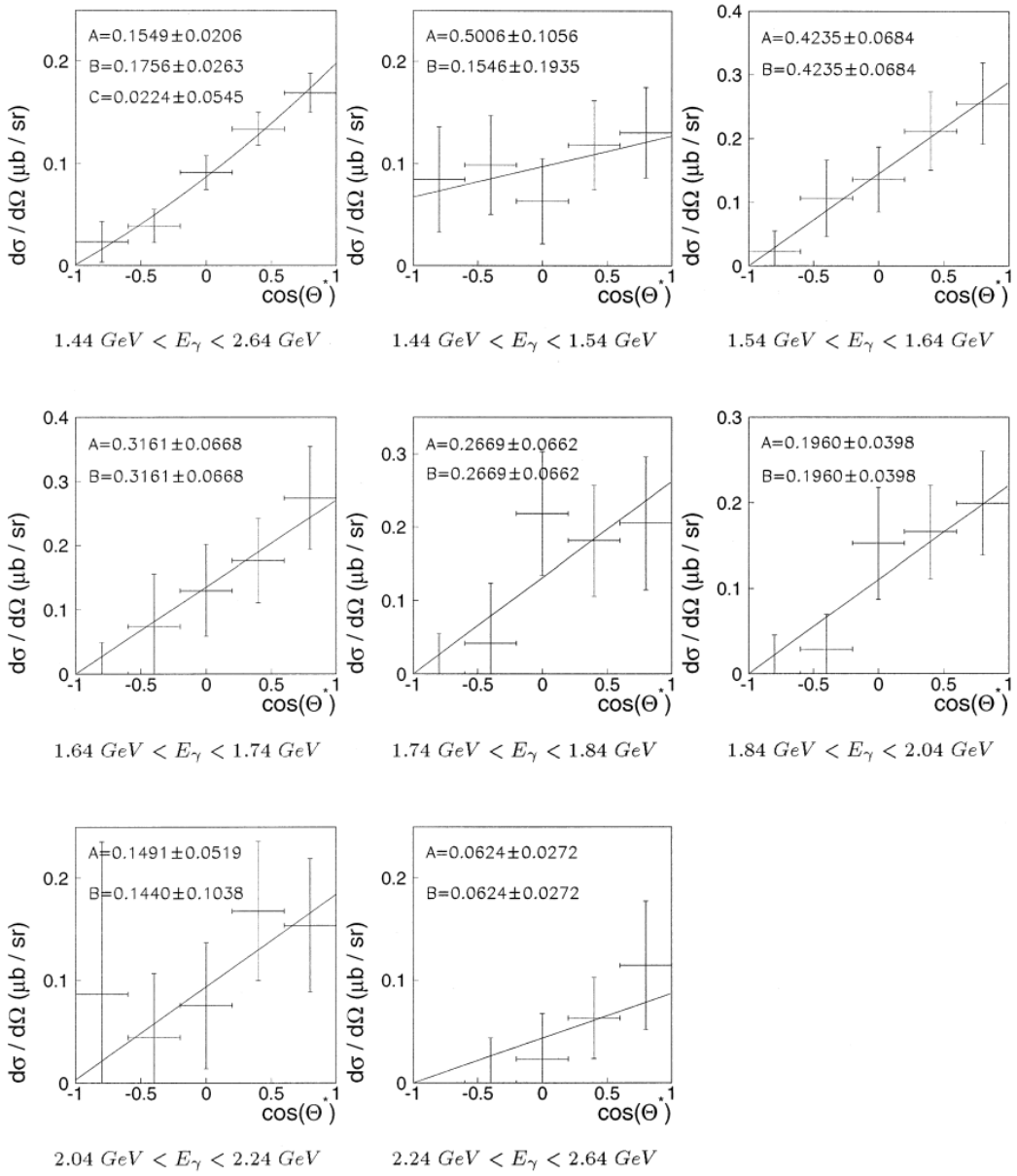

Fig. 1.4: Angular dependence of η' photoproduction measured by SAPHIR [33].

A measurement by the CBELSA/TAPS collaboration was also reported at exactly the same time as CLAS09 [37]. This experiment was conducted at the ELSA facility and was unique in that it used a series of electromagnetic calorimeters. In this experiment, the Crystal Barrel (CB) calorimeter made of CsI crystal, covering 30 degrees $< \theta_{\gamma p}^{\mathrm{Lab}} <$ 168 degrees around the target, and the TAPS calorimeter made of BaF_2 crystal, covering 5 degrees $< \theta_{\gamma p}^{\mathrm{Lab}} <$ 30 degrees at forward angles, were used. These calorimeters covered 99 % of the solid angle and measured the $\eta' \to \pi^0\pi^0\eta \to 6\gamma$ decay mode from the $\gamma p \to \eta' p$ reaction. As well, a photon beam generated by bremsstrahlung was irradiated onto a liquid hydrogen target. They identified 5.1×10^3 events of η' to report the cross section in the photon energy range of 1.5 GeV $< E_\gamma <$ 2.5 GeV. It

should also be noted that they measured the cross section of the quasi-free $\gamma n \to \eta' n$ reaction using a deuteron target (reported in 2011) [38].

The data reported by the A2 collaboration at MAMI in 2017 is the most accurate measurement of the η' photoproduction cross section near the threshold, specifically in the lower W region [39]. The Crystal Ball (CB) calorimeter made of NaI(Tl) scintillator and the TAPS calorimeter were combined and installed in the Mainz Microtron (MAMI) A2 tagged photon facility at Mainz University, surrounding the hydrogen target which was irradiated with γ beams from bremsstrahlung radiation. The neutral decay modes of $\eta' \to \gamma\gamma$ and $\eta' \to \pi^0\pi^0\eta \to 6\gamma$ after the $\gamma p \to \eta' p$ reaction were measured. The cross section close to the energy threshold $W = 1896$ GeV was investigated in detail by the present measurement, and the results strongly support the existence of the N $(1895)\, \frac{1}{2}^-$ resonance just below the threshold.

The experiment reported in 2015 by the LEPS collaboration is unique among other experiments mentioned above due to its focus on measuring η' at ultra-backward angles [40]. Although reactions at forward or backward angles relative to the beam axis are sensitive to the presence of high spin resonances, experimental data are very limited due to the difficulty in setting up measurements. They applied a deep-UV 257 nm laser to the 8 GeV electron beam provided by the SPring-8 facility and generated a photon beam by backward Compton scattering with energy up to $E_\gamma < 3.0$ GeV [41, 42] to irradiate it onto a liquid hydrogen target. Scattered protons were detected using the LEPS forward magnetic spectrometer, and at the same time, emitted charged pions were detected by a time projection chamber surrounding the target. This experiment reported the differential cross section of η' photoproduction in the angular range of $-1.0 < \cos\theta^{\mathrm{CM}}_{\gamma\eta'} < -0.8$, which shows an up-and-down dependence for changes in W [40]. Fig. 1.5 shows the W-dependence of the backward differential cross section as reported by the LEPS collaboration. They pointed out that there might be a bump structure around 2.35 GeV. Additionally, they observed subtle ups and downs across other W regions. A theoretical calculation that fully explains this behavior has not yet been achieved.

1.3.3 Theoretical background

Since this reaction channel has not been experimentally measured until now, no theoretical calculations currently exist to describe η' electroproduction with finite $Q^2 > 0$. However, various calculations have been developed to describe photoproduction, which ensures $Q^2 = 0$. The earliest theories seem to have been designed in the 1990s, matching the improvement of experimental accuracy of that time [44, 45]. The η and η' mesons share the same quantum numbers except for mass, which theoretically allows to be described within a unified framework. Among such theoretical calculations, one can find some models based on the quark model in Refs. [46, 47]. However, the most widely referenced and useful theories are those by EtaMAID [30, 45, 48], BnGa [49, 50], and Nakayama *et al.* [43, 51], which are constructed using a framework known as the "isobar model." The isobar model is a framework for describing the electro- and photoproduction of mesons, using an effective Lagrangian that operates within the degrees of freedom

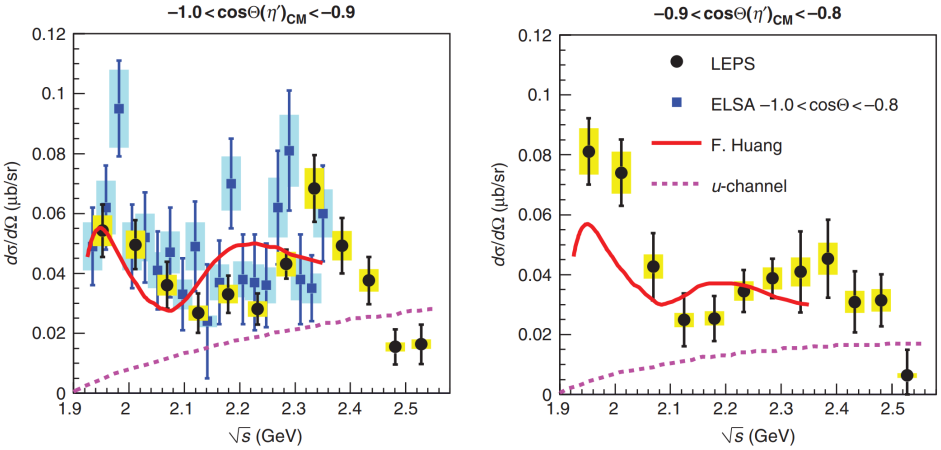

Fig. 1.5: Differential cross section of η' photoproduction at ultra-backward angles measured by LEPS (Fig. from ref. [40]. Data of CBELSA/TAPS [37] and isobar model calculation by F. Huang *et. al.* [43] are also shown.

of hadrons, meaning it does not get into the quark level. In many models, only the lowest-order perturbations in the s, t, and u-channels, known as "tree-level" diagrams as shown in Fig. 1.6, are considered without taking loops into account (see also Fig. 1.6). Various nucleon excited states are assumed as intermediate states that couple to the initial and final states, in addition to the ground state of the nucleon. The strength of the coupling with each state represents an uncertain parameter in theoretical calculations, and these parameters are determined by fitting them to databases of experiment. Therefore, each model differs in its characteristics depending on which resonances are assumed as intermediate states and which resonances have the strongest coupling that predominantly influences the cross section, even among theoretical calculations based on similar isobar models.

On the other hand, when one focuses on other meson production channels, theoretical models for electroproduction of π and K mesons have already been developed and are currently available [52–56]. In particular, the calculations for the elementary process of kaon electroproduction also plays a fundamental role in hypernuclear spectroscopy experiments, giving a crucial foundation for understanding the cross section of hypernuclei. Theoretical descriptions of meson electroproduction with finite $Q^2 > 0$ have been systematically organized based on OPEA in constructing these models, and photoproduction can be generalized as a special case where $Q^2 \to 0$. Therefore, if this unified framework can be extrapolated to the case of η' electroproduction, a new theoretical calculation could be constructed, providing useful comparisons for interpreting the experimental results obtained in the present study. Of course, for experimental physicists like the author, such a development is by no means an easy task. Fortunately, however, the author has been able to discuss some aspects of this work with experts in theoretical physics who are developing kaon electroproduction models known as BS models [57, 58]. In particular, the differential cross section of η' electroproduction, measured for the first time in the present study, adds the new degree of freedom of the Q^2 dependence to past photoproduction experiments. It

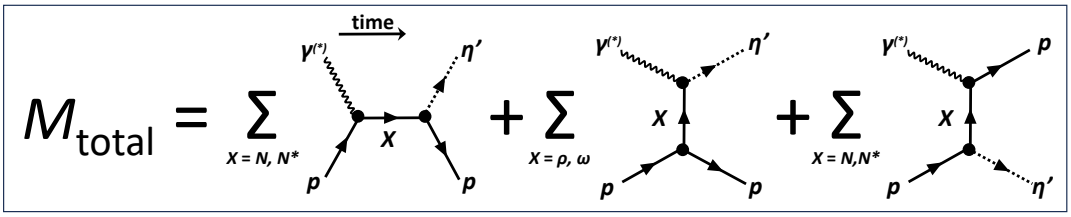

Fig. 1.6: Tree-level Feynman diagrams depicting s-, u-, and t-channel exchanges for η' real- or virtual-photoproduction as an example of an isobar model. The first and third terms (s- and u-channel coupling respectively) contain not only ground state nucleon couplings but also resonance couplings.

is worth examining whether the theoretical framework that successfully describes finite $Q^2 > 0$ scattering processes for other mesons, such as π and K mesons, can also be applied to η' production. Furthermore, the quenching of the cross section at finite $Q^2 > 0$ exhibits different behavior corresponding to the spin-parity of each resonance. By measuring these subtle differences by an experimental measurement, the author hope to give new theoretical constraints in the context of study of meson and baryon resonances.

1.4 Purpose of the present research

As mentioned several times in the previous sections, the purpose of the present study is to measure the differential cross section of the electroproduction of the η' meson. The present thesis reports the first experimental measurements of η' electro-induced production at finite $Q^2 > 0$. Additionally, the author aims to analyze the behavior of η' production by comparing the results of the present study with newly constructed theoretical calculations based on the One-Photon-Exchange Approximation (OPEA) and the isobar model.

However, the present experiment, JLab E12-17-003 conducted in 2018, was not originally designed or dedicated for η' production. The author and collaborators initially planned to measure the $^3\mathrm{H}\,(\mathrm{e},\mathrm{e}'\mathrm{K}^+)nn\Lambda$ reaction as part of the experimental campaign with a tritium target at that time. The $nn\Lambda$ state, which the author does not discuss in detail here, is a hypernucleus with atomic number $Z = 0$ and mass number $A = 3$. It has been a subject of debate regarding its existence since the HypHI collaboration reported a controversial enhancement in the $t + \pi^-$ invariant mass spectrum in 2013 [59]. The principal goal of JLab E12-17-003, at least in the experimental proposal, was to clarify the existence of this $nn\Lambda$ state through the $(e, e'K^+)$ reaction missing mass spectroscopy, using a cooled tritium target and two high-resolution magnetic spectrometers. During the experiment, the authors and collaborators also collected a substantial amount of ^{1}H target data for energy scale calibration. This method is commonly used in hypernuclear spectroscopy experiments with electromagnetic production, where the energy scale of the missing mass is calibrated using two peaks from the $^1\mathrm{H}\,(e, e'K^+)\,\Lambda/\Sigma^0$ reactions, and

its approarch was adopted also for the present experiment. The ^{1}H data, which was collected without any particle identification at the online trigger level, naturally includes scattered pions and protons in addition to kaons. Then one can obtain the spectrum of η' electroproduction by selecting the $^1\mathrm{H}\,(e, e'p)\,\eta'$ reaction channel with this data. As the author will mention later, the $p_{e'}$-$p_{p_{\mathrm{scat}}}$ correlation in η' production kinematics lies between the $p_{e'}$-p_{K^+} correlation in Λ and Σ^0 production kinematics, allowing η' events to naturally mix into the data acceptance of the hypernuclear experiment, and making it possible to analyze them. If such valuable data on η' production can be obtained simultaneously as a byproduct of the Λ hypernuclear spectroscopy, this new attempt is interesting. In the present experiment, only the scattered electron and proton were measured, with the η' identified solely by the peak in the missing mass spectrum. Such measurements typically contain a large number of background events, and indeed, in the data from the present experiment, numerous broad multi-meson production events are present under the η' peak. Nevertheless, thanks to the high momentum resolution of the spectrometers used in the present experiment, the author was able to successfully identify a significant number of η' production events. As seen in the previous section, all past photoproduction experiments derived production cross sections by selecting a specific decay chain of the η' meson and dividing by its branching ratio. This method might involve unexpected systematic errors. The present experiment, however, provides the first semi-inclusive measurement independent of decay particles from the η', which the author believes offers highly reliable data. Moreover, It should also be noted that the angular region covered in the present experiment is mostly $\cos\theta^{\mathrm{CM}}_{\gamma\eta'} \approx -1$, which corresponds to very backward angles. This extreme angular setting was designed based on the physical characteristic that the differential cross section of hypernuclei, the intended research thema of the present experiment, increases for forward-scattered K^+ mesons. Applied to the $(e, e'p)$ reaction, this setting means that the proton is detected in the very forward direction, and the generated η' is scattered almost 180 degrees backward in the CM frame. Generally, the angular dependence of the differential cross section at forward and backward angles is significantly influenced by underlying resonances with high spin. Therefore, the author expect that, by providing the cross section data at such unique angles—where past databases are limited, the present experiment may yield new information or constraints for theories regarding N^* resonances strongly coupled to the $\eta' p$ channel.

Chapter 2

Experiment

2.1 Principle

The η' mesons are produced with the $e+p \to e+p+\eta'$ reactions in the present measurement. A schematic diagram based on the One-Photon-Exchange Approximation (OPEA) of the reaction is shown in Fig. 2.1. A high-energy electron hits a fixed proton target and is scattered with some probability of virtual photon emission. The virtual photon (γ^*) with the energy and momentum $q = (\omega, \boldsymbol{q}) = (E_e - E_{e'}, \boldsymbol{p}_e - \boldsymbol{p}_{e'})$ reacts with a proton to produce a η' meson. The momenta of scattered electrons (e') and recoil protons ($p_{\rm scat}$) are measured by two magnetic spectrometers. The mass of the missing particle, *i.e.* the missing mass, is obtained using the following equation deduced from the energy and momentum conservation,

$$m_{\rm X} = \sqrt{\{(E_e - E_{e'}) + m_p - E_{p_{\rm scat}}\}^2 - \{(\boldsymbol{p}_e - \boldsymbol{p}_{e'}) - \boldsymbol{p}_{p_{\rm scat}}\}^2}. \tag{2.1}$$

Events with the η' productions are observed as a peak on the missing mass spectrum.

In the One-Photon-Exchange Approximation, the triple differential cross section of the electroproduction of meson X is written as

$$\frac{{\rm d}^3\sigma}{{\rm d}E_{e'}{\rm d}\Omega_{e'}{\rm d}\Omega_{\rm X}^{\rm CM}} = \Gamma\left(\frac{{\rm d}\sigma_{\gamma^*}}{{\rm d}\Omega_{\rm X}^{\rm CM}}\right), \tag{2.2}$$

where Γ and $\frac{{\rm d}\sigma_{\gamma^*}}{{\rm d}\Omega_{\rm X}^{\rm CM}}$ are the flux of the virtual photons and the differential cross section in the center of mass (CM) frame of the hadron production by the virtual photon, respectively [60]. Conventionally, quantities for hadrons are described in the CM frame, whereas those for leptons are described in the laboratory frame. An important benefit of OPEA is that, as in this expression, the triple differential cross section can be separated into two parts: electron scattering accompanied by virtual photon emission and the virtual photoproduction of mesons. Then one can understand the reactions with virtual photons ($Q^2 > 0$) by analogy from the reactions with real photons ($Q^2 = 0$) and compare them with each other. Here, Q^2 is the four-momentum transfer with the electron scattering described as

$$Q^2 = -q^2 = 2E_eE_{e'} - 2{m_e}^2 - 2\,|\boldsymbol{p}_e|\,|\boldsymbol{p}_{e'}|\cos\theta_{ee'}. \tag{2.3}$$

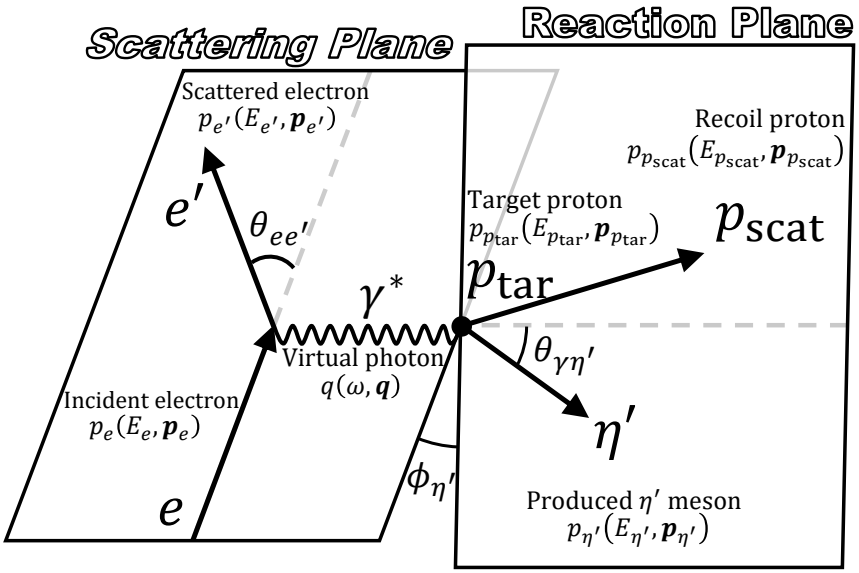

Fig. 2.1: A schematic diagram based on OPEA of the $e + p \to e + p + \eta'$ reaction.

It is worth to be noted that, in the present measurement, the author and collaborators measured the recoil protons instead of the generated η' mesons. The observable is therefore $\frac{\mathrm{d}^3\sigma}{\mathrm{d}E_{e'}\mathrm{d}\Omega_{e'}\mathrm{d}\Omega_p^{\mathrm{CM}}}$ (or $\left(\frac{\mathrm{d}\sigma_{\gamma^*}}{\mathrm{d}\Omega_p^{\mathrm{CM}}}\right)_{\gamma^* p \to p\eta'}$). However, this cross section is equivalent to the above equation since the recoil angle in a two-body reaction in the CM frame is back-to-back. The virtual photon flux Γ is calculated by the following formula using the momentum of the incident and scattered electrons:

$$\Gamma = \frac{\alpha}{2\pi^2 Q^2} \frac{E_\gamma}{1-\epsilon} \frac{E_{e'}}{E_e} \tag{2.4}$$

$$Q^2 = -q^2 = 2E_e E_{e'} - 2{m_e}^2 - 2\left|\boldsymbol{p}_e\right|\left|\boldsymbol{p}_{e'}\right|\cos\theta_{ee'} \tag{2.5}$$

$$\epsilon = \left[1 + 2\frac{\left|\boldsymbol{q}\right|^2}{Q^2}\tan^2\left(\frac{\theta_{ee'}}{2}\right)\right]^{-1} \tag{2.6}$$

$$E_\gamma = \omega + \frac{q^2}{2m_p}, \tag{2.7}$$

where ϵ denotes the transverse polarization of the virtual photons, respectively. One can determine the total number of virtual photons by integrating Γ with the total charge of the beam electrons and the acceptance of the electron spectrometer. Then, the cross section of the $\gamma^* + p \to p + \eta'$ reaction, $\frac{\mathrm{d}\sigma_{\gamma^*}}{\mathrm{d}\Omega_{\eta'}^{\mathrm{CM}}}$, is obtained.

The cross section for virtual photoproduction $\frac{\mathrm{d}\sigma_{\gamma^*}}{\mathrm{d}\Omega_{\eta'}^{\mathrm{CM}}}$ can be expanded as follows depending on the polarization of the virtual photons,

$$\frac{\mathrm{d}\sigma_{\gamma^*}}{\mathrm{d}\Omega_{\eta'}^{\mathrm{CM}}} = \frac{\mathrm{d}\sigma_{\mathrm{T}}}{\mathrm{d}\Omega_{\eta'}^{\mathrm{CM}}} + \epsilon\frac{\mathrm{d}\sigma_{\mathrm{L}}}{\mathrm{d}\Omega_{\eta'}^{\mathrm{CM}}} + \sqrt{2\epsilon\left(1+\epsilon\right)}\frac{\mathrm{d}\sigma_{\mathrm{LT}}}{\mathrm{d}\Omega_{\eta'}^{\mathrm{CM}}}\cos\phi_{\eta'} + \epsilon\frac{\mathrm{d}\sigma_{\mathrm{TT}}}{\mathrm{d}\Omega_{\eta'}^{\mathrm{CM}}}\cos 2\phi_{\eta'}, \tag{2.8}$$

where, the particular contributions of $\frac{\mathrm{d}\sigma_{\mathrm{T}}}{\mathrm{d}\Omega_{\eta'}^{\mathrm{CM}}}$, $\frac{\mathrm{d}\sigma_{\mathrm{L}}}{\mathrm{d}\Omega_{\eta'}^{\mathrm{CM}}}$, $\frac{\mathrm{d}\sigma_{\mathrm{LT}}}{\mathrm{d}\Omega_{\eta'}^{\mathrm{CM}}}$, and $\frac{\mathrm{d}\sigma_{\mathrm{TT}}}{\mathrm{d}\Omega_{\eta'}^{\mathrm{CM}}}$ correspond to the transverse, longitudinal, transverse-longitudinal interference and transverse-transverse interference modes of the virtual photon [60]. The terms "L" and "LT" appear only in reactions with virtual

photons since real photons have only transverse wave components. In the case of $Q^2 \to 0$, $\frac{d\sigma_{\gamma^*}}{d\Omega^{CM}_{\eta'}}$ agrees with that for real photons. Therefore, measuring meson electroproduction in the region of relatively small Q^2, where the cross section approaches that of real photons but is not exactly the same due to the non-zero longitudinal wave component, is quite important for developing theoretical models extended from photoproduction. Moreover, the use of an electron beam allows us to detect protons emitted at approximately 0 degrees relative to the virtual photons and to observe the η' mesons at backward angles. This is another unique characteristic in the present measurement.

A more detailed theoretical description of meson electroproduction can be found in Appendix A.

2.2 Thomas Jefferson National Accelerator Facility (JLab)

The present experiment was performed in an experimental hall, Hall-A at the Thomas Jefferson National Accelerator Facility (JLab). JLab is a national laboratory located in Newport News, Virginia, the United States. It features an accelerator that provides high-luminosity electron beams and includes four experimental halls: Hall-A, B, C, and D (Fig. 2.2).

2.2.1 Continuous Electron Beam Accelerator Facility (CEBAF)

The Continuous Electron Beam Accelerator Facility (CEBAF) at JLab consists of two superconducting linear accelerators (linacs), an electron injector, and arcs for bending the beam. The electron beam can be accelerated up to 12 GeV by circulating through two linacs up to 5.5 times and can be simultaneously supplied to each experimental hall. The maximum beam current and duty cycle are approximately 85 μA and nearly 100 %, respectively. Such a high-current continuous beam is suitable for coincidence experiments that measure reactions on the order of 10 nb, such as the production of hypernuclei. Additionally, due to the RF frequency of 499 MHz at

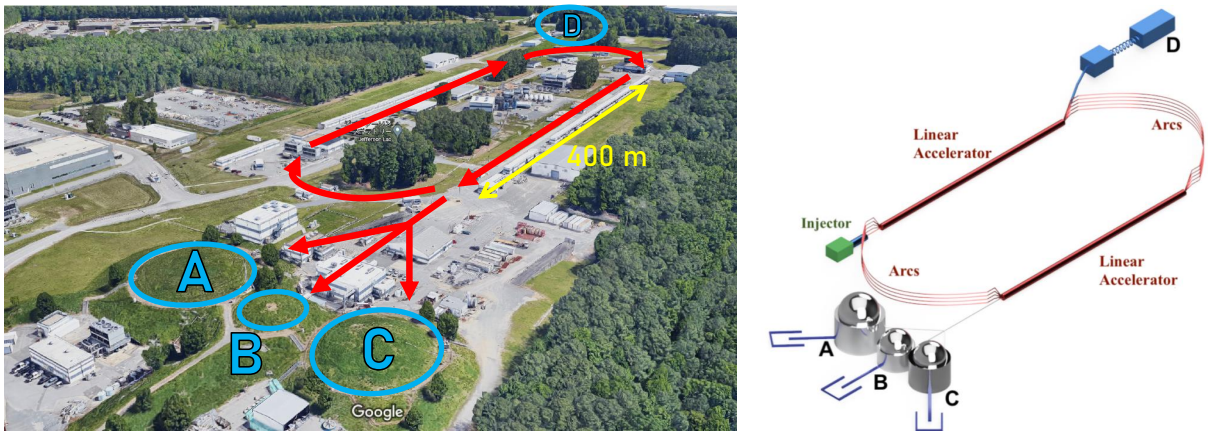

Fig. 2.2: Aerial photograph of JLab [61] and CEBAF's schematic view [62].

Table 2.1: Specifications of CEBAF [63].

Contents	Values
Maximum beam energy (Hall-A,B,C)	11 GeV
Maximum beam energy (Hall-D)	12 GeV
Maximum beam current (Hall-A,C/B)	85 μA/5 μA
Emittance at max. energy (horizontal/vertical)	10 nmrad/2 nmrad
Energy spread at max. energy (Hall-A,B,C)	5×10^{-4}
Energy spread at max. energy (Hall-D)	50×10^{-4}
Bunch length (rms)	$\sim$ 1 ps
Maximum Polarization	80 %

the beam switching yard, the beam has a 2 ns bunch structure at the hall. Table 2.1 shows the typical specifications of CEBAF.

2.2.2 Hall-A beamline

The electron beam is distributed from CEBAF to Hall-A and directed onto the target. In the present experiment, a two-pass beam (having circulated CEBAF twice) was used. The layout inside Hall-A is shown in Fig. 2.3. The Hall-A beamline includes various devices to measure the position, energy, and current of the beam electrons upstream of the target, as well as the High Resolution Spectrometer (HRS) to measure the scattered particles downstream of the target.

The position and direction of the electron beam irradiated onto the target were measured by two Beam-Position Monitors (BPMs) [65]. Each BPM is installed 7.524 m and 1.286 m upstream of the target position. It consists of a cavity with four antennas perpendicular to the beam axis and can measure the direction and relative position of the passing electron by detecting the distance from each antenna to the beam moment by moment. The beam position at the target can be determined within 100 μm, and corresponding magnification at the reference plane is comparable to the positional resolution of tracking detectors. Hence, it is reasonable to assume that the reaction occurred at a single point. Beam measurement by the BPM is non-destructive, but it uses wire scanners called "superharps" for calibration [65]. Superharps are installed adjacent to each BPM and can measure the absolute position of the beam before using the BPM. In the present experiment, the author and collaborators rastered the electron beam to avoid damaging the target system from the heat generated by the beam's energy deposition. The beam can be swung vertically and horizontally by dipole magnets placed 23 m upstream from the target. The frequency and the size of the beam raster were 25 kHz and 2 mm $\times$ 2 mm, respectively. The change in the reaction position perpendicular to the beam axis due to the raster can be calibrated by the BPMs.

The beam energy was determined by a technique called the arc method. Fig. 2.4 shows the outline of the arc method. In this method, the beam energy is obtained from the relationship

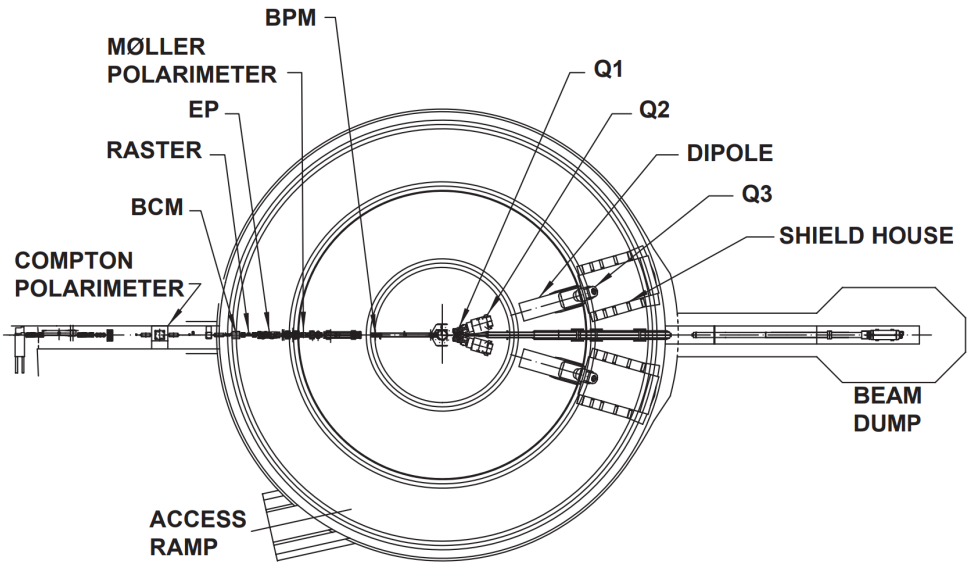

Fig. 2.3: A schematic drawing of the JLab Hall-A beamline [64]. This is a top view of the entire hall. The experimental hall has a diameter of 174 ft. The electron beam is supplied from left to right. The BCM and BPM are the Beam Current Monitor and Beam Position Monitor described in detail in the main text. The Q1, Q2, DIPORE, and Q3, located from the center of the experimental hall downstream, are electromagnets for the two High Resolution Spectrometers (HRSs).

between the beam position passing through the arc section from CEBAF to Hall-A and the magnetic field in the dipole magnets. It is represented by the following formula:

$$|\boldsymbol{p_e}| = k \int \frac{\boldsymbol{B} \cdot d\boldsymbol{l}}{\theta_{\mathrm{bend}}}, \tag{2.9}$$

where $k = 0.299792$ (GeV/c) rad T^{-1} m^{-1}. The arc section consists of nine dipoles with a total length of 40 m. The bending angle of the eight dipoles connected to Hall-A is $\theta_{\mathrm{bend}} = 24.3$ degrees, as measured by the superharps. Although the magnetic field traversed by the beam cannot be directly measured during the experiment, the beam momentum can be determined by measuring the magnetic field of the ninth dipole, which is identical to and powered in series with the other dipoles with NMR ports.

The electron beam charge was measured by Beam Current Monitors (BCMs). Each BCM is located 25 m upstream of the target and consists of a Parametric Current Transformer (PCT) and two resonant-RF cavities enclosed in thermally and magnetically shielded boxes (see Fig. 2.5). The PCT toroid also called Unser monitor [66], and is sensitive against the DC component of the magnetic field by the passing electrons. The advantage of a PCT monitor is that it is self-calibrating. An absolute value calibration between the beam current and the frequency of the PCT toroid can be achieved by passing a known current through a wire inside the beam pipe. However, it is not suitable for long-term continuous measurement, as the offset value of the frequency drifts on the timescale of several minutes. On the other hand, the two RF cavities

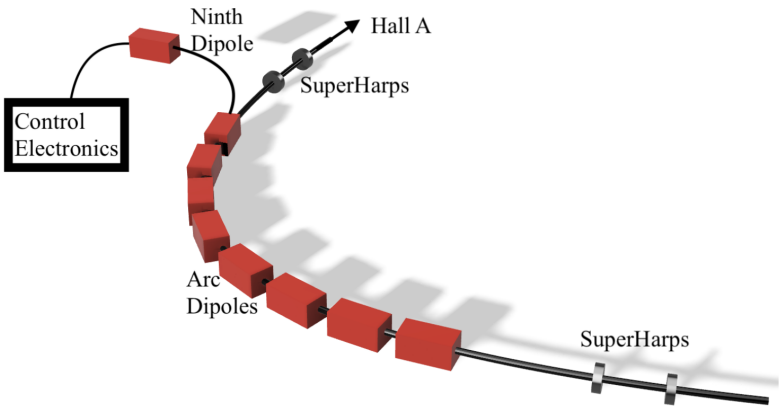

Fig. 2.4: A schematic view of the arc section [62]. The length of this beamline is approximately 40 m. There are nine arc dipoles, each identical, with a bending angle of 34.3 degrees per dipole. The ninth dipole is placed separately from the other eight for magnetic field measurement.

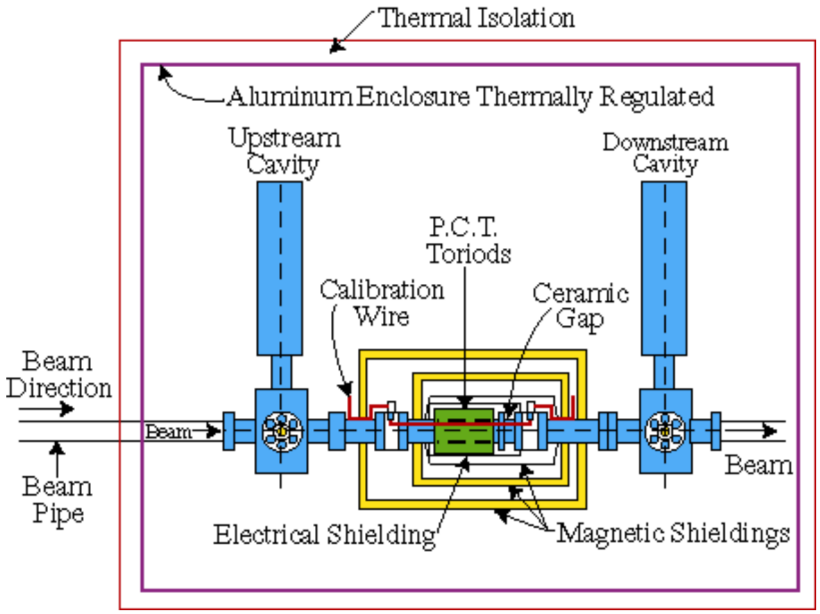

Fig. 2.5: A schematic drawing of the Beam Current Monitor (BCM) [67]. The PCT troid is thermally and electrically isolated and sandwiched by two RF cavities.

sandwiching the PCT have much more stable output, maintaining a precision of ±5 % for a few months, although they require an external calibration source. Therefore, the RF cavity is calibrated using the information from the simultaneously self-calibrated PCT monitor. The total amount of electric charge irradiated to the target can be obtained by integrating the measured current over the duration of the beamtime.

2.3 JLab E12-17-003 experiment

JLab E12-17-003 experiment was conducted in 2018 with the motivation of advancing hypernuclear physics. The titled purpose in the submitted proposal was to measure the missing mass spectrum of the ${}^{3}\mathrm{H}\,(e, e'K^{+})\,X$ reaction and to search for the $nn\Lambda$ state, which has been controversial since the HypHI Collaboration reported in 2013 that some events appeared to be a bound state in the $t + \pi^{-}$ invariant mass distribution [59]. In the present experiment, the author and collaborators irradiated a tritium gas target with a primary electron beam and measured both the scattered electrons and associated hadrons using two magnetic spectrometers called HRSs (High Resolution Spectrometers). Fig. 2.6 is a schematic of the experimental setup. Fig. 2.7 gives a photograoh at the present experiment.

In hypernuclear spectroscopy, protons detected in the hadron spectrometer are essentially considered background particles because K^{+} identification is crucial to tag hypernuclear events. Particle identification (PID) is performed using threshold type Cerenkov detectors placed behind the reference plane of the spectrometer, as well as through momentum analysis by the spectrometer. However, the data of E12-17-003 experiment includs not only the $(e, e'K^{+})$ reaction but also the $(e, e'p)$ reaction without any rejection by the PID detectors, as they did not participate in the data acquisition trigger. Additionally, the production of the η' mesons falls within the kinematic acceptance of the experiment. Therefore, by analyzing the $(e, e'p)$ reaction instead of the $(e, e'K^{+})$ reaction with the same dataset, one can investigate the electroproduction of the η' meson.

The author and collaborators collected data using a hydrogen gas target in addition to the tritium target, originally for the purpose of energy calibration of the missing mass spectrum. Consequently, one can obtain the cross section of the elementary process of the ${}^{1}\mathrm{H}\,(e, e'p)\,\eta'$ reaction by analyzing the hydrogen data.

2.4 Target

The cryogenic gas target system used in the present experiment is shown in Fig. 2.8. The target gases (${}^{3}\mathrm{H}$, ${}^{1}\mathrm{H}$, and ${}^{3}\mathrm{He}$) were sealed in a cell unit and installed into a vacuum chamber. Table 2.3 summarizes the thickness of each target used in E12-17-003 experiment. This target module was developed to safely handle radioactive ${}^{3}\mathrm{H}$ as an experimental target. The target gas is completely enclosed in the aluminum cell for safety reasons. During the experiment, the gas temperature was cooled down to 40 K using a 15 K liquid helium circulation system and a copper heat sink, and was maintained stably. The cell is made of aluminum alloy (ASTM B209 aluminum 7075-T651) and is 25 cm long with a 12.7 mm diameter. The thickness of the aluminum wall surrounding the cylindrical gas space, measured at 8 locations on each cell, is approximately 400 μm (see Table 2.2 and Fig. 2.9). Gas targets other than ${}^{3}\mathrm{H}$, which are naturally non-radioactive, were also enclosed in identical cells and irradiated with the beam in order to properly calibrate the effect of particles passing through the target cell.

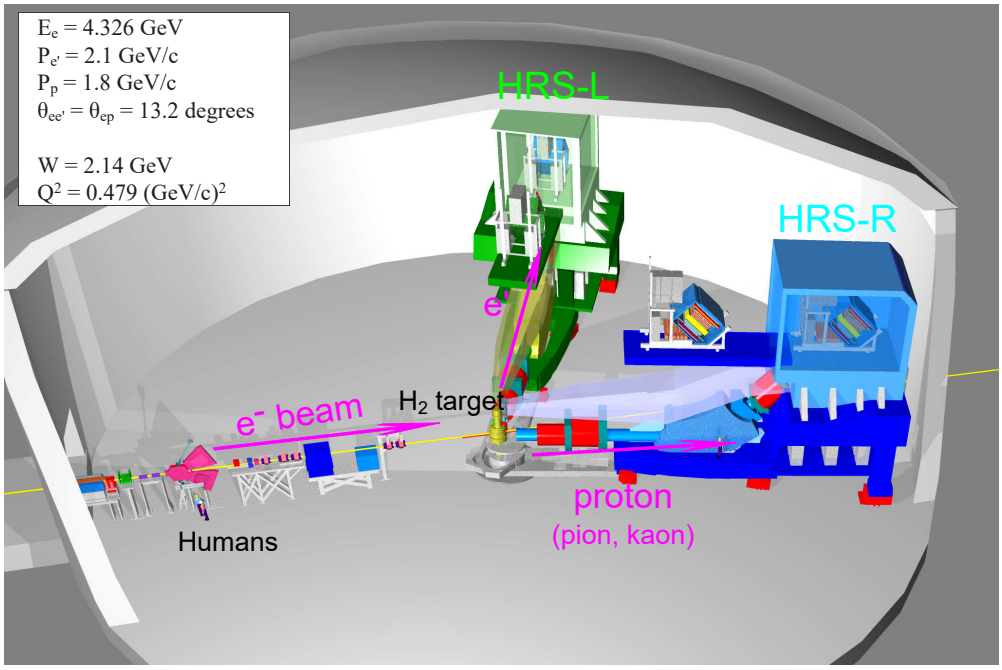

Fig. 2.6: A schematic of the experimental setup of E12-17-003. The electron beam was directed from left to right. A target was placed at the center of experimental Hall-A, and the scattered electrons and positively charged hadrons were measured using the HRS-Left and HRS-Right, respectively. The central scattering angles are $\theta_{\text{HRS-L}} = \theta_{\text{HRS-R}} = 13.2$ degrees.

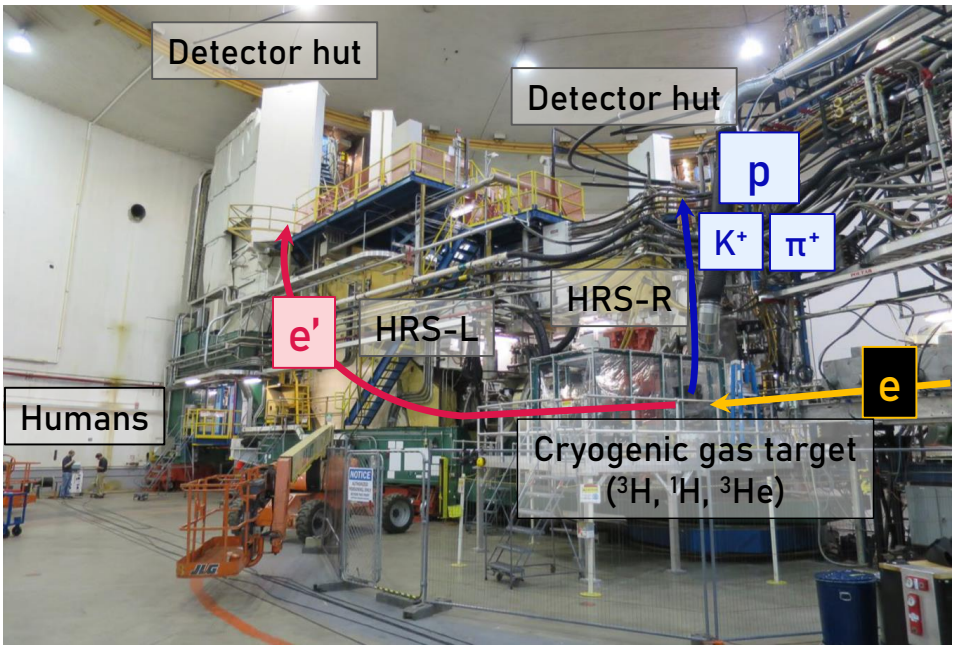

Fig. 2.7: A photograph of the experimental setup of E12-17-003.

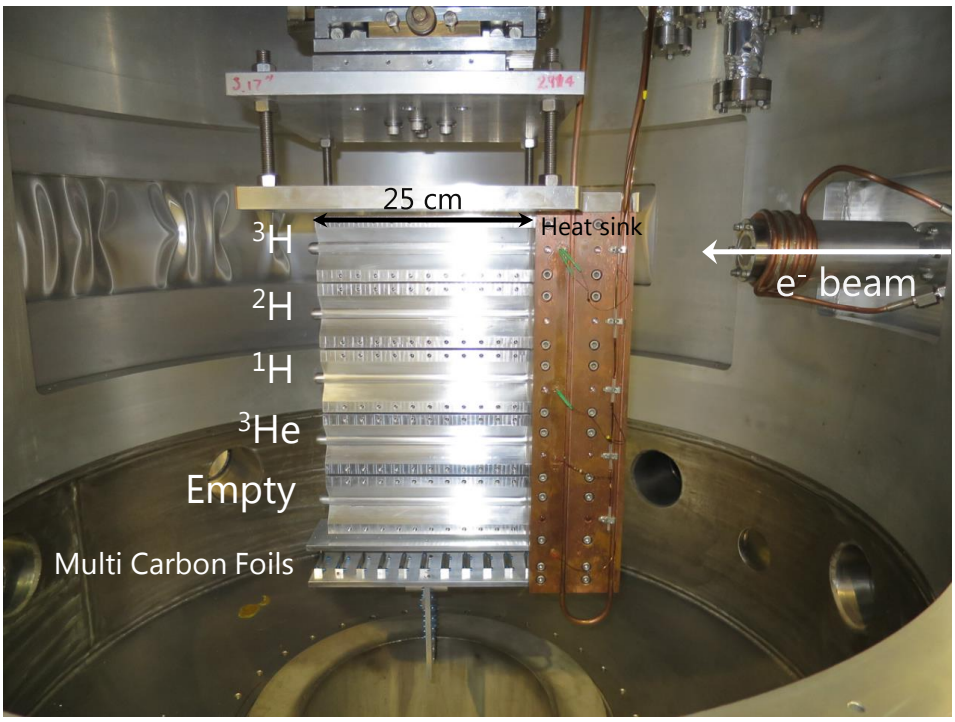

Fig. 2.8: A photograph of the cryogenic gas target system in the experiment. Each gas is enclosed in a cigar-shaped aluminum cell. By moving the entire system vertically, the target irradiated by the beam can be switched.

Table 2.3: List of targets and their thicknesses.

State	Target	Thickness $[\mathrm{mg/cm^2}]$
Gas	^{1}H	70.8 ± 0.4
Gas	^{3}H	85.1 ± 0.8
Gas	^{3}He	53.4 ± 0.6
Solid	Multi carbon foils	883

At the bottom of the cells, 10 solid carbon targets, called multi-foils, are placed along the beam axis. Each foil is 2 mm thick and 25 mm apart from the next target. The role of this carbon multi-foils array is to calibrate the reaction position along the beam axis (called the Z-vertex). In the present experiment, the author and collaborators used two arms of the HRS, which bend the scattered particles vertically (as described in Sec. 2.6), to ensure the resolution for gas targets spread out and distributed along the beam direction. The Z-vertex resolution of a single HRS arm is approximately 5 mm in σ. Therefore, the Z-vertex distribution can be well calibrated by the positions of each foil, separated by 25 mm. One position was left vacant to prevent confusion between the front and back positions.

2.5 Sieve slit

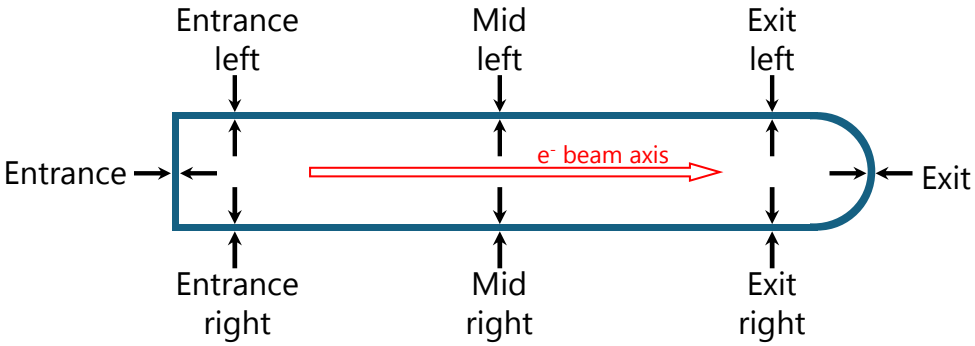

Fig. 2.9: A schematic drawing of the aluminum target cell. The target cell has a cigar-like shape, and the electron beam travels from left to right. The aluminum cell has a length of 25 cm and an outer diameter of 12.7 mm. The thickness of the aluminum walls is measured at eight locations on the cell (see also Table 1).

Table 2.2: A list of aluminum wall thicknesses at each position of the target cell [68]. Measurements were performed for all four cells, but the values presented here are for the cell containing ^{1}H.

Location	^{1}H Cell thickness (mm)
Entrance	0.311 ± 0.001
Exit	0.330 ± 0.063
Exit left	0.240 ± 0.019
Exit right	0.519 ± 0.009
Mid left	0.374 ± 0.004
Mid right	0.503 ± 0.005
Entrance left	0.456 ± 0.010
Entrance right	0.457 ± 0.006

Sieve slits are metal plates with many through holes, installed in front of the spectrometers' entrance on both sides. A drawing and a photo of the sieve slits is given in Fig. 2.10 and Fig. 2.11, respectively. During the optics calibration run, the author and collaborators calibrated the scattering angle by reconstructing images of particles that passed through the holes. The sieve slits were made of lead and were 2.04 cm thick. Each plate contains 140 holes with a diameter of 4 mm and two holes with a diameter of 6 mm. The larger holes serve the purpose of identifying whether the coordinate axes are positive or negative.

2.6 High Resolution Spectrometer (HRS)

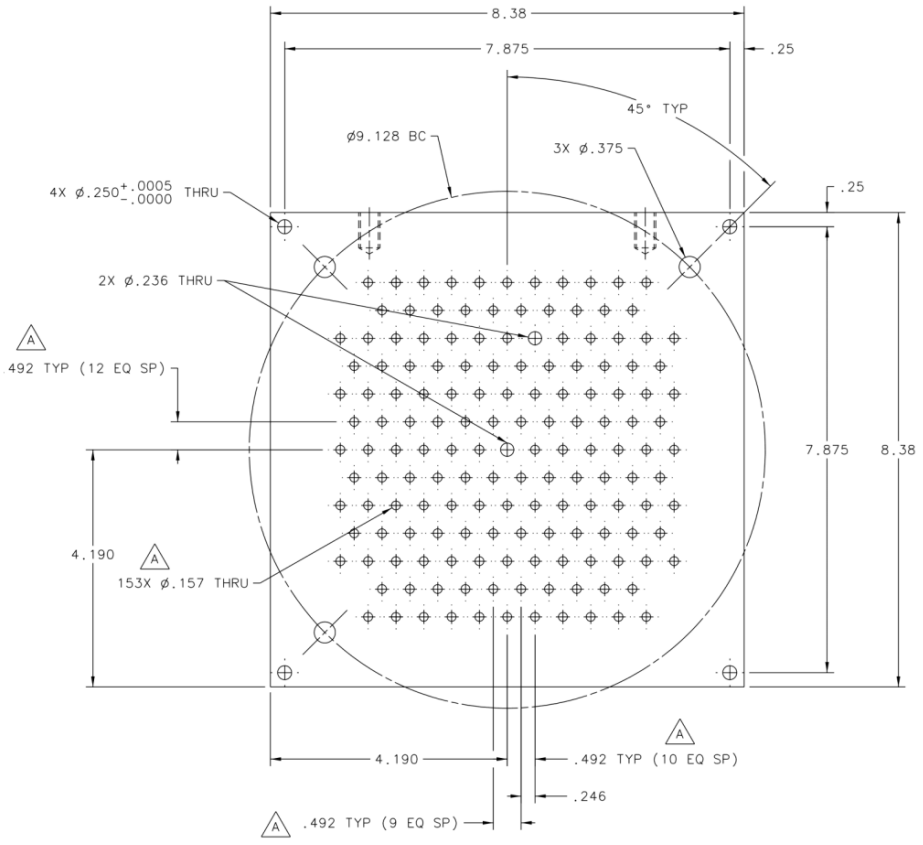

Fig. 2.10: A schematic drawing of the sieve slit. The unit is inch (1 inch = 2.54 cm).

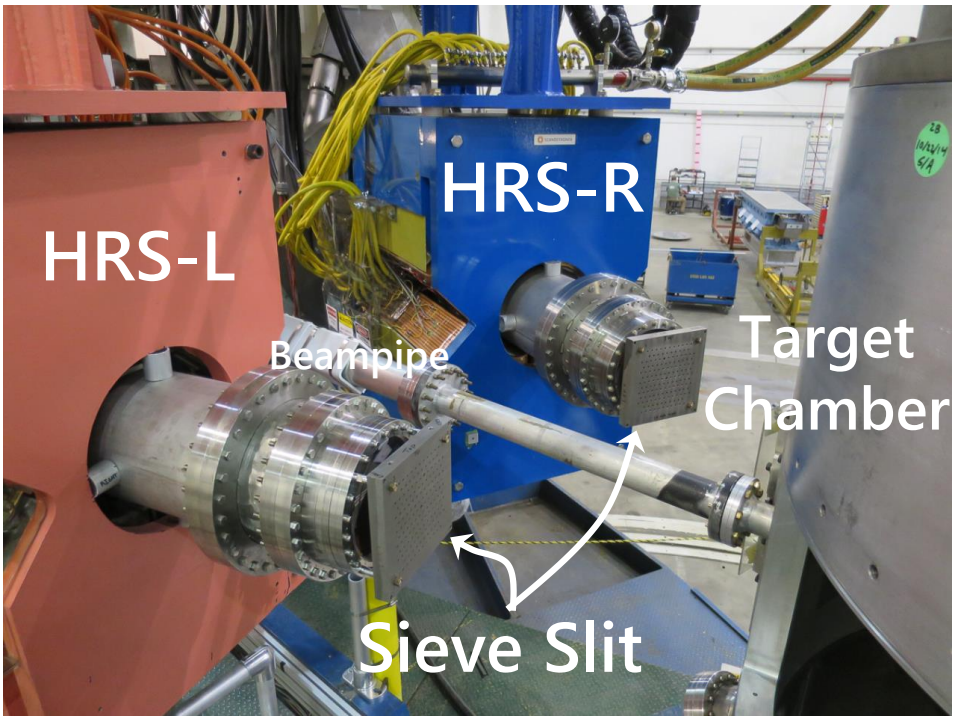

Fig. 2.11: A photograph of the sieve slits.

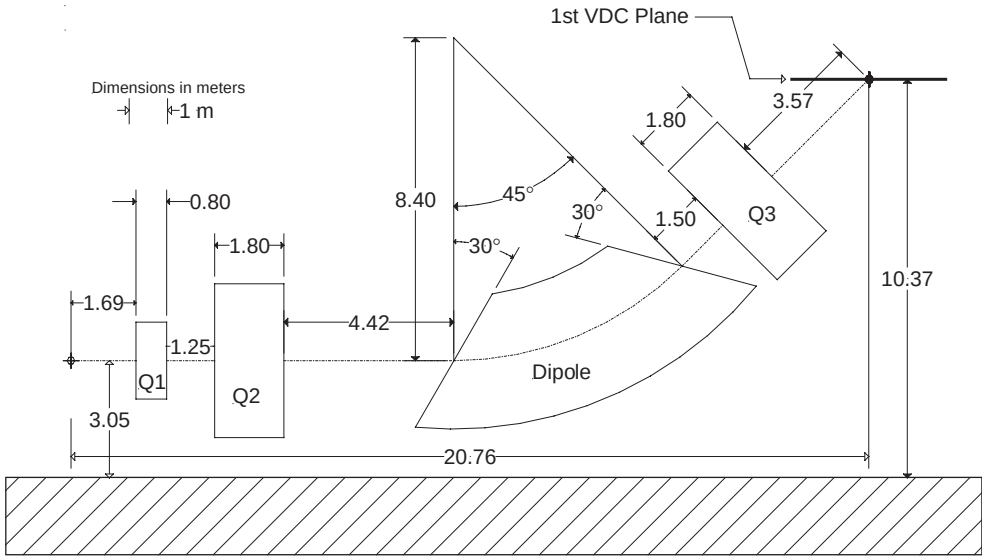

Fig. 2.12: The design of HRS [64]. This is side view. A beam comes from left to upper right.

Table 2.4: The numerical design and specifications of HRS [64].

Magnet configuration	QQDQ vertical bend
Benging angle	45 degrees
Optical length	23.4 m
Momentum range	0.3–4.0 GeV/c
Momentum accpentance $\Delta p/p$	4.5 %
Momentum resolution (FWHM)	1.0×10^4
Angular range (HRS-L)	12.5–150 degrees
Angular range (HRS-R)	12.5–150 degrees
Angular acceptance (horizontal)	$\pm$30 mrad
Angular acceptance (vertical)	$\pm$60 mrad
Angular resolution (horizontal)	0.5 mrad
Angular resolution (vertical)	1.0 mrad

HRS is the standard pair of magnetic spectrometers at JLab Hall-A. In the present experiment, the author and collaborators measured scattered electrons using HRS-Left and positive hadrons using HRS-Right. A schematic view of HRS can be seen in Fig. 2.12. HRS has a magnet configuration of QQDQ and a detector package downstream of it. The numerical design and specifications of HRS are shown in Table 2.4. The dipole magnets of HRS bend the particles vertically, which allows decoupling the momentum dispersion and the Z-vertex dispersion on the focal plane. The typical resolutions achieved are $\Delta p/p \sim 1 \times 10^{-4}$ (FWHM) and $\Delta z \sim 0.5$ cm (RMS), respectively.

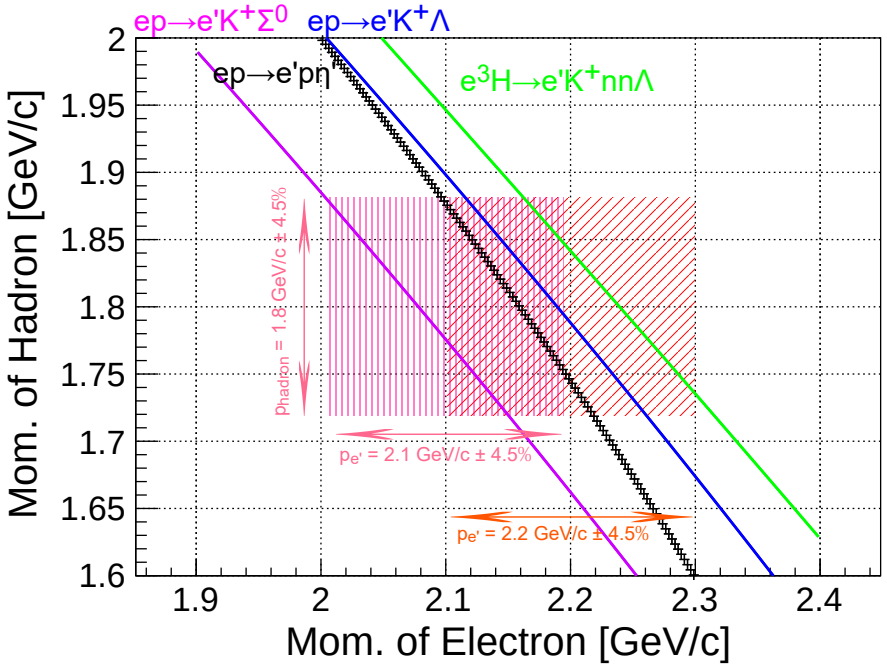

Fig. 2.13: The momentum correlation between scattered electrons and hadrons. The blue, magenta, and green lines indicate the relationship at the ${}^{1}\mathrm{H}\,(e, e'K^{+})\,\Lambda$, ${}^{1}\mathrm{H}\,(e, e'K^{+})\,\Sigma^{0}$, and ${}^{3}\mathrm{H}\,(e, e'K^{+})\,nn\Lambda$ reactions, respectively. These calculations assume the central angle of the measurement, $\theta^{\mathrm{Lab}}_{ee'} = \theta^{\mathrm{Lab}}_{eK^{+}} = 13.2$ [degrees] and $\phi^{\mathrm{Lab}}_{ee'} = \phi^{\mathrm{Lab}}_{eK^{+}} = 0$ [degrees]. The areas shaded by pink vertical lines and orange diagonal lines are the momentum acceptance of the hydrogen kinematics and the tritium kinematics, respectively. Also, the black plot is the correlation of both momentums in the ${}^{1}\mathrm{H}\,(e, e'p)\,\eta'$ reaction.

There is a pivot in the center of the experimental hall allowing the spectrometers to rotate on rails around the target. In E12-17-003 experiment, which originally aimed at searching for $nn\Lambda$ states, the measurement of forward-scattered electrons and kaons was important for gaining the yield. Therefore, Two spectrometers were set to measure forward-angle particles without interfering with each other. The angular setup in the present measurement was $\theta^{\mathrm{Lab}}_{ee'} = \theta^{\mathrm{Lab}}_{ep} =$ 13.2 degrees.

There were two momentum settings for the present experiment. The central momentum was adjusted to $(p_e,\ p_{\mathrm{hadron}}) = (2.1,\ 1.8)$ [GeV/c] for 20.3 % of the total beam charge and $(p_e,\ p_{\mathrm{hadron}}) = (2.2,\ 1.8)$ [GeV/c] for the remaining 79.7%. The former setting is called "hydrogen kinematics" and was used for optics calibration, including ${}^{1}\mathrm{H}$ data. The latter is called "tritium kinematics" and corresponded to the tritium run. The reason for setting these two kinematics was that the momentum acceptance of HRS was not large enough to simultaneously acquire the ${}^{1}\mathrm{H}\,(e, e'K^{+})\,\Lambda/\Sigma^{0}$ and the ${}^{3}\mathrm{H}\,(e, e'K^{+})\,nn\Lambda$ reactions. Fig. 2.13 shows the kinematic correlation of p_e and p_{hadron} for each reaction. The pink-shaded region represents the momentum coverage of "hydrogen kinematics," while the orange-shaded region represents the momentum

coverage of "tritium kinematics." Overlaid on these regions are the kinematically calculated momentum correlations for $p \to K^+\Lambda$ production (blue), $p \to K^+\Sigma^0$ production (purple), and ${}^3\mathrm{H} \to K^+nn\Lambda$ production (green). These kinematic calculations assume the central angle of the spectrometer. The settings for hydrogen kinematics and tritium kinematics are designed such that the calibration processes with Λ/Σ^0 production and search for $nn\Lambda$ production are well within the spectrometer acceptance. Additionally, the black crosses plotted in the figure represent the momentum correlations for $p \to \eta' p$ production, which are positioned between the curves for Λ and Σ^0 production. Therefore, the hydrogen kinematics of the present experiment naturally include the production of η' mesons within the spectrometer acceptance.

2.7 Detectors

At the end of the spectrometer, the detector packages, as shown in Fig. 2.14, are located around the focal plane. All the detectors are standard units used in HRS. In the present experiment, the author and collaborators used the following detectors:

- Drift chambers (VDC1 and VDC2) for tracking measurements
- Scintillation hodoscopes (S0 and S2) for timing measurements
- Aerogel Cherenkov detectors (AC1 and AC2, used only for the momentum calibration in the present analysis) for hadron identification.

2.7.1 Vertical drift chambers (VDC)

The vertical drift chambers (VDC) measure the particle's trajectory in both HRS-L and HRS-R. Fig. 2.15 shows the schematic drawing of the VDC. While the incoming angle of particles on the detector plane is 45 degrees diagonally upward, two VDCs are placed horizontally at the entrance of the detector plane. Both HRS-L and HRS-R have two identical VDCs each, with a distance of 33.5 cm between VDC1 and VDC2. Each VDC has a sensitive area of 28.8 cm $\times$ 211.8 cm, containing 368 sense wires oriented in two directions (U, V) tilted $\pm$45 degrees with respect to the outer frame of VDC (also see Fig. 2.15). As particles pass through, the electric field between the wires ionizes the chamber gas (a mixture of 62 % argon and 38 % ethane), and the timing of the electrical signal induced in the sense wires is recorded. The distance from the track to the wire can be calculated using the hit timing and drift velocity. The coordinates of the cross point in the wire plane, (U_1, V_1) for VDC1 and (U_2, V_2) for VDC2, are derived by linear fitting (see Fig. 2.16). The positional resolution per plane is 235 μm (FWHM).

The reconstruction of the momentum vector and reaction point at the target position is performed using the position and angle on the intermediate plane between VDC1 and VDC2 (referred to as the "reference plane" from this section), which can be calculated with (U_1, V_1) and (U_2, V_2). Details of the reconstruction are described in Sec. 3.2.

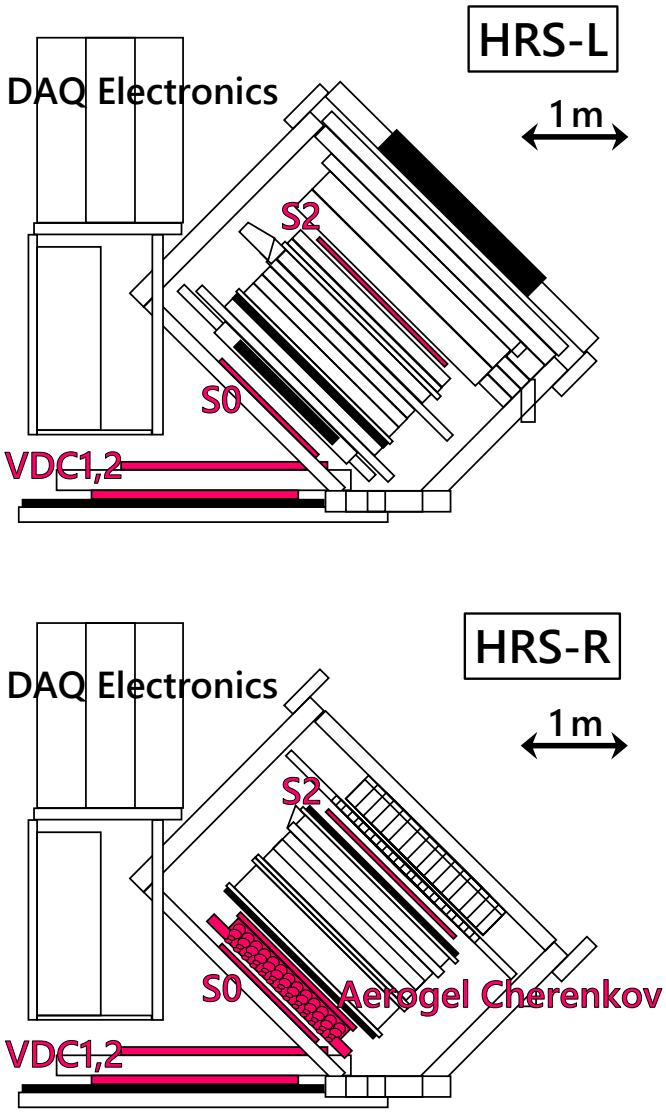

Fig. 2.14: The detector package of HRS [64]. This is side view. The external dimensions of the detector hut are identical on both the left and right sides. Although many instruments were included, only VDC, S0, S2, AC1 and AC2 were used in the present measurement. The other regions were vacant in the present experiment.

2.7.2 Scintillation hodoscopes

Two scintillation hodoscopes were used in both HRS-L and HRS-R in the present experiment. They are named as "S0" and "S2" in order from the upstream side. These hodoscopes are responsible for the data acquisition trigger and time-of-flight measurements.

S0 is a single-segment scintillation counter placed just behind VDC2. It has a simple structure with two 3-inch photomultiplier tubes (Photonic XP2312) attached to both ends of a plastic scintillator plate (BICRON408) with an effective area of 170 mm $\times$ 250 mm and a thickness of 10 mm. The time resolution of S0 is about $\sigma_{S0} \approx 0.2$ ns.

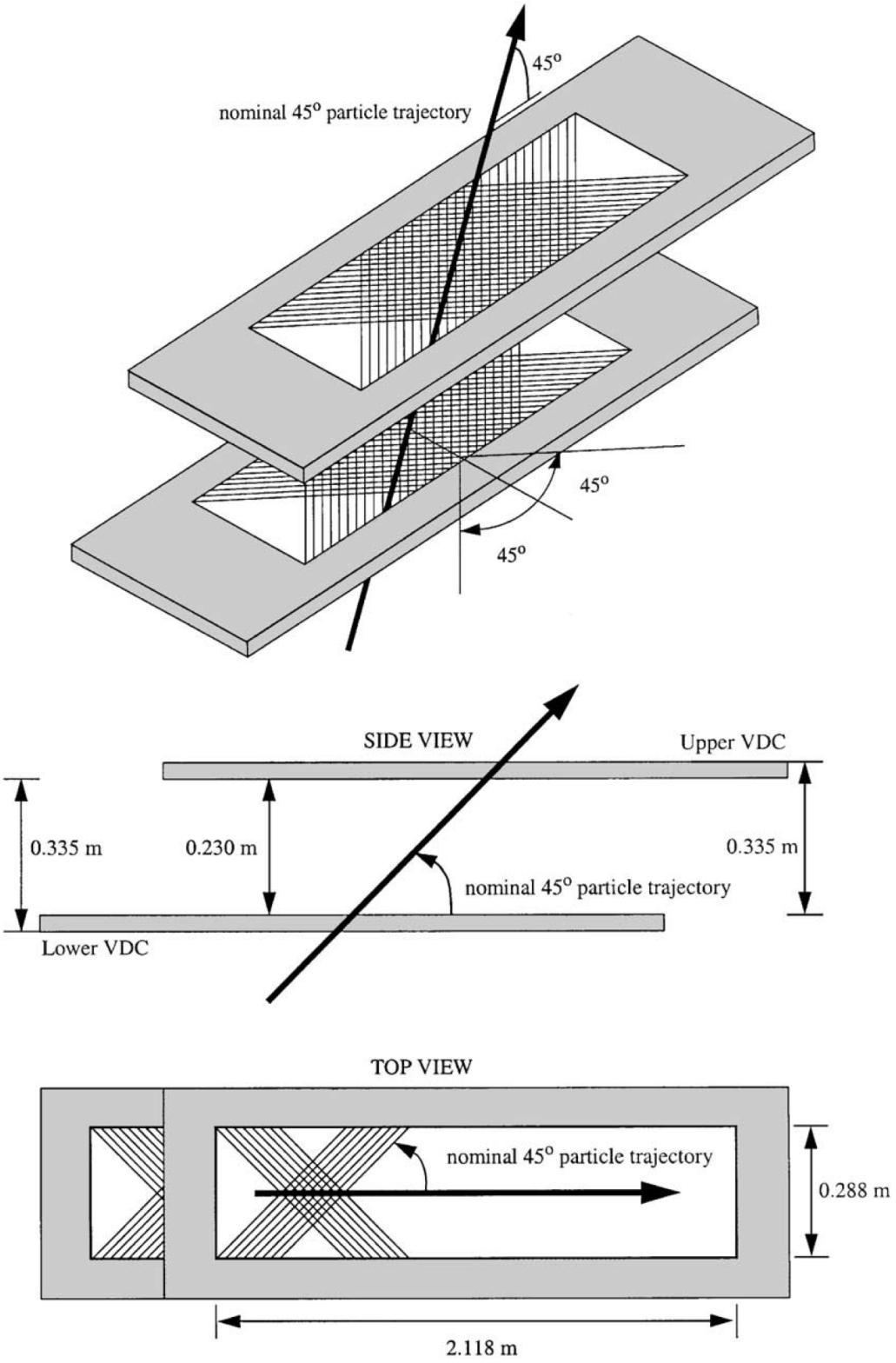

Fig. 2.15: The schematic drawing of VDC [69]. Two VDCs were installed at an angle of 45 degrees to the flight direction of the particles. The wire directions (U, V) are set at ± 45 degrees from the VDC frame.

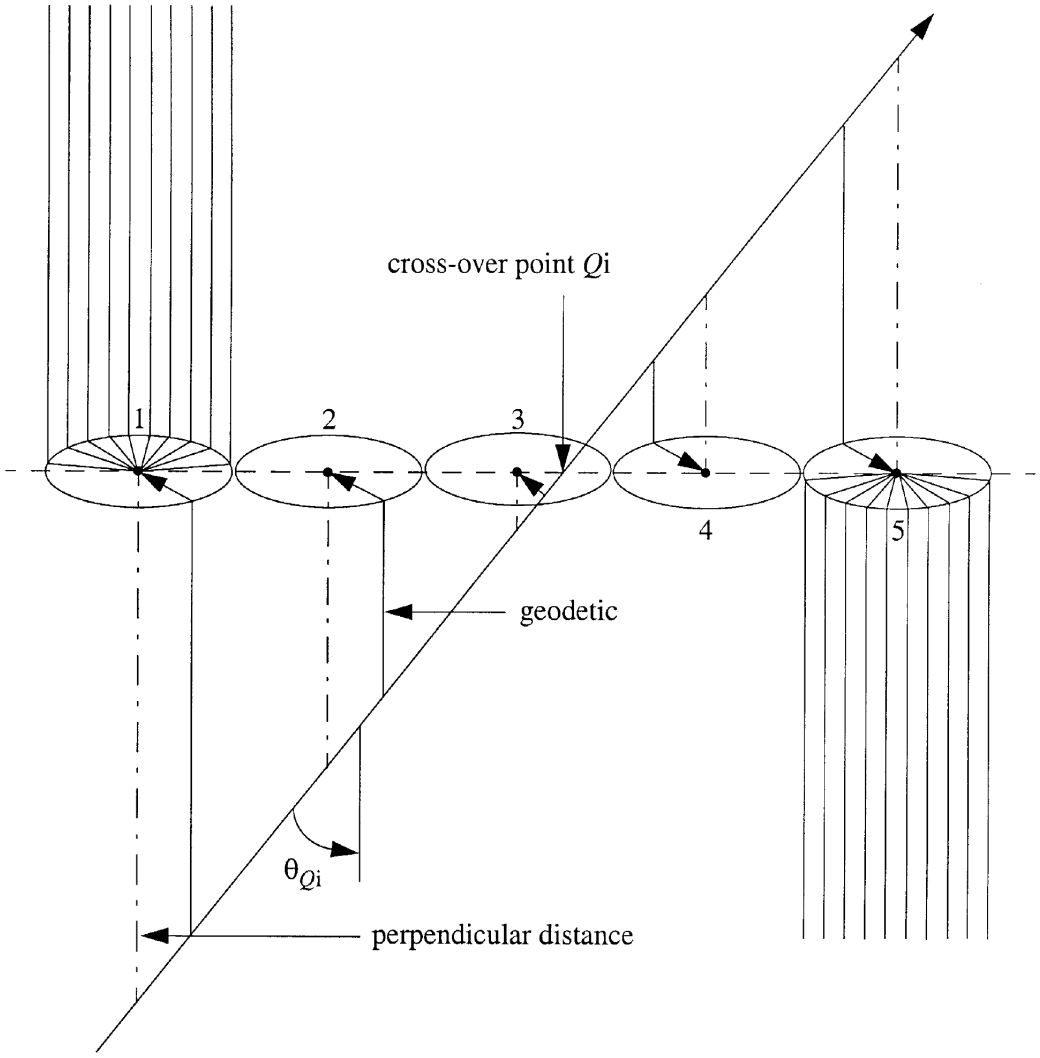

Fig. 2.16: Tracking detection by VDC (side view) [69]. The slanted arrow represents particle's trajectory. The electrons produced by the ionization are drifted longitudinally towards the wires labeled 1 to 5 in this figure. The intersection point Q_i in the wire plane can be obtained by fitting the distance between each wire and the track, calculated from the detection time and the drift time for each wire. The angle θ_{Qi} between the particle trajectory and the wire direction is obtained from the hit positions in the two VDCs, (U_1, V_1) and (U_2, V_2).

S2 is a 16-segmented hodoscope placed 2 m downstream from S0. The total active area is 17 in $\times$ 88 in = 432 mm $\times$ 2235 mm, made of a 50 mm thick plastic scintillator (ES-230) with two 2-inch photomultiplier tubes (Photonis XP2282) attached to each segment (see Fig. 2.17). The time resolution of S2 is about $\sigma_{\mathrm{S2}} \approx 0.1$ ns.

2.7.3 Cherenkov detectors

Cherenkov radiation is an electromagnetic radiation phenomenon in which light is emitted in a cone-shaped direction at an angle $\theta = \arccos(1/n\beta)$ with respect to the traveling direction of

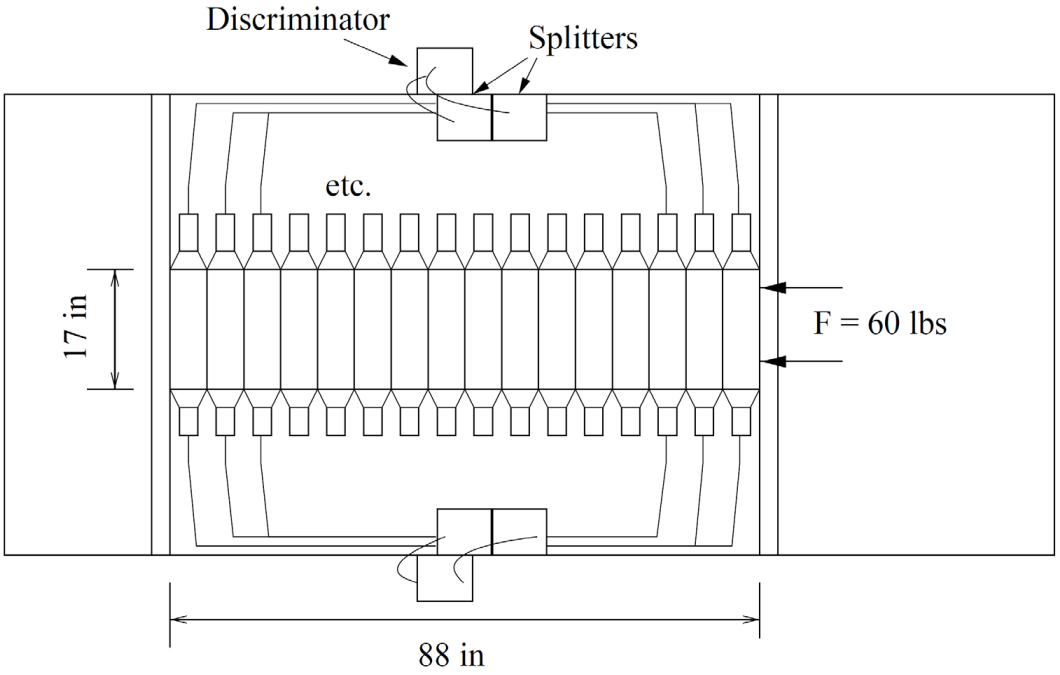

Fig. 2.17: The schematic drawing of the S2 hodoscope [70]. S2 consists of a group of scintillation counters divided into 16 segments, each measuring 17 in $\times$ 5.5 in = 432 mm $\times$ 140 mm. A 60 lbs lateral load is applied to eliminate gaps between the segments.

a charged particle moving at a speed exceeding the speed of light in the material (c/n, where n is the refractive index). The number of emitted photons per thickness of the radiator x and the wavelength of light λ is written as follows:

$$\frac{d^2N}{dxd\lambda} = \frac{2\pi\alpha z^2}{\lambda^2}\left(1 - \frac{1}{\beta^2 n^2(\lambda)}\right) \quad \text{when } \frac{c}{n} < \beta, \tag{2.10}$$

N: Number of Photons,
x: Path length in the radiator,
λ: Wavelength of Cherenkov light,
α: Fine structure constant,
z: Charge of the particle,
β: speed of the particle,
n: refractive index of the material.

A threshold-type Cherenkov detector discriminates differences in the speed of particles, $\beta\left(= p/\sqrt{p^2+m^2}\right)$, at a given momentum p, corresponding to differences in mass m, by the presence or amount of emitted photons.

Two types of threshold-type Cherenkov detectors (AC1 and AC2) were installed on the HRS-R side to identify hadrons. They use silica aerogel with different refractive indices as radiators, with photomultiplier tubes attached to both ends of each segment. AC1 and AC2 identify

π^+/K^+ and K^+/p, respectively, around the spectrometer's central momentum of 1.8 GeV/c by using the information on the number of photoelectrons. For the analysis of the $(e, e'p)$ reactions, information from AC1 and AC2 was not used because particle identification with a method called "coincidence time," which uses the timing information from scintillation hodoscopes, was sufficient for proton selection (described in Sec. 3.4). However, for momentum calibration, where K^+ event selection was necessary (the number of kaons is only about 3% of protons and about 2% of pions), event selection by AC1 and AC2 was performed in addition to the coincidence time analysis.

The layout of a single segment of AC1 and AC2 is shown in Fig. 2.18. Table 2.5 summarizes the specifications of AC1 and AC2. The radiators of AC1 and AC2 are silica aerogels with refractive indices of $n = 1.015$ for AC1 and $n = 1.055$ for AC2, manufactured by Matsushita Electric Works Ltd. (now Panasonic Electric Works, Co. Ltd). The relationship between the momentum and the number of photons in AC1 and AC2, calculated by eq. (2.10), is shown in Fig. 2.19 and Fig. 2.20. The shaded area in the figures represents the momentum acceptance of HRS-R. In AC1, π^+ can be removed from protons and K^+ by excluding events with Cherenkov photons, and in AC2, kaons and pions can be separated by selecting events with photon numbers over a suitable threshold. Therefore, it is possible to properly identify pions, kaons, and protons by combining AC1 and AC2 with different refractive indices, even when selecting kaons.

Typical numbers of photoelectrons for $\beta = 1$ particles are approximately 8 p.e. for AC1 and approximately 30 p.e. for AC2.

Table 2.5: Specifications of AC1 and AC2. The unit of size is cm.

Name	Radiator Model	Index	Tile Size	Radiator Size	Num. of PMTs	PMT Model
AC1	SP15	1.015	$10 \times 10 \times 1$	$170 \times 32 \times 9$	24	RCA 8854
AC2	SP50	1.055	$10 \times 10 \times 1$	$192 \times 30 \times 5$	26	XP 2572B

2.8 Data taking trigger and data aquisition system (DAQ)

Data acquisition was carried out when hits on both arms of HRS-L and HRS-R coincided.

$$\text{(Coincidence Trigger)} = \text{(HRS-L Trigger)} \otimes \text{(HRS-R Trigger)}.$$

The trigger signal for each single arm was generated by simultaneous hits of S0 and S2, as shown in the following equations:

$$\begin{aligned}\text{(HRS-L Trigger)} &= (\text{S0} \otimes \text{S2})_{\text{HRS-L}} \\ \text{(HRS-R Trigger)} &= (\text{S0} \otimes \text{S2})_{\text{HRS-R}}.\end{aligned}$$

S0 consists of a single segment counter, so a simultaneous hit on both PMTs mounted on its two sides forms the S0 logical signal. On the other hand, S1 is a hodoscope consisting of 16 segments,

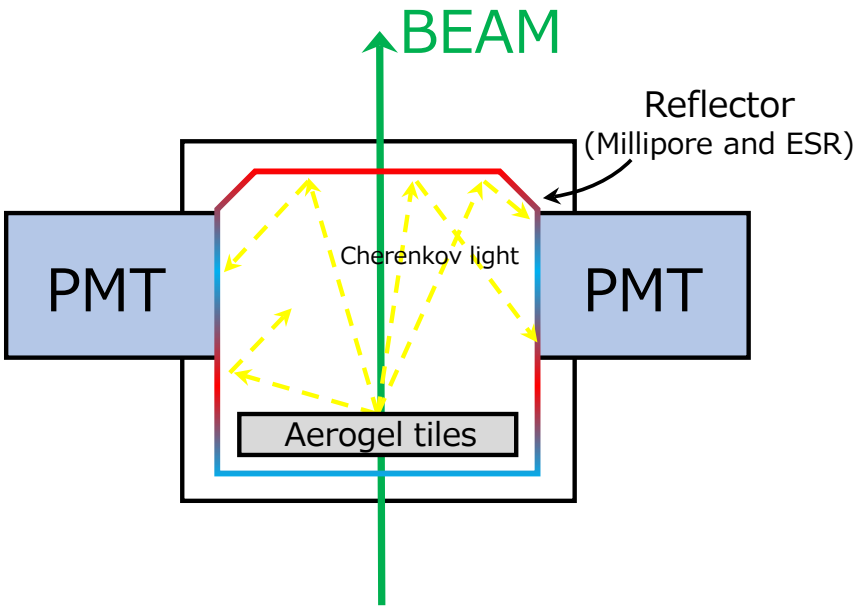

Fig. 2.18: Configuration of AC1/AC2 (not in scale). This is cross-section lateral view of single segment. It consists of 2 PMTs (Burle RCA 8854 for AC1 and Photonix XP 4572B for AC2), a radiator of aerogel tiles (Matsushita SP15 for AC1 and SP50 for AC2) and light reflectors (Millipore filter paper GSWP0010 and Enhanced Specular Reflector (ESR)).

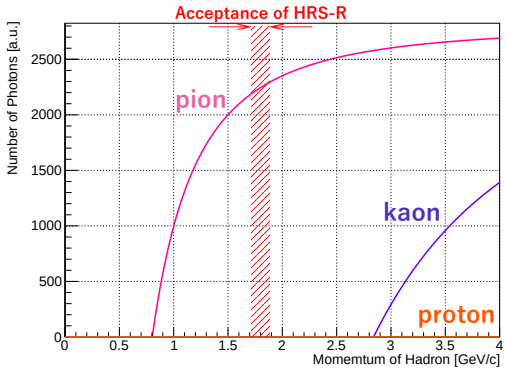

Fig. 2.19: Relationship between particle's momentum and number of Cherenkov photons at AC1. Refractive index is $n = 1.015$.

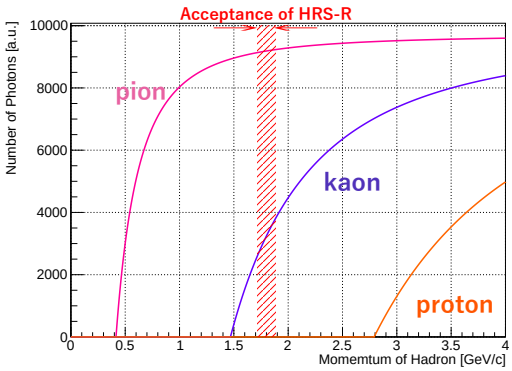

Fig. 2.20: Relationship between particle's momentum and number of Cherenkov photons at AC2. Refractive index is $n = 1.055$.

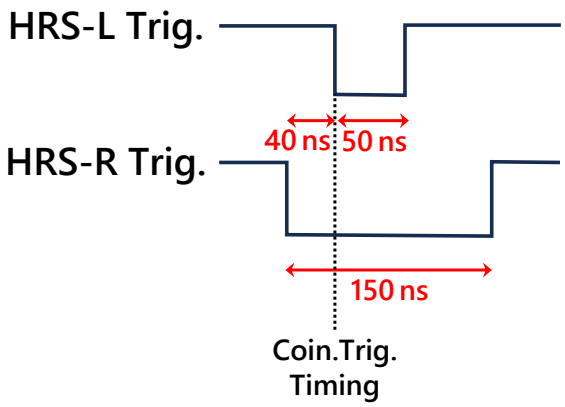

Fig. 2.21: Relationship between HRS-L and HRS-R trigger timing.

where the logical OR of simultaneous detections by the upper and lower PMTs attached to each segment forms the S1 logical signal. The logical AND of the S0 and S1 signals constitutes the spectrometer's individual triggers, namely HRS-L trigger and HRS-R trigger. Then the data acquisition trigger required the coincidence of these two triggers. Typical counting rates for the ^{1}H target of 70.8 mg/cm^2 and a beam current of 20 μA were 11 kHz for HRS-L, 11 kHz for HRS-R, and 60 Hz for the coincidence trigger. Fig.2.21 shows the timing of the coincidence trigger. The signal widths of HRS-L and HRS-R were set to 50 ns and 150 ns, respectively, with the timing adjusted so that the signal from HRS-L came later. Therefore, the HRS-L trigger determined the trigger timing.

For signal processing from each detector, various types of NIM modules were used. For data acquisition (DAQ), hardware digitization devices, such as ADCs, TDCs, and scalers, based on the Fastbus and VME standards were employed. An integrated system called "CODA" (CEBAF On-line Data Acquisition System) [71], which was developed for experiments in JLab Hall-A operates these devices and components cohesively.

2.9 Summary of beamtime and kinematics

The beamtime for E12-17-003 experiment was conducted from October to November 2018. The beam irradiation on the ^{1}H target was allocated approximately 25 % of the total beamtime, with data acquisition conducted during both the first and second halves of the beamtime. The run numbers for the ^{1}H runs are from 111141 to 111220 and from 111480 to 111542. The energy of the electron beam was 4.318 GeV, and the beam current was 22.5 μA. The central values of the momentum and angle for scattered particles, as well as the energy of the incoming electron beam, were summarized in Table 2.6. Each kinematical parameters in the $^1\mathrm{H}\,(e, e'p)\,\eta'$ reaction are listed in Table 2.7. It enumerates the values for the central ray obtained using Table 2.6 as well as the mean values of the distribution of acquired data, and Monte Carlo simulations. Fig. 2.22 and Fig. 2.23 show the run dependence of the beam energy and beam current, respectively. As

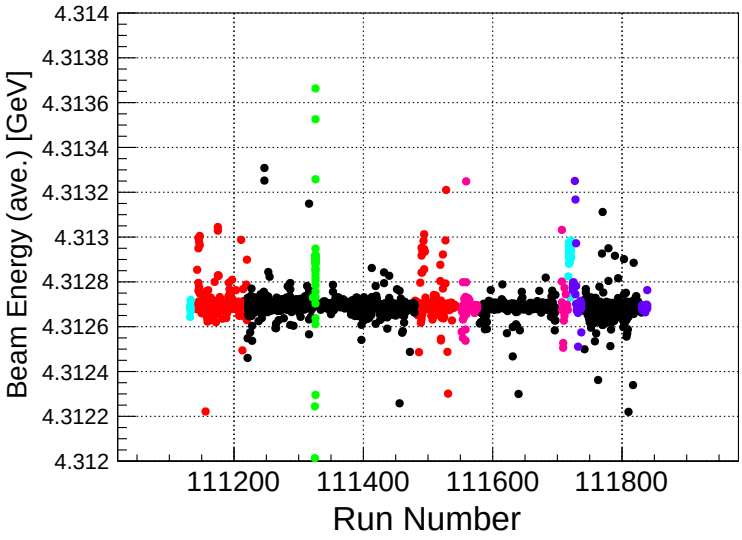

Fig. 2.22: Run dependence of the beam energy during the beamtime. Black indicates the ^{3}H target, red indicates the ^{1}H target (hydrogen kinematics), pink indicates ^{1}H (tritium kinematics), purple indicates ^{3}He, green indicates empty, and light blue indicates the calibration run.

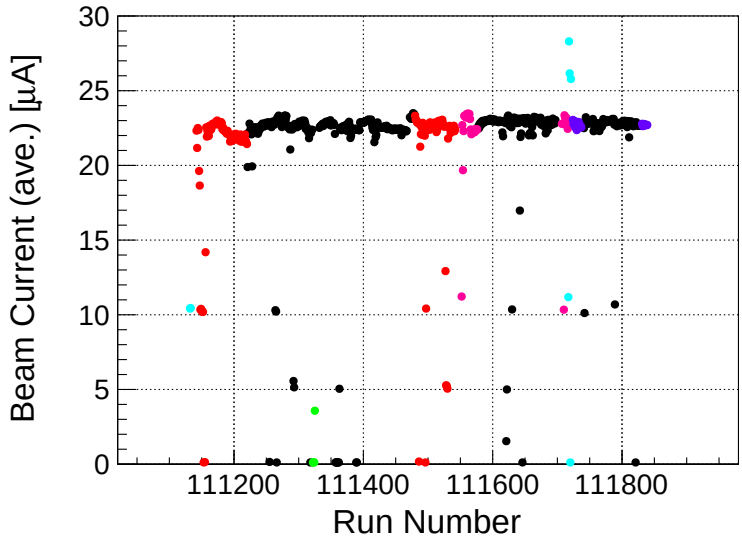

Fig. 2.23: Run dependence of the beam current during the beamtime. The color legend is the same as in Fig. 2.22.

is evident from these figures, data acquisition was generally stable throughout the beamtime. The total charge irradiated on the ^{1}H target was 4.6 C, which corresponds to $N_e = 2.9 \times 10^{19}$ electrons.

Table 2.6: Central values of energy, momenta and angles of incoming/scattered beams adjusted in the present measurement. These values are for the hydrogen kinematics. Zenith angles are the angle from the incoming electron beam.

Item	Explanation	Value
E_e	Energy of electron beam (e)	4.326 GeV
$p_{e'}$	Momentum of scattered electron (e')	2.1 GeV/c
p_p	Momentum of scattered proton (p)	1.8 GeV/c
$\theta_{ee'}$	Zenith angle between e and e'	13.2 degrees
$\phi_{ee'}$	Azimuthal angle between e and e'	90 degrees
θ_{ep}	Zenith angle between e and p	13.2 degrees
ϕ_{ep}	Azimuthal angle between e and p	270 degrees

Table 2.7: Kinematical parameters of the $^1\mathrm{H}\,(e, e'p)\,\eta'$ reaction in the present setup. See Fig. 2.1 and eq. (2.2)–(2.8) for variable definitions. Values in the lines with the labels of "Central Ray," "Data Mean" and "Sim. Mean" are representing central values in the experimental setup, mean values of the distributions acquired data and mean values of the distribution by a Monte Carlo simulation (SIMC), respectively. The data also includes background events from multi-meson production, and on the other hand, the simulation include pure-η' production.

Item	Central Ray	Data Mean	Sim. Mean
ω [GeV]	2.22	2.19	2.20
E_γ [GeV]	1.96	1.94	1.93
Q^2 $\left[(\mathrm{GeV}/c)^2\right]$	0.479	0.467	0.497
W [GeV]	2.14	2.13	2.13
$\theta^{\mathrm{CM}}_{\gamma\eta'}$ [degrees]	175	169	169
$\phi^{\mathrm{CM}}_{\gamma\eta'}$ [degrees]	0	-5.55	-1.58
ϵ	0.768	0.774	0.773
$\left(\frac{d\sigma}{d\Omega}\right)_{\mathrm{Lab}} / \left(\frac{d\sigma}{d\Omega}\right)_{\mathrm{CM}}$	0.0647	0.0679	0.0682

Chapter 3

Analysis

3.1 Overview

Fig. 3.1 shows the analysis procedure of the present work. In the missing mass formula,

$$M_{\mathrm{X}} = \sqrt{\{(E_e - E_{e'}) + M_p - E_{p_{\mathrm{scat}}}\}^2 - \{(\boldsymbol{p}_e - \boldsymbol{p}_{e'}) - \boldsymbol{p}_{p_{\mathrm{scat}}}\}^2}, \tag{3.1}$$

$\boldsymbol{p}_{e'}$ and $\boldsymbol{p}_{p_{\mathrm{scat}}}$ are both momentum vectors at the target position, which are reconstructed from the hit information at the focal planes of the spectrometers. Therefore, the calibration necessary for calculating the missing mass must be performed first (described in Sec. 3.2). This is followed by event selection for the Z-vertex at the reaction point and the identification of scattered protons (Sec. 3.3 and 3.4, respectively). Then the count-based missing mass spectrum is derived (Sec. 3.5). After that, various variables necessary for the derivation of the cross section—background distribution on the missing mass (Sec. 3.6), spectrometers' acceptance (Sec. 3.7), number of targets (Sec. 3.8), number of virtual photon beam (Sec. 3.10), and various efficiencies (Sec. 3.12)—are evaluated. Some of them use a Monte Carlo simulation that models the

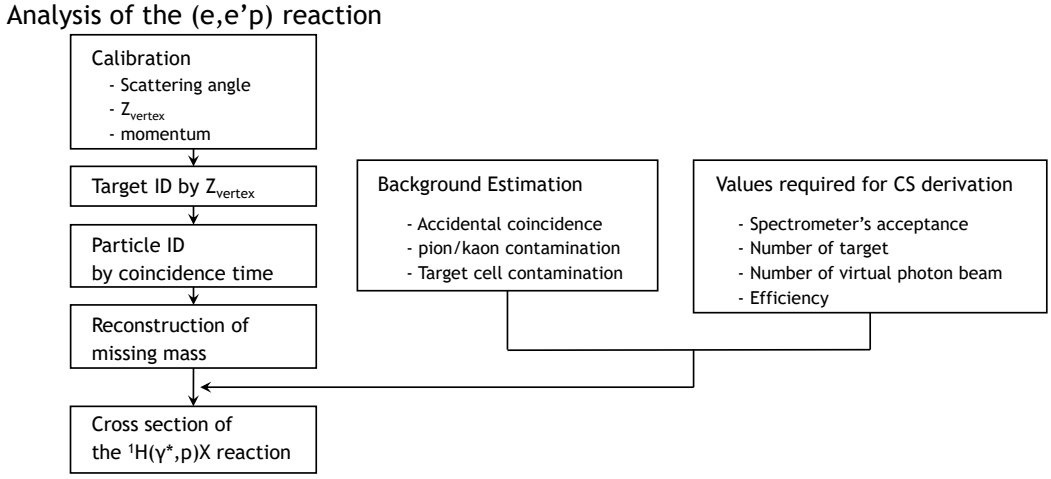

Fig. 3.1: An analysis flowchart.

experimental setup. Various conditions of the simulation are also described in Sec. 3.7. Then, Sec. 3.13 discusses the derivation of the cross section and its results, including the error.

3.2 Calibration

The role of magnets in nuclear physics experiments is often compared to optical elements. This is because dipole magnets with uniform magnetic fields bend beam particles at angles dependent on their momentum, behaving like prisms, while quadrupole magnets focus or diverge beam particles toward a focal point, acting like convex or concave lenses. Thus, when particles emitted from a specific reaction point reach the reference plane after deflection by dipole magnets, focusing by quadrupole magnets, and drifts between these magnets, the positions, angles, and momenta at two points can be expressed as a first-order transformation in matrix form:

$$\begin{pmatrix} x_{\mathrm{rp}} \\ x'_{\mathrm{rp}} \\ y_{\mathrm{rp}} \\ y'_{\mathrm{rp}} \\ p_{\mathrm{rp}} \end{pmatrix} = M \begin{pmatrix} x_{\mathrm{tar}} \\ x'_{\mathrm{tar}} \\ y_{\mathrm{tar}} \\ y'_{\mathrm{tar}} \\ p_{\mathrm{tar}} \end{pmatrix}. \tag{3.2}$$

Here, $x_{\mathrm{tar}}, y_{\mathrm{tar}}, x'_{\mathrm{tar}}, y'_{\mathrm{tar}}$ and p_{tar} represents the horizontal position, vertical position, horizontal angle, vertical angle and momentum at the target, while $x_{\mathrm{rp}}, y_{\mathrm{rp}}, x'_{\mathrm{rp}}, y'_{\mathrm{rp}}$ and p_{rp} represents the corresponding quantities at the reference plane. The matrix M is referred to as the beam transport matrix. This relationship is a critical consequence of beam optics, and all beamlines for experiments handling charged particles are designed based on this equation to optimize resolution. Writing the equation in reverse implies that the information at the target can be expressed in terms of the information at the reference plane:

$$\begin{pmatrix} x_{\mathrm{tar}} \\ x'_{\mathrm{tar}} \\ y_{\mathrm{tar}} \\ y'_{\mathrm{tar}} \\ p_{\mathrm{tar}} \end{pmatrix} = M^{-1} \begin{pmatrix} x_{\mathrm{rp}} \\ x'_{\mathrm{rp}} \\ y_{\mathrm{rp}} \\ y'_{\mathrm{rp}} \\ p_{\mathrm{rp}} \end{pmatrix}. \tag{3.3}$$

Here, M^{-1} is the inverse of M, and it is called the backward transfer matrix.

In the preset experiment, the magnitude of momenta and angles at the reaction point in the target is required in order to calculate the missing mass. These quantities are reconstructed from the hit positions and angles at the reference plane. The setup of the present experiment, specifically the backward transfer matrices in HRS-L and HRS-R, describes this relationship. Calibration in the present study involves tuning the elements of the backward transfer matrix to reproduce reference values using data obtained for calibration purposes. These reference values are defined as the hole patterns in the sieve slit for angles and the peaks in the missing mass distribution from the ${}^{1}\mathrm{H}\,(e, e'K^{+})\,\Lambda/\Sigma^{0}$ reaction for momentum.

There are a few points to note here. First, the backward transfer matrix in eq. (3.3) represents the simplest expression under ideal conditions. In reality, however, the magnetic field

generated in the electromagnets is not perfectly uniform, and magnetic field leakage outside the electromagnet distort the relationship between the target position and the reference plane. The present study and previous research describe these effects by adding second-order and higher-order correction terms, such as in a Taylor expansion. As a result, the reconstruction from the reference plane to the target position is no longer a first-order linear combination represented by a square matrix, but rather a higher-order polynomial. The authors and collaborators refer to the coefficients of these polynomials also as the "backward transfer matrix." The second point to mention concerns the z_{tar}. In the present study, a target stretched in the beam axis direction (the z-direction) was used, and a spectrometer bending particles in the vertical direction was employed. This causes differences in z_{tar} to disperse in the direction orthogonal to momentum on the reference plane. Thus, the z_{tar} can also be reconstructed using the backward transfer matrix. Moreover, the matrix used to reconstruct other kinematic parameters ($x_{\mathrm{tar}}, y_{\mathrm{tar}}, x'_{\mathrm{tar}}, y'_{\mathrm{tar}}$ and p_{tar}) explicitly incorporates the reconstructed z_{tar}. Specifically, z_{tar} is reconstructed using a matrix M_z:

$$z_{\mathrm{tar}} = M_z \begin{pmatrix} x_{\mathrm{rp}} \\ x'_{\mathrm{rp}} \\ y_{\mathrm{rp}} \\ y'_{\mathrm{rp}} \\ {x_{\mathrm{rp}}}^2 \\ x_{\mathrm{rp}} x'_{\mathrm{rp}} \\ \vdots \end{pmatrix}. \tag{3.4}$$

Other quantities are expressed using the matrix M_o:

$$\begin{pmatrix} x_{\mathrm{tar}} \\ x'_{\mathrm{tar}} \\ y_{\mathrm{tar}} \\ y'_{\mathrm{tar}} \\ p_{\mathrm{tar}} \end{pmatrix} = M_o \begin{pmatrix} x_{\mathrm{rp}} \\ x'_{\mathrm{rp}} \\ y_{\mathrm{rp}} \\ y'_{\mathrm{rp}} \\ z_{\mathrm{tar}} \\ {x_{\mathrm{rp}}}^2 \\ x_{\mathrm{rp}} x'_{\mathrm{rp}} \\ \vdots \end{pmatrix}. \tag{3.5}$$

These equations can also be expanded using the individual matrix elements $C_z, C_{x'}, C_{y'}$, and C_p:

$$z_{\mathrm{tar}} = \sum_{i+j+k+l \le n} C_z\,(i,j,k,l)\, x^i_{\mathrm{rp}} y^j_{\mathrm{rp}} {x'}^k_{\mathrm{rp}} {y'}^l_{\mathrm{rp}} \tag{3.6}$$

$$x'_{\mathrm{tar}} = \sum_{i+j+k+l+m \le n} C_{x'}\,(i,j,k,l,m)\, x^i_{\mathrm{rp}} y^j_{\mathrm{rp}} {x'}^k_{\mathrm{rp}} {y'}^l_{\mathrm{rp}} z^m_{\mathrm{tar}} \tag{3.7}$$

$$y'_{\mathrm{tar}} = \sum_{i+j+k+l+m \le n} C_{y'}\,(i,j,k,l,m)\, x^i_{\mathrm{rp}} y_{\mathrm{rp}} j {x'}^k_{\mathrm{rp}} {y'}^l_{\mathrm{rp}} z^m_{\mathrm{tar}} \tag{3.8}$$

$$p_{\mathrm{tar}} = \sum_{i+j+k+l+m \le n} C_p\,(i,j,k,l,m)\, x^i_{\mathrm{rp}} y^j_{\mathrm{rp}} {x'}^k_{\mathrm{rp}} {y'}^l_{\mathrm{rp}} z^m_{\mathrm{tar}}. \tag{3.9}$$

The tuning of matrix elements for z, angles, and momentum will be described in the following subsections.

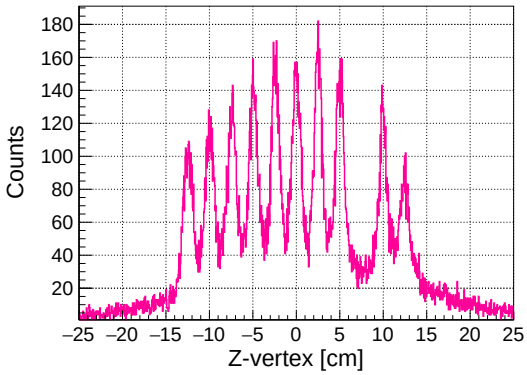

Fig. 3.2: Z_{vertex} distribution using multi-foil target in HRS-L.

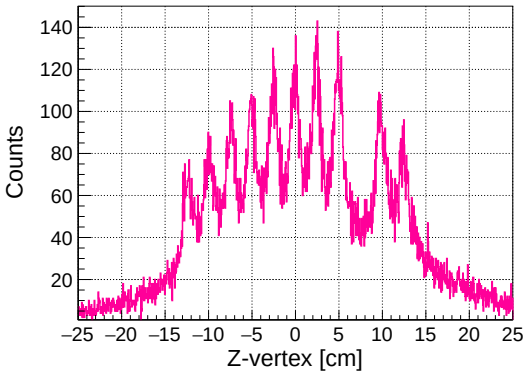

Fig. 3.3: Z_{vertex} distribution using multi-foil target in HRS-R.

3.2.1 Z-vertex calibration

The Z-vertex (z_{tar}), which was expressed by eq. (3.6), is calibrated using the carbon multi-foil target. A description of the target can be found in Sec.2.4. The origin of the scattered particles can be identified from each foil since the thin (0.25 mm thick) solid targets are placed at exactly 25 mm intervals. Matrix tuning was done by minimizing the following χ^2_z,

$$\chi^2_z = \sum_{j=1}^{10} \chi^2_{zj} \tag{3.10}$$

$$\chi^2_{zj} = \sum_{i=1}^{N} \frac{\left(z_j^{\mathrm{ref}} - z_i\right)^2}{\sigma^2_{zj}} \tag{3.11}$$

where, j is the label for the carbon foil and i is the label for events when the j-th foil region ($\left|z^{\mathrm{ref}_j} - z_i\right| < 2.5$ cm) was selected. Also, σ^2_{zj} is the standard deviation for the peak of j-th foil. Fig. 3.2 and Fig. 3.3 show the Z-vertex distributions on HRS-L and HRS-R in the calibration run after tuning. Clear peaks corresponding to carbon multi-foil are seen in the distributions.

3.2.2 Angle calibration

x'_{tar} and y'_{tar} are reconstructed by eq. (3.7) and (3.8). They were calibrated using sieve slits placed in front of both spectrometers. Particles passing through a hole in the sieve slit reach the reference plane, making it possible to use the hole posittion as a reference to calibrate the scattering angles. The angle $(x'_{\mathrm{tar}}, y'_{\mathrm{tar}})$ at the reaction point and the position $(x_{\mathrm{SS}}, y_{\mathrm{SS}})$ on the sieve slit can be described by the following relations:

$$y_{\mathrm{SS}} = (l_0 - z_{\mathrm{tar}} \cos\theta_0)\, y'_{\mathrm{tar}} - z_{\mathrm{tar}} \sin\theta_0 \tag{3.12}$$

$$x_{\mathrm{SS}} = (l_0 - z_{\mathrm{tar}} \cos\theta_0)\, x'_{\mathrm{tar}} \tag{3.13}$$

where, $\theta_0 = 13.2$ degrees is the central scattering angle of the spectrometer, and also, l_0 represent the lengths from the center of the sieve slits to the center of the target ($z_{\mathrm{tar}} = 0$). Matrix tuning

for ${x'}_{\rm tar}$ and ${y'}_{\rm tar}$ was done by minimizing $\chi^2_{\rm ss}$ (where "ss" represents either x' or y') as follows:

$$\chi^2_{\rm ss} = \sum_{k=1}^{10} \sum_{j=1}^{N_{\rm hole}} \chi^2_{{\rm ss}j,k} \tag{3.14}$$

$$\chi^2_{{\rm ss}j,k} = \sum_{i=1}^{N} \frac{\left({\rm ss}^{\rm ref}_j - {\rm ss}_i\right)^2}{\sigma^2_{j,k}} \tag{3.15}$$

where k, j, and i are the labels for each foil, each hole, and the events around the hole when choosing foil and hole in (j,k). Also, ${\rm ss}^{\rm ref}_j$ represents a known hole position. The holes of the sieve slit can be successfully seen as shown in Fig. 3.4 and Fig. 3.5 by tuning in this way.

3.2.3 Momentum calibration

Optimization of the matrix elements C_p of eq. (3.9), which is involved in the momentum reconstruction of scattered electrons and hadrons, was performed using the missing mass spectrum of the ${}^1{\rm H}\,(e,e'K^+)\,\Lambda/\Sigma^0$ reaction with a ^{1}H target. The masses of Λ and Σ^0 hyperons are well known with an accuracy of better than 0.1 MeV/c ($m_\Lambda = 1115.683 \pm 0.006$ MeV/c^2, $m_{\Sigma^0} = 1192.642 \pm 0.024$ MeV/c^2 [9]), so the author and collaborators optimized the matrix element C_p of both arms using the positions of these two mass peaks as references. The following χ^2 was defined and minimized for events near the two peaks:

$$\chi^2_{\Lambda,\Sigma^0} = \sum_{j=1}^{N} \frac{\left(m_{\Lambda,\Sigma^0} - m_i\right)^2}{\sigma^2_{\Lambda,\Sigma^0}}, \tag{3.16}$$

where m_i is the missing mass value in the event of the calibration data, and $\sigma^2_{\Lambda,\Sigma^0}$ is the standard deviation of the corresponding peak for each hyperon.

For the identification of K^+ in HRS-R, event selections by Cherenkov light intensity of AC1 and AC2 (AC1 separates π^+/K^+ with a refractive index $n = 1.015$ and AC2 separates K^+/p with index $n = 1.055$) as well as event cuts by coincidence time (explained in Sec. 3.4) were applied.

Besides, in the momentum calibration, it is necessary to take into account the beam's energy loss within the target cell. For example, focusing on the incident electron beam, if an electron beam with an initial energy E_e is directed at the target, it deposits energy δE_e in the gas target and the materials of the target cell before a reaction occurs. Therefore, the energy at the reaction vertex becomes $E_e - \delta E_e$. The effect of such energy loss similarly applies to the scattered electrons and hadrons. At the reaction vertex, their energy is reconstructed as $E_{e'} + \delta E_{e'}$ or $E_{K,p} + \delta E_{K,p}$, where $\delta E_{e'}$ and $\delta E_{K,p}$ is the energy loss within the target added to the energy $E_{e'}$ and $E_{K,p}$ reconstructed by the spectrometer. The energy loss of the incident electrons is assumed to be the most probable value of 0.29 MeV derived from the thickness of the entrance wall of the aluminum target cell (measurement values summarized in Table 2.2). For the scattered particles, due to the cigar-shaped target cell structure, the effective thickness of the aluminum wall depends on the Z-vertex. This is because if a reaction occurs relatively upstream

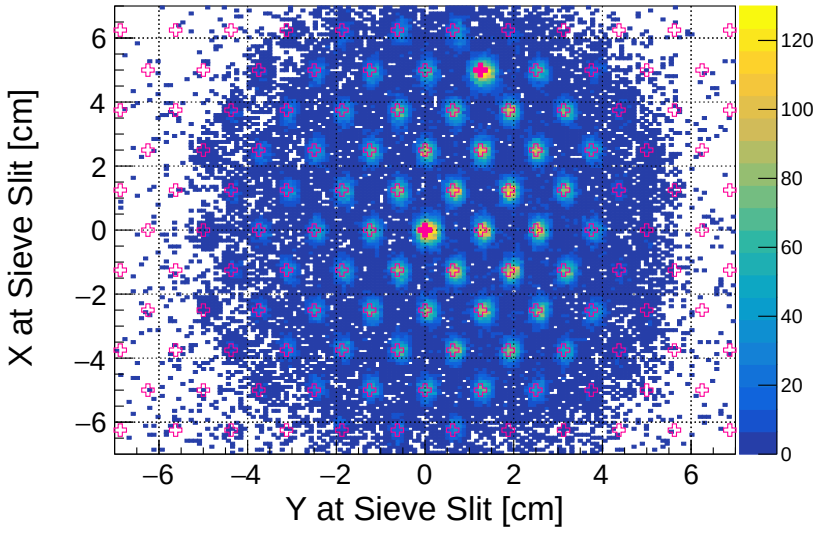

Fig. 3.4: Hole pattern of the sieve slit reconstructed from the reference plane in HRS-L. The red cross markers indicate the positions of the holes.

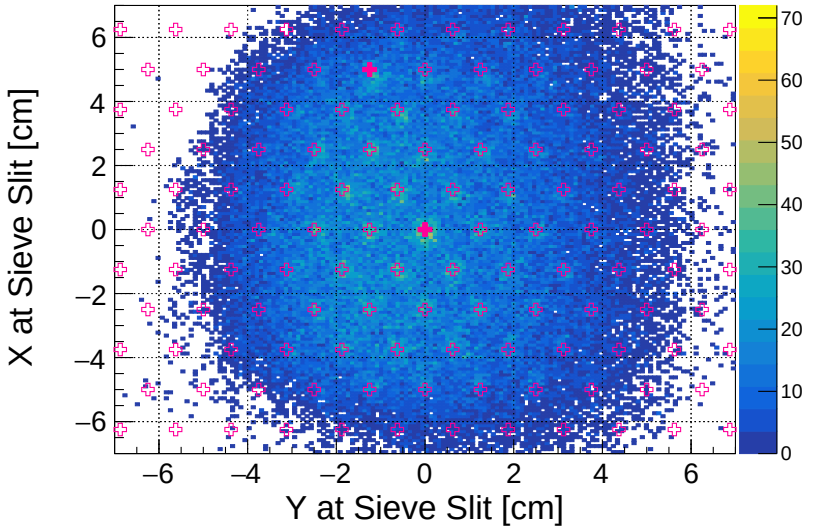

Fig. 3.5: Hole pattern of the sieve slit reconstructed from the reference plane in HRS-R.

in the target cell, particles traverse the side wall of the target cell at an angle of approximately $\theta_{ee'}^{\mathrm{Lab}} \approx \theta_{eK,ep}^{\mathrm{Lab}} \approx 13.2$ degrees. On the other hand, if the reaction occurs downstream, particles hit the rounded exit wall of the target cell almost perpendicularly. The threshold of Z-vertex that distinguishes these cases is determined geometrically to be $z_{\mathrm{tar}} = 9.2$ cm. When a particle passes through the side wall of the cell, the effective thickness it traverses is approximately $\frac{1}{\sin\theta} \approx 4.4$ times greater than in the case of the rear wall, but this value depends on the emission angle $\theta_{ee'}^{\mathrm{Lab}}$ and $\theta_{eK,ep}^{\mathrm{Lab}}$ (corresponding to the parameter y'_{tar} to be calibrated) in each event. Fig. 3.6 and Fig. 3.7 illustrate the y'_{tar}-dependence of the energy loss δE in the target for HRS-L and HRS-R,

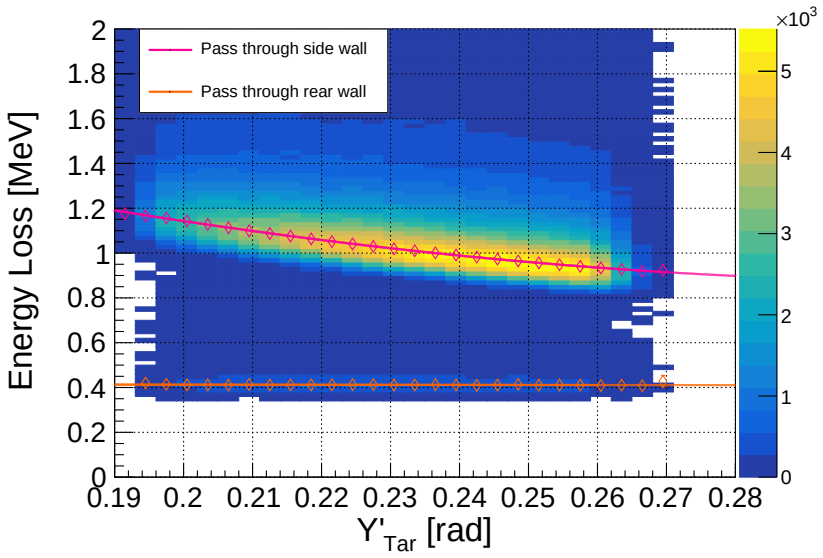

Fig. 3.6: Correlation between energy loss in the target cell and angle y'_{tar} in HRS-L (obtained by Monte Carlo simulations).

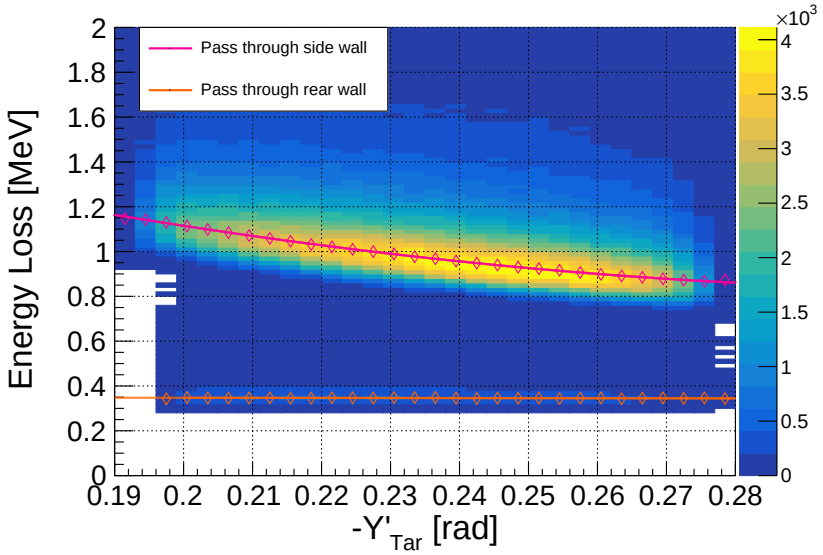

Fig. 3.7: Correlation between energy loss in the target cell and angle y'_{tar} in HRS-R (obtained by Monte Carlo simulations).

respectively, as estimated by Monte Carlo simulations. The explanation of the simulation itself is provided in Sec. 3.7.1 but it assume a target structure modeled after the actual target cell. Events where electrons and hadrons are generated inside the target and accepted within the solid angles of both spectrometers are filled into these two-dimensional distributions.

In Fig. 3.6 and Fig. 3.7, the cluster of events with the largest count represents events where particles passed through the side wall of the target cell. Smaller clusters at lower energy losses represent events where particles passed through the rear wall of the target cell. To describe

and correct for the energy loss of scattered particles in the target cell, the author assumed the following functional form:

$$\delta E\left(y'_{\rm tar}\right) = \begin{cases} p_0 \sin\left(-p_1 \delta_{\rm HRS} y'\right) + p_2 & (z_{\rm tar} < 9.2 \text{ cm}) \\ p_3 \delta_{\rm HRS} y'_{\rm tar} + p_4 & (z_{\rm tar} \geq 9.2 \text{ cm}) \end{cases}, \tag{3.17}$$

where, $\delta_{\rm HRS} = -1$ for HRS-L and $\delta_{\rm HRS} = +1$ for HRS-R, respectively. By fitting the δE - $y'_{\rm tar}$ correlation of the two event groups in Fig. 3.6 and Fig. 3.7 to this function, each parameters in eq. (3.17) were determined. The values of parameters obtained from the fitting are summarized in Table 3.1. In Fig. 3.6 and Fig. 3.7, the overlaid pink and orange curves represent the functions for particles passing through the side wall and rear wall of the target cell, respectively.

Table 3.1: Results of fittins of the energy loss function. Refer also to eq. (3.17).

Parameters	Values for e'	Values for K^+	Values for p
p_0/MeV	-1.70 ± 0.01	-1.74 ± 0.01	-1.86 ± 0.02
p_1	-5.00 ± 0.02	-4.96 ± 0.02	-4.81 ± 0.03
p_2/MeV	2.57 ± 0.01	2.57 ± 0.01	2.78 ± 0.02
p_3/MeV	0.02 ± 0.02	0.03 ± 0.01	-0.01 ± 0.02
p_4/MeV	0.42 ± 0.01	0.35 ± 0.01	0.38 ± 0.01

Fig. 3.8 shows the missing mass spectrum of $^1\mathrm{H}\left(e, e'K^+\right)\Lambda/\Sigma^0$ after matrix tuning and energy loss correction. It must be noted that the tail component on the right side of each peak is mainly due to the radiation of scattered electrons in the target cell, and therefore these events are also truly Λ/Σ^0 production events.

3.3 Target selection by the Z-vertex cut

As discussed in Sec. 2.4, the present experiment used a gas target enclosed in an aluminum cell. Events with reactions in the aluminum walls in front of and behind the gas region become background events for the analysis of the $^1\mathrm{H}\left(\mathrm{e}, \mathrm{e'p}\right)\eta'$ reaction. These events can be removed using the Z-vertex distribution calibrated in Sec. 3.2.1. The following Fig. 3.9 shows the 2D distribution of the Z-vertex reconstructed with both the left and right arms. One can clearly find the region of the hydrogen gas (an area of positive correlation with a length of 25 cm), the region of the aluminum wall (located at $\pm$12.5 cm), and the area of accidental events (other areas). The area enclosed by the violet dashed line is the gate for selecting events used for analysis based on the Z-vertex. The cut conditions are as follows:

$$-2.5 \text{ cm} < z^{\text{HRS-R}} - z^{\text{HRS-L}} < +2.5 \text{ cm} \tag{3.18}$$

$$-20 \text{ cm} < z^{\text{HRS-R}} + z^{\text{HRS-L}} < +20 \text{ cm}. \tag{3.19}$$

The former condition is set to exclude accidental coincidence events, that is, events where particles from different reactions are observed in both arms. On the other hand, the latter condition

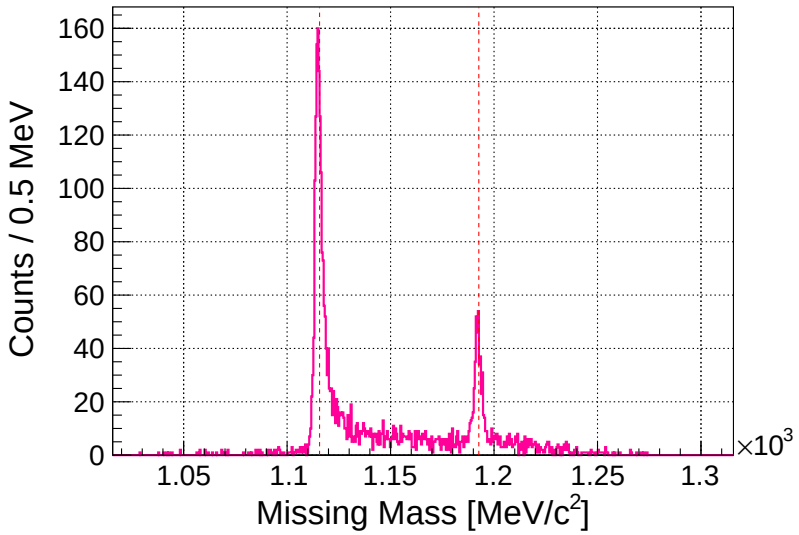

Fig. 3.8: Mising mass spectrum of the $^1\mathrm{H}\,(e, e'K^+)\,\Lambda/\Sigma^0$ reactions after the matrix tuning. The red dashed lines represent the mass of the Λ and Σ^0 hyperons ($m_\Lambda = 1115.683 \pm 0.006$ MeV/c^2, $m_{\Sigma^0} = 1192.642 \pm 0.024$ MeV/c^2 [9]).

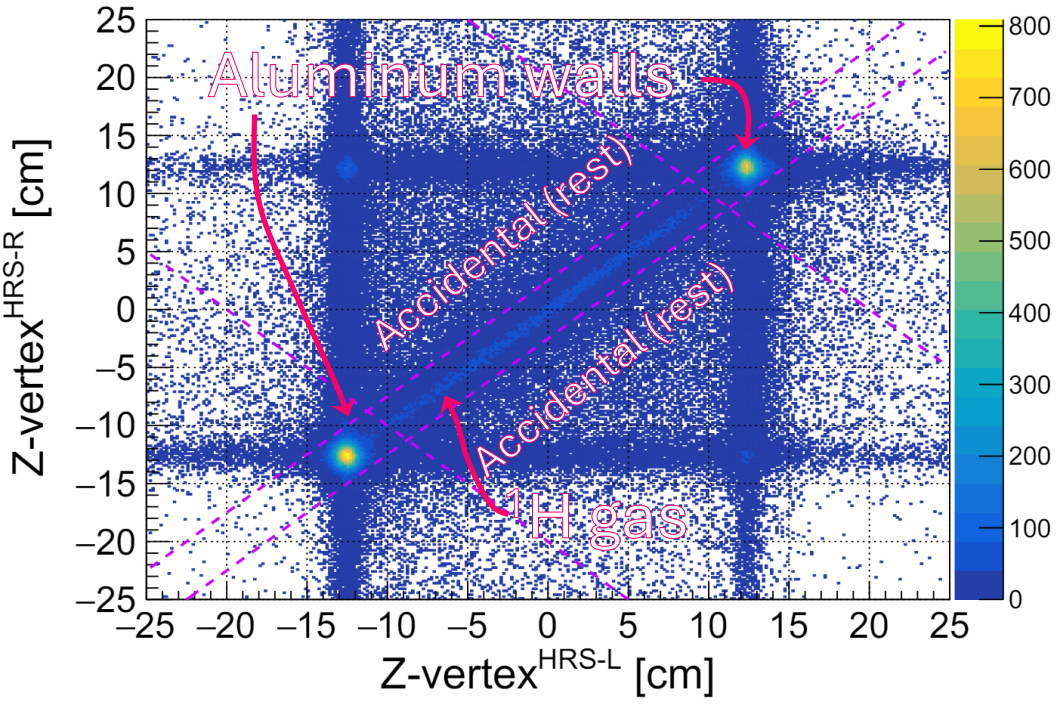

Fig. 3.9: 2D distribution of the Z-vertex reconstructed with both the HRS-L and HRS-R. The regions of hydrogen gas and aluminum cells are clearly seen among the accidental background event. The violet dashed lines represent the gate of the target position selection for analysis.

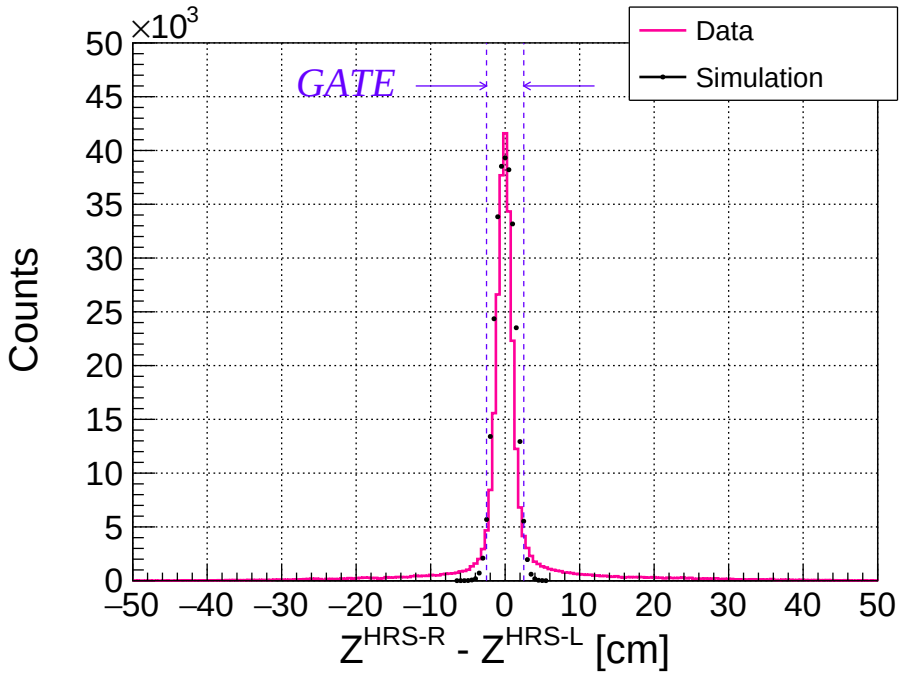

Fig. 3.10: The $z^{\text{HRS-R}} - z^{\text{HRS-L}}$ distribution. The pink histogram represents the distribution from the experimental data, and the black plots represent the distribution from a simulation. Accidental background events have been subtracted. The blue dashed lines represents the gate for accepting events.

is set to eliminate contamination from the aluminum cell.

Consider the Z-vertex selection efficiency. The total efficiency ε_z for the cuts applied in eq. (3.18) and eq. (3.19) is expressed as:

$$\varepsilon^Z = \varepsilon^Z_{\text{diff}} \times \varepsilon^Z_{\text{ave}}, \tag{3.20}$$

Here, $\varepsilon^Z_{\text{diff}}$ represents the efficiency of the cut described by eq. (3.18), and $\varepsilon^Z_{\text{ave}}$ corresponds to the efficiency of the cut described by eq. (3.18). First, $\varepsilon^Z_{\text{diff}}$, which involves the difference between the Z-vertices reconstructed in the left and right arms, reflects the extent to which pairs of electrons and hadrons originating from the same true reaction survive the cut. Fig. 3.10 shows the one-dimensional distribution of $z^{\text{HRS-R}} - z^{\text{HRS-L}}$. The accidental background has been subtracted. As the distance from the center of the distribution increases, it indicates that Z-vertex was not reconstructed correctly due to interactions with the target or other materials. The region enclosed by the blue dashed lines represents the gate for accepting events. The ratio of accepted events to the total number of events corresponds to $\varepsilon^Z_{\text{diff}}$, and its value was found as follows:

$$\varepsilon^Z_{\text{diff}} = 0.757 \pm 0.002 \text{ (stat)}. \tag{3.21}$$

On the other hand, $\varepsilon^{\text{ave}}_z$, which involves the average value of the Z-vertices reconstructed in both arms (described by eq. (3.19)), indicates the extent to which events truely occurring in the

hydrogen gas target survive the cut. This efficiency is defined for events where a cut is applied based on the difference in Z-vertex reconstructed from the left and right arms. The author estimated $\varepsilon_z^{\mathrm{ave}}$ by fitting the distribution of the averaged Z-vertex:

$$z^{\mathrm{ave}} = \frac{z^{\text{HRS-R}} + z^{\text{HRS-L}}}{2}. \tag{3.22}$$

Fig. 3.11 shows the distribution of the averaged Z-vertex, and overlaid blue curve represents the fitting function applied to the distribution. The response function is expressed as:

$$\begin{aligned} F(x) := \quad & f(\mu = -12.5 \text{ cm}; x) \\ & + f(\mu = +12.5 \text{ cm}; x) \\ & + \int_{-\infty}^{+\infty} g(t)\, f(\mu = 0; x - t)\, \mathrm{d}t, \end{aligned} \tag{3.23}$$

where,

$$f(\sigma_1, \sigma_2, \mu_2, C_2; \mu, C; x) := C\left[e^{-\left(\frac{x-\mu}{2\sigma_1}\right)^2} + C_2 e^{-\left(\frac{x-\mu+\mu_2}{2\sigma_2}\right)^2}\right] \tag{3.24}$$

$$g(a, b, c; x) := \begin{cases} 0 & (|x| > 12.5 \text{ cm}) \\ a(x-b)^2 + c & (|x| < 12.5 \text{ cm}). \end{cases} \tag{3.25}$$

It consists of a double-Gaussian function $f(x)$ with shared parameters representing the walls of the two aluminum cells, and a function $g(x)$ of a polynomial convoluted with the double-Gaussian, which represents the gas region. The black and orange dashed lines in Fig. 3.11 represent the components of the function corresponding to the aluminum cell regions and the gas region, respectively. The cut condition of eq. (3.19) corresponds to a cut on z^{ave} such that:

$$|z^{\mathrm{ave}}| < 10 \text{ cm}. \tag{3.26}$$

The reason for imposing a somewhat tighter cut condition compared to the gas region $[12.5 \text{ cm}, +12.5 \text{ cm}]$ is to reduce the contamination of events originating from the aluminum cell, due to the Z-vertex resolution of the spectrometer. The efficiency of this cut was estimated using the fitting function by calculating the ratio of the events remaining after the cut to the total events in the gas region component. The value obtained was:

$$\varepsilon_{\mathrm{ave}}^{Z} = 0.835 \pm 0.001(\mathrm{stat}). \tag{3.27}$$

Moreover, the number of events originating from the aluminum cell that remain even after applying this cut can also be estimated using the fitting function. The fraction of events from the cell walls relative to the total number of events after the cut was estimated as:

$$\varepsilon^{\mathrm{Al}} = 0.0007 \pm 0.0002(\mathrm{stat})^{+0.0046}_{-0}(\mathrm{sys}). \tag{3.28}$$

In addition to statistical errors, systematic errors are also presented. These were determined by considering the surplus events observed at left- and right-ends of Fig. 3.11. Fig. 3.12 and Fig. 3.13 illustrate the changes in $\varepsilon_z^{\mathrm{ave}}$ and $\varepsilon_{\mathrm{Al}}$ as the cut range $|z^{\mathrm{ave}}| < X$ is varied. Taking the

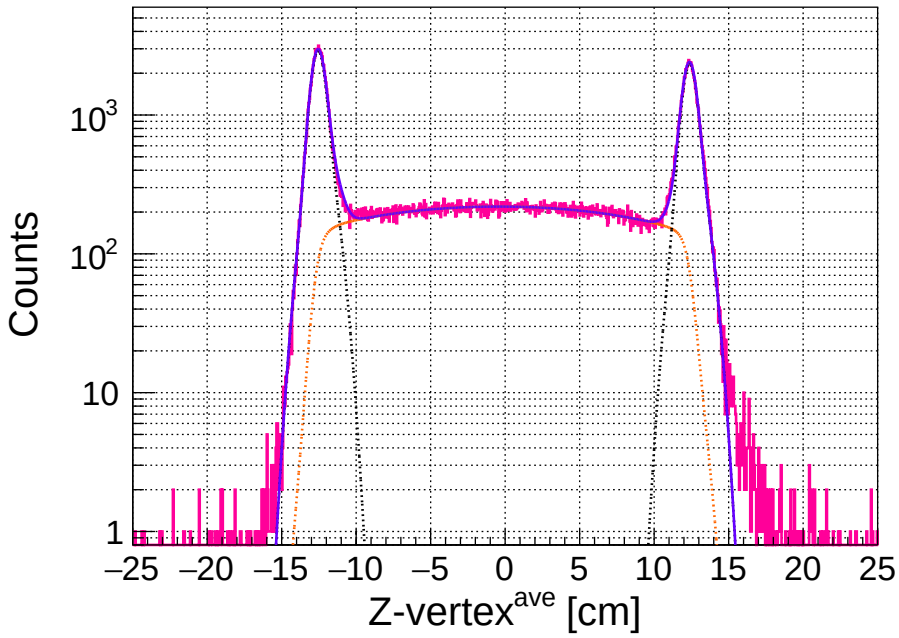

Fig. 3.11: The average Z-vertex distribution of both arms. The histogram was fitted by a function of eq. (3.23)–(3.25). The blue line represents the entire fitting function, the black dotted line represents the peak components of the aluminum cell, and the orange dotted line represents the continuous components of the gas region.

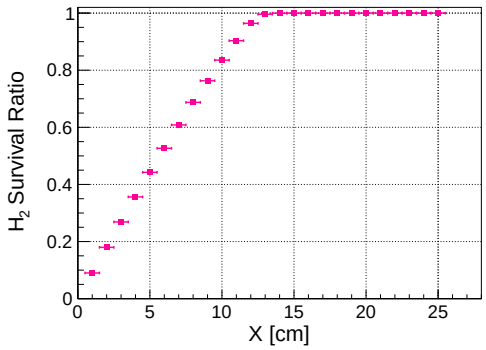

Fig. 3.12: The selection efficiency of the ^{1}H gas region by the Z-vertex cut. The horizontal axis is the gate width on the z^{ave} distribution.

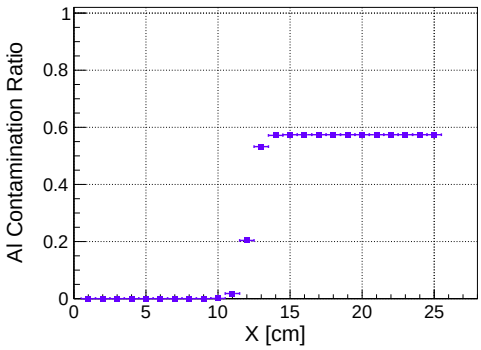

Fig. 3.13: The Al contamination ratio by the Z-vertex cut by the Z-vertex cut. The horizontal axis is the gate width on the z^{ave} distribution.

two efficiencies of $\varepsilon_z^{\text{diff}}$ and $\varepsilon_z^{\text{ave}}$ into consideration, the total cut efficiency ε_z for the Z-vertex was estimated as:

$$\varepsilon^Z = 0.654 \pm 0.002 \text{ (stat)}, \tag{3.29}$$

with the associated uncertainties included.

3.4 Particle identification (PID)

The matching of protons and electrons emitted from the $(e, e'p)$ reaction was performed using the distribution called "coincidence time." The coincidence time T_{coin} is defined as the timing difference between reaction times at the target position reconstructed in both the left and right arms,

$$T_{\text{coin}} := t_{\text{HRS-L}}\,(\text{Target}) - t_{\text{HRS-R}}\,(\text{Target})\,. \tag{3.30}$$

Time at the target $t\,(\text{Target})$ can be calculated from the time at the trigger counter S2 ($t\,(\text{S2})$), path length from the target to S2 ($l_{\text{path}} = 27.3\text{m}$), and the particle's velocity β,

$$t\,(\text{Target}) := t\,(\text{S2}) - \frac{l_{\text{path}}}{\beta c} \tag{3.31}$$

$$= t\,(\text{S2}) - \frac{\sqrt{p^2c^2 + m_p^2c^4} \times l_{\text{path}}}{pc^2}. \tag{3.32}$$

Here, β can be calculated by assuming the proton mass m_p and the momentum p reconstructed by the backward transfer matrix. Fig. 3.14 shows the coincidence time distribution when the ^{1}H gas region is selected in the Z-vertex distribution. Since scattered electrons and protons in the $(e, e'p)$ reaction are emitted from the target position at the same time, the coincidence time calculated by eq.(3.30) should be 0. In Fig. 3.14, one can clearly find a peak at 0 ns, which corresponds to the correct combination of e' and proton. On the other hand, as in eq. (3.32), the proton mass was assumed when calculating β, so different hadrons such as π^+ and K^+ make peaks at different timings corresponding to the mass difference. Proton events were selected by applying a timing gate indicated by two dashed lines in Fig. 3.14. The gate adopted for the analysis is $|T_{\text{coin}}| < 2$ ns. Events that lie across the coincidence time distribution are accidental coincidences that mismatch e' with hadrons produced in different reactions. Such events are also inside the timing gate for cuts. Not only the proton cut efficiency but also the contamination ratio of other hadrons such as pions and kaons were estimated by fitting the coincidence time distribution. Functions obtained by fitting are also overlaid in Fig. 3.15. The black line is the total fit, the blue line is the proton peak, the green line is the pion peak, and the orange line is the kaon peak. Fitting to the three main peaks was performed with a double-Gaussian function expressed by the following equations:

$$f_{\text{DG}}\,(\sigma_1, \sigma_2, \mu, C, C_2; x) := C\left[e^{-\left(\frac{x-\mu}{2\sigma_1}\right)^2} + C_2 e^{-\left(\frac{x-\mu}{2\sigma_2}\right)^2}\right]. \tag{3.33}$$

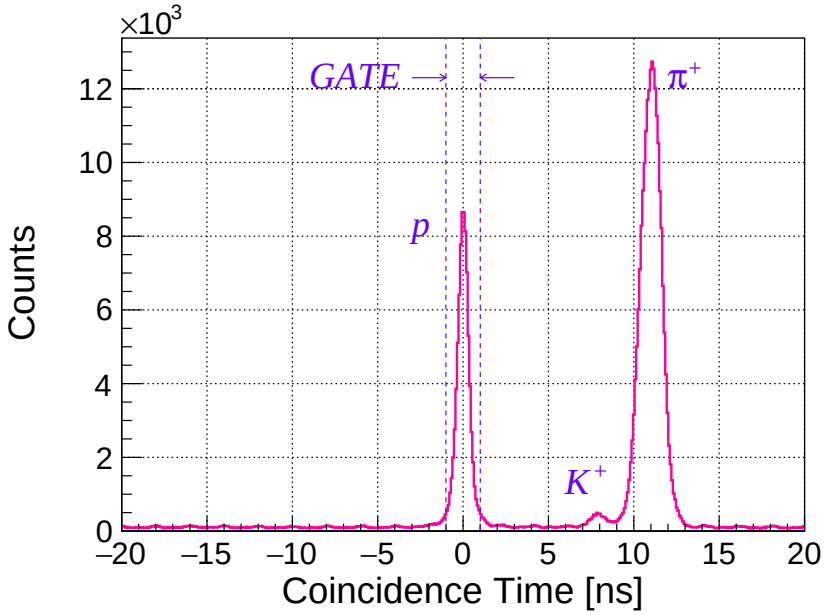

Fig. 3.14: Coincidence time distribution (in linear scale). The Z-vertex cut (see Sec. 3.3) and the focal plane cut (see Sec.3.9.1) were applied. The peaks located at 0 ns, $\sim$ 7.8 ns, $\sim$ 11.1 ns correspond to proton, kaon, and pion, respectively. Accidental coincidence events are distributed uniformly beneath the three peaks. The two blue dashed-lines represent the timing gate for proton selection.

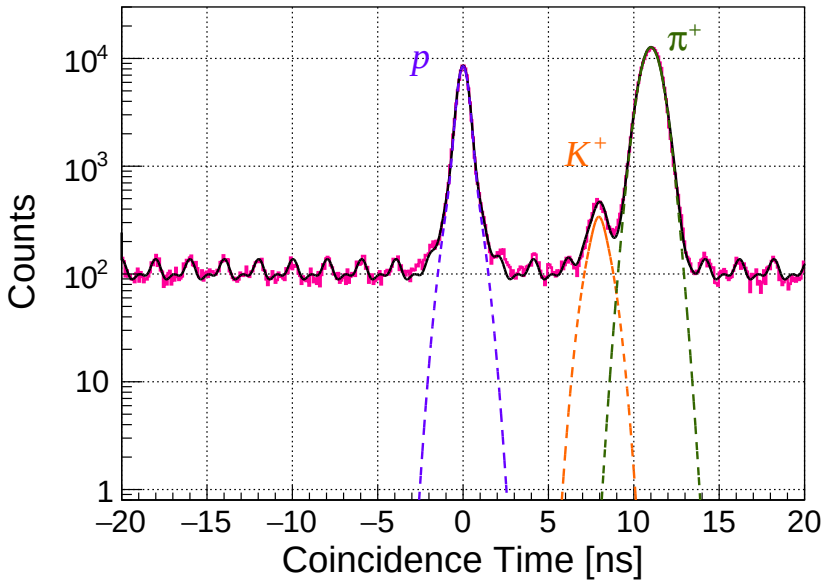

Fig. 3.15: Coincidence time distribution (in log scale). The overlaid black curve represents the total fit result. The blue, orange and green curves represent a single component of double-Gaussian function corresponding to protons, kaons and pions, respectively.

The shape of the accidental coincidence was reproduced by scaling the height of the double-Gaussian functions of the main peaks, shifting them laterally to form a 2 ns bunch structure, and superimposing them. Using the fitting results, it is possible to estimate the efficiency of selecting protons within a 2 ns coincidence time gate, as well as the ratio of other hadrons that may contaminate the gate. First, the fraction $\varepsilon^{\mathrm{CT}}$ of protons remaining after applying the gate, relative to the number of protons before applying the coincidence time gate, can be determined by taking the ratio of the integral of the double-Gaussian function component corresponding to protons over the range $[-\infty, +\infty]$ to the integral over the range $[-1\ \mathrm{ns}, +1\ \mathrm{ns}]$. This yields:

$$\varepsilon^{\mathrm{CT}} = 0.965 \pm 0.005. \tag{3.34}$$

Next, the ratio of π^+ and K^+ mesons that contaminate the coincidence time gate can also be determined by numerically calculating the integral of the double-Gaussian function components corresponding to each particle over the range $[-1\ \mathrm{ns}, +1\ \mathrm{ns}]$. The estimated values are small as,

$$\varepsilon_K, \varepsilon_\pi < 10^{-5}. \tag{3.35}$$

Thus, these contributions are so small that one can neglect when determining the differential cross section for η' production.

3.5 Missing mass spectrum of the $p\,(e,e'p)\,X$ reaction

The missing mass in the ${}^1\mathrm{H}\,(e,e'p)\,X$ reaction can be calculated by the following formula:

$$M_{\mathrm{X}} = \sqrt{\{(E_e - E_{e'}) + M_p - E_{p_{\mathrm{scat}}}\}^2 - \{(\boldsymbol{p}_e - \boldsymbol{p}_{e'}) - \boldsymbol{p}_{p_{\mathrm{scat}}}\}^2}. \tag{3.36}$$

The momentum vectors of scattered particles are written as follows using p, $x'\,(:= p_x/p_z)$, and $y'\,(:= p_y/p_z)$ reconstructed with the backward matrix explained in eq. (3.7) to eq. (3.9):

$$\boldsymbol{p} = \begin{pmatrix} p_x \\ p_y \\ p_z \end{pmatrix} = \frac{p}{\sqrt{1 + x'^2 + y'^2}} \begin{pmatrix} x' \\ y' \\ 1 \end{pmatrix}. \tag{3.37}$$

Fig. 3.16 is the histogram of the missing mass calculated by eq. (3.36). The dashed line represents the mass of the η' meson, 0.95778 GeV/c^2 cited from PDG [9]. A peak is clearly seen at the mass of the η', which corresponds to the event from the ${}^1\mathrm{H}\,(e,e'p)\,\eta'$ reaction. On the other hand, a large number of background events are broadly distributed beneath the η' peak. It must be emphasized that, as previously mentioned, the ratio of other hadrons such as π^+ and K^+, and accidental coincidence events is very small, thus most of the background events in Fig. 3.16 are the correct coincidence events of the $(e,e'p)$ reaction. These background events are presumed to be multi-meson production $(2\pi, 3\pi, \cdots)$. The shape of the distributions will be studied using simulation in a later section.

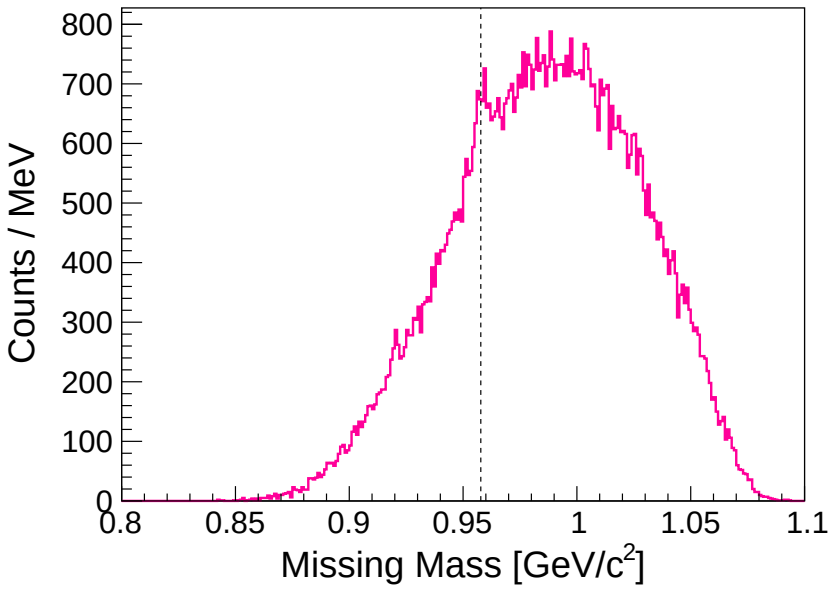

Fig. 3.16: Missing mass distribution of the $^1\mathrm{H}\,(e, e'p)\,X$ reaction (count-based). The dashed-line represents the mass of η' ($m_{\eta'} = 957.78$ MeV/c^2 [9]).

3.6 Subtractable background

The primary background caused by multi-pion production aside, the following three background sources can be considered:

1. Accidental coincidence events
2. Events from reactions involving the aluminum target cell
3. Events from the $(e, e'K^+)$ and $(e, e'\pi^+)$ reactions.

Although the total contributions from these sources are small, their distributions and total amounts can be accurately determined using experimental data. Thus, they can be subtracted from the missing mass distribution of the $(e, e'p)$ reaction. Among these, the contamination from the third item, $(e, e'K^+)$ and $(e, e'\pi^+)$ reactions, has been found to be negligibly small based on the discussions in the previous section. On the other hand, a precise understanding regarding the first and second items has been achieved using the methods employed by the collaborators in prior studies [72–76].

3.6.1 Accidental coincidence

An accidental coincidence event (or accidental background) refers to an event in which completely unrelated scattered electrons and hadrons are detected in the spectrometers of both the left and right arms. Such events are distributed almost uniformly within the timing gate of the coincidence trigger. In Fig. 3.15 background events are distributed constantly across all

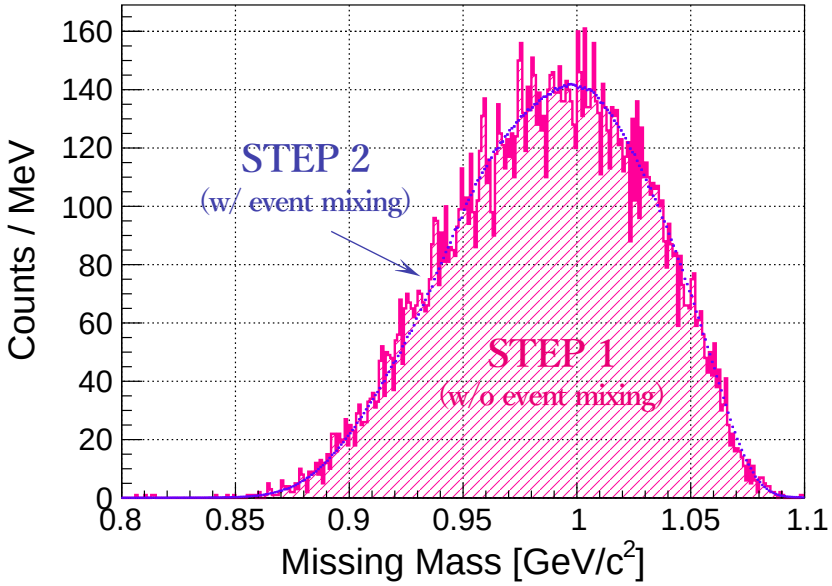

Fig. 3.17: Missing mass spectrum of the accidental coincidence events. The pink histogram represents a spectrum befor the event mixing while the blue plot represents a spectrum after the event mixing.

coincidence times, with a certain amount also comtaminated into the timing gate for selecting protons. First, the author obtained the missing mass distribution generated by accidental coincidence events by gating specific regions in coincidence time where the true three peaks are excluded, specifically $[-9\text{ ns}, -5\text{ ns}]$, $[1\text{ ns}, 5\text{ ns}]$, and $[15\text{ ns}, 19\text{ ns}]$. The spectrum is shown as the pink histogram (labeled STEP 1) in Fig. 3.17. The spectrum is roughly hill-shaped but exhibits statistical fluctuations per bin. To address this, the author proceeded to the next step, which involved event mixing—a deliberate mixing up an event ID that linking electrons and hadrons. Since accidental coincidence events essentially mean detecting uncorrelated electron-hadron pairs separated in time and space, the newly generated events through the event mixing behave exactly same. Repeating the event mixing thus extremely increases the statistical size of the sample. The distribution of accidental coincidences obtained from 1,000 iterations of event mixing is shown as the blue plot (labeled STEP 2) in Fig. 3.17. As can be seen, the statistical error is now so small that it is no longer visible. Therefore, when subtracting the accidental background distribution from the missing mass of protons, the error propagation due to sample size can be minimized to zero. The scaling factor for the subtraction is simply the reciprocal of the ratio between the proton gate width of 2 ns in the coincidence time distribution and the gate width of 12 ns used to sample the accidental background, which is $\frac{1}{6}$.

3.6.2 Contamination from the target cell

The contamination of scattered electrons and hadrons caused by reactions in the aluminum target cell is significantly suppressed by the Z-vertex cut described in Sec. 3.3. The survival ratio after the cut is calculated using eq. (3.28) and although the value is very small, it is finite when considering the associated errors. Based on this ratio, the author derived the distribution originating from the aluminum target cell that should be subtracted from the missing mass spectrum of the proton. In Fig. 3.18, the blue-shaded region represents the gate selecting the aluminum cell within the averaged Z-vertex distribution. The missing mass spectrum obtained based on eq. (3.1) which assumes the target mass of the proton, is shown in Fig. 3.19. The author scales this distribution according to the aluminum survival rate given in eq. (3.28) and subtracts it from the proton's missing mass distribution.

3.7 Acceptance

The acceptance in high-energy experiments is broadly refered to the ratio of the number of particles actually detected to that of emitted particles. Generally, this encompasses measurement efficiency due to the detector's response, the effects of particle decay, energy loss due to interactions with matter, and secondary reactions outside the target. Here, the author estimates the acceptance in the narrow sence by extracting the effective solid angle encompassing the geometrical coverage of the spectrometer and the interactions between particles and materials. Due to the unique target shape used in the present experiment, whether particles emitted from the target reach the detection plane of the HRS depends not only on their momentum and emission angle but also on the Z-vertex of the reaction point. The author estimates the acceptance of HRSs by Monte Carlo simulations that model the experimental setup, including the real spectrometer and target. Specifically, the simulation implements physical interactions such as particle ionization and radiation, converting the effects of energy loss into an effective solid angle distribution.

3.7.1 SIMC

SIMC is a program code widely used to simulate GeV-order experiments at JLab Hall-A and Hall-C. The original code was written by T.G. O'Neill and N.C. Makins to study the $A\,(e, e'p)$ quasi-elastic scattering, and has since been developed to accommodate various reactions and experimental conditions [77, 78]. SIMC implements realistic materials and geometries for the various spectrometers used in Hall-A and Hall-C (*e.g.*, HMS, SOS, SHMS, HRS, etc.). Therefore, instead of calculating particle trajectories and secondary interactions in small steps and accumulating them as in Geant4 [79, 80], the advantage of SIMC lies in its implementation of an accurate description of the magnetic transport matrices for each spectrometer. SIMC also realistically reproduces interactions between a beam and a material, such as radiative effects, multiple scattering, ionization energy loss, and particle decay, by means of practical empirical

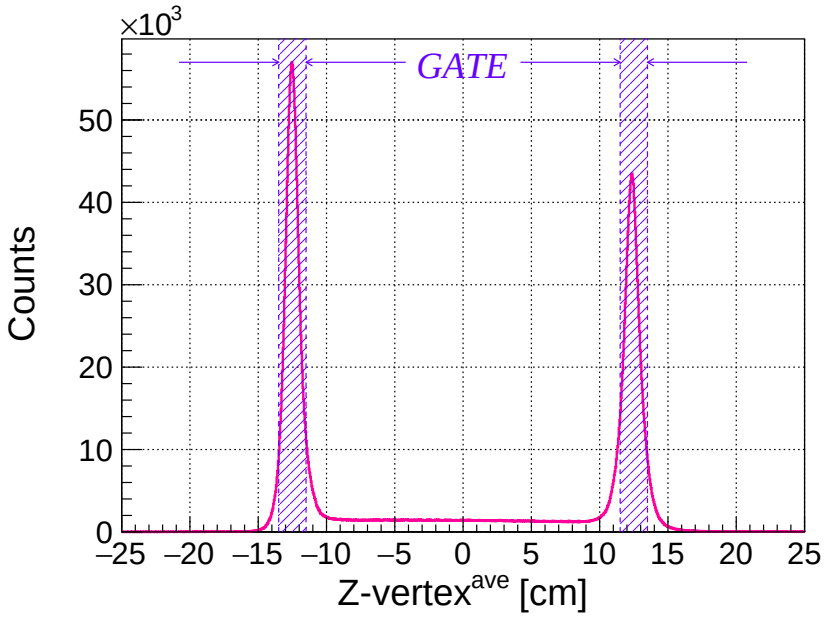

Fig. 3.18: Z-vertex cut for selecting the aluminum target cell (blue-shaded region).

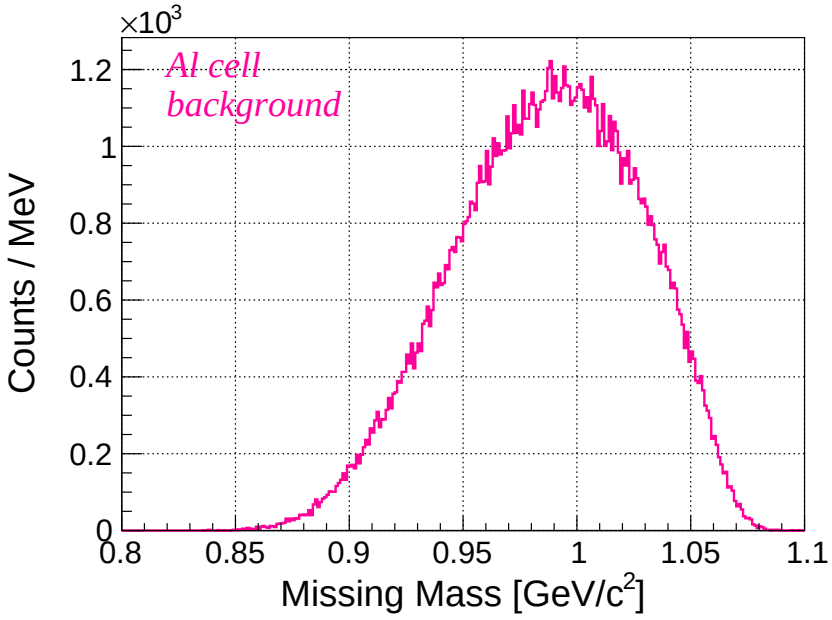

Fig. 3.19: Missing mass spectrum of the events from the aluminum cell.

rules and Monte Carlo methods. In order to accurately estimate the acceptance and the influence of interactions under the present experimental conditions, the cigar-like-shaped aluminum target cell was modeled and newly implemented in the SIMC code.

3.7.2 Estimation of acceptance by SIMC

One can estimate the single-arm acceptance of HRS by the following procedure:

1. Generate particles from the position of the target in the simulation. The particle's momentum was uniformly generated within a range of ±2.5 % around the central momentum of the spectrometer. The emission angles were generated uniformly across the entire solid angle. The Z-vertex was uniformly generated within the range of $[-10\ \mathrm{cm}, +10\ \mathrm{cm}]$. All these ranges sufficiently cover the acceptance of the HRS.
2. Record the total number of generated particles N_{gen} and the number of accepted particles in the detector plane N_{acc}. Then, using these values and the solid angle where the particles were generated ($\Delta\Omega_{\mathrm{gen}}$), the solid angle of the spectrometer can be determined by the following formula:

$$\Delta\Omega_{\mathrm{acc}} = \frac{N_{\mathrm{acc}}}{N_{\mathrm{gen}}}\Delta\Omega_{\mathrm{gen}} \tag{3.38}$$

The following Fig. 3.20 and 3.21 show the two-dimensional dependence of the solid angle on momentum and Z-vertex for HRS-L and HRS-R, respectively.

3.8 Number of target atoms

The number of target atoms is obtained according to the following equation using the mass thickness described in Table 2.3,

$$N_{\mathrm{Target}} = \frac{\mathrm{Thickness}\ \left[\mathrm{g/cm^2}\right]}{\mathrm{Molecular\ Mass}\ \left[\mathrm{g/mol}\right]} \cdot N_{\mathrm{A}}\left[/\mathrm{mol}\right] \cdot N_p \cdot F_{\mathrm{decrease}}\left(I\right). \tag{3.39}$$

where N_{Target} is the number of target atoms, and N_p represents the number of protons in a single molecule and $N_p = 2$ in the case of hydrogen. Also, F_{decrease} is the factor of density decrease depending on the beam current. When irradiating a cryo-gas target, the high-current electron beam heats the gas around the beam path by its energy loss, and locally reduces the gas density. The current dependence of this effect was measured by detecting the yield of electron scattering with the same setup as in the present experiment [68]. Fig. 3.22 represents the quantity called charge normalized yield (corresponding to F_{decrease}), which is the yield of electrons normalized with the total charge of the electron beam and the detection efficiency:

$$F_{\mathrm{decrease}} = \frac{PS \cdot N}{Q \cdot \varepsilon \cdot LT}, \tag{3.40}$$

where,

$$\begin{aligned} PS &= \text{Prescale faccor of DAQ}, \\ N &= \text{Number of detected electrons}, \\ Q &= \text{Integrated charge of electron beam}, \\ \varepsilon &= \text{Detector efficiency}, \\ LT &= \text{Live time}. \end{aligned}$$

This variable reach 1.0 in the limit of weak current of beam. In ref. [68], the measured data of

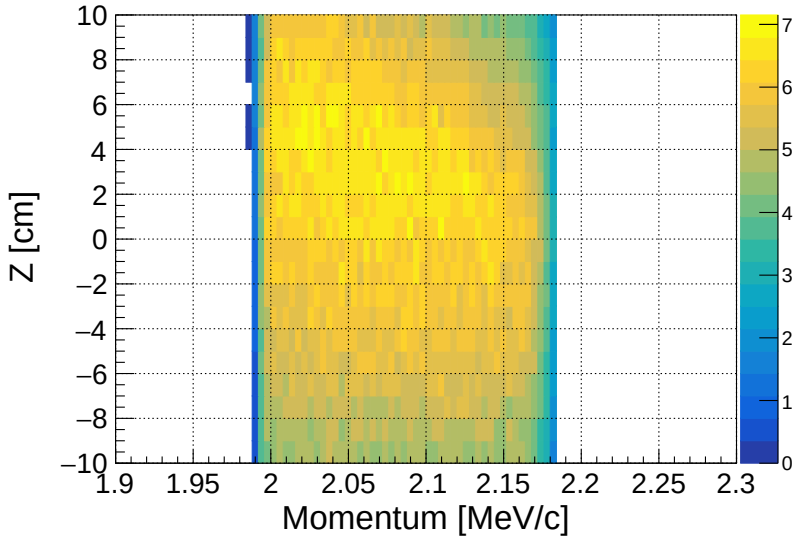

Fig. 3.20: The two-dimensional dependence of the solid angle on momentum and Z-vertex for HRS-L.

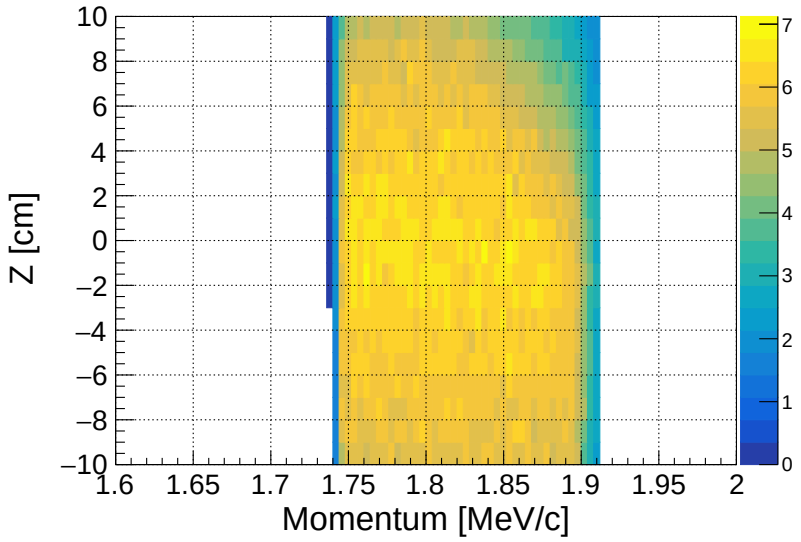

Fig. 3.21: The two-dimensional dependence of the solid angle on momentum and Z-vertex for HRS-R.

F_{decrease} was fitted with the following quadratic function:

$$F_{\mathrm{decrease}}\left(I\right) = aI^2 + bI + c, \tag{3.41}$$

the parameters a, b and c for the ^{1}H taraget was obtained by the fitting. The values of the parameters are shown in Table 3.23. At the beam current of the experiment $I = 22.5$ [μA], the value of F_{decrease} is

$$F_{\mathrm{decrease}}\left(I = 22.5\ \ [\mu\mathrm{A}]\right) = 0.884 \pm 0.01. \tag{3.42}$$

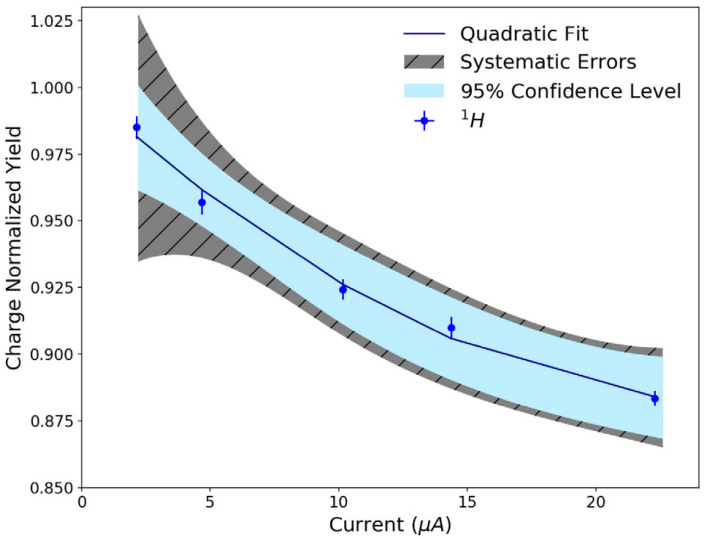

Fig. 3.22: The relationship between the normalized density of ^{1}H and beam current [68].

Fig. 3.23: Parameters of F_{decrease} [68].

Target	Parameter	Value
^{1}H	a	$(1.70 \pm 0.47) \times 10^{-4}$
	b	$(-9 \pm 0.12) \times 10^{-3}$
	c	$1. \pm 0.006$

Therefore, the number of target atoms in the present experiment is calculated as

$$N_{\text{Target}} = 0.0375 \pm 0.00014 \ \left[\text{b}^{-1}\right]. \tag{3.43}$$

3.9 Additional event selection

3.9.1 Reference plane cut

The author applied additional event cuts on the correlation of the position and the angle on the reference plane of the HRS. Fig. 3.24 and Fig. 3.25 represent the distribution of x_{rp} versus x'_{rp} at the focal plane. The two quantitiess of x_{rp} and x'_{rp} have a positive correlation because the reference plane of the HRS (in other words, the plane where the two parallel VDCs measure particles) is angled at 45 degrees relative to the particle trajectory. However, in the measured data in Fig. 3.24 and Fig. 3.25, there are some events that deviate from the correlation possibly due to incorrect tracking in the VDC. Such unexpected events from somewhere were eliminated according to the following cut condition, and the events with correct correlation were selected

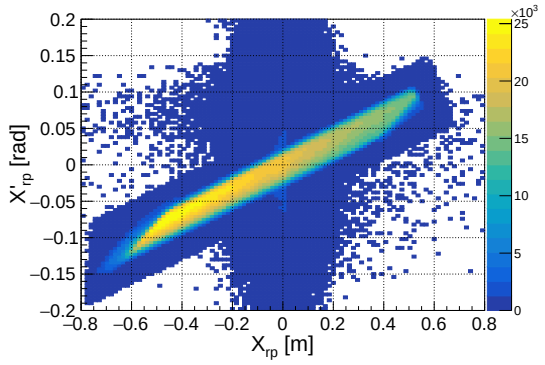

Fig. 3.24: Distribution of x'_{rp} v.s x_{rp} at the reference plane in HRS-L.

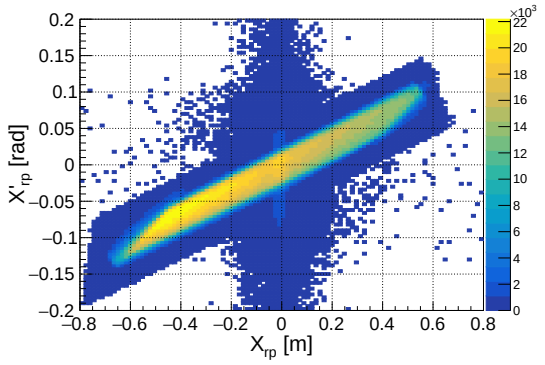

Fig. 3.25: Distribution of x'_{rp} v.s x_{rp} at the reference plane in HRS-R.

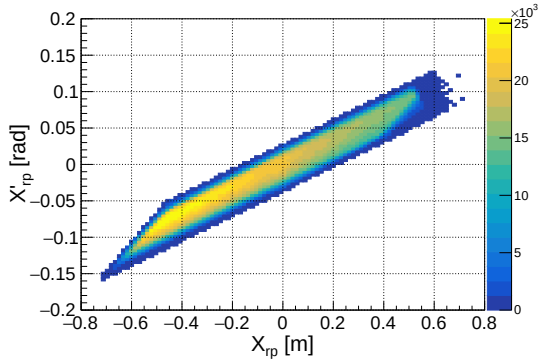

Fig. 3.26: Distribution of x'_{rp} v.s x_{rp} after the focal plane cut in HRS-L

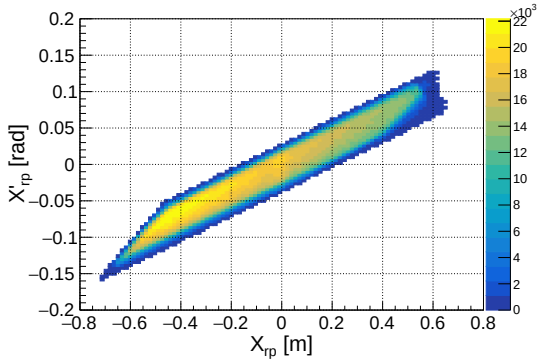

Fig. 3.27: Distribution of x'_{rp} v.s x_{rp} after the focal plane cut in HRS-R

for further analysis:

$$x'_{\mathrm{rp}}\ [\mathrm{rad}] < 0.17 x_{\mathrm{rp}}\ [\mathrm{m}] + 0.025, \tag{3.44}$$

$$x'_{\mathrm{rp}}\ [\mathrm{rad}] > 0.17 x_{\mathrm{rp}}\ [\mathrm{m}] + 0.035, \tag{3.45}$$

$$x'_{\mathrm{rp}}\ [\mathrm{rad}] < 0.40 x_{\mathrm{rp}}\ [\mathrm{m}] + 0.130. \tag{3.46}$$

The distribution after the cut is shown in Fig .3.26 and Fig .3.27. The cut condition is identical in both HRS-L and HRS-R. This selection left a total of 88.63 ± 0.05 (stat.) % of events in both the left and right arms.

3.9.2 Cut for track multiplicity

Multi-track events, which refer to a series of events where multiple particles are recorded at a single trigger timing, are excluded on the HRS-L. In principle, the timing information recorded for each track can be used to calculate the coincidence time explained in Sec. 3.4, However, during the beamtime, there were periods when the TDC on the HRS-L side could not record correctly due to failure of an electronic circuit modules. To address this problem, the author used the trigger timing as the timing for $t\,(\mathrm{S2})_{\mathrm{HRS\text{-}L}}$. This method cannot be applied to multi-

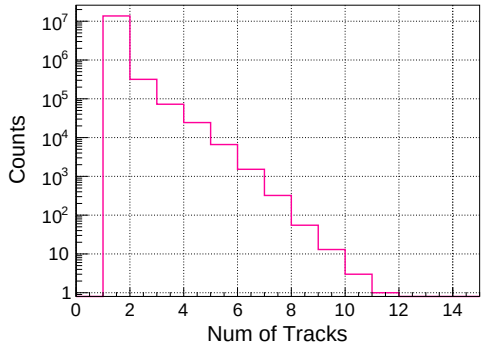

Fig. 3.28: Distributions of number of tracks for HRS-L.

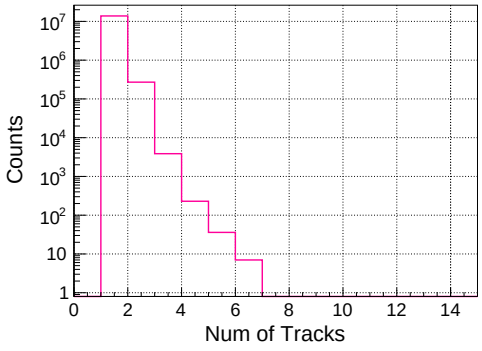

Fig. 3.29: Distributions of number of tracks for HRS-R.

track events, and the coincidence time can be correctly calculated only for the particle that hits first in each event. Fig. 3.28 and Fig. 3.29 show the number of tracks in HRS-L and HRS-R. For the reasons above, only events with one track in HRS-L were selected for analysis, and the selected events account for 97.00 ± 0.04 (stat.) % of all coincidence events. On the other hand, the HRS-R side was not filtered by the number of tracks, and all events with more than or equal to one track were used for analysis.

3.9.3 Cut for momenta at the acceptance edge

Although SIMC has been dedicatedly developed with significant effort, it does not perfectly reproduce all the details of reality. Users must carefully evaluate the extent of how accurately a simulation can replicate the real setup when using the simulation. Generally, it is expected that the degree of mismatch will increase at the edges of the acceptance. The author set the following event selection for particle's momentum to exclude events located at the edges of the acceptance:

$$2.002 \text{ [GeV/c]} < p_{e'} < 2.176 \text{ [GeV/c]}, \tag{3.47}$$

$$1.758 \text{ [GeV/c]} < p_p < 1.902 \text{ [GeV/c]}. \tag{3.48}$$

The following Fig. 3.30 and Fig. 3.31 show the momentum distributions of scattered electrons and protons obtained from the experimental data. The region between the red dashed lines in the figures represents the accept region for momentum as defined by eq. (3.47) and eq. (3.48).

3.9.4 Kinematical cut

The production of η' is not necessarily observed across the entire range of all momentum acceptance. This is because the momentum of the scattered electron and proton involved in the η' production are correlated, and when the curve crosses the edges of the momentum acceptance, η' cannot be observed in regions beyond those limits. Fig. 3.32 shows the momentum-momentum correlation of scattered electrons and protons from the simulation of the

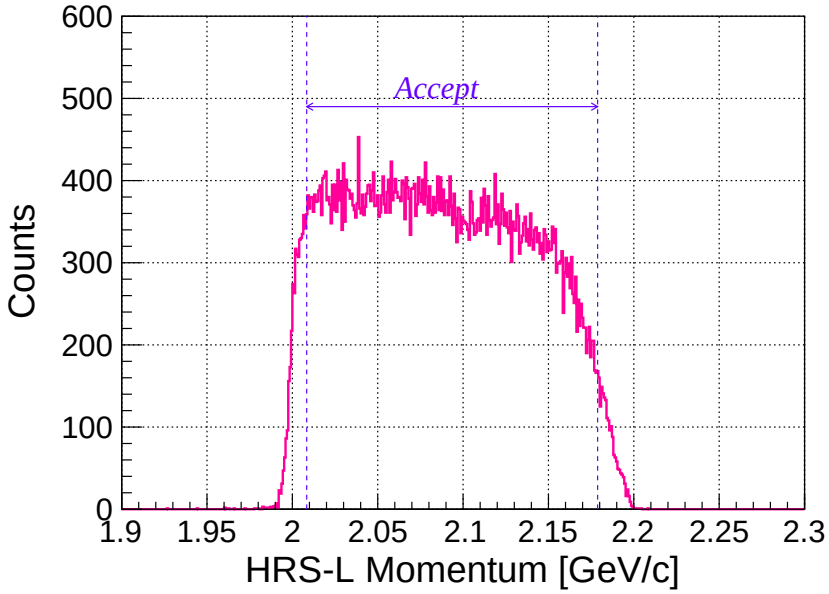

Fig. 3.30: Momentum distribution of HRS-L in the experimental data. The blue dashed lines represent the region of momentum selection for analysis given in eq. (3.47).

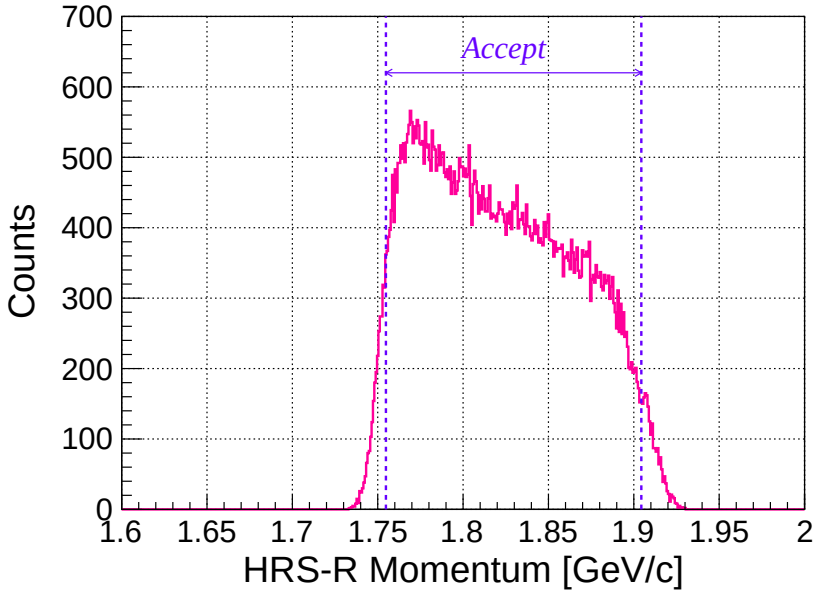

Fig. 3.31: Momentum distribution of HRS-R in the experimental data. The blue dashed lines represent the region of momentum selection for analysis given in eq. (3.48).

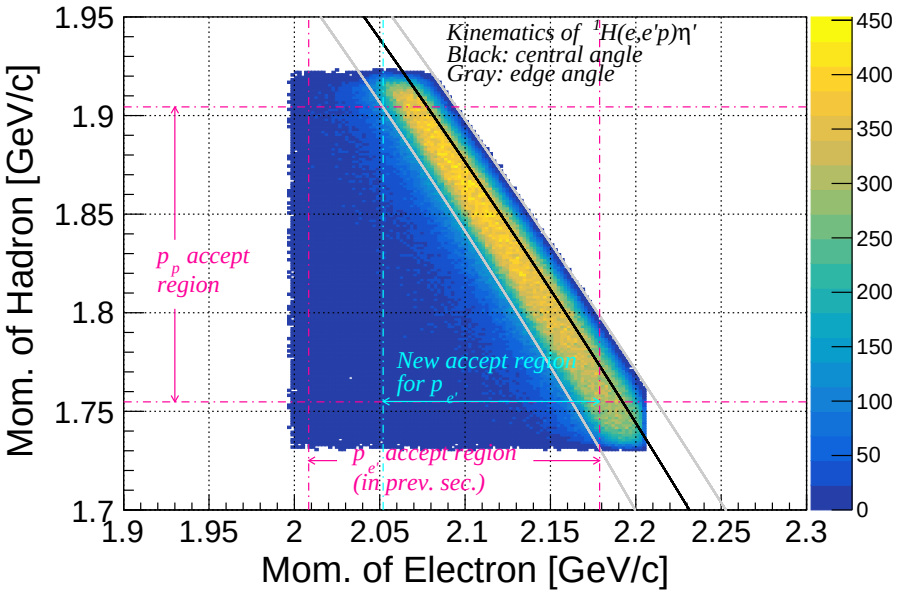

Fig. 3.32: Corralation of $p_{e'}$ v.s p_p in the $^1\mathrm{H}\,(e, e'p)\,\eta'$ reaction (simulation). Three black and gray lines represents the kinematical calculation at the central ray and the edges of acceptance, respectively. Pink lines shows the momentum range for analysis (eq. (3.47) and eq. (3.48)). Cyan line indicates the energy threshold of scattered electrons to invoke the η' production within the experimental acceptance.

$^1\mathrm{H}\,(\mathrm{e}, \mathrm{e'p})\,\eta'$ reaction. The overlaid solid black line represents the kinematic correlation assuming the central angles of the spectrometer, $\left(\theta_{ee'}^{\mathrm{Lab}}, \theta_{ep}^{\mathrm{Lab}}\right) = (13.2 \text{ degrees}, 13.2 \text{ degrees})$. The colid gray lines represent the kinematic correlation assuming the edges of the angular acceptance, $\left(\theta_{ee'}^{\mathrm{Lab}}, \theta_{ep}^{\mathrm{Lab}}\right) = (15.2 \text{ degrees}, 15.2 \text{ degrees})$ and $\left(\theta_{ee'}^{\mathrm{Lab}}, \theta_{ep}^{\mathrm{Lab}}\right) = (11.5 \text{ degrees}, 11.5 \text{ degrees})$. Most of the events generated in the simulation are distributed within this angular range. On the other hand, there are also events that are faintly distributed outside this region. These are attributed to energy loss due to radiation between the beam or scattered electrons and the material (primarily the aluminum cell). Such events appear in the missing mass distribution as a long-tailed component on the higher energy side (also refer to Fig. 3.8 shown during calibration). The acceptance range for momentum determined in the previous subsection is also indicated by the pink dashed line. The kinematic correlation curve for the $^1\mathrm{H}\,(e, e'p)\,\eta'$ reaction intersects the lower boundary of the hadron momentum range, where the electron momentum is $p_{e'} = 2.060$ GeV/c represented by the cyan dashed line in Fig. 3.32. In other words, the present experiment does not have sensitivity to the η' production for electrons with momentum below this threshold. Excluding this region essentially reduces the multi-pion background without affecting the observed η' count. Therefore, the author imposes a tighter event selection criterion for the $p_{e'}$ momentum than the range mentioned in the previous section:

$$2.060 \text{ [GeV/c]} < p_{e'} < 2.176 \text{ [GeV/c]}. \tag{3.49}$$

3.10 Number of virtual photons

The number of virtual photons emitted by electron scattering is calculated by integrating the virtual photon flux $\Gamma > 0$ with the number of electrons and within the spectrometer's acceptance,

$$N_{\gamma^*} = N_e \int \Gamma d\omega d\Omega. \tag{3.50}$$

As discussed in Sec. 2.1, the virtual photon flux Γ is described by the following formula:

$$\Gamma = \frac{\alpha}{2\pi^2 Q^2} \frac{E_\gamma}{1-\epsilon} \frac{E_{e'}}{E_e} \tag{3.51}$$

$$\epsilon = \left[1 + 2\frac{|\boldsymbol{q}|^2}{Q^2} \tan^2\left(\frac{\theta_{ee'}}{2}\right) \right]^{-1} \tag{3.52}$$

$$E_\gamma = \omega + \frac{q^2}{2m_p}, \tag{3.53}$$

The integral of eq. (3.50) is estimated by Monte Carlo integration using SIMC. After generating four parameters $(\cos\theta_{e'}, \phi_{e'}, E_{e'}, \Gamma)$ uniformly and randomly in HRS-L, one can obtain the integrated virtual photon flux (IVFP) from the ratio of detected events satisfying $\Gamma < \Gamma(\theta_{e'}, \phi_{e'}, E_{e'})$,

$$\int \Gamma d\omega d\Omega \sim \frac{N_{\rm acc}}{N_{\rm gen}} \Delta\Omega_{\rm gen} \Delta E_{\rm gen} \Delta\Gamma_{\rm gen}. \tag{3.54}$$

IVPF within the momentum range of eq. (3.49) is

$$\int \Gamma d\omega d\Omega = (2.458 \pm 0.005\ (\text{stat.})) \times 10^{-6}\ [/\text{electron}]\,, \tag{3.55}$$

that is converted to the number of virtual photons by substituting into eq. (3.50),

$$N_{\gamma^*} = (7.132 \pm 0.001\ (\text{stat.})) \times 10^{13}. \tag{3.56}$$

3.11 Number of η' mesons

Fig. 3.33 represents the missing mass distribution after applying the event selection. The overlaid black histogram shows the accidental coincidences, and the blue histogram represents the distribution originating from reactions in the aluminum cell. Fig. 3.34–Fig. 3.37 show the distributions divided into two regions by Q^2 and W. The coverage of Q^2 and W as well as the boundary dividing the data are shown in Fig. 3.38. The central values of Q^2 and W coverage are 0.47 $(\text{GeV}/c)^2$ and 2.13 GeV, respectively. These values divide the acceptance range of Q^2 and W into two equal parts. The number of η' mesons will be obtained by fitting these distributions.

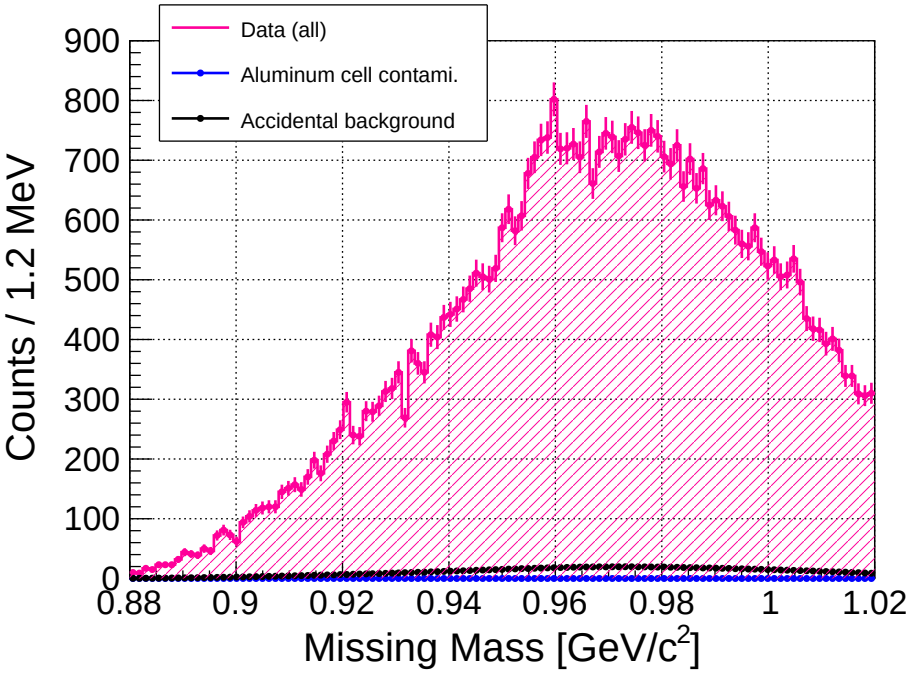

Fig. 3.33: Missing mass spectrum after applying the event selection (for all data).

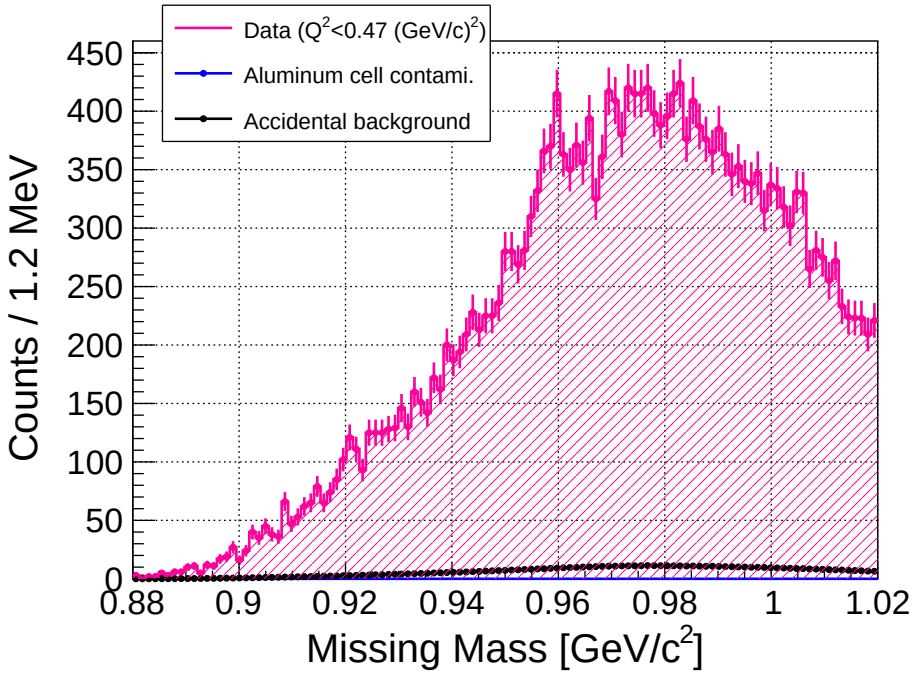

Fig. 3.34: Missing mass spectrum for $Q^2 < 0.47\ (\mathrm{GeV}/c)^2$.

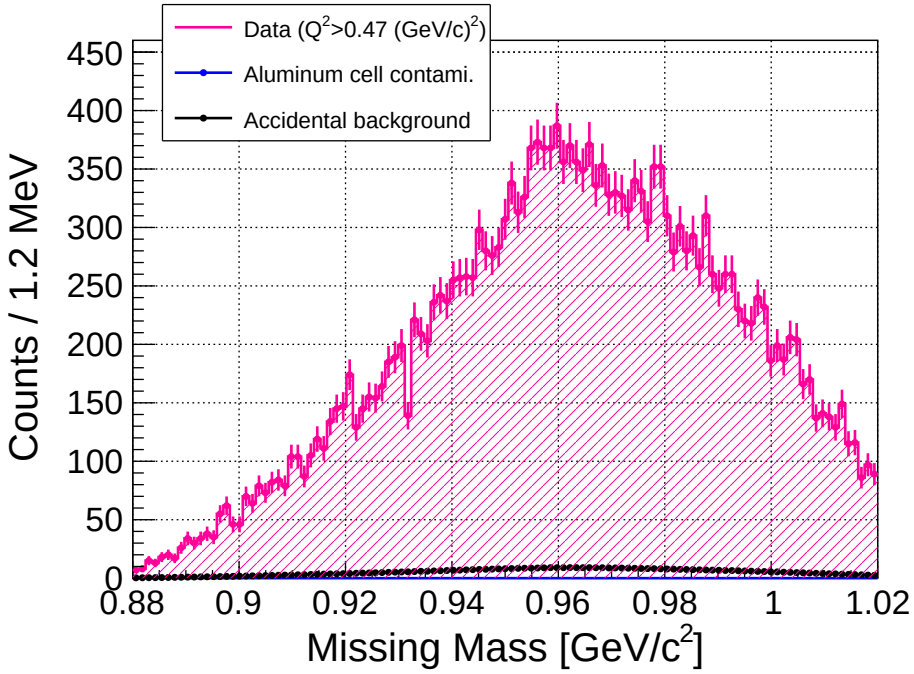

Fig. 3.35: Missing mass spectrum for $Q^2 \geq 0.47\ (\mathrm{GeV}/c)^2$.

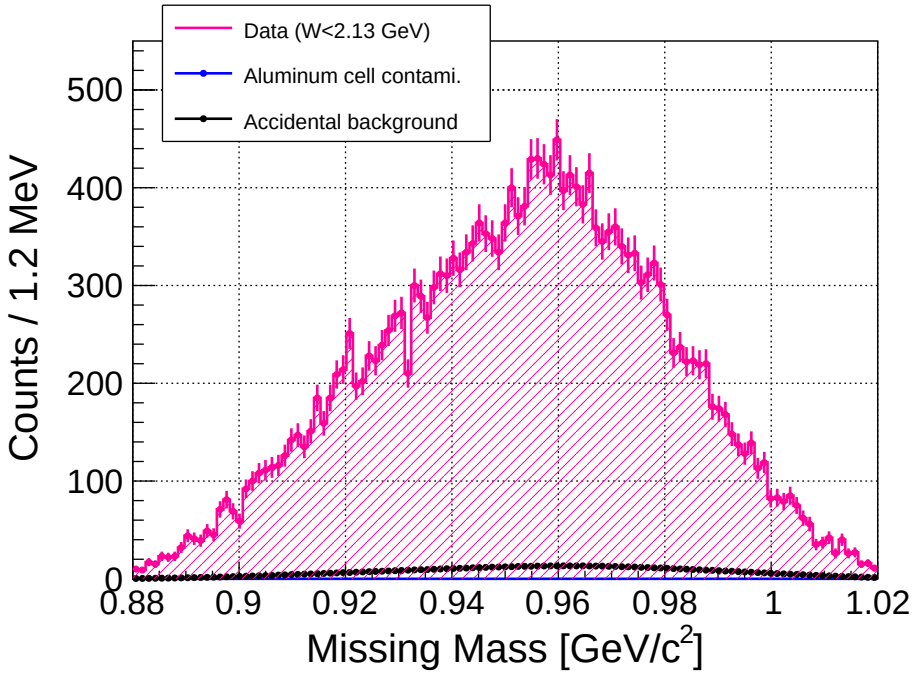

Fig. 3.36: Missing mass spectrum for $W < 2.13$ GeV.

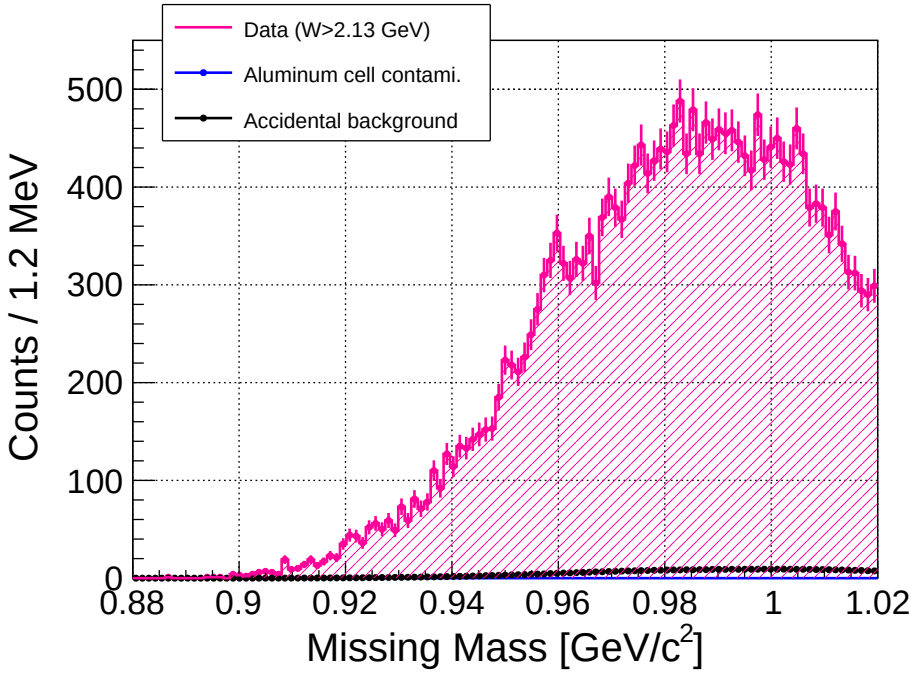

Fig. 3.37: Missing mass spectrum for $W \geq 2.13$ GeV.

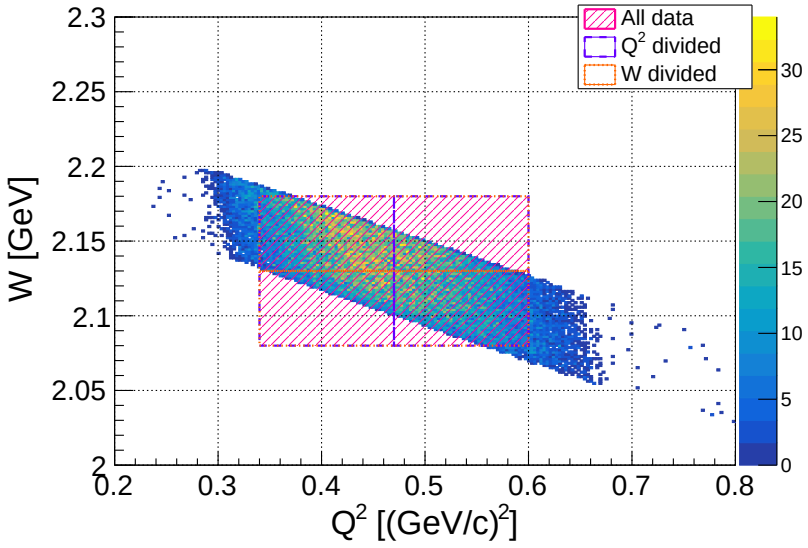

Fig. 3.38: The regions of Q^2 and W covered by the present data, as well as the boundary dividing the data into two regions.

3.11.1 Function for the η' peak

As seen in the missing mass spectrum for the $^1\mathrm{H}\,(e, e'K^+)\,\Lambda/\Sigma^0$ reaction (Fig. 3.8), the peak on the missing mass spectrum has a long high-energy tail component. The present thesis will refer to it as the "radiative tail." The radiative tail is generated due to the bremsstrahlung radiation occurring between the incoming and scattered electrons and the target system, resulting in a greater energy loss. In the present experiment, a thick aluminum target cell was used to handle a gaseous target, which significantly contributed to the prominence of this tail component in the missing mass spectrum. It is crucial to note that the radiative tail is not background noise but part of the true signal for the η' production reaction to be analyzed. Therefore, using a function that accurately describes the shape of the peak including the tail component is essential for estimating the total number of η' mesons and their differential cross section. As previously seen, the η' peak in the actual data is buried in the background events of multi-pion production, making it difficult to estimate the shape of the peak from here. Therefore, the author determines the appropriate function shape for spectral fitting through simulation. SIMC is also applicable for studied incorporating the effects of radiation with matter, as well as multiple Coulomb scattering, ionization through Monte Carlo manner. The reproducibility of the radiative tail when compared to actual experimental spectra has been discussed in detail in previous research in Λ/Σ^0 production channels, and it is highly regarded for its reliability [81].

There are two main types of radiation reactions implemented in SIMC. One, referred to by the authors as "external radiation," is the ordinal bremsstrahlung radiation between the material and the beam patricle, which is described in many textbooks on experimental particle physics. It was first formalized by Y-S. Tsai [82, 83], who derived a famous empirical formula representing

the probability that an electron beam with incident energy E loses energy ΔE when it enters a material with atomic number Z and thickness t:

$$I_{\text{ext}}(E, \Delta E, t) = \frac{bt}{\Delta E}\left(\frac{\Delta E}{E}\right)^{bt} \tag{3.57}$$

$$b = \frac{4}{3}\left[1 + \frac{1}{9}\left(\frac{Z+1}{Z+\eta}\right)\left(\ln\left(183Z^{-1/3}\right)\right)^{-1}\right] \tag{3.58}$$

$$\eta = \ln\left(\frac{1440Z^{-2/3}}{183Z^{-1/3}}\right). \tag{3.59}$$

SIMC also implements a different type of radiation reaction. This is caused by the scattering of the beam particles by the electric field of the target nucleus itself, which induces meson production reactions. The author refers to this as "internal radiation," which was formalized in a paper by M. Vanderhaeghen [84]. The reaction probability for internal radiation is represented by the following formula:

$$I_{\text{int}}(E, \Delta E, t) = \frac{a}{\Delta E}\left(\frac{\Delta E}{E}\right)^{a} \tag{3.60}$$

$$a = \frac{\alpha}{\pi}\left[\ln\left(\frac{Q^2}{m_e^2}\right) - 1\right]. \tag{3.61}$$

When comparing eq.(3.60) with eq.(3.57), they both depend identically on the incident energy E and energy loss ΔE. In other words, the internal radiation represented by eq.(3.60) can be considered equivalent to the external radiation with an effective thickness $t_r = \frac{a}{b}$. For this reason, in SIMC implementations, both internal and external radiation reactions are calculated as if external radiation with thickness $(t + t_r)$ is occurring (see also Fig. 3.39).

Then, the author determines the function shape for the η' peak on the missing mass. The missing mass distribution of η' production events simulated by SIMC is shown in Fig. 3.40. As clearly seen in the figure, the peak has a long tail component on the high-energy side. The author conducted a fitting of this simulation distribution by assuming a certain response function. It is represented by the sum of two Gaussians sharing a peak position and an exponentially decaying function that is smeared by them:

$$F^{\text{Peak}}(x) := F^{\text{DG}}(x) + \int_{-\infty}^{+\infty} F^{\text{DG}}(x-t)\, F^{\text{Exp}}(t)\, \mathrm{d}t \tag{3.62}$$

$$F^{\text{DG}}(x) := A(1-C)\left[Re^{-\frac{(x-\mu)^2}{2\sigma_1^2}} + (1-R)\, e^{-\frac{(x-\mu)^2}{2\sigma_2^2}}\right] \tag{3.63}$$

$$F^{\text{Exp}}(x) := \begin{cases} 0 & (x < \mu + \mu') \\ AC\tau e^{-\frac{x-(\mu'+\mu)}{\tau}} & (\mu + \mu' \leq x) \end{cases}. \tag{3.64}$$

Here, μ is the center of the Gaussian peak, σ is the width of the Gaussian, and τ is the decay constant of the exponential function, and A, C and R is scaling factors related to the area of the function. The fitting result using this function shape is overlaid on the spectrum in Fig. 3.40. The black curve represents the total function $F(x)$ as per eq.(3.62), while the blue line represents the double-Gaussian peak component ($F^{\text{DG}}(x)$) and the orange line represents

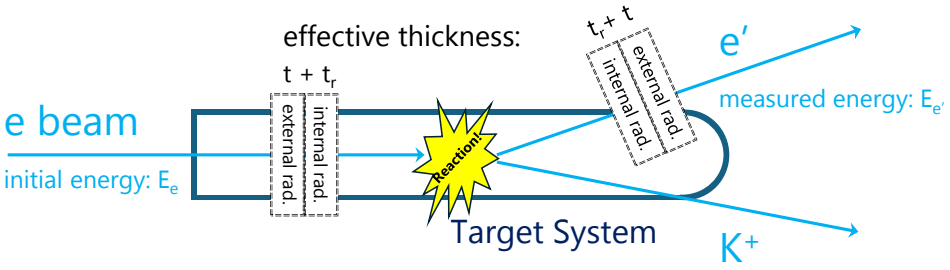

Fig. 3.39: Conceptual diagram of radiation between incident/scattered electron beams and the target system. The effects of radiation need to be calculated for both incident and scattered electrons. For both, internal radiation (scattering with the target nucleus itself) is treated as equivalent to external radiation (scattering with other materials) at an effective thickness t_r.

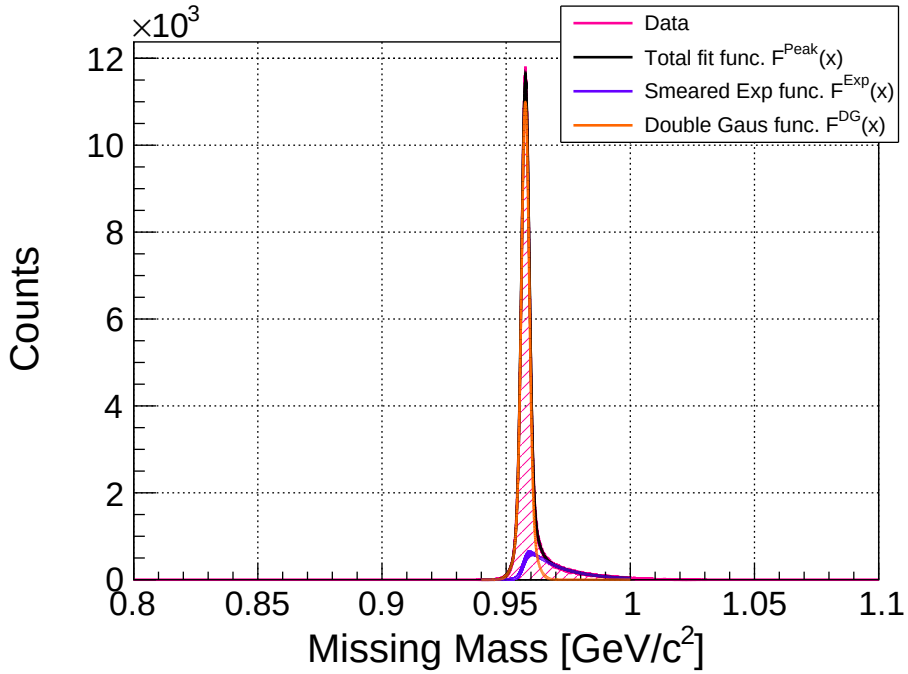

Fig. 3.40: η' peak generated by SIMC (with fitting).

the component of the smeared exponential function ($F^{\mathrm{Exp}}(x)$). In the next to next subsection, the author will estimate the total number of produced η' mesons by fitting the experimental spectrum, and during the procerude, the parameters of the fitting function will be fixed to the values determined by the current simulation fit to reduce the degrees of freedom in the fit.

3.11.2 Function for the background

Case 1: polynomial function

The simplest method to estimate the background shape is to assume a polynomial of an appropriate degree. In other words, a background function $F^{\mathrm{Bg}} := A_0 + A_1 x + A_2 x^2 + \cdots$ is

assumed, and along with the peak function F^{peak} defined in the previous section, the total function $F^{\mathrm{Peak}}(x) + F^{\mathrm{Bg}}(x)$ is used to fit the missing mass distribution. The number of parameters determined through the fitting is the sum of the coefficients A_j $(j = 0, 1, 2, \cdots)$ of the polynomial and the total area A of the peak function, resulting in $(n + 1)$ parameters in total. The degree n of the polynomial should be sufficient to describe the rise and fall of the background while being kept as small as possible to maintain the degrees of freedom in the fitting. As shown in later fitting plots, a polynomial of up to the 3rd degree ($n = 3$) is sufficient to describe the background distribution within an appropriate fitting range. The results of this fitting will be collectively described in later sections.

Case 2: function determined by simulation

Here, the author wishes to explore another slightly more sophisticated method. The reason is that, under conditions such as $Q^2 > 0.47$ $(\mathrm{GeV}/c)^2$ or $W < 2.13$ GeV (refer to Fig. 3.35 and Fig. 3.36), the enhancement of background events overlaps with the η' peak position. In such cases, a polynomial function determined completely freely might inherently include systematic uncertainties in its functional shape. Additionally, the author suppose that it is beneficial to discuss the background shape using a more advanced method for datasets divided by Q^2 or W, where the peak statistics are reduced. In the missing mass distribution, the smoothly distributed background are assumed to be originated from reactions in which multiple pions are simultaneously produced in a single interaction with a virtual photon, namely, $\gamma^* + p \to p + N \times \pi$ $(N = 2, 3, \cdots)$. To investigate this, the author generated a large number of such events using SIMC-based simulations. The overview of the procedure for generating N-body particles in the simulation is shown in Fig. 3.41.

1. First, the total energy W in the center-of-mass (CM) frame of the entire system (*i.e.,* $\gamma^* + p_{\mathrm{tar}}$) is determined as an input from the scattered electron detected in the left arm. The relation is given by:

$$W = \sqrt{(\omega + m_p)^2 - |\boldsymbol{q}|^2} \tag{3.65}$$

$$= \sqrt{(E_e - E_{e'} + m_p)^2 - |\boldsymbol{p}_e - \boldsymbol{p}_{e'}|^2} \tag{3.66}$$

$$:= \sum_{j=1}^{N} (M_j + T_j), \tag{3.67}$$

   where, M_j and T_j represent the mass and kinetic energy of the j-th particle, respectively. The total kinetic energy is denoted as T_{cm}, such that:

$$T_{\mathrm{cm}} := \sum_{j=1}^{N} T_j \tag{3.68}$$

$$= W - \sum_{j=1}^{N} M_j. \tag{3.69}$$

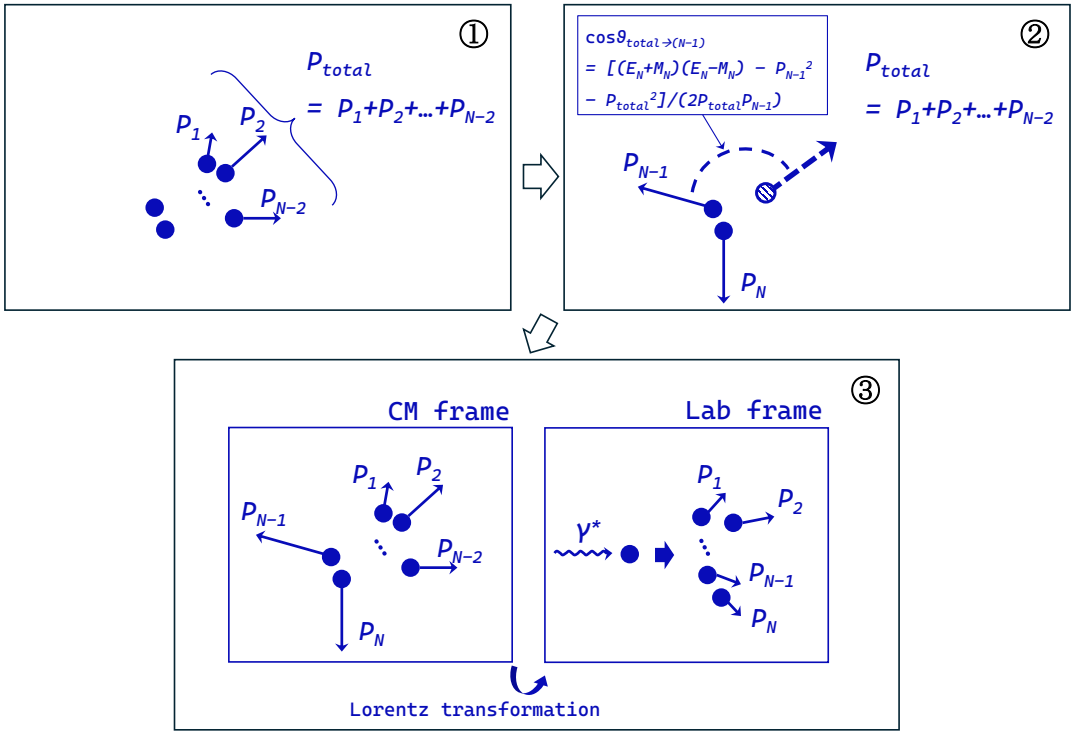

Fig. 3.41: Conceptual diagram of computational procedures of generating multi-pion production. Refer to the main text for detailed explanations.

The author define the total momentum vector $\boldsymbol{P}_{\text{total}}$ of particles from the 1st to the $(N-2)$-th particle as:

$$\boldsymbol{P}_{\text{total}} := \sum_{j=1}^{N-2} \boldsymbol{P}_j. \tag{3.70}$$

The momentum vectors $\boldsymbol{P}_1, \boldsymbol{P}_2, \cdots, \boldsymbol{P}_{N-2}$ of particles from the 1st to $(N-2)$-th are freely determined under the following conditions:

$$T_1 > 0, T_2 > 0, \cdots, T_{N-2} > 0 \tag{3.71}$$
$$0 < T_1 + T_2 + \cdots + T_{N-2} < T_{\text{cm}}. \tag{3.72}$$

2. If the kinetic energy T_{N-1} (or equivalently, the magnitude of the momentum vector $\boldsymbol{P}_{N-1}$) of the $(N-1)$-th particle is freely determined, the kinetic energy T_N (or equivalently, the magnitude of the momentum vector $\boldsymbol{P}_N$) of the remaining N-th particle will be automatically determined to satisfy energy conservation. Meanwhile, the angle θ between $\boldsymbol{P}_{\text{total}}$ and $\boldsymbol{P}_{N-1}$ is expressed using the law of momentum conservation, or the cosine rule as follows:

$$\cos\theta_{\boldsymbol{P}_{\text{total}} \to \boldsymbol{P}_{N-1}} = \frac{(E_N + M_N)(E_N - M_N) - \boldsymbol{P}_{N-1}^2 - \boldsymbol{P}_{\text{total}}^2}{2\,|\boldsymbol{P}_{\text{total}}|\,|\boldsymbol{P}_{N-1}|}. \tag{3.73}$$

The cosine must satisfy:

$$-1 < \cos\theta_{\boldsymbol{P}_{\text{total}} \to \boldsymbol{P}_{N-1}} < +1. \tag{3.74}$$

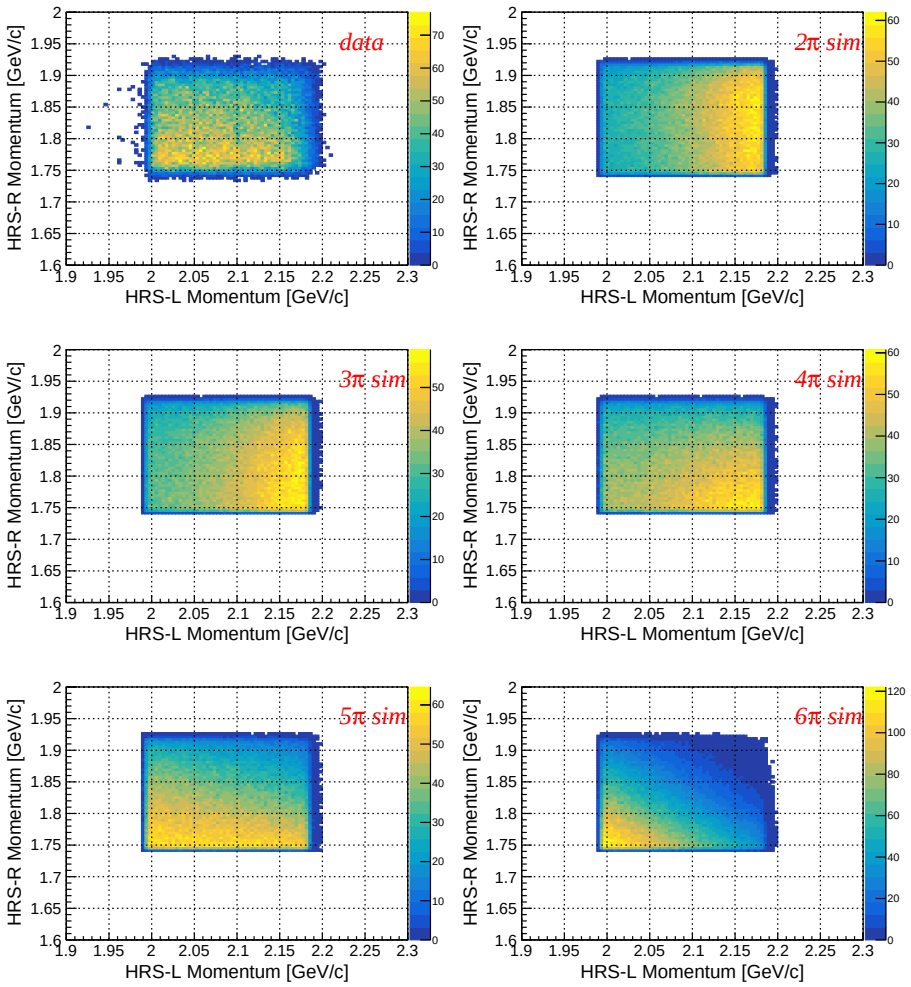

Fig. 3.42: $p_{e'}$ v.s p_p distribution for data and multi-pi simulation.

This condition ensures the existence of momentum vectors $\boldsymbol{P}_{N-1}$ and $\boldsymbol{P}_N$ that satisfy the momentum conservation law $\boldsymbol{P}_{\text{total}} + \boldsymbol{P}_{N-1} + \boldsymbol{P}_N = \boldsymbol{0}$. In the programming, if this condition is not met, the event is rejected and the procedure restarts from the beginning.

3. If all momenta $\boldsymbol{P}_1, \boldsymbol{P}_2, \cdots, \boldsymbol{P}_N$ of the N-particles are successfully determined under this condition, a Lorentz transformation is applied to these momenta to obtain that in the laboratory frame, where the target proton is at rest.

For the cases of $N = 2, 3, 4, 5$ and 6 are assumed, Fig. 3.42 shows the $p_{e'}$ v.s p_p correlation obtained from the simulation of multi-pion generation, as well as the same correlation observed in the experimental data. The distributions from each simulation are scaled such that their total areas match the number of events in the data. Firstly, when comparing the simulations for different N, it is evident that as N increases, the momentum carried away by the pions becomes larger. This results in a tendency for the momenta of the scattered electron and proton to decrease. Next, when comparing the simulations with the experimental data, the case of $N = 5$ appears to better match the distribution observed in the data. This suggests

Table 3.2: Summary of number of η' obtained by data fitting.

Data	Background Function	Num. of η'	χ^2/n.d.f
All	polynomial	520 ± 86 (stat.)	1.11
	multi-pi simulation	467 ± 85 (stat.)	1.51
$Q^2 < 0.47$ $(\mathrm{GeV/c})^2$	polynomial	306 ± 61 (stat.)	1.16
	multi-pi simulation	306 ± 60 (stat.)	0.96
$Q^2 \geq 0.47$ $(\mathrm{GeV/c})^2$	polynomial	231 ± 62 (stat.)	0.95
	multi-pi simulation	197 ± 61 (stat.)	1.29
$W < 2.13$ GeV/c^2	polynomial	223 ± 67 (stat.)	0.90
	multi-pi simulation	196 ± 66 (stat.)	1.20
$W \geq 2.13$ GeV/c^2	polynomial	334 ± 57 (stat.)	0.92
	multi-pi simulation	331 ± 55 (stat.)	1.15

that, in multi-pion production events included in the experimental data, the averaged number of pions is estimated to be approximately five. The author then generated the missing mass spectrum for the $^1H\,(e, e'p)\,N \times \pi$ reaction based on the accepted events in the simulation. This spectrum was fitted using the sum of four Gaussian functions with free parameters to derive the spectral response function. For the fitting of the missing mass spectrum of the experimental data, the background distribution was described using the superposition of all 2π–6π production processes. The ratios of each distribution were determined by minimizing χ^2 to best reproduce the experimental two-dimensional distribution of $p_{e'}$ v.s p_p. Indeed, even with the determined ratios, the 5π production was found to be the most dominant component, with a small contribution from the 2π distribution included. The averaged number of pions implies 4.86, obtained in the χ^2 minimization. Then, the response function obtained from the simulation was used with its parameters (except for the total area) fixed, as well as the peak function of η' described in Sec. 3.11.1.

3.11.3 Fitting

Fitting of the missing mass spectra using the different types of functions described in the previous subsections is shown in Fig. 3.43 and Fig. 3.44. Additionally, the fitting results for the data divided into two regions of Q^2 and W are presented in Fig. B.2 to Fig. B.10 in Appendix B. The counts of the η' peak obtained from these fittings are summarized in Table 3.2. The differences between the two fitting functions are comparable to or smaller than the statistical uncertainty.

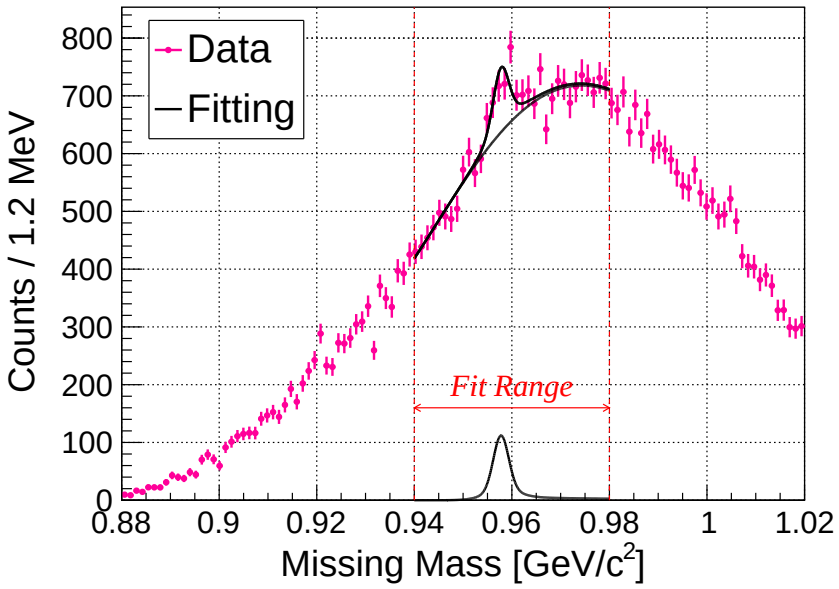

Fig. 3.43: Fitting of the missing mass spectrum with using a polynomial function for background. The spectrum includes all data.

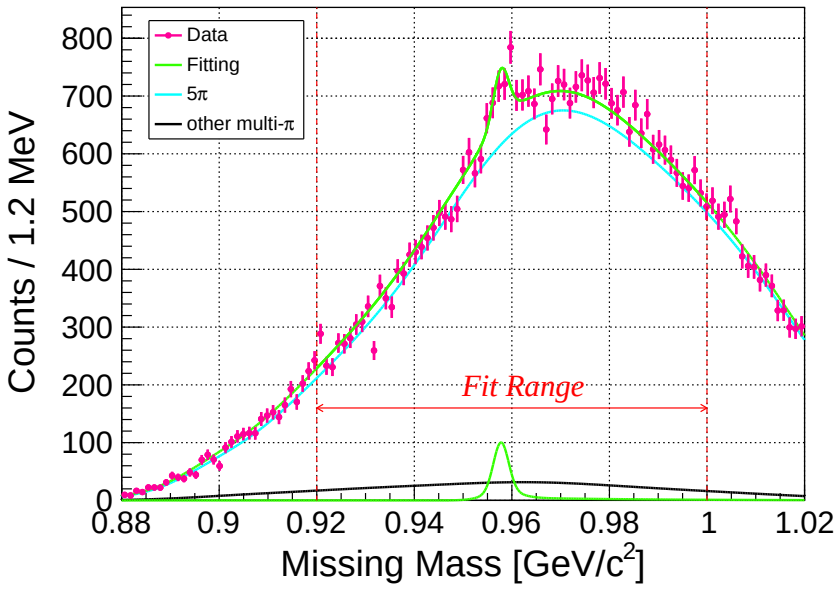

Fig. 3.44: Fitting of the missing mass spectrum with using a simulation-based function for background. The spectrum includes all data.

3.12 Efficiency

3.12.1 Z-vertex cut

The author applied an event cut based on the Z-vertex when selecting the gas region of the target (for details, see Sec. 3.3). A correction must be made in deriving the differential cross section by considering what fraction of the target ^{1}H atoms survive this cut. The efficiency of the Z-vertex cut was already estimated in Sec. 3.3.

$$\varepsilon^{\mathrm{Z}} = 0.654 \pm 0.002 \ \ (\mathrm{stat.}) \tag{3.75}$$

3.12.2 Coincidence time cut

Event cut on the coincidence time distibution was applied to select scattered protons (for details, see Sec. 3.4). The efficiency of the coincidence time cut was already estimated,

$$\varepsilon^{\mathrm{CT}} = 0.965 \pm 0.005 \ \ (\mathrm{stat.}) \tag{3.76}$$

3.12.3 Reference plane cut

Consider the efficiency of the cut based on the hit distribution in the focal plane discussed in Sec. 3.9.1, which can be determined by taking the ratio of the number of events after the cut to the total number of events,

$$\varepsilon^{\mathrm{RP}} = 0.886. \tag{3.77}$$

3.12.4 Track multiplicity cut

The calculation of the coincidence time is only possible for events where the number of tracks in HRS-L is one (for detailed description, see Sec. 3.9.2). Therefore, the ratio of single-track events to the total number of events represents the fraction of analyzable events,

$$\varepsilon^{\mathrm{Single}} = 0.970, \tag{3.78}$$

as described in Sec. 3.9.2.

3.12.5 Tracking

Here, the author refers to the trajectory of particles reconstructed from hits on numerous wires in the VDC of the HRS as “tracks,” and describes the tracking efficiency, which indicates how many of the particles passing through the reference plane can be recognized as tracks during the analysis process. As mentioned in Sec. 2.7.1, the VDC consists of four planes: U_1, V_1, U_2 and V_2. Typically, electrical signals are detected on about five wires for each plane the particle passes through, and the timing information is recorded. Each of these sense wires has a finite (and very high) detection efficiency, meaning that there is a certain probability that a hit is not

Table 3.3: VDC plane efficiency and tracking efficiency [85].

	HRS-L [%]	HRS-R [%]
U_1 plane efficiency $\varepsilon^{\mathrm{Track}}_{\mathrm{U1\ plane}}$	99.72	99.78
V_1 plane efficiency $\varepsilon^{\mathrm{Track}}_{\mathrm{V1\ plane}}$	99.65	99.64
U_2 plane efficiency $\varepsilon^{\mathrm{Track}}_{\mathrm{U2\ plane}}$	99.80	99.78
V_2 plane efficiency $\varepsilon^{\mathrm{Track}}_{\mathrm{V2\ plane}}$	99.73	99.80
Tracking efficiency $\varepsilon^{\mathrm{Track}}_{\mathrm{L,R}}$	$98.90^{+0.12}_{-0.18}$	$99.18^{+0.09}_{-0.19}$

recorded even though the particle passed nearby. This quantity is called "wire efficiency." It is defined by the following equation:

$$\varepsilon_{\mathrm{wire}} := \frac{\Sigma_i \delta_i\,(j-1)\,\delta_i\,(j)\,\delta_i\,(j+1)}{\Sigma_i \delta_i\,(j-1)\,\delta_i\,(j+1)}. \tag{3.79}$$

Here, $\delta_i\,(j)$ represents the i-th hit on the j-th sense wire,

$$\delta_i\,(j) = \begin{cases} 1 & (i\text{-th event hit on the } j\text{-th sense wire}) \\ 0 & (\text{otherwise}). \end{cases} \tag{3.80}$$

In other words, the above equation expresses the efficiency of the third sense wire when there are hits on two sense wires with the third sense wire in between. K.G. Fissum *et al.* reported an evaluation of wire efficiency based on the above equation in ref. [69]. Fig. 3.45 below shows the wire efficiency of the U_1 plane obtained during this evaluation. As can be seen from the figure, the value of the efficiency is very high, exceeding 99.9 %.

Prior research conducted by a collaborator estimated the efficiency of each layer of the VDC, *i.e.*, the ratio at which tracks can be reconstructed in a single plane when particles pass through, based on each wire efficiency, using Monte Carlo calculations [85]. The author of the present thesis cites the values as the tracking efficiency. First, he generated hit wires for an event using the number of hits distribution of all wires (Fig. 3.46 left) and the cluster size distribution for a single particle (Fig. 3.46 right) obtained from the present experiment as input for the simulation. Next, he invalidated some of the wire hits based on wire efficiency and observed whether the cluster generation in the analysis process was disrupted. The estimated plane efficiencies of all layers are summarized in Table 3.3. In the end, the efficiency in the coincidence analysis of HRS-L and HRS-R is expressed as the product of all efficiencies obtained here,

$$\varepsilon^{\mathrm{Track}}_{\mathrm{L,R}} := \varepsilon^{\mathrm{Track}}_{\mathrm{U1\ plane}} \times \varepsilon^{\mathrm{Track}}_{\mathrm{V1\ plane}} \times \varepsilon^{\mathrm{Track}}_{\mathrm{U2\ plane}} \times \varepsilon^{\mathrm{Track}}_{\mathrm{V2\ plane}} \tag{3.81}$$

$$\varepsilon^{\mathrm{Track}} := \varepsilon^{\mathrm{Track}}_{\mathrm{L}} \times \varepsilon^{\mathrm{Track}}_{\mathrm{R}} \tag{3.82}$$

$$= \left(98.90^{+0.12}_{-0.18}\ \%\right) \times \left(99.18^{+0.09}_{-0.19}\ \%\right) = 98.09^{+0.21}_{-0.37}\ \%. \tag{3.83}$$

It was determined with an error of less than 0.1 %.

3.12.6 DAQ

The DAQ efficiency was given by the ratio of DAQ dead time in every run. Fig. 3.47 represents DAQ efficiency for all runs during the beamtime. These values are applied to the cross section

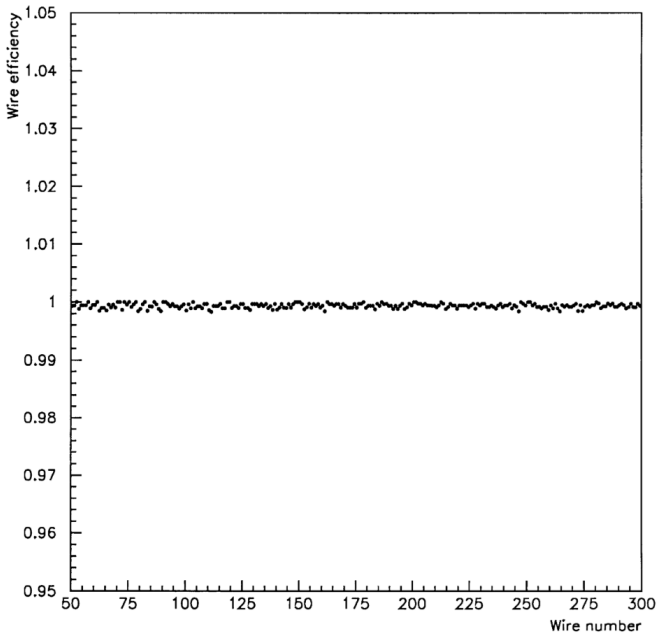

Fig. 3.45: Wire efficiency of VDC on HRS (U_1 plane) [69].

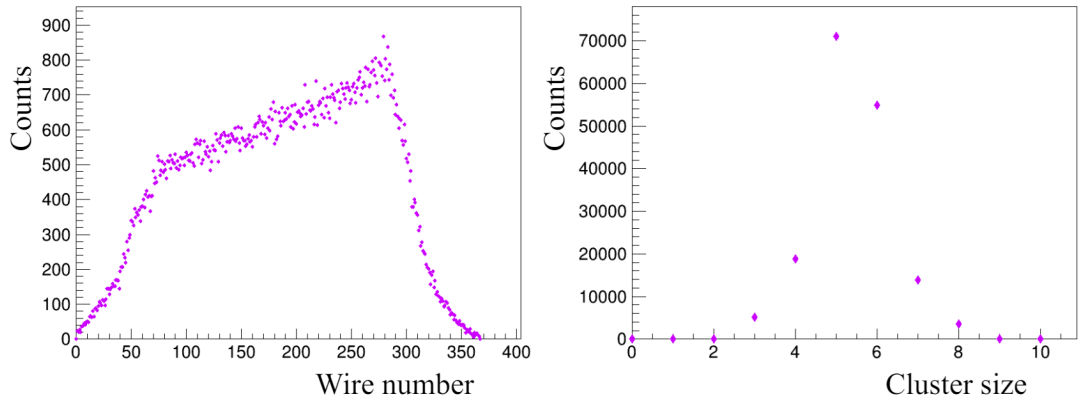

Fig. 3.46: **left:** Hit position distribution on VDC, **right:** cluster size distribution of typical run [85].

calculation by run. The average DAQ efficiency gives,

$$\varepsilon_{\text{ave}}^{\text{DAQ}} = 0.96. \tag{3.84}$$

3.12.7 Proton absorption

The protons after the reaction can be absorbed with a certain probability through nuclear reactions mainly in the target cell. The proportion of such events was estimated through simulations using Geant4 [79, 80]. In the simulation, the author placed an aluminum plate with a thickness of 400 μm/ $\sin\theta_{ep}$ and irradiate protons with a momentum of 1.8 GeV/c, counting the number of protons that passed through. By excluding electromagnetic interactions and registering only the physical processes of hadronic interactions, the contribution from nuclear reactions

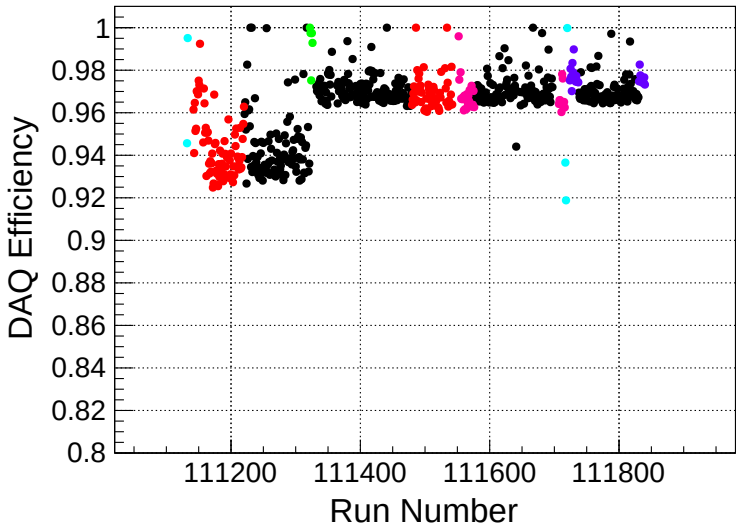

Fig. 3.47: Run dependence of DAQ efficiency. Black indicates the ^{3}H target, red indicates the ^{1}H target (hydrogen kinematics), pink indicates ^{1}H (tritium kinematics), purple indicates ^{3}He, green indicates empty, and light blue indicates the calibration run.

alone could be considered. The protons lost in the aluminum wall were estimated to be 0.6 %, corresponding to a transmission efficiency of

$$\varepsilon^{\mathrm{Abs}} = 0.994 \pm 0.001\,(\mathrm{stat})\ {}^{+0.001}_{-0.002}\,(\mathrm{sys})\,. \tag{3.85}$$

The systematic error reflects the change in the effective thickness of the aluminum wall caused by the variation in θ_{ep}.

3.12.8 Detector

The detector efficiency needs to be considered only for the scintillation hodoscopes, since only the S0 and S2 hodoscopes participated in the data-taking trigger. Both S0 and S2 have a sufficient number of photoelectrons, and the efficiency is

$$\varepsilon^{\mathrm{Detector}} > 0.999. \tag{3.86}$$

3.13 Differential cross section

3.13.1 Calculation

The differential cross section of the ${}^{1}\mathrm{H}\left(\gamma^{*},p\right)X$ reaction was calculated for the accepted events as follows,

$$\left(\frac{\mathrm{d}\sigma_{\gamma^{*}p\to Xp}}{\mathrm{d}\Omega_{p}}\right)^{\mathrm{Lab}}=\frac{1}{N_{\mathrm{Target}}}\cdot\frac{1}{\varepsilon}\sum_{i=1}^{N_{\mathrm{Event}}}\frac{1}{N_{\gamma^{*}}\left(p_{e'},z\right)\cdot\varepsilon_{i}^{\mathrm{DAQ}}\cdot\Delta\Omega_{\text{HRS-R}}\left(p_{p},z\right)} \tag{3.87}$$

$$\left(\frac{\mathrm{d}\sigma_{\gamma^{*}p\to Xp}}{\mathrm{d}\Omega_{p}}\right)^{\mathrm{CM}}=\frac{1}{N_{\mathrm{Target}}}\cdot\frac{1}{\varepsilon}\sum_{i=1}^{N_{\mathrm{Event}}}\frac{f^{\mathrm{Lab}\to\mathrm{CM}}}{N_{\gamma^{*}}\left(p_{e'},z\right)\cdot\varepsilon_{i}^{\mathrm{DAQ}}\cdot\Delta\Omega_{\text{HRS-R}}\left(p_{p},z\right)} \tag{3.88}$$

$$\varepsilon=\varepsilon^{Z}\cdot\varepsilon^{\mathrm{CT}}\cdot\varepsilon^{\mathrm{RP}}\cdot\varepsilon^{\mathrm{Single}}\cdot\varepsilon^{\mathrm{Track}}\cdot\varepsilon^{\mathrm{Abs}}\cdot\varepsilon^{\mathrm{Detector}}. \tag{3.89}$$

The value of ε means the product of all the efficiencies except for the DAQ estimated in the previous sections. Of the DAQ efficiency, different values by run are applied for the calculation. An acceptance map $\Delta\Omega_{\text{HRS-R}}\left(p,z\right)$ binned by momentum and Z-vertex is used for the calculation since the solid angle $\Delta\Omega_{\mathrm{HRS-R}}$ has momentum and Z-vertex dependence (as mentioned in Sec. 3.7). Similarly, $N_{\gamma^{*}}$ is applied by using a map that depends on momentum and Z-vertex, reflecting the acceptance of HRS-L. The value of $f^{\mathrm{Lab}\to\mathrm{CM}}$ is a relativistic factor to convert the cross section from the laboratory frame to the center of mass frame, and is given event-by-event.

$$f^{\mathrm{Lab}\to\mathrm{CM}}=\frac{\gamma\left(p_{p}^{\mathrm{CM}}\right)^{2}\left(p_{p}^{\mathrm{CM}}\cos\theta_{\gamma p}^{\mathrm{CM}}+\beta E_{p}^{\mathrm{CM}}\right)}{\left[\left(p_{p}^{\mathrm{CM}}\right)^{2}\sin^{2}\theta_{\gamma p}^{\mathrm{CM}}+\gamma^{2}\left(p_{p}^{\mathrm{CM}}\cos\theta_{\gamma p}^{\mathrm{CM}}+\beta E_{p}^{\mathrm{CM}}\right)^{2}\right]^{3/2}} \tag{3.90}$$

$$\beta=\frac{|\boldsymbol{q}|}{\omega+m_{p}} \tag{3.91}$$

$$\gamma=\frac{1}{\sqrt{1-\beta^{2}}}=\frac{\omega+m_{p}}{W}. \tag{3.92}$$

3.13.2 Fitting

Fig. 3.48 represents the missing mass spectrum converted into the differential cross section of the ${}^{1}\mathrm{H}\left(\gamma^{*},p\right)X$ reaction. The overlaid cyan curve represents the fitting of the histograms by the η'-peak function of eq. (3.62)–eq. (3.64) combined with a simulation-based function for the background events. Thus, the integral of the fitting function gives the differential cross section of the η' virtual-photoproduction for all data,

$$\left(\frac{d\sigma_{\gamma^{*}p\to\eta' p}}{d\Omega_{\eta'}}\right)^{\mathrm{CM}}=4.4\pm0.8\ \ (\mathrm{stat.})\ \ \left[\mathrm{nb/sr}\right]. \tag{3.93}$$

Fig. 3.49–Fig. 3.52 show the spectra divided into two regions by Q^{2} and W. These spectra represents the data divided by the boundaries of Q^{2} and W shown in Fig. 3.38 of the previous section, while the spectra in Fig. 3.48 represent the averaged differential cross section over the entire region covered by the data. Two histograms, divided by Q^{2}, were simultaneously fitted with a constraint ensuring that the average area of the background function matches

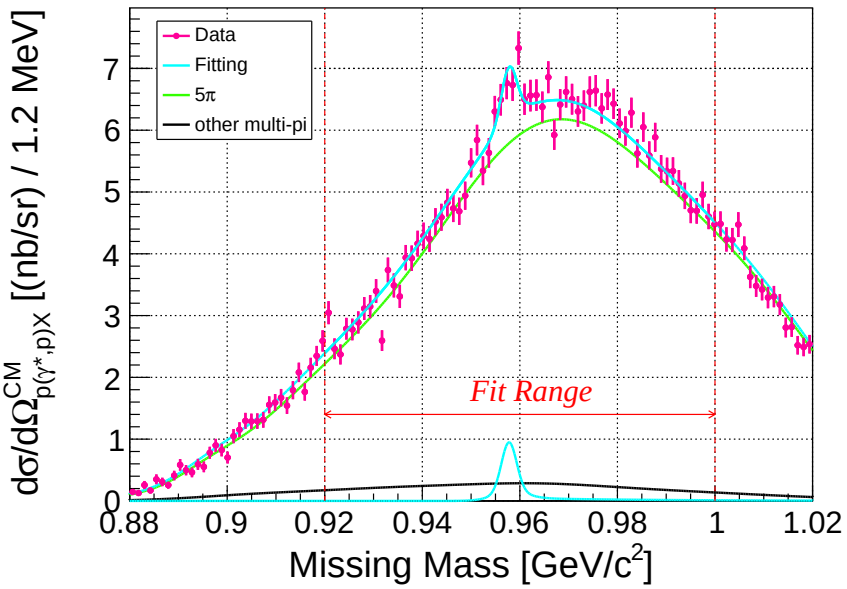

Fig. 3.48: Fitting of the differential cross section on the missing mass with using a simulation-based function for background. The spectrum includes all data.

the background of the all data, namely $0.5 \times \left(S^{Q^2\mathrm{low}} + S^{Q^2\mathrm{high}}\right) = S^{\mathrm{All}}$, where $S^{Q^2\mathrm{low}}$ and $S^{Q^2\mathrm{high}}$ represented the background areas determined by the heights of the corresponding two fitting functions, and they were variable parameters determined by the fit. The same procedure was applied for W as well. Additionally, apart from this result, the fitting results using a third-order polynomial function as the background function, as well as the fitting results where a simulation-based function for multi-pion production was used as the background function but with the background area treated as a free parameter without applying any constraints on the region, are presented in Fig. B.11–Fig. B.15 and Fig. B.16–Fig. B.20 in Appendix B, respectively. The primary result of the present thesis adopts the values from constraint fittings using the simulation-based function, treating the differences arising from other functions and fitting methods as systematic errors. The statistical uncertainty of the background area of all data used in the constrain fit results in only a small uncertainty compared to the systematic errors arising from the dependence on such fit functions and fitting methods, and it is encompassed within them. Results of fitting for all W- and Q^2-binned spectra are summarized in Table 3.4.

3.13.3 Systematic error

The author estimates the systematic error of the differential cross section as an uncertainty propagated several variables. Each error component can be considered independent of the others. The systematic uncertainty of the differential cross-section is given by:

$$\frac{\Delta\left(\frac{\mathrm{d}\sigma}{\mathrm{d}\Omega}\right)_{\mathrm{sys.}}}{\left(\frac{\mathrm{d}\sigma}{\mathrm{d}\Omega}\right)} = \left[\left(\frac{\Delta\left(\frac{\mathrm{d}\sigma}{\mathrm{d}\Omega}\right)_{\mathrm{fit}}}{\left(\frac{\mathrm{d}\sigma}{\mathrm{d}\Omega}\right)}\right)^2 + \left(\frac{\Delta N_{\mathrm{Target}}}{N_{\mathrm{Target}}}\right)^2 + \left(\frac{\Delta\varepsilon}{\varepsilon}\right)^2 + \left(\frac{\Delta\left(\frac{\mathrm{d}\sigma}{\mathrm{d}\Omega}\right)_{\mathrm{acc}}}{\left(\frac{\mathrm{d}\sigma}{\mathrm{d}\Omega}\right)}\right)^2\right]^{\frac{1}{2}}. \quad (3.94)$$

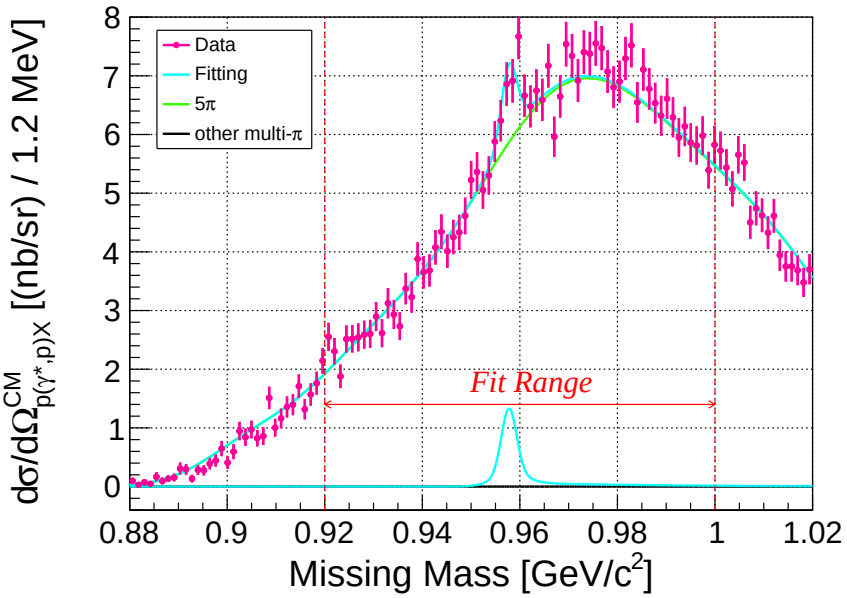

Fig. 3.49: Missing mass spectrum (in differential cross section) for $Q^2 < (0.47\ \mathrm{GeV}/c)^2$ with a fitting using a simulation-based function for background. The background area was fitted with a constraint applied so that its average with the background area in Fig. 3.50 is equal to the background area of the all data.

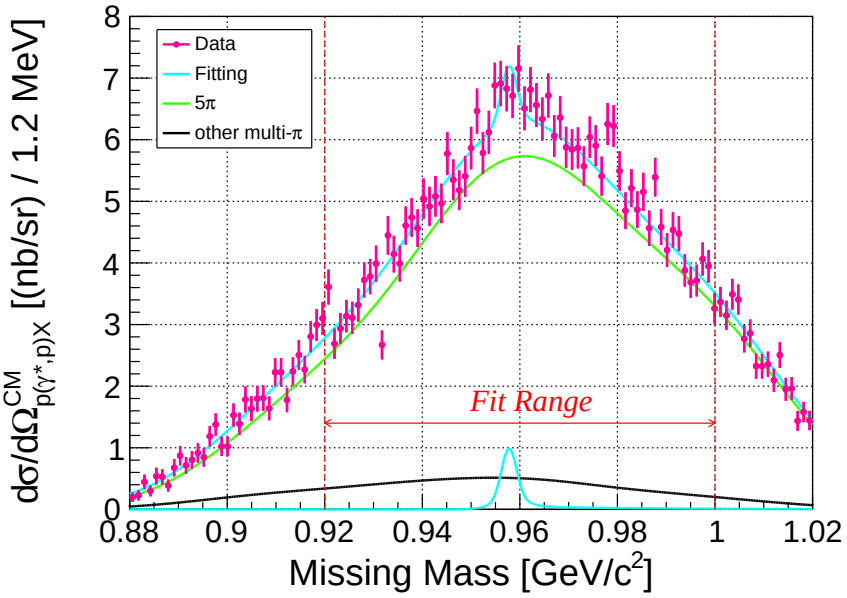

Fig. 3.50: Missing mass spectrum (in differential cross section) for $Q^2 \geq (0.47\ \mathrm{GeV}/c)^2$ with a fitting using a simulation-based function for background. The background area was fitted with a constraint applied so that its average with the background area in Fig. 3.49 is equal to the background area of the all data.

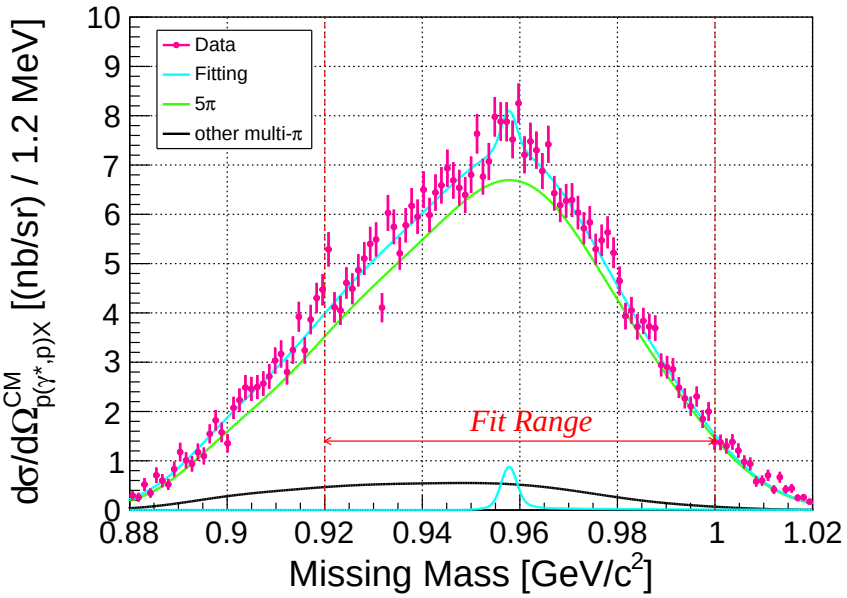

Fig. 3.51: Missing mass spectrum (in differential cross section) for $W < 2.13$ GeV with a fitting using a simulation-based function for background. The background area was fitted with a constraint applied so that its average with the background area in Fig. 3.52 is equal to the background area of the all data.

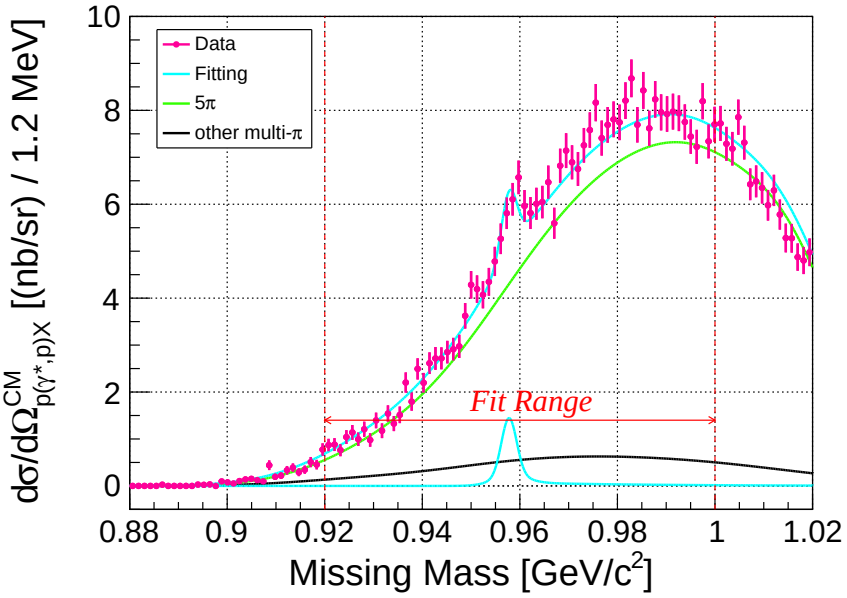

Fig. 3.52: Missing mass spectrum (in differential cross section) for $W \geq 2.13$ GeV with a fitting using a simulation-based function for background. The background area was fitted with a constraint applied so that its average with the background area in Fig. 3.51 is equal to the background area of the all data.

Table 3.4: Summary of differential cross section obtained by data fitting. The term "free" in parentheses indicates a case where the background area is treated as a free parameter when fitting. On the other hand, "constraint" refers to a case where a constraint is applied during fitting so that the average background area of the two divided datasets is equal to the background area of all data.

Data	Background Function	Differential Cross Section [nb/sr]	χ^2/n.d.f
All	polynomial	4.7 ± 0.8 (stat.)	1.07
	multi-pi	4.4 ± 0.8 (stat.)	1.49
$Q^2 < 0.47$ $(\mathrm{GeV/c})^2$	polynomial	5.6 ± 1.2 (stat.)	0.93
	multi-pi (free)	5.4 ± 1.2 (stat.)	0.92
	multi-pi (constraint)	5.9 ± 1.1 (stat.)	1.24
$Q^2 \geq 0.47$ $(\mathrm{GeV/c})^2$	polynomial	4.1 ± 1.2 (stat.)	1.00
	multi-pi (free)	3.7 ± 1.2 (stat.)	1.51
	multi-pi (constraint)	4.3 ± 1.1 (stat.)	1.24
$W < 2.13$ GeV/c^2	polynomial	3.8 ± 1.3 (stat.)	0.97
	multi-pi (free)	3.1 ± 1.2 (stat.)	1.25
	multi-pi (constraint)	3.7 ± 1.2 (stat.)	1.23
$W \geq 2.13$ GeV/c^2	polynomial	5.8 ± 1.1 (stat.)	0.96
	multi-pi (free)	6.2 ± 1.1 (stat.)	1.18
	multi-pi (constraint)	6.5 ± 1.0 (stat.)	1.23

It should be noted that $\Delta\left(\frac{\mathrm{d}\sigma}{\mathrm{d}\Omega}\right)_{\mathrm{fit}}$ represents the systematic error arising from differences in the fitting functions as described in Sec. 3.11.3 and Sec. 3.13.2. Also, $\Delta\left(\frac{\mathrm{d}\sigma}{\mathrm{d}\Omega}\right)_{\mathrm{acc}}$ represents the systematic error arising from error of acceptance. This contribution is estimated from the variation in the differential cross section caused by changing the momentum cut range defined in Sec. 3.9.3. In addition to the cut conditions adopted in the present analysis, the author applied tighter cuts:

$$2.064 \text{ [GeV/c]} < p_{e'} < 2.160 \text{ [GeV/c]} \tag{3.95}$$
$$1.777 \text{ [GeV/c]} < p_p < 1.890 \text{ [GeV/c]} \tag{3.96}$$

and looser cuts:

$$2.040 \text{ [GeV/c]} < p_{e'} < 2.200 \text{ [GeV/c]} \tag{3.97}$$
$$1.740 \text{ [GeV/c]} < p_p < 1.920 \text{ [GeV/c]} \tag{3.98}$$

(also see Fig. 3.53 and Fig. 3.54). Using the same analysis procedure, the differential cross section was derived under these conditions. The differential cross sections determined by the three types of momentum cuts are summarized in Table 3.5. Additionally, the fitting of the missing mass spectra for the tighter cut and looser cut is shown in Fig. B.21 and Fig. B.22 in Appendix B. Based on these results, it is estimated that the central value of the differential cross

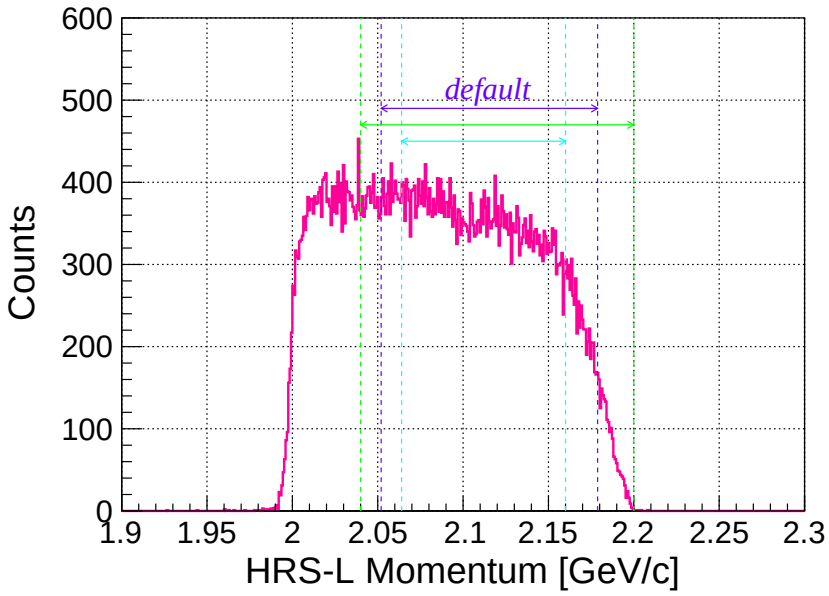

Fig. 3.53: Three types of momentum cut conditions for $p_{e'}$. The blue dashed lines represent the default cut, while the green dashed lines represent the looser cut and the cyan dasued lines represent the tighter cut.

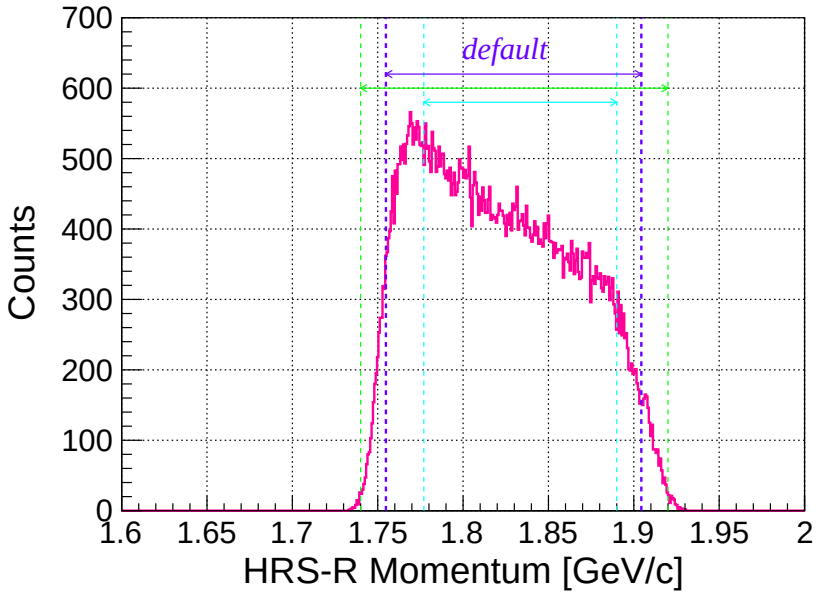

Fig. 3.54: Three types of momentum cut conditions for p_p. The color legend is the same as in Fig. 3.53.

section obtained from the spectrum fitting changes by 6 %. This variation is incorporated into the systematic error as the uncertainty in the acceptance of both spectrometers determined by the simulation. Table 3.6 summarizes the individual errors that constitute the systematic error and their respective contributions. The total systematic error of the differential cross section for all data corresponds to 9 %. Most of the error is due to the accuracy of the solid angle estimation as well as the difference in fitting functions.

Table 3.5: Summary of the differential cross sections determined by the three types of momentum cuts.

Momentum Cut	Background Function	Differential Cross Section [nb/sr]	χ^2/n.d.f
default	multi-pi simulation	4.4 ± 0.8 (stat.)	1.49
looser	multi-pi simulation	4.1 ± 0.7 (stat.)	1.84
tighter	multi-pi simulation	4.4 ± 0.8 (stat.)	1.19

Table 3.6: Individual errors that constitute the systematic error of the differential cross section. The value of $\Delta\left(\frac{d\sigma}{d\Omega}\right)_{\rm fit}/\left(\frac{d\sigma}{d\Omega}\right)$ represents the average of five patterns: one where all the data is analyzed, and four where the data is divided into two regions based on Q^2 and W. In the final results described in the next chapter, individual error values are applied according to each condition.

Valuable	$\Delta\left(\frac{d\sigma}{d\Omega}\right)_{\rm fit}/\left(\frac{d\sigma}{d\Omega}\right)$	$\frac{\Delta N_{\rm Target}}{N_{\rm Target}}$	$\frac{\Delta\varepsilon}{\varepsilon}$	$\Delta\left(\frac{d\sigma}{d\Omega}\right)_{\rm acc}/\left(\frac{d\sigma}{d\Omega}\right)$
Error value	0.11	0.004	0.01	0.06

Chapter 4

Result and Discussion

4.1 Results of the present measurement

The cross section of the ${}^{1}\mathrm{H}\,(\gamma^{*}, p)\,\eta'$ reaction was obtained for the first time by fitting the missing mass spectrum:

$$\left(\frac{d\sigma_{\gamma^{*}p\to\eta' p}}{d\Omega_{\eta'}}\right)^{\mathrm{CM}} = 4.4 \pm 0.8 \ \ (\mathrm{stat.}) \pm 0.4 \ \ (\mathrm{sys.}) \ \ [\mathrm{nb/sr}]\,. \tag{4.1}$$

When the data is divided into two regions for Q^2 and W, the cross section is

$$\left(\frac{d\sigma_{\gamma^{*}p\to\eta' p}}{d\Omega_{\eta'}}\right)^{\mathrm{CM}} \left(Q^2 < (0.47\ \mathrm{GeV}/c)^2\right) = 5.9 \pm 1.1 \ \ (\mathrm{stat.}) \pm 0.6 \ \ (\mathrm{sys.}) \ \ [\mathrm{nb/sr}] \tag{4.2}$$

$$\left(\frac{d\sigma_{\gamma^{*}p\to\eta' p}}{d\Omega_{\eta'}}\right)^{\mathrm{CM}} \left(Q^2 \geq (0.47\ \mathrm{GeV}/c)^2\right) = 4.3 \pm 1.1 \ \ (\mathrm{stat.}) \pm 0.6 \ \ (\mathrm{sys.}) \ \ [\mathrm{nb/sr}] \tag{4.3}$$

$$\left(\frac{d\sigma_{\gamma^{*}p\to\eta' p}}{d\Omega_{\eta'}}\right)^{\mathrm{CM}} (W < 2.13\ \mathrm{GeV}) = 3.7 \pm 1.2 \ \ (\mathrm{stat.}) \pm 0.7 \ \ (\mathrm{sys.}) \qquad [\mathrm{nb/sr}] \tag{4.4}$$

$$\left(\frac{d\sigma_{\gamma^{*}p\to\eta' p}}{d\Omega_{\eta'}}\right)^{\mathrm{CM}} (W \geq 2.13\ \mathrm{GeV}) = 6.5 \pm 1.0 \ \ (\mathrm{stat.}) \pm 0.8 \ \ (\mathrm{sys.}) \qquad [\mathrm{nb/sr}]. \tag{4.5}$$

Fig. 4.1 is a comparison of our experimental results and the existing database of the (γ, p) reactions at relatively nearby W. The present result at $W = 2140$ MeV and $\cos\theta^{\mathrm{CM}}_{\gamma\eta'} \approx -1$ is represented by a plot with red error bars. Data points from past experiments include measurements by CLAS06 [34] ($W = 2143$ MeV, purple), CLAS09 [35] ($W = 2130$ MeV, blue), CBELSA/TAPS [37] ($W = 2142$ MeV, orange) and LEPS [40] ($W = 2125$ MeV, pink). At backward angles, our measurements show a small cross section compared to LEPS data. This discrepancy is thought to be due to the difference between virtual photon and real photon, that is, the dependence on the four-momentum transfer Q^2 in the amplitude.

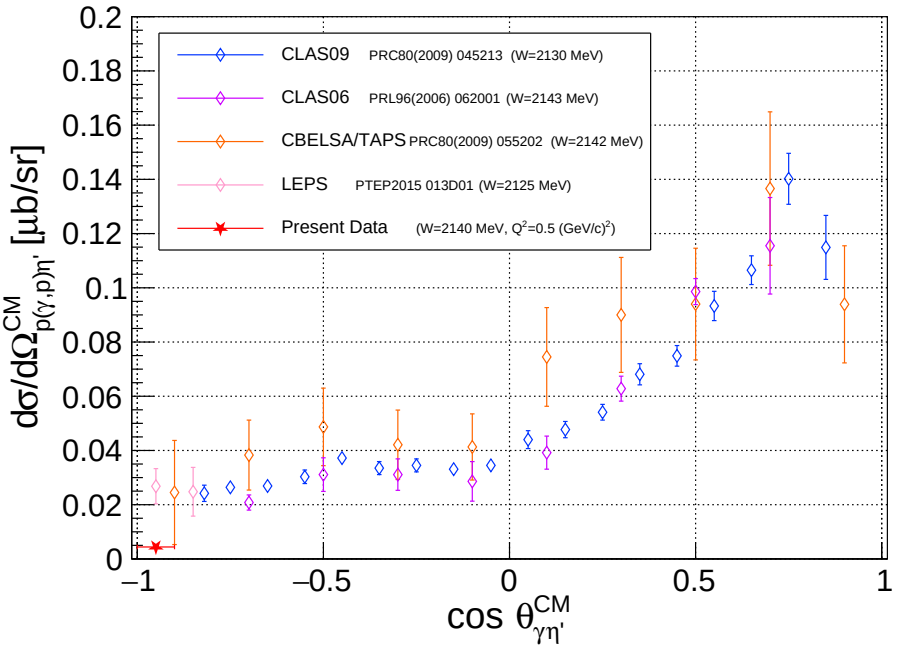

Fig. 4.1: Comparison between the present result of η' electroproduction and previous research of photoproduction.

4.2 Decomposition of differential cross section

As mentioned at the beginning of Chapter 2, the differential cross section of meson electroproduction by virtual photons is decomposed into four terms of $\frac{d\sigma_T}{d\Omega^{CM}_{\eta'}}$, $\frac{\sigma_L}{d\Omega^{CM}_{\eta'}}$, $\frac{d\sigma_{LT}}{d\Omega^{CM}_{\eta'}}$, and $\frac{d\sigma_{TT}}{d\Omega^{CM}_{\eta'}}$:

$$\frac{d\sigma_{\gamma^*}}{d\Omega^{CM}_{\eta'}} = \frac{d\sigma_T}{d\Omega^{CM}_{\eta'}} + \varepsilon\frac{d\sigma_L}{d\Omega^{CM}_{\eta'}} + \sqrt{2\varepsilon(1+\varepsilon)}\frac{d\sigma_{LT}}{d\Omega^{CM}_{\eta'}}\cos\phi_{\eta'} + \varepsilon\frac{d\sigma_{TT}}{d\Omega^{CM}_{\eta'}}\cos 2\phi_{\eta'}. \tag{4.6}$$

The experimental setup for the present measurement has an almost constant acceptance of -90 [degrees] $< \phi_{\eta'} < +90$ [degrees] for the angle $\phi_{\eta'}$ between the reaction plane and the scattering plane (refer to Fig. 2.1). Averaging within this $\phi_{\eta'}$ range cancels the $\frac{d\sigma_{TT}}{d\Omega^{CM}_{\eta'}}$ term and brings

$$\left(\frac{d\sigma_{\gamma^*}}{d\Omega^{CM}_{\eta'}}\right)_{ave.} = \frac{d\sigma_T}{d\Omega^{CM}_{\eta'}} + \varepsilon\frac{d\sigma_L}{d\Omega^{CM}_{\eta'}} + \frac{2}{\pi}\sqrt{2\varepsilon(1+\varepsilon)}\frac{d\sigma_{LT}}{d\Omega^{CM}_{\eta'}}. \tag{4.7}$$

This $\left(\frac{d\sigma_{\gamma^*}}{d\Omega^{CM}_{\eta'}}\right)_{ave.}$ corresponds to the results observed in the present experiment.

The author discuss the comparison between the present results and calculations based on the isobar model from the next section. In calculations, it is possible to directly calculate $\frac{d\sigma_T}{d\Omega^{CM}_{\eta'}}$, $\frac{d\sigma_L}{d\Omega^{CM}_{\eta'}}$, $\frac{d\sigma_{LT}}{d\Omega^{CM}_{\eta'}}$, and $\frac{d\sigma_{TT}}{d\Omega^{CM}_{\eta'}}$ in the specific kinematics. The author composes $\left(\frac{d\sigma_{\gamma^*}}{d\Omega^{CM}_{\eta'}}\right)_{ave.}$ from each term for comparison with the experimental results.

4.3 Construction of an Isobar Model

Thanks to the collaborators, a new isobar model calculation is demonstrated to describe η' photo- and electro-production continuously. The calculation developed for the present work makes it possible to physically interpret the cross section of η' electroproduction and to discuss it in conjunction with existing the dataset of photoproduction experiments. It was made by extending to the $\eta' N$ electroproduction channel from a framework of the BS models [57, 58], which have been established successfully by P. Bydžovský and D. Skoupil in the $K^+\Lambda$ channel.

As already mentioned in Chapter 1, the isobar model is an effective theory with considering the Lagrangian on hadronic degrees of freedom, and does not discribe quarks in itself. However, the set of resonance candidates assumed in the calculations reveals the contribution of the nucleon's excitation that appears in the intermediate state of the reaction. The selection of the resonance set plays an important role in the characteristics of the theoretical model. In the isobar model, only the first order perturbation represented by the tree-level diagram is usually incorporated, but the rescattering effect due to the final state interaction is taken into account by the effective coupling constant determined by data fitting.

The fitting parameter G in the calculation code is always a product of the strong coupling constant and the electromagnetic coupling constant at two vertices:

$$G = \frac{f_{\rm s} g_{\rm em}}{M_{\rm norm}}. \tag{4.8}$$

Adequate normalization factor $M_{\rm norm}$ has different forms depending on the diagram [56].

- For ρ and ω meson exchanges, $M_{\rm norm}$ is arbitrary and takes 1 GeV.
- For spin=1/2 resonance, take $M_{\rm norm} = M_R + M_p$ ($M_{R,p}$ is the mass of the resonance and proton, respectively).
- For spin=3/2 resonance, two transverse coupling parameters are required based on the Rarita-Schwinger equation [86][87],

$$G_1 = \frac{f_{\rm s} g_{\rm em}^{(1)}}{M_R^2 M_{\eta'} (M_R + M_p)} \tag{4.9}$$

$$G_2 = \frac{f_{\rm s} g_{\rm em}^{(2)}}{M_R^2 M_{\eta'} (M_R + M_p)}. \tag{4.10}$$

- Similarly, in the case of spin=5/2 resonance,

$$G_1 = \frac{f_{\rm s} g_{\rm em}^{(1)}}{16 M_{\eta'}^4 M_p^4} \tag{4.11}$$

$$G_2 = \frac{f_{\rm s} g_{\rm em}^{(2)}}{32 M_{\eta'}^4 M_p^5}. \tag{4.12}$$

They are parametrized to best reproduce the angular distribution database (CLAS06 [34], CLAS09 [35], CBELSA/TAPS[37], A2MAMI [39] and LEPS [40]). It requires the minimization of χ^2 between the data points with errors and the calculated values. The author and

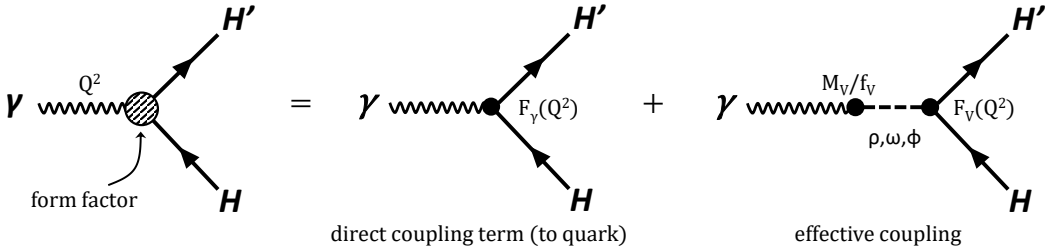

Fig. 4.2: A concept of the Extended Vector Meson Dominance (EVMD) model. In a coupling at hadron vertex, a form factor consisting of two terms is incorporated: one representing the direct coupling with a quark within the hadron in high-Q^2 region, and the other describing a superposition of couplings with vector mesons having the same quantum number. These have an explicit dipole-shape Q^2 dependence and play an crucial role on the differential cross section of the meson electroproduction. The ratio of each effect is parameterized by the theoretical model.

collaborators constructed a least-squares fitting procedure in the calculation code using the MINUIT [88].

Also, a different type of form factor for description of the internal structure of hadrons is applied with each of the two vertices. The electromagnetic form factor is based on the Extended Vector Meson Dominance (EVMD) model, that is proposed to describe hadronic photocoupling as a sum of a direct coupling term with a quark inside hadrons and a term of exclusive coupling terms with vector mesons ($\rho, \omega,$ and ϕ) having same quantum numbers (as shown in Fig. 4.2) [89][90]. The electromagnetic form factor has explicit dipole Q^2 dependence, and it makes a crucial contribution to the Q^2 dependence in electroproduction cross section. The present calculation uses the parametlization by R.A. Williams *et. al.* [91] for t-channel meson coupling and the GKex(02S) model by E.L. Lomon [92] for baryon. On the other hand, hadronic form factor is introduced in the hadron vertex, and in the present calculation it is a multi-dipole function for Mandelstam variables $x = s, t$ and u as shown in the following expression,

$$F_{\text{h.f.f.}} = \left[\frac{\Lambda^4}{\left(x - M_R^2\right)^2 + \Lambda^4} \right]^{J_R+1/2}, \tag{4.13}$$

where J_R is the resonance spin. The introduction of the hadronic form factor has importance for consistency with photoproduction data. Cutoff parameters Λ for resonance and background channels are also determined by data fitting.

The author adopted three patterns of resonance set, named as Model I, II and III, for the considering calculations. Table 4.1 lists the resonances introduced in each model. Model I selected four essential resonances that have been reported to couple with $\eta' p$ production (according to PDG's summarization [9]). In addition to these, Model II includes more two resonances $N\,(1880)\,\frac{1}{2}^+$ and $N\,(2060)\,\frac{5}{2}^-$ that are rated three stars (***) by PDG [9]. Model III selected six resonances that significantly contributed to total cross section of EtaMAID2018 [30], that has been developed for calculation of η and η' photoproduction.

Table 4.1: Summary of resonance sets incorporated into the isobar model calculation Model I–III. All three models have $\rho\,(770)$ and $\omega\,(782)$ meson coupling in t-channel. Model I includes four essential resonances for the $\eta' p$ channel in s- and u-channels. A pair of three-star (***) resonances is also given into Model II. Model III is intended for EtaMAID[30]-like calculation.

Resonance	PDG status [9]	Model I	Model II	Model III
$\rho\,(770)$		✓	✓	✓
$\omega\,(782)$		✓	✓	✓
$N\,(1860)\,\frac{5}{2}^+$	**			✓
$N\,(1880)\,\frac{1}{2}^+$	***		✓	✓
$N\,(1895)\,\frac{1}{2}^-$	****	✓	✓	✓
$N\,(1900)\,\frac{3}{2}^+$	****	✓	✓	✓
$N\,(2000)\,\frac{5}{2}^+$	**			✓
$N\,(2060)\,\frac{5}{2}^-$	***		✓	
$N\,(2100)\,\frac{1}{2}^+$	***	✓	✓	
$N\,(2120)\,\frac{3}{2}^-$	***	✓	✓	✓

The values of each parameter in Model I–III determined are shown in the Table 4.2. In addition, the angular dependence of Model I–III at energy of W = 1901–2620 MeV is shown in Fig. 4.3. It can be found that all models well reproduce the behavior of the experimental data. However, predictions at extremely forward and backward angles are inconsistent. This discrepancy is an uncerteinty remaining in the models due to the lack of experimental data or/and the resonance set dependence. χ^2 between dataset and calculation is the smallest in Model II. Note that our experimental results at $W = 2140$ MeV are excluded from this fitting, but also plotted in Fig. 4.3 with red error bars. Comparing with the calculations and other experimental data, it can be seen that electroproduction with a finite momentum transfer Q^2 yields a smaller cross section.

Table 4.2: Summary of parameters for Model I-III. Width of each resonance is according to the listing by PDG [9]. Values of the parameters are determined by fitting with the cross section database of photoproduction experiments.

Parameter	Width (GeV/c^2)	Model I	Model II	Model III
$g_{\eta' NN}$		-0.179	-0.326	-0.549
Λ_{bg}		1.40	0.888	0.763
Λ_{res}		1.25	1.43	1.25
G_V (ρ)	0.153	-0.607	6.16	13.4
G_T (ρ)	0.153	-11.0	15.0	15.0
G_V (ω)	0.0085	0.93	-6.58	-13.4
G_T (ω)	0.0085	10.9	-15.0	-13.9
G_1 $(N(1860)\frac{5}{2}^+)$	0.300			-1.01
G_2 $(N(1860)\frac{5}{2}^+)$	0.300			1.36
G $(N(1880)\frac{1}{2}^+)$	0.300		0.813	-0.216
G $(N(1895)\frac{1}{2}^-)$	0.120	-0.139	0.0620	-0.0706
G_1 $(N(1900)\frac{3}{2}^+)$	0.200	-0.0503	0.0915	-0.186
G_2 $(N(1900)\frac{3}{2}^+)$	0.200	0.0663	0.0258	0.0306
G_1 $(N(2000)\frac{5}{2}^+)$	0.300			0.189
G_2 $(N(2000)\frac{5}{2}^+)$	0.300			-0.149
G_1 $(N(2060)\frac{5}{2}^-)$	0.400		0.0195	
G_2 $(N(2060)\frac{5}{2}^-)$	0.400		0.0346	
G $(N(2100)\frac{1}{2}^+)$	0.300	0.240	-0.532	
G_1 $(N(2120)\frac{3}{2}^-)$	0.300	-0.643	0.0454	-0.0708
G_2 $(N(2120)\frac{3}{2}^-)$	0.300	-0.480	0.0415	-0.0642
χ^2/n.d.f		2.89	1.94	2.51

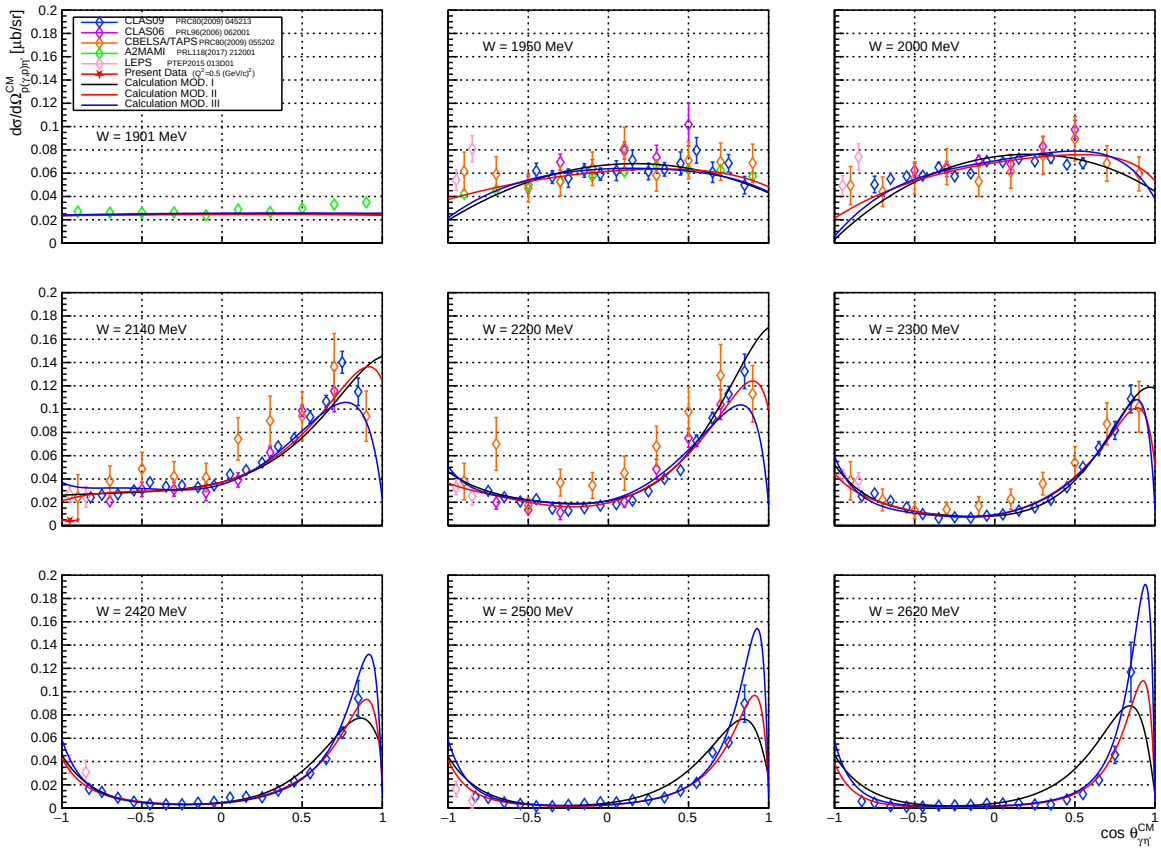

Fig. 4.3: Angular dependence of η' photoproduction with various energy range. Plots with different colors corresponds to data by different experiment including CLAS06 [34], CLAS09 [35], CBELSA/TAPS [37], A2MAMI [39] and LEPS [40]. A red star with error bars represents the result of the present result at $W = 2140$ MeV and $\cos\theta^{\mathrm{CM}}_{\gamma\eta'} \approx -1$. Smooth curves give the solution of Model I–III. Note that the Ws in the legends represent the energy of the theoretical calculations, and although the experimental W is the closest, it may not match completely.

4.4 Discussion 1: Q^2 dependence

Here the author considers the cross section with finite $Q^2 > 0$ obtained in the present experiment. First, the results of the the present experiment are given on the Q^2 dependence plot by Model I–III in Fig. 4.4. Kinematics assumed in the three calculations follows the experimental condition of $W = 2140$ MeV, $\cos\theta^{\rm CM}_{\gamma\eta'} = -0.95$ $\left(\theta^{\rm CM}_{\gamma\eta'} = 170 \text{ degrees}\right)$, and $\epsilon = 0.7$. The dashed lines are calculations without using the electromagnetic form factor, and the solid lines are calculation with it. The plots at $Q^2 = 0.47$ $(\text{GeV}/c)^2$ are the result of the present experiment, where the pink represents all data and the brown represents data divided into 2 bins. Error bars in the plot are statistical errors in cross section, and boxes are systematic errors. The plots at $Q^2 = 0$ are the phoptoduction data of $W = 2125$ MeV and $W = 2179$ MeV at backward angles of $\cos\theta^{\rm CM}_{\gamma\eta'} \approx -1$ in 2016 LEPS [40]. The cross section of the present experiment decreases to about 1/6 of the photoproduction data with the closest W.

The calculations without the electromagnetic form factor show the purely dynamical Q^2-dependence that appears in the transition matrix describing meson electroproduction. However, these calculations exhibit a dependence where the cross section increases at finite $Q^2 > 0$, which does not agree with the results of the present experiment. On the other hand, the calculations

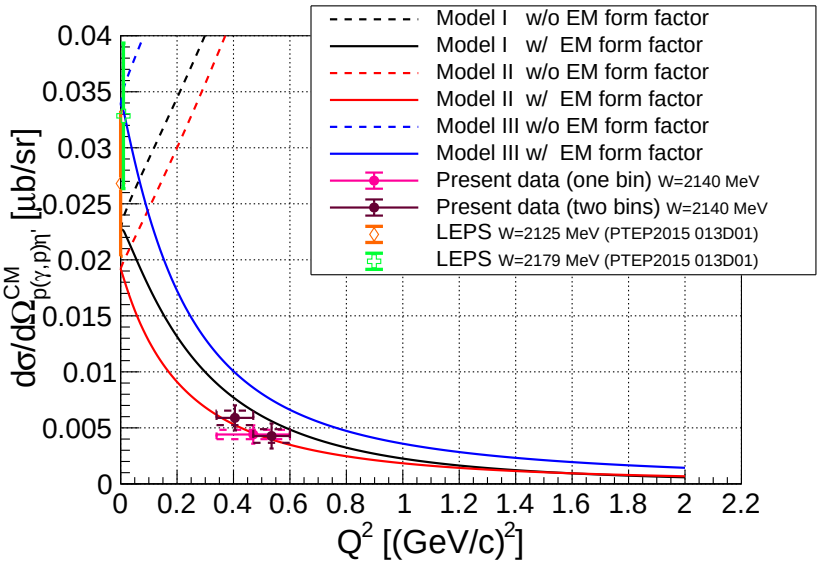

Fig. 4.4: Q^2 dependence of the differential cross section in electroproduction of the η'. Solid/dashed curves correspond to calculation with/without the electromagnetic formfactor. The pink plot with errors represents the result of the present experiment in a single bin. In contrast, the brown plots are the results diveded into two bins. The error bars to each plot represent statistical errors, while the boxes represent systematic errors. The green and orange plots at $Q^2 = 0$ (orverlapping each other) are the value of existing data at nearby W of photoproduction measured by LEPS [40].

incorporating the EM form factor, which describes the charge distribution of hadrons with a Lorentz-type Q^2-dependence, indicates that starting from photoproduction at $Q^2 = 0$, the cross section quenches as Q^2 increases. These theoretical models reasonably reproduce both our experimental results of the electroproduction at finite $Q^2 > 0$ and the photoproduction at $Q^2 = 0$. The comparison between the theories and the experimental results highlights that the inclusion of the EM form factor plays a crucial role in understanding meson electroproduction. This understanding is consistent with other meson production channels as well. The present experimental results support the validity of the theoretical framework employed in these calculations.

4.5 Discussion 2: W dependence

Fig. 4.5 – 4.7 represents comparisons of the results of the present experiment and prediction by Model I–III on the W dependence. The pink plot at $W = 2140$ MeV shows all data, and the brown plots show data divided into two bins. The theoretical curve follows the kinematics of the present experiment: $Q^2 = 0.46$ $(\mathrm{GeV}/c)^2$, $\cos\theta^{\mathrm{CM}}_{\gamma\eta'} = -0.95$, and $\epsilon = 0.7$. The dashed curves with various colors correspond to the individual contribution of each resonance.

The behavior of the W dependence predicted by the three calculations differs greatly. A contribution of each resonance for these calculations were determined to best reproduce the angular dependence of photoproduction by fitting in Sec. 4.3. However, the most contributiong resonances to explain the database varies each other by assumption of the resonance set. This discrepancy is clearly visible in the W-dependent behavior at backward electroproduction. Among the three theoretical models, Model II is the most preferred for explaining the results of the present experiment (besides, Model II also shows the best agreement with the angular dependence of photoproduction). Furthermore, when comparing the increase or decrease of cross sections in the energy region of interest, Models I and II exhibit an increasing trend with W, whereas Model III shows a slowly decreasing trend, behaving differently from the other two models. Examining the contributions from individual resonances, $N\,(2120)\,\frac{3}{2}^-$ is the most dominant in Model I, while $N\,(2100)\,\frac{1}{2}^+$ dominates in Model II. In contrast, Model III attributes the cross section primarily to couplings with lower-energy resonances. The experimental result obtained in the present study show an increasing trend in dependence beyond $W = 2130$ MeV, which also supports Models I and II. Therefore, the present measurement suggests an important role of (a) resonance(s) near an energy of ~ 2100 MeV. The new data imposes additional constraints on future resonance searches; however, more detailed discussions require experimental data with a broader range of covering W, or, more precise statiscal errors.

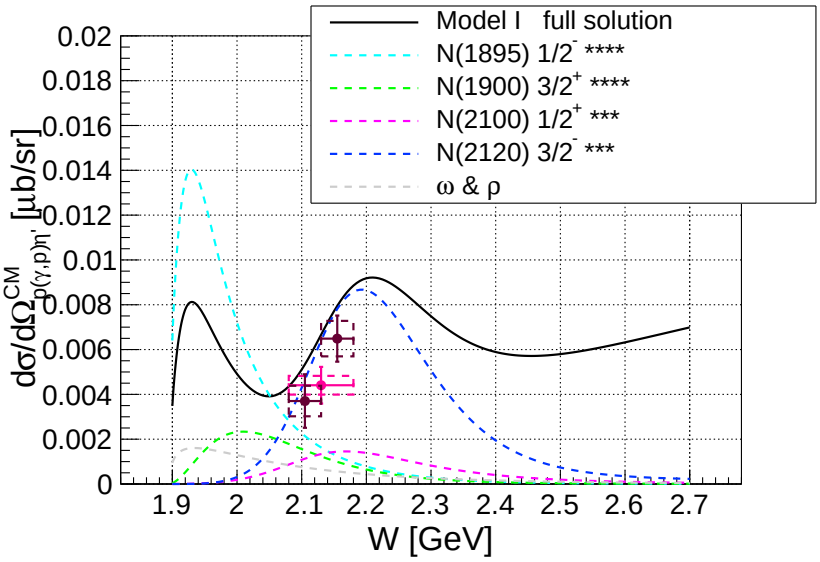

Fig. 4.5: W dependence of the differential cross section of the η' electroproduction (compared with Model I). The pink plot with errors represents the result of the present experiment in a single bin. In contrast, The brown plots are the results diveded into two bins. The error bars to each plot represent statistical errors, while the boxes represent systematic errors. The solid curve gives the full solution of Model I at the specific kinematics, and the dashed curves give the individual contributions of different resonances.

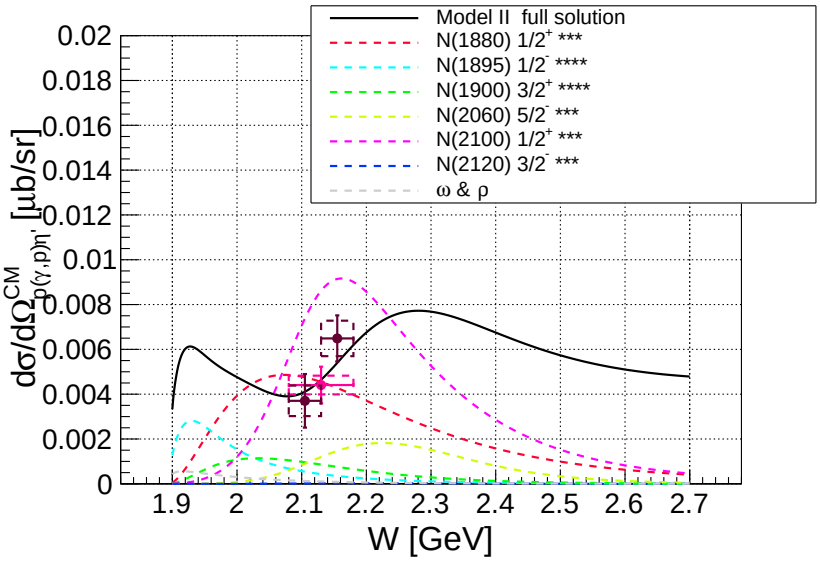

Fig. 4.6: W dependence of the differential cross section of the η' electroproduction (compared with Model II).

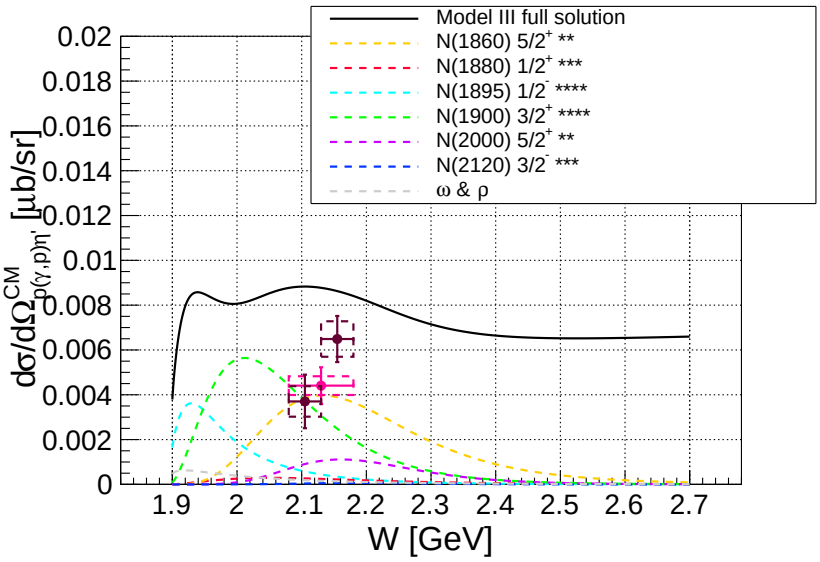

Fig. 4.7: W dependence of the differential cross section of the η' electroproduction (compared with Model III).

4.6 In future

As described, the present study established that it is possible to derive the differential cross section of the $^{1}\mathrm{H}\,(e,e'p)\,\eta'$ reaction at backward angles by analyzing the data obtained from high-resolution mass spectrometry experiments of Λ hypernuclei. Additionally, with the aid of theoretical calculations, this unique experimental data not only verified the validity of the meson electroproduction model based on the One-Photon-Exchange Approximation but also provided valuable information regarding the existence of nucleon excited states with slightly higher energy, in other words, the energy structure of the nucleon. Towards the end of this discussion, The author wished to describe the potential developments in future follow-up research according to the own thoughts.

The JLab hypernuclear collaboration has been conducting missing mass spectrometry experiments of Λ hypernuclei at JLab. Table 4.3 provides an overview of the experiments conducted so far, the present experiment, and those planned for the future. The collaboration have been producing and measuring Λ hypernuclei by the $K^{+}\Lambda$ electroproduction from various nuclear targets. In all these experiments, the elementary process of Λ/Σ^{0} electroproduction from proton targets has been simultaneously measured. This is because data from these reaction is indispensable for the energy calibration of the missing mass spectra. Therefore, by analyzing the proton target data from other past or future hypernuclear experiments using the same procedures as the present study, it should be possible to observe the η' meson generated as a by-product. Notably, despite the existence of past experimental data spanning over 20 years, no senior students or researchers have seriously attempted to analyze the η' production channel.

These experiments have been conducted at JLab Hall-A and Hall-C. The spectrometers used differ for each experiment as a result of the setup being refined over time. The present experiment, E12-17-003, was conducted at Hall-A in 2018, as part of a series of experimental campaigns using tritium targets at JLab. This was somewhat irregular among the hypernuclear

Table 4.3: Summary of the spectroscopic experiments of Λ hypernuclei at JLab. The four planned future experiments are scheduled to be conducted consecutively during a continuous beamtime session.

Experiment	Year	Hall	Spectrometers	E_e [GeV]	$p_{e'}$ [GeV/c]	p_{K^+} [GeV/c]	W^{γ^*+p} [GeV]	Target
E89-009	2000	C	ENGE+SOS	1.864	0.283	1.2	1.96	CH_2, ^{12}C
E01-011	2004	C	ENGE+HKS	1.851	0.316	1.2	1.94	CH_2, ^{7}Li, ^{12}C, ^{28}Si
E94-017	2004	A	HRS+HRS	3.66	1.45	1.96	2.23	CH_2, H_2O, ^{12}C
E05-115	2009	C	HES+HKS	2.344	0.844	1.2	1.91	CH_2, ^{7}Li, ^{10}B, ^{12}C, ^{52}Cr
E12-17-003	2018	A	HRS+HRS	4.326	2.1	1.8	2.14	^{1}H, ^{3}H, ^{3}He
E12-24-003	2026?	C	HES+HKS	2.344	0.844	1.2	1.91	CH_2, ^{208}Pb
E12-24-004	2026?	C	HES+HKS	2.344	0.844	1.2	1.91	CH_2,^{6} Li, ^{9}Be, ^{11}Be
E12-24-011	2026?	C	HES+HKS	2.344	0.844	1.2	1.91	CH_2,^{27} Al
E12-24-011	2026?	C	HES+HKS	2.344	0.844	1.2	1.91	CH_2,^{40} Ca, ^{48}Ca

experiments conducted solely by the collaboration. On the other hand, both the previous experiment and the planned future experiment will be conducted at Hall-C. In these, HES is used on the scattered electron side spectrometer and HKS on the hadron side spectrometer. This setup is designed to maximize the cross section of the Λ hyperon: observing the forward scattered electrons and K^+ is common to all experiments, but the energy of the incident electrons is about ~ 2 GeV smaller than that of the experiment at Hall-A. Consequently, the total energy in the $p + \gamma^*$ system is $W = 1.9$ GeV, which is the energy at which the total cross section of the $p + \gamma \to \Lambda + K^+$ reaction make a peak. The momentum coverage of HES-HKS setup in Hall-C experiment also contains the η' production events (Fig. 4.8). Additionally, the solid angle of HKS is about 12 msr, which is approximately twice that of the 5 msr HRS, making it superior from the perspective of yield.

Analyzing the $(e, e'p)$ reaction channel using proton target data obtained under such Hall-C experimental conditions would provide one or two data points for the differential cross section of the η' electroproduction under different kinematic conditions than the present experiment. Particularly, while data from the present experiment allowed discussion of the resonant state around $W = 2000$–2100 MeV, analysis of the Hall-C experimental data would likely observe the contribution of resonant states in different W regions. It is especially noteworthy that the total energy $W = 1900$ MeV is just above the threshold of the $p + \gamma \to p + \eta'$ reaction ($W_{\mathrm{th}} = 1896$ MeV). From measurements at such energy, the strength of couplings with $N\,(1895)\,\frac{1}{2}^-$ or

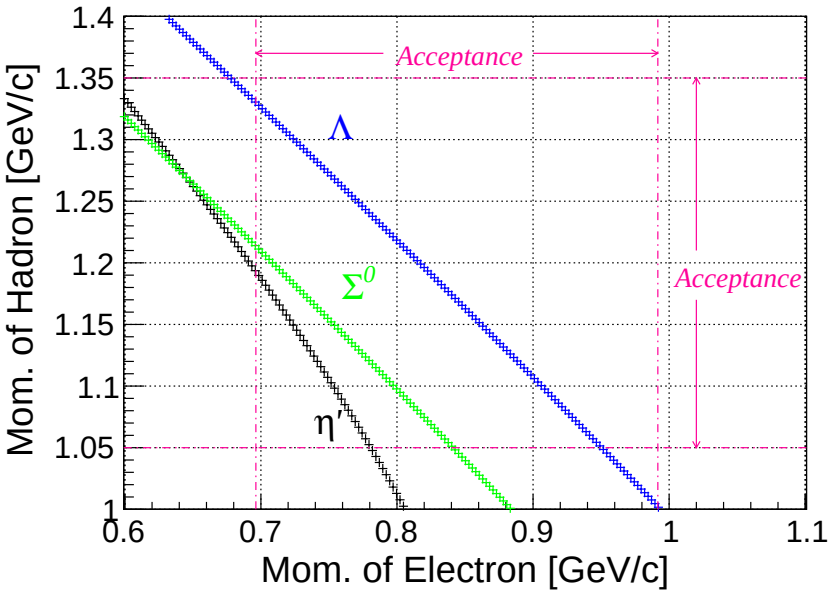

Fig. 4.8: The p_{hadron}-$p_{e'}$ corralation in the kinematics of Hall-C experiment. The blue, green and black plots give the ${}^1\mathrm{H}\,(e, e'K^+)\,\Lambda$, ${}^1\mathrm{H}\,(e, e'K^+)\,\Sigma^0$ and ${}^1\mathrm{H}\,(e, e'p)\,\eta'$ reactions, respectively. The pink dashed lines represent the momentum acceptance of HES and HKS, the spectrumeters used in the past and future Hall-C experiment.

$N(1900)\,\frac{3}{2}^+$, which have similar masses, could be discussed from the differential cross section, potentially imposing new constraints on theoretical models.

On the other hand, several technical hurdles remain in the data analysis of the Hall-C experiment. The author will mention those here.

One challenge is PID (Particle Identification). In the hypernuclear experiments at Hall-C, two types of Cherenkov detectors, one with silica aerogel and the other with pure water as radiators, are used in the hadron side spectrometer (HKS) to distinguish kaons from hypernuclei against protons and pions. These Cherenkov detectors are part of the online trigger during data acquisition. This is a significant difference from the present experiment, E12-17-003, where the trigger was composed solely of the hodoscope. Therefore, if one was to analyze η' production, one would have to identify protons that leaked into the data where kaons were selectively chosen by the Cherenkov detectors, and to know the proton survival ratio with those detectors precisely. Table 4.4 shows the proton survival ratio in the online triggers using Cherenkov detectors for E05-115 experiment and next-generation experiments. (Of particular note, the author is not very familiar with how seriously these values were estimated during the past E05-115 experiment.) In E05-115 experiment, approximately five times the calibration data of the present experiment was obtained. However, the expected number of η' mesons was reduced to $\sim \frac{3}{4}$ of that of the present experiment, due to the online triggers of the Cherenkov detectors. In contrast, in the next-generation experiment, significant improvements in event rate capacity are expected through upgrades to high-speed FPGAs for triggering and faster DAQ systems. Moreover, particularly for the CH_2 target, which serves as the source of calibration, there is a restriction that the target must not melt due to energy deposition from the beam. Under the condition that the beam current itself cannot be increased, it is expected that the data acquisition system will have vast capacity, to the extent that online PID will no longer be necessary. As a result, assuming the same statistical amount of calibration data as E05-115 experiment is obtained, $N_{\eta'} \sim 2100$ events will be recorded as by-products, leading to a significant improvement in the observed number of η' mesons.

Another issue is the background distribution. In the present thesis, the author struggled considerably to estimate the shape of the background in the missing mass distribution (refer to Sec. 3.11.2). The Hall-C experiment data should contain a large number of background

Table 4.4: Summary of $N_{\eta'}$ and N_Λ in the previous, present and future experiments. It should be noted that in the new experiment, it is highly likely that online triggers using Cherenkov detectors will not be employed for the polyethylene target.

Experiment	N_Λ	$\varepsilon^{\text{proton}}$	$\varepsilon^{\text{kaon}}$	$N_{\eta'}$
E05-115 (previous)	5991 ± 135 [93]	0.12 [93]	0.92 [93]	363 ± 63 (estimation)
E12-17-003 (present)	1360^{-92}_{+58} [81]	1	1	467 ± 85
next-generation	-	(0.05 [94])	(0.99 [94])	3150 ± 188 (estimation)

events from multi-pion production, too. Additionally, in the case of the Hall-C experiment, a polyethylene target is used instead to provide proton data for calibration, and the carbon nuclei in the target generate additional background. In the present experiment, E12-17-003, the author was able to eliminate this background source by using gaseous H_2 target. However, the Hall-C experiment using the HES-HKS configuration can only handle thin solid targets due to poor resolution along the beam axis direction (Z-vertex). Therefore, one have to use polyethlene target instead in the calibration run, and reactions generated by the carbon nuclei are also mixed in. Events from carbon nuclei are likely to be almost entirely due to quasi-free production of mesons, and they all appear as broad distributions in the spectrum of the $^1\mathrm{H}\,(e, e'p)\,X$ reaction. Assuming a simple calculation based on the liquid drop model, the cross section $\sigma \propto A^{\frac{2}{3}}$ for carbon with an atomic mass of 12.0 is estimated to be about 5.24 times that of hydrogen nuclei. Considering the ratio of number of atoms of carbon to hydrogen is 1 : 2, it can be predicted that a background event from carbon nuclei amount approximately equal to that from hydrogen nuclei will be newly generated. On the other hand, using a solid polyethylene target also has a significant advantage in energy resolution. In fact, for Λ/Σ^0 production, the resolution of the missing mass distribution from the proton target in E05-115 experiment was 1.5 MeV (FWHM), which is about half of the 3.3 MeV (FWHM) in E12-17-003 experiment. The largest factor for this difference is likely that, in the present experiment, a target cell with a significant material thickness was required to contain the gas target, causing energy straggling. In the Hall-C experiment, since the target is a thin solid, the influence of straggling can be significantly reduced, resulting in spectra with improved energy resolution compared to the present experiment. Thus, even if the background increases by about double, the expectation of observing the peak of the η' meson through higher-resolution missing mass spectroscopy remains sufficiently high. Taking into account the improvements in resolution, the deterioration in the signal-to-noise (S/N) ratio, the increase in statistics, and the precision of the results in the present experiment, it appears feasible to determine the differential cross section of η' electroproduction with an accuracy of 6 % in the analysis of next-generation experimental data. The author assert that this makes it worthwhile to analyze further.

Chapter 5

Summary

The electroproduction of η' mesons from a ^{1}H target was observed from calibration data of the Λ hypernuclear spectroscopy experiment at Jefferson Lab. A 4.326 GeV electron beam provided by CEBAF was irradiated onto a hydrogen gas target cooled to 40 K. Scattered electrons with a momentum of approximately 2.1 GeV/c and positive hadrons with a momentum of about 1.8 GeV/c, emitted at 13.2 degrees from the beam axis, were measured by two High Resolution Spectrometers. A peak of η' mesons consisting of 428 ± 78 events was observed in the missing mass spectrum of the $^1\mathrm{H}\,(e, e'p)\,X$ reaction. The observed number of η' mesons, when converted to the differential cross section of the $\gamma^* + p \to \eta' + p$ reaction at $W = 2140$ MeV, $Q^2 = 0.47\ \ (\mathrm{GeV}/c)^2$, and $\cos\theta^{\mathrm{CM}}_{\gamma\eta'} \approx -1.0$ in the One-Photon-Exchange Approximation, corresponds to $\left(\frac{\mathrm{d}\sigma_{\gamma^* p \to \eta' p}}{\mathrm{d}\Omega_{\eta'}}\right)^{\mathrm{CM}} = 4.4 \pm 0.8\ \ (\mathrm{stat.}) \pm 0.4\ \ (\mathrm{sys.})\ \ [\mathrm{nb/sr}]$. This value is approximately one-sixth of that of backward photoproduction at $Q^2 = 0$ measured by the LEPS collaboration. To analyze the present experimental results, a theoretical calculation based on the isobar model was demonstrated: it describes both the database of angular dependence of photoproduction in various past experiments and the virtual photoproduction in the present experiment within the same framework. The new calculations consistently reproduced the observed decrease in differential cross section at finite $Q^2 > 0$ by introducing an electromagnetic form factor at the virtual-photocoupling vertex. Furthermore, the W dependence derived by dividing the experimental data into two bins showed a rising behavior at the boundary of $W = 2140$ MeV, and the degree of agreement with the theoretical calculations varies depending on the combination of resonance sets introduced in each theoretical model. The new data suggests that (a) N^* resonance(s) with energy of approximately 2000–2100 MeV might play an important role for the coupling to the $\eta' p$ final state, and imposes new constraints for a future resonance search.

Acknowledgement

First and foremost, I would like to express my deepest gratitude to my supervisor, Prof. Dr. Satoshi N. Nakamura. He has guided me over the past seven years since I joined the experimental nuclear physics laboratory at Tohoku University. Without his attentiveness, extensive knowledge for physics and experiments, precise and thoughtful advice, and vast network of researchers, I could not have completed my doctoral thesis. I deeply respect his exceptional leadership, which remains a distant goal for me.

I would like to extend my heartfelt thanks to Dr. Petr Bydžovský and Dr. Dalibor Skoupil. As experts in the theoretical framework of the $K^+\Lambda$ electroproduction, they provided invaluable theoretical support in interpreting the results of the present research. When I visited the Czech Republic in 2023, they warmly welcomed me and engaged in thorough discussions, despite my lack of familiarity with such theories at the time. Their assistance greatly enriched the depth of the present study. They also meticulously reviewed Chapter 1 and Appendix A of the present thesis.

I am grateful to the members of the JLab Hypernuclear Collaboration, who made significant contributions to the execution of JLab E12-17-003 experiment. In particular, I thank the spokespersons Prof. Dr. Liguang Tang, Prof. Dr. Pete Markowitz, Prof. Dr. Joerg Reinhold, Prof. Dr. Franco Garibaldi, and Prof. Dr. Guido Urciuoli. I also extend my gratitude to the Hall-A Tritium Collaboration and the technical staff at JLab for their dedication throughout the experimental campaign.

I wish to thank the members of ELS group in the experimental nuclear physics laboratories at Tohoku University and the University of Tokyo. Prof. Dr. Masashi Kaneta, Dr. Toshiyuki Gogami, Dr. Sho Nagao, and Dr. Yuichi Toyama taught me a lot of things, for example, the principles of detector operation and the fundamentals of data analysis when I was still new to the field. Dr. Kazuki N. Suzuki, Dr. Kosuke Itabashi, Dr. Bishnu Pandey, and Dr. Kazuki Okuyama, who were part of JLab E12-17-003 analysis team, developed many of the data analysis methods used in the present study. My research is built upon their dedication and outstanding work. I am also grateful to my junior colleagues—Mr. Masaya Mizuno, Ms. Ryoko Kino, Mr. Tatsuiro Ishige, Mr. Daigo Watanabe, Mr. Shota Toyama, Mr. Kotaro Nishi, Mr. Ken Nishida, Mr. Shunsuke Niwa, and Mr. Kaito Higashimoto—for their encouragement and support.

I would like to thank the members of my dissertation review committee, Prof. Dr. Hirokazu Tamura, Prof. Dr. Koji Miwa, Prof. Dr. Hiroaki Ohnishi, and Prof. Dr. Atsuko K. Ichikawa. The discussions during the preliminary defence highlighted gaps in my data analysis and helped me to improve the overall quality of my thesis.

I also extend my gratitude to the Graduate Program on Physics for the Universe (GP-PU)

at Tohoku University for their financial support. Thanks to GP-PU, I was able to focus on my research without financial worries during my time in graduate school. Their funding also enabled me to conduct the present research and participate in other experimental projects during my trips to the Czech Republic and Germany.

Finally, and most importantly, I express my indescribable gratitude to my mother and grandmother, Yumiko and Suzuko Akiyama, as well as to my partner, Sumireno Uramoto, for their unwavering love, support, and encouragement throughout this journey.

in Sendai, February 2025
Takeru Akiyama

Appendix A

Theoretical description of meson electroproduction

See also Fig. 2.1 for reference to kinematic variables.

This theoretical description is based on the theoretical model constructed by P. Bydžovský and D. Skoupil for the electro-induced reaction of $e + p \to e' + \Lambda + K^+$. The reference is [57].

Four momentum of particles before and after the reaction is expressed by p:

$$e\left(p_e\right) + p_{\mathrm{tar}}\left(p_{p_{\mathrm{tar}}}\right) \to e'\left(p_{e'}\right) + p_{\mathrm{scat}}\left(p_{p_{\mathrm{scat}}}\right) + \eta'\left(p_{\eta'}\right). \tag{A.1}$$

The cross section for this reaction is written as

$$\begin{aligned}\mathrm{d}\sigma_{i\to f} = &\frac{2m_e 2m_p}{4\sqrt{\left(p_{p_{\mathrm{tar}}}\cdot p_e\right)^2 - m_e^2 m_p^2}}\left(2\pi\right)^4 \delta^{(4)}\left(p_e + p_{p_{\mathrm{tar}}} - p_{e'} - p_{p_{\mathrm{scat}}} - p_{\eta'}\right)\\ &\times \left|M_{\mathrm{fi}}\right|^2 \frac{m_e}{E_{e'}}\frac{\mathrm{d}^3 p_{e'}}{\left(2\pi\right)^3}\frac{m_p}{E_{p_{\mathrm{scat}}}}\frac{\mathrm{d}^3 p_{p_{\mathrm{scat}}}}{\left(2\pi\right)^3}\frac{1}{2E_{\eta'}}\frac{\mathrm{d}^3 p_{\eta'}}{\left(2\pi\right)^3},\end{aligned} \tag{A.2}$$

where M_{fi} is a spin-dependent invariant matrix element. Averaging over spin of the initial particles, summing over spin of the final particles, and integrating over $\mathrm{d}^3 p_{p_{\mathrm{scat}}}$ and $\mathrm{d}p_{\eta'}$ using the delta function one obtains the following expression for the triple-differential cross section,

$$\frac{\mathrm{d}^3\sigma}{\mathrm{d}E_{e'}\mathrm{d}\Omega_{e'}\mathrm{d}\Omega_{\eta'}} = \frac{m_e^2 m_p}{\left(2\pi\right)^5}\frac{\left|\boldsymbol{p}_{e'}\right|}{\left|\boldsymbol{p}_e\right|}\frac{1}{4}\sum_{\mathrm{spin}}\left|M_{\mathrm{fi}}\right|^2\frac{\left|\boldsymbol{p}_{\eta'}^{\mathrm{CM}}\right|}{2W}. \tag{A.3}$$

Quantum electrodynamics (QED) explains the dynamics of electron scattering reactions. Since the coupling constant $\alpha = \frac{e^2}{4\pi} \approx \frac{1}{137} \ll 1$ indicates the strength of the interaction, perturbative extension is effective. Therefore, One Photon Exchange Approximation (OPEA) as shown in Fig. 2.1 is justified. In OPEA, a single virtual photon with momentum

$$q = \left(\omega, \boldsymbol{q}\right) = p_e - p_{e'}, \tag{A.4}$$

mediates the meson production. The invariant matrix element is the product of the hadronic current J^μ that is mediated by the photon propagator and the leptonic current $l_\mu = e\bar{u}\left(p_{e'}\right)\gamma_\mu u\left(p_e\right)$,

$$M_{\mathrm{fi}} = \frac{e^2}{m_e q^2} l_\mu J^\mu. \tag{A.5}$$

Thus,

$$\frac{1}{4}\sum_{\text{spin}}|M_{\text{fi}}|^2 = \frac{e^4}{4m_e^2 q^4} L_{\mu\nu} W^{\mu\nu}, \tag{A.6}$$

where, L is the leptonic tensor and W is the hadronic tensor. As a result, the original triple differential cross section is separated into the flux of virtual photons Γ and the cross section of the binary process $\gamma + p \to \eta' + p$:

$$\frac{\mathrm{d}^3\sigma}{\mathrm{d}E_{e'}\mathrm{d}\Omega_{e'}\mathrm{d}\Omega_p^{\text{CM}}} = \frac{\alpha}{2\pi^2}\frac{|\boldsymbol{p}_{e'}|}{|\boldsymbol{p}_{e'}|}\left(-\frac{1}{q^2}\right)\frac{E_\gamma}{1-\epsilon} \times \frac{\alpha}{16\pi}\frac{\left|\boldsymbol{p}_{\eta'}^{\text{CM}}\right|}{E_\gamma}\frac{m_{\eta'}}{W}\left(-\frac{2\,(1-\epsilon)}{q^2}L_{\mu\nu}W^{\mu\nu}\right) \tag{A.7}$$

$$:= \Gamma \times \left(\frac{\mathrm{d}\sigma_{\gamma^*}}{\mathrm{d}\Omega_{\eta'}^{\text{CM}}}\right), \tag{A.8}$$

where,

$$\Gamma = \frac{\alpha}{2\pi^2 Q^2}\frac{E_\gamma}{1-\epsilon}\frac{|\boldsymbol{p}_{e'}|}{|\boldsymbol{p}_{e'}|} \tag{A.9}$$

$$Q^2 = -q^2 = 2E_e E_{e'} - 2{m_e}^2 - 2\,|\boldsymbol{p}_e|\,|\boldsymbol{p}_{e'}|\cos\theta_{ee'} \tag{A.10}$$

$$\epsilon = \left[1 + 2\frac{|\boldsymbol{q}|^2}{Q^2}\tan^2\left(\frac{\theta_{ee'}}{2}\right)\right]^{-1} \tag{A.11}$$

$$E_\gamma = \omega + \frac{q^2}{2m_p}. \tag{A.12}$$

The variable ω is the photon energy in the laboratory frame, and E_γ is the effective photon energy. This factorization of the invariant amplitude into the leptonic and hadronic parts is an important consequence of OPEA. The virtual photon flux Γ can be calculated from the momentum of incident and scattered electrons. A parameter ϵ mean transverse polarization of the virtual photons. By extracting the cross section of the $\gamma^* + p \to p + \eta'$ reaction $\frac{\mathrm{d}\sigma_{\gamma^*}}{\mathrm{d}\Omega_{\eta'}^{\text{CM}}}$, one can understand the meson electroproduction by analogy with experiments and theoretical calculations for photoproduction.

The author and collaborators measured the recoil protons instead of the generated η' mesons in the present measurement. The observable is hence $\frac{\mathrm{d}^3\sigma}{\mathrm{d}E_{e'}\mathrm{d}\Omega_{e'}\mathrm{d}\Omega_p^{\text{CM}}}$ (or $\left(\frac{\mathrm{d}\sigma_{\gamma^*}}{\mathrm{d}\Omega_p^{\text{CM}}}\right)_{\gamma^* p \to p\eta'}$). However, these cross section is equal to the above equation since the recoil angle in two-body reaction at the CM frame is back-to-back.

Matrix elements of the hadronic current are decomposed into six covariant gauge-invariant contributions,

$$J^\mu \varepsilon_\mu = \sum_{j=1}^{6} A_j\,\bar{u}\left(p_{p_{\text{scat}}}\right)\gamma^5 M_j\, u\left(p_{p_{\text{tar}}}\right), \tag{A.13}$$

where, M_j is an explicitly gauge invariant operator as follows,

$$M_1 = \left(\not{q}\not{\varepsilon} - \not{\varepsilon}\not{q}\right)/2 \tag{A.14}$$
$$M_2 = p_{p_{\rm tar}} \cdot \varepsilon - q \cdot p_{p_{\rm tar}} q \cdot \varepsilon / q^2 \tag{A.15}$$
$$M_3 = p_{p_{\rm scat}} \cdot \varepsilon - q \cdot p_{p_{\rm star}} q \cdot \varepsilon / q^2 \tag{A.16}$$
$$M_4 = \not{\varepsilon} q \cdot p_{p_{\rm tar}} - \not{q} p_{p_{\rm tar}} \cdot \varepsilon \tag{A.17}$$
$$M_5 = \not{\varepsilon} q \cdot p_{p_{\rm scat}} - \not{q} p_{p_{\rm star}} \cdot \varepsilon \tag{A.18}$$
$$M_6 = \not{q} q \cdot \varepsilon - \not{\varepsilon} q^2, \tag{A.19}$$

and ε_μ is the polarization vector of the virtual photon. The scalar amplitude A_j in this notation includes contributions from the Feynmann diagrams of the $\gamma^* + p \to \eta' + p$ reaction. On the other hand, another notation describing the same matrix element as two-component spinor amplitudes, is called Chew, Goldberger, Low, and Nambu (CGLN) amplitudes. It is in the laboratory frame,

$$J^\mu \varepsilon_\mu = \chi^\dagger_{p_{\rm scat}} F \chi_{p_{\rm tar}}, \tag{A.20}$$

where $\chi_{p_{\rm scat}}$ and $\chi_{p_{\rm tar}}$ are Pauli's spinors, and F is

$$\begin{aligned} F = & f_1 \boldsymbol{\sigma} \cdot \boldsymbol{\varepsilon} - i f_2 \boldsymbol{\sigma} \cdot \hat{\boldsymbol{p}}_{\eta'} \boldsymbol{\sigma} \cdot (\hat{\boldsymbol{q}} \times \boldsymbol{\varepsilon}) \\ & + f_3 \boldsymbol{\sigma} \cdot \hat{\boldsymbol{q}} \hat{\boldsymbol{p}}_{\eta'} \cdot \boldsymbol{\varepsilon} + f_4 \boldsymbol{\sigma} \cdot \hat{\boldsymbol{p}}_{\eta'} \hat{\boldsymbol{p}}_{\eta'} \cdot \boldsymbol{\varepsilon} \\ & + f_5 \boldsymbol{\sigma} \cdot \hat{\boldsymbol{q}} \hat{\boldsymbol{q}} \cdot \boldsymbol{\varepsilon} + f_6 \boldsymbol{\sigma} \cdot \hat{\boldsymbol{p}}_{\eta'} \hat{\boldsymbol{q}} \cdot \boldsymbol{\varepsilon}, \end{aligned} \tag{A.21}$$

where $\hat{\boldsymbol{q}} = \boldsymbol{q}/|\boldsymbol{q}|$, $\hat{\boldsymbol{p}}_{\eta'} = \boldsymbol{p}_{\eta'}/|\boldsymbol{p}_{\eta'}|$, $\boldsymbol{\sigma}$ are the Pauli matrices and $\boldsymbol{\varepsilon}$ is the spatial component of the virtual photon polarization vector. Using these CGLN amplitudes f_j, the differential cross section by an unpolarized virtual photon and a proton can be written down for four components,

$$\frac{{\rm d}\sigma_{\gamma^*}}{{\rm d}\Omega^{\rm CM}_{\eta'}} = \frac{{\rm d}\sigma_{\rm T}}{{\rm d}\Omega^{\rm CM}_{\eta'}} + \epsilon \frac{{\rm d}\sigma_{\rm L}}{{\rm d}\Omega^{\rm CM}_{\eta'}} + \sqrt{2\epsilon(1+\epsilon)} \frac{{\rm d}\sigma_{\rm LT}}{{\rm d}\Omega^{\rm CM}_{\eta'}} \cos\phi_{\eta'} + \epsilon \frac{{\rm d}\sigma_{\rm TT}}{{\rm d}\Omega^{\rm CM}_{\eta'}} \cos 2\phi_{\eta'}, \tag{A.22}$$

$$\begin{aligned} \frac{{\rm d}\sigma_{\rm T}}{{\rm d}\Omega^{\rm CM}_{\eta'}} = & C {\rm Re} \Big\{ |f_1|^2 + |f_2|^2 - 2 f_1 f_2^* \cos\theta_{\eta'} \\ & + \sin^2\theta_{\eta'} \left[\frac{1}{2} \left(|f_3|^2 + |f_4|^2 \right) + f_1 f_4^* \right] + f_2 f_3^* \cos\theta_{\eta'} \Big\} \end{aligned} \tag{A.23}$$

$$\frac{{\rm d}\sigma_{\rm L}}{{\rm d}\Omega^{\rm CM}_{\eta'}} = \frac{Q^2}{\omega^2} C {\rm Re} \left\{ \left| \tilde{f}_5 \right|^2 + \left| \tilde{f}_6 \right|^2 + 2 \tilde{f}_5 \tilde{f}_6{}^* \cos\theta_{\eta'} \right\} \tag{A.24}$$

$$\begin{aligned} \frac{{\rm d}\sigma_{\rm LT}}{{\rm d}\Omega^{\rm CM}_{\eta'}} = & \sqrt{\frac{Q^2}{\omega^2}} C {\rm Re} \Big\{ (f_1 + f_4) \tilde{f}_6{}^* + (f_2 + f_3) \tilde{f}_5{}^* \\ & + \left(f_3 \tilde{f}_6{}^* + f_4 \tilde{f}_5{}^* \right) \cos\theta_{\eta'} \Big\} \sin\theta_{\eta'}, \end{aligned} \tag{A.25}$$

$$\frac{{\rm d}\sigma_{\rm TT}}{{\rm d}\Omega^{\rm CM}_{\eta'}} = C {\rm Re} \left\{ \frac{1}{2} \left(\left| \tilde{f}_5 \right|^2 + \left| \tilde{f}_5 \right|^2 \right) + f_1 f_4^* + f_2 f_3^* + f_4 f_3^* \cos\theta_{\eta'} \right\} \sin^2\theta_{\eta'} \tag{A.26}$$

where the definitions of $\tilde{f}_{5,6}$ are,

$$\tilde{f}_5 = f_1 + f_3 \cos\theta_{\eta'} + f_5 \tag{A.27}$$
$$\tilde{f}_6 = f_4 \cos\theta_{\eta'} + f_6, \tag{A.28}$$

and the normalization factor C is given as,

$$C = (\hbar c)^2 \frac{\alpha}{4\pi} \frac{m_p \left|\boldsymbol{p}_{\eta'}\right|}{|\boldsymbol{q}|\, W}. \tag{A.29}$$

The W is the total energy in the CM frame. The particular contributions of $\frac{\mathrm{d}\sigma_{\mathrm{T}}}{\mathrm{d}\Omega^{\mathrm{CM}}_{\eta'}}$, $\frac{\mathrm{d}\sigma_{\mathrm{L}}}{\mathrm{d}\Omega^{\mathrm{CM}}_{\eta'}}$, $\frac{\mathrm{d}\sigma_{\mathrm{LT}}}{\mathrm{d}\Omega^{\mathrm{CM}}_{\eta'}}$, and $\frac{\mathrm{d}\sigma_{\mathrm{TT}}}{\mathrm{d}\Omega^{\mathrm{CM}}_{\eta'}}$ correspond to the transverse, longitudinal, transverse-longitudinal interference and transverse-transverse interference modes of the virtual photon [60].

Further, the correspondence between the CGLN amplitudes f_j and the scalar amplitude A_j is expressed as,

$$f_1 = N^* \left[-\left(W - m_p\right) A_1 + q \cdot p_{p_{\mathrm{tar}}} A_4 + q \cdot p_{p_{\mathrm{scat}}} A_5 - q^2 A_6 \right] \tag{A.30}$$

$$\begin{aligned} f_2 = N^* & \frac{|\boldsymbol{q}|\left|\boldsymbol{p}_{\eta'}\right|}{\left(E^*_{p_{\mathrm{scat}}} + m_p\right)\left(E_{p_{\mathrm{tar}}} + m_p\right)} \left[\left(W + m_p\right) A_1 \right. \\ & \left. + q \cdot p_{p_{\mathrm{tar}}} A_4 + q \cdot p_{p_{\mathrm{scat}}} A_5 - q^2 A_6 \right] \end{aligned} \tag{A.31}$$

$$f_3 = N^* \frac{|\boldsymbol{q}|\left|\boldsymbol{p}_{\eta'}\right|}{E_{p_{\mathrm{tar}}} + m_p} \left[A_3 + \left(W + m_p\right) A_5\right] \tag{A.32}$$

$$f_4 = N^* \frac{\left|\boldsymbol{p}_{\eta'}\right|^2}{E_{p_{\eta'}} + m_{\eta'}} \left[A_3 - \left(W - m_p\right) A_5\right] \tag{A.33}$$

$$\begin{aligned} f_5 = N^* & \frac{\left|\boldsymbol{p}_{\eta'}\right|^2}{E^*_{p_{\mathrm{scat}}} + m_p} \left\{ A_1 - \frac{1}{q^2} \left[\left(q^2 - q \cdot p_{p_{\mathrm{tar}}}\right) A_2 + q \cdot p_{p_{\mathrm{scat}}} A_3\right] \right. \\ & \left. - \left(W + m_p\right)\left(A_4 + A_6\right)\right\} \end{aligned} \tag{A.34}$$

$$\begin{aligned} f_6 = N^* & \frac{E^*_\gamma\, |q|\, \left|\boldsymbol{p}_{\eta'}\right|}{\left(E^*_{p_{\mathrm{scat}}} + m_p\right)\left(E^*_{p_{\mathrm{tar}}} + m_p\right)} \left\{ A_1 - m_p A_4 \right. \\ & + \frac{q \cdot p_{p_{\mathrm{scat}}}}{E^*_\gamma} A_5 + \frac{\left(E^*_{p_{\mathrm{scat}}} + m_p\right)}{E^*_\gamma q^2} \left[\left(q^2 - q \cdot p_{p_{\mathrm{tar}}}\right) A_2 + q \cdot p_{p_{\mathrm{scat}}} A_3\right] \\ & \left. - \left(W - m_p\right) A_6 \right\}, \end{aligned} \tag{A.35}$$

where $E^*_{p_{\mathrm{tar}}}$, $E^*_{p_{\mathrm{scat}}}$, $E^*_{\eta'}$ and E^*_γ are the c.m. energies of the target proton, scattered proton, η' meson and photon, respectively. The normalization factor N^* is

$$N^* = \sqrt{\frac{\left(E^*_{p_{\mathrm{scat}}} + m_p\right)\left(E^*_{p_{\mathrm{tar}}} + m_p\right)}{4 m_p^2}}. \tag{A.36}$$

The invariant amplitude is decomposed into s, t, and u-channels according to the Feynman rules, as shown in Fig. A.1. The calculations adopted in the present thesis consider only first-order perturbations, known as tree-level. The author presents the expressions for the invariant amplitude corresponding to each diagram as follows.

- **Born s-channel:** In the case called Born terms, the ground state appears as the intermediate state. The invariant amplitude in s-channel is described by two factors: the electromagnetic vertex function V^{EM}_μ, which is given by the γNN coupling, and the strong vertex function V_S, which is given by the $\eta' NN$ coupling.

$$V^{\mathrm{EM}}_\mu = F_1\left(k^2\right)\gamma_\mu + \frac{1 - F_1\left(k^2\right)}{k^2} k_\mu \gamma \cdot k + i \frac{F_2\left(k^2\right)}{2 m_p} \sigma_{\mu\nu} k^\nu \tag{A.37}$$

$$V_{\mathrm{S}} = i g_{\eta' NN} \gamma_5. \tag{A.38}$$

Here, $F_1\left(k^2\right)$ and $F_2\left(k^2\right)$ are the standard Dirac/Pauli electromagnetic form factors, respectivelly, where $F_1\left(0\right) = 0$ and $F_2\left(0\right) = \kappa_p$, where κ_p is the anomalous magnetic moment of the proton. Additionally, $g_{\eta' NN}$ is the coupling constant at the strong vertex and is one of the parameters determined by fitting. Note that the momentum of the photon has been changed from q to k. The invariant amplitude is expressed as:

$$M_{\mathrm{Bs}} = \bar{u}\left(p_{p_{\mathrm{scat}}}\right) V_{\mathrm{S}} \frac{\not{p}_{p_{\mathrm{tar}}} + \not{k}_{\gamma} + m_p}{s - m_p^2} V_{\mu}^{\mathrm{EM}} \varepsilon^{\mu} u\left(p_{p_{\mathrm{tar}}}\right) \tag{A.39}$$

$$= \bar{u}\left(p_{p_{\mathrm{scat}}}\right) \gamma_5 \left[A_1 M_1 + A_2 M_2 + A_4 M_4 + A_6 M_6 + g_{\eta' NN} \frac{k \cdot \varepsilon}{k^2} \right] u\left(p_{p_{tar}}\right). \tag{A.40}$$

(See also eq. (A.13) – (A.18) for the expression of the hadronic matrix elements.) The final term in the brackets in the eq. (A.40) is the gauge-invariance breaking term. The amplitude determined by fitting to the photoproduction database corresponds to the scalar amplitudes,

$$A_1 = \frac{g_{\eta' NN}}{s - m_p^2} \left(F_1\left(k^2\right) + F_2\left(k^2\right) \right) \tag{A.41}$$

$$A_2 = 2 \frac{g_{\eta' NN}}{s - m_p^2} F_1\left(k^2\right) \tag{A.42}$$

$$A_4 = 2 \frac{g_{\eta' NN}}{s - m_p^2} \frac{F_2\left(k^2\right)}{m_p} = -2A_6. \tag{A.43}$$

- **Born t-channel:** There is no contribution from the Born t-channel term since the electric charge of η' is zero. However, the coupling via the non-Born t-channel involving the ρ^0 and ω mesons contributes, as the decays $\eta' \to \rho^0 + \gamma$ and $\eta' \to \omega + \gamma$ are possible (observed). According to the latest PDG, the respective branching ratios are 29.5 % and 2.52% [9].
- **Born u-channel:** In the Born u-channel, both of the electromagnetic γNN vertex factor V_{μ}^{EM} and the strong vertex factor V_{S} has same forms as that for the Born s-channel. Using these, the invariant amplitude is expressed as:

$$M_{\mathrm{Bu}} = \bar{u}\left(p_{p_{\mathrm{scat}}}\right) V_{\mu}^{\mathrm{EM}} \frac{\not{p}_{p_{\mathrm{scat}}} - \not{k}_{\gamma} + m_p}{u - m_p^2} V_{\mathrm{S}} \varepsilon^{\mu} u\left(p_{p_{\mathrm{tar}}}\right) \tag{A.44}$$

$$= \bar{u}\left(p_{p_{\mathrm{scat}}}\right) \gamma_5 \left[A_1 M_1 + A_3 M_3 + A_5 M_5 + A_6 M_6 - g_{\eta' pp} \frac{k \cdot \varepsilon}{k^2} \right] u\left(p_{p_{tar}}\right). \tag{A.45}$$

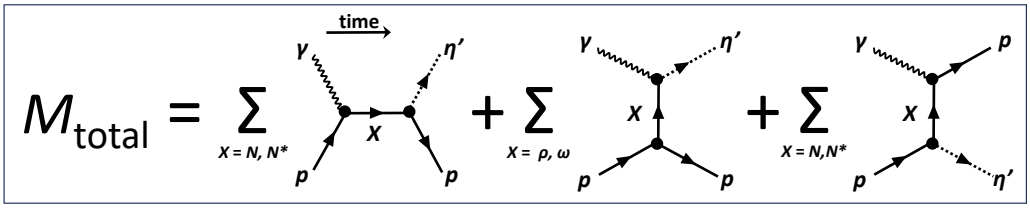

Fig. A.1: The total amplitude is decomposed by s, t and u-channels (same as Fig. 1.6). The ground or excited states of hadrons are exchanged in the intermediate states.

The last term in the brackets in eq. (A.45) breaks gauge invariance and has the opposite sign than the gauge-invariance breaking term in the s-channel in eq. (A.40). Therefore, the these terms the s- and u-channels cancel each other out, preserving overall gauge invariance. The correspondence with the scalar amplitudes, using $g_{\eta' NN}$ is:

$$A_1 = \frac{g_{\eta' NN}}{u - m_p^2} \left(F_1\left(k^2\right) + F_2\left(k^2\right) \right) \tag{A.46}$$

$$A_2 = 2\frac{g_{\eta' NN}}{u - m_p^2} F_1\left(k^2\right) \tag{A.47}$$

$$A_5 = 2\frac{g_{\eta' NN}}{u - m_p^2} \frac{F_2\left(k^2\right)}{m_p} = 2A_6. \tag{A.48}$$

- **Non-Born s-channel with $N^*\left(\frac{1}{2}^{\pm}\right)$ exchange:** The amplitude for the reaction involving the exchange of an N^* resonance with spin $\frac{1}{2}^*$ in the s-channel is expressed as:

$$M_{\mathrm{NBs}}^{N^*(1/2)} = i\bar{u}\left(p_{p_{\mathrm{scat}}}\right) g_{\eta' NN^*}\gamma_5\Gamma \frac{\not{p}_{p_{\mathrm{tar}}} + \not{k}_\gamma + m_R}{s - m_R^2 + i m_R\Gamma_R} \frac{\mu_{pR}}{m_p + m_R} \sigma^{\mu\nu} k_\nu \Gamma \varepsilon_\mu u\left(p_{p_{\mathrm{tar}}}\right) \tag{A.49}$$

where, μ_{pR} gives the electromagnetic transition coupling in the vertex $p + \gamma^* \to N^*$. It is divided by the mass factor $m_p + m_R$ for a convinience. In reactions with resonances, the expression changes depending on the intrinsic parity of the particle; in the above equation, the factor denoted by Γ is defined as:

$$\Gamma = \begin{cases} 1 & (P = +1) \\ \gamma_5 & (P = -1)\,. \end{cases} \tag{A.50}$$

It is worth noting that the coupling constant $g_{\eta' NN^*}$ is a parameter determined by fitting to the photoproduction database. The scalar amplitudes are:

$$A_1 = \frac{g_{\eta' NN^*}}{s - m_R^2 + i m_R\Gamma_R} \frac{m_R \pm m_p}{m_R + m_p} \mu_{pR} \tag{A.51}$$

$$A_4 = \pm\frac{g_{\eta' NN^*}}{s - m_R^2 + i m_R\Gamma_R} \frac{2\mu_{pR}}{m_R + m_p} \tag{A.52}$$

$$A_6 = -\frac{1}{2} A_4, \tag{A.53}$$

where, the upper (lower) sign corresponds to positive (negative) parity of the resonance.

- **Non-Born s-channel with $N^*\left(\frac{3}{2}^{\pm}\right)$ exchange:** The exchange of a resonance with spin $\frac{3}{2}$ is more complicated. Its amplitude is given by:

$$\begin{aligned} M_{\mathrm{NBs}}^{N^*(3/2)} = \bar{u}\left(p_{p_{\mathrm{scat}}}\right) \Gamma \frac{if}{m_R m_{\eta'}} \epsilon_{\mu\nu\lambda\rho}\gamma_5\gamma^\lambda q^\mu p_{\eta'}^\rho \frac{\not{q} + m_R}{s - m_R^2 + i m_R\Gamma_R} \\ \times \left(g^{\nu\beta} - \frac{1}{3}\gamma^\nu\gamma^\beta \right) \frac{1}{m_R\left(m_R + m_p\right)} \left(g_1 q^\alpha F_{\alpha\beta} \right. \\ \left. + g_2 \not{q} F_{\beta\alpha}\gamma^\alpha - g_2\gamma_\beta q^\alpha F_{\alpha\tau}\gamma^\tau \right) \Gamma\gamma_5 u\left(p_{p_{\mathrm{tar}}}\right), \end{aligned} \tag{A.54}$$

where, g_1 and g_2 are the electromagnetic coupling constants, and f is the strong coupling constant. In this equation, q inplies the momentum of intermediate particle, *i.e.* of N^*,

and $q = k_\gamma + p_{\rm tar}$. Also, $g_{\nu\beta}$ is the metric tensor with zero non diagonal elements and diagonal ones are $(+1,-1,-1,-1)$. $F_{\alpha\beta}$ is the anti symmetric electromagnetic tensor,

$$F_{\alpha\beta} = k_\alpha \varepsilon_\beta - \varepsilon_\alpha k_\alpha, \tag{A.55}$$

where, k_α and ε_β is the photon momentum and polarization vector, respectively. After casting into eq. (A.13), the scalar amplitudes are expressed as:

$$\begin{aligned}
A'_1 &= -\frac{G_1}{3}\left(q\cdot p_{p_{\rm scat}} \pm m_R m_p\right) q\cdot k + \frac{G_2}{3}\left(2sq\cdot p_{p_{\rm scat}} - 3sk\cdot p_{p_{\rm scat}} + 2sm_p^2\right. \\
&\quad \left. \mp m_R m_p q\cdot k \pm 2sm_R m_p \pm 2m_p m_R q\cdot p_{p_{\rm scat}} + 2q\cdot p_{p_{\rm scat}} q\cdot k\right) && \text{(A.56)}\\
A'_2 &= G_1\left[sk\cdot p_{p_{\rm scat}} \mp m_R m_p k\cdot p_{p_{\rm scat}} - \frac{1}{3}q\cdot p_{p_{\rm scat}} k^2 \mp m_R m_p k^2\right] \\
&\quad + G_2\left[-2sk\cdot p_{p_{\rm scat}} \mp \frac{1}{3}m_p m_R k^2 + \frac{2}{3}k^2 q\cdot p_{p_{\rm scat}}\right] && \text{(A.57)}\\
A'_3 &= G_1\left(\pm m_R mp - s\right) q\cdot k + G_2\left(2q\cdot k - k^2\right) s && \text{(A.58)}\\
A'_4 &= G_1\left[-\frac{1}{3}sm_p + \frac{1}{3}\left(m_p^2 m_R\right) q\cdot p_{p_{\rm scat}} \pm \frac{1}{3}m_p^2 m_R \pm m_R q\cdot p_{p_{\rm scat}}\right] \\
&\quad - G_2\left[-sm_p \mp \frac{1}{3}m_p^2 m_R + \frac{2}{3}m_p q\cdot p_{p_{\rm scat}}\right] && \text{(A.59)}\\
A'_5 &= \mp G_1 m_R q\cdot k + G_2\left(\pm m_R + m_p\right) s && \text{(A.60)}\\
A'_6 &= G_1\left[\mp\frac{1}{3}m_p^2 m_R + \mp m_R k\cdot p_{p_{\rm scat}} + \frac{1}{3}m_p s - \frac{1}{3}q\cdot p_{p_{\rm scat}}\left(m_p \mp m_R\right)\right] \\
&\quad + G_2\left[-\frac{1}{3}m_p s \mp \frac{1}{3}m_p^2 m_R + \frac{2}{3}q\cdot p_{p_{\rm scat}}\left(m_p \pm m_R\right)\right], && \text{(A.61)}
\end{aligned}$$

where, the relation between A_j and $A'_j, j = 1,\cdots,6$ is given by:

$$A_j = \frac{1}{s - m_R^2 + i m_R \Gamma_R} A'_j. \tag{A.62}$$

Parameters G_1 and G_2 are the product of the electromagnetic coupling constant and the strong coupling constant as given in eq. (4.8). The upper (lower) sign corresponds to positive (negative) parity of the resonance.

- **Non-Born s-channel with $N^*\left(\frac{5}{2}^{\pm}\right)$ exchange:** The amplitude is expressed as:

$$\begin{aligned}
M_{\rm NBs}^{N^*(5/2^{\pm})} &= -\frac{f}{4m_{\eta'}}\bar{u}\left(p_{p_{\rm scat}}\right)\gamma_5\Gamma q^2 p_{\eta'}^{\mu} p_{\eta'}^{\nu}\frac{\not{q} + m_R}{s - m_R^2 + i m_R\Gamma_R} \\
&\quad \times P_{\mu\nu,\lambda\rho}\left(q\right) q^2 p_{p_{\rm scat}}^{\lambda}\left[\frac{g_1}{\left(2m_p\right)^4}\gamma_\alpha F^{\alpha\rho} + \frac{g_2}{\left(2m_p\right)^5}p_\alpha F^{\alpha\rho}\right]\Gamma u\left(p_{p_{\rm tar}}\right) && \text{(A.63)}
\end{aligned}$$

In this formula, $P_{\mu\nu,\lambda\rho}$ is the projection operator for the spin-$\frac{5}{2}$ particles (also see eq. (A1)

in ref. [95]). The correspondence with the scalar amplitudes is:

$$
\begin{aligned}
A'_1 = G_1 \Big\{ & \mp Q_{p_{p_{\rm scat}} p_{p_{\rm tar}}} Q_{k p_{p_{\rm scat}}} \pm \frac{1}{5} Q_{p_{p_{\rm scat}} p_{p_{\rm scat}}} Q_{k p_{p_{\rm tar}}} - \frac{1}{5} Q_{k p_{p_{\rm scat}}} \left(B \cdot q \cdot p_{p_{\rm tar}} \right. \\
& \left. + \; C m_p \right) + \frac{1}{5} Q_{p_{p_{\rm scat}} p} \left[2Cmp + (2s - q \cdot k) B \right] \Big\} - \frac{G_2}{5} Q_{p_{p_{\rm scat}} p_{p_{\rm tar}}} C k \cdot p_{p_{\rm tar}}, \qquad \text{(A.64)} \\
A'_2 = G_1 \Big\{ & \pm Q_{p_{p_{\rm scat}} p_{p_{\rm tar}}} \left(k^2 q \cdot p_{p_{\rm scat}} - 2sk \cdot p_{p_{\rm scat}} \right) \pm \frac{1}{5} Q_{p_{p_{\rm scat}} p_{p_{\rm scat}}} k^2 \left(q \cdot p_{p_{\rm tar}} + s \right) \\
& - \frac{1}{5} \Big[\mp 2 q \cdot p_{p_{\rm scat}} k \cdot p_{p_{\rm scat}} q \cdot k s \pm k^2 \left(q \cdot p_{p_{\rm scat}} \right)^2 \left(q \cdot k + s \right) \\
& + 2 s m_R m_p k \cdot p_{p_{\rm scat}} q \cdot k - m_R m_p k^2 q \cdot p_{p_{\rm scat}} \left(q \cdot k + s \right) + C m_p k^2 q \cdot p_{p_{\rm scat}} \Big] \\
& - \frac{1}{5} Q_{p_{p_{\rm scat}} p_{p_{\rm tar}}} k^2 B \Big\} + G_2 \left\{ (m_R \pm m_p) Q_{p_{p_{\rm scat}} p_{p_{\rm tar}}} D \right. \\
& - \frac{1}{5} (m_R \pm m_p) k^2 q \cdot p_{p_{\rm tar}} Q_{p_{p_{\rm scat}} p_{p_{\rm scat}}} \\
& + \frac{1}{5} \left(sk \cdot p_{p_{\rm scat}} - k^2 q \cdot p_{p_{\rm scat}} \right) \left(B m_p q \cdot k - C k \cdot p_{p_{\rm tar}} \right) \\
& \left. - \frac{1}{5} Q_{p_{p_{\rm scat}} p_{p_{\rm tar}}} B m_p k^2 \right\}, \qquad \text{(A.65)} \\
A'_3 = G_1 \Big\{ & \pm s Q_{p_{p_{\rm scat}} p_{p_{\rm tar}}} \left(2k \cdot p_{p_{\rm tar}} + k^2 \right) - \frac{1}{5} \left[\left(2k \cdot p_{p_{\rm tar}} q \cdot k - k^2 q \cdot p_{p_{\rm scat}} \right) B \right. \\
& \left. - m_p k^2 C \right] \Big\} + G_2 \left\{ s \left(m_R \pm m_p \right) k \cdot p_{p_{\rm tar}} Q_{p_{p_{\rm scat}} p_{p_{\rm tar}}} \right. \\
& \left. - \frac{1}{5} s k \cdot p_{p_{\rm tar}} \left(B m_p q \cdot k - C k \cdot p_{p_{\rm tar}} \right) \right\}, \qquad \text{(A.66)} \\
A'_4 = G_1 \Big\{ & \frac{1}{5} \left(m_R \mp m_p \right) q \cdot k Q_{p_{p_{\rm scat}} p_{p_{\rm scat}}} - A Q_{p_{p_{\rm scat}} p_{p_{\rm tar}}} + \frac{1}{5} \left\{ q \cdot p_{p_{\rm scat}} \left[B m_p q \cdot k \right. \right. \\
& \left. + C \;\; \left(2k^2 + k \cdot p \right) + 2 s m_R k \cdot p_{p_{\rm scat}} \right] \pm 2k \cdot p_{p_{\rm scat}} s^2 m_p \Big\} \\
& - \frac{1}{5} Q_{p_{p_{\rm scat}} p_{p_{\rm tar}}} \left[m_p \left(m_R m_p \mp 3s \right) + \left(3 m_R \mp m_p \right) q \cdot p_{p_{\rm scat}} \right] \Big\} \\
& + G_2 \Big\{ \pm \frac{1}{5} k^2 q \cdot p Q_{p_{p_{\rm scat}} p_{p_{\rm scat}}} \mp D Q_{p_{p_{\rm scat}} p_{p_{\rm tar}}} + \frac{1}{5} D E \\
& - \frac{1}{5} Q_{p_{p_{\rm scat}} p_{p_{\rm tar}}} \left[m_R m_p \left(k^2 \mp s \right) + q \cdot p_{p_{\rm scat}} \left(m_R m_p \mp k^2 \right) \right. \\
& \left. \pm s \left(q \cdot p_{p_{\rm scat}} - m_p^2 \right) \right] \Big\} \qquad \text{(A.67)} \\
A'_5 = G_1 \Big\{ & s \left(\pm m_R - m_R i \right) Q_{p_{p_{\rm scat}} p_{p_{\rm tar}}} - \frac{1}{5} s \left(B m_p q \cdot k - C k \cdot p_{p_{\rm tar}} \right) \Big\} \\
& + G_2 \Big\{ \pm s k \cdot p_{p_{\rm tar}} Q_{p_{p_{\rm scat}} p_{p_{\rm tar}}} + \frac{1}{5} E s k \cdot p_{p_{\rm tar}} \Big\}, \qquad \text{(A.68)} \\
A'_6 = G_1 \Big\{ & A Q_{p_{p_{\rm scat}} p_{p_{\rm tar}}} - \frac{1}{5} q \cdot p_{p_{\rm tar}} \left(\pm m_p - m_R \right) Q_{p_{p_{\rm scat}} p_{p_{\rm scat}}} \\
& - \frac{1}{5} q \cdot p_{p_{\rm scat}} \left(B m_p q \cdot k C k \cdot p_{p_{\rm tar}} \right) \\
& - \frac{1}{5} Q_{p_{p_{\rm scat}} p_{p_{\rm tar}}} \left[m_p \left(\pm s - m_R m_p \right) + A \right] \Big\} \\
& - G_2 \Big\{ \pm q \cdot p_{p_{\rm tar}} k \cdot p_{p_{\rm scat}} Q_{p_{p_{\rm scat}} p_{p_{\rm tar}}} \pm \frac{1}{5} q \cdot p_{p_{\rm tar}} k \cdot p_{p_{\rm tar}} Q_{p_{p_{\rm scat}} p_{p_{\rm scat}}} \\
& + \frac{1}{5} q \cdot p_{p_{\rm scat}} k \cdot p_{p_{\rm tar}} E + \frac{1}{5} Q_{p_{p_{\rm scat}} p_{p_{\rm tar}}} B k \cdot p_{p_{\rm tar}} \cdot \Big\} \qquad \text{(A.69)}
\end{aligned}
$$

In the equations, A, B, C, D and E are defined as follows:

$$A = q \cdot p_{p_{\rm scat}} \left(\pm m_p - m_R\right), \tag{A.70}$$
$$B = \pm q \cdot p_{p_{\rm scat}} - m_p m_R, \tag{A.71}$$
$$C = \pm s m_p - m_R q \cdot p_{p_{\rm scat}}, \tag{A.72}$$
$$D = k^2 q \cdot p_{p_{\rm scat}} - s k \cdot p_{p_{\rm scat}}, \tag{A.73}$$
$$E = m_p C - q \cdot p_{p_{\rm tar}} B, \tag{A.74}$$

and additionally, the terms $Q_{p_{p_{\rm scat}} p_{p_{\rm tar}}}, Q_{k p_{p_{\rm tar}}}, Q_{p_{p_{\rm scat}} p_{p_{\rm scat}}}$ and $Q_{k p_{p_{\rm tar}}}$ is generally defined by the following equation:

$$Q_{XY} = sX \cdot Y - X \cdot qY \cdot q. \tag{A.75}$$

Similar to the case of $J^P = \frac{3}{2}^{\pm}$, G_1 and G_2 represent the product of the electromagnetic coupling constant and the strong coupling constant, and the upper (lower) sign corresponds to the positive (negative) parity of the resonance.

- **Non-Born t-channel with $\rho\,(770)\,/\omega\,(782)$ exchange:** The theoretical calculation takes into account the exchange of vector mesons $\rho\,(770)$ and $\omega\,(780)$ (both with spin-parity of $J^P = 1^-$). The amplitude is represented as follows:

$$\begin{aligned} M_{\rm NBt}^{\rho/\omega} = {} & i\bar{u}\left(p_{p_{\rm scat}}\right) \frac{g}{m} \epsilon^{\mu\nu\alpha\beta} k_\alpha \left(p_{p_{\rm scat}} - p_{p_{\rm tar}}\right)_\beta \\ & \times \frac{-g_{\nu\sigma} + \left(p_{p_{\rm tar}} - p_{p_{\rm scat}}\right)_\nu \left(p_{p_{\rm tar}} - p_{p_{\rm scat}}\right)_\sigma / m_{\rho/\omega}^2}{t - m_{\rho/\omega}^2 + i m_{\rho/\omega} \Gamma_{\rho/\omega}} \\ & \times \left[f_V \gamma^\sigma + \frac{f_T}{2m_p} \left(\not{p}_{p_{\rm scat}} - \not{p}_{p_{\rm tar}} \right) \gamma^\sigma \right] \varepsilon_\mu u\left(p_{p_{\rm scat}}\right), \end{aligned} \tag{A.76}$$

where, $\frac{g}{m}$ gives the strong coupling constant in the vertex proton-proton-ρ^0 or proton-proton-ω. The correspondence with the scalar amplitude A_j is as follows:

$$A_1 = \frac{2m_p G_V + \frac{G_T t}{(2m_p)}}{t - m_{\rho/\omega}^2 + i m_{\rho/\omega} \Gamma_{\rho/\omega}} \tag{A.77}$$
$$A_2 = \frac{2k \cdot p_{p_{\rm scat}} G_T}{2m_p \left(t - m_{\rho/\omega}^2 + i m_{\rho/\omega} \Gamma_{\rho/\omega} \right)} \tag{A.78}$$
$$A_3 = \frac{-2k \cdot p_{p_{\rm tar}} G_T}{2m_p \left(t - m_{\rho/\omega}^2 + i m_{\rho/\omega} \Gamma_{\rho/\omega} \right)} \tag{A.79}$$
$$A_4 = \frac{G_V}{t - m_{\rho/\omega}^2 + i m_{\rho/\omega} \Gamma_{\rho/\omega}} \tag{A.80}$$
$$A_5 = A_4 \tag{A.81}$$

where, $G_{V,T} = g f_{V,T}/m$. The mass scaling with m is arbitarily taken as 1 GeV.

- **Non-Born u-channel with $N^*\left(\frac{1}{2}^{\pm}\right)$ exchange:** The amplitude with the exchange of an N^* resonance with spin $\frac{1}{2}$ in the u-channel is expressed as:

$$M_{\rm NBu}^{N^*(1/2)} = i\bar{u}\left(p_{p_{\rm scat}}\right) \frac{\mu_{pR}}{2m_p} \sigma^{\mu\nu} k_\nu \Gamma \frac{\not{p}_{p_{\rm scat}} - \not{k}_\gamma + m_R}{u - m_R^2 + i m_R \Gamma_R} g_{\eta' N N^*} \gamma_5 \Gamma \varepsilon_\mu u\left(p_{p_{\rm tar}}\right). \tag{A.82}$$

The factor denoted by Γ is defined in eq. (A.50). The scalar amplitudes are:

$$A_1 = \frac{g_{\eta' NN^*}}{u - m_R^2 + i m_R \Gamma_R} \frac{m_R \pm m_p}{m_R + m_p} \mu_{pR} \tag{A.83}$$

$$A_4 = \pm \frac{g_{\eta' NN^*}}{u - m_R^2 + i m_R \Gamma_R} \frac{2\mu_{pR}}{m_R + m_p} \tag{A.84}$$

$$A_6 = \frac{1}{2} A_4, \tag{A.85}$$

where, the upper (lower) sign corresponds to positive (negative) parity of the resonance.

- **Non-Born u-channel with $N^*\left(\frac{3}{2}^{\pm}\right)$ exchange:** The exchange of a resonance with spin $\frac{3}{2}$ in the $u-$channel is given by:

$$\begin{aligned} M_{\mathrm{NBu}}^{N^*(3/2)} = {} & \bar{u}\left(p_{p_{\mathrm{scat}}}\right) \Gamma \gamma_5 \frac{1}{m_R \left(m_R + m_p\right)} \left[g_1 q^\alpha F_{\alpha\beta} + g_2 \left(\not{q} F_{\beta\alpha} \gamma^\alpha - \gamma_\beta q^\alpha F_{\alpha\rho} \gamma^\rho \right) \right] \\ & \times \frac{\not{q} + m_R}{u - m_R^2 + i m_R \Gamma_R} \left(g^{\beta\nu} - \frac{1}{3} \gamma^\beta \gamma^\nu \right) \\ & \times \Gamma \frac{if}{m_R m_{\eta'}} \epsilon_{\mu\nu\lambda\rho} \gamma_5 \gamma^\lambda q^\mu q_{\eta'}^\rho u\left(p_{p_{\mathrm{tar}}}\right) \end{aligned} \tag{A.86}$$

where, g_1 and g_2 are the electromagnetic coupling constants, and f is the strong coupling constant. The scalar amplitudes are expressed as:

$$\begin{aligned} A_1' = {} & -\frac{1}{3} G_1 q \cdot k \left(\pm m_R m_p + q \cdot p_{p_{\mathrm{tar}}} \right) + \frac{1}{3} G_2 \left[\pm 5 m_R m_p q \cdot k \pm 2 m_R m_p u \right. \\ & \left. \pm m_R m_p q \cdot p_{p_{\mathrm{tar}}} + 2 u q \cdot p_{p_{\mathrm{tar}}} + 2 m_p^2 u + 3 p_{p_{\mathrm{tar}}} \cdot k \right] \end{aligned} \tag{A.87}$$

$$A_2' = G_1 q \cdot k \left(\pm m_R m_p - u \right) + G_2 \left(2 q \cdot k u - u k^2 \mp 4 m_R m_p q \cdot k \right) \tag{A.88}$$

$$\begin{aligned} A_3' = {} & G_1 \left[\frac{1}{3} k^2 \left(\pm m_p m_R + q \cdot p_{p_{\mathrm{tar}}} \right) + p_{p_{\mathrm{tar}}} \cdot k \left(u \mp m_R m p \right) \right] \\ & + G_2 \left[\pm 4 m_R m_p p_{p_{\mathrm{tar}}} \cdot k \mp \frac{5}{3} m_R m_p k^2 \frac{2}{3} q \cdot p_{p_{\mathrm{tar}}} k^2 - 2 p_{p_{\mathrm{tar}}} \cdot k u \right] \end{aligned} \tag{A.89}$$

$$A_4' = \mp G_1 m_R q \cdot k + G_2 \left[\pm 4 m_R q \cdot k + u \left(\pm m_R + m_p \right) \right] \tag{A.90}$$

$$\begin{aligned} A_5' = {} & \frac{1}{3} \left[q \cdot p_{p_{\mathrm{tar}}} \left(\pm m_R - m_p \right) \mp m_R m_p^2 + u m_p + 3 m_R p_{p_{\mathrm{tar}}} \cdot k \right] \\ & G_2 \left[\pm \frac{5}{3} m_R m_p^2 \mp 4 m_R p_{p_{\mathrm{tar}}} \cdot k - \frac{1}{3} u m_p + \frac{2}{3} m_p q \cdot p_{p_{\mathrm{tar}}} \mp \frac{4}{3} m_R q \cdot p_{p_{\mathrm{tar}}} \right] \end{aligned} \tag{A.91}$$

$$\begin{aligned} A_6' = {} & \frac{1}{3} \left[q \cdot p_{p_{\mathrm{tar}}} \left(\pm m_R - m_p \right) \mp m_R m_p^2 + u m_p + 3 m_R p_{p_{\mathrm{tar}}} \cdot k \right] \\ & G_2 \left[\pm \frac{5}{3} m_R m_p^2 \mp 4 m_R p_{p_{\mathrm{tar}}} \cdot k \mp 2 m_R q \cdot p_{p_{\mathrm{tar}}} - u m_p + \frac{2}{3} m_p q \cdot p_{p_{\mathrm{tar}}} \right], \end{aligned} \tag{A.92}$$

where, the relation between A_j and $A_j', j = 1, \cdots, 6$ is given by:

$$A_j = \frac{1}{u - m_R^2 + i m_R \Gamma_R} A_j'. \tag{A.93}$$

Parameters G_1 and G_2 are given in eq. (4.8), and the upper (lower) sign corresponds to positive (negative) parity of the resonance.

It is worth to mention here that the hadron form factor is included in the strong vertex. It is introduced in the same manner as the electromagnetic form factor; it is simply multiplied to

the coupling constant, $G \to FG$, where G is the coupling constant, and F is the hadron form factor. Note here that, with the introduction of the hadron form factor, the gauge noninvariant terms in eq. (A.40) and (A.45) no longer cancel each other, thereby breaking gauge invariance. A remedy to this problem is the introduction of the contact term M_{contact}:

$$M_{\text{contact}} = -g_{\eta' NN}\bar{u}\left(p_{p_{\text{scat}}}\right)\gamma_5\left[\frac{2p^{\mu}_{p_{\text{tar}}} + \not{k}\gamma^{\mu}}{s - m_p^2}\left(\hat{F}_{\text{DW}} - F_s\right)\right.$$
$$\left. + \frac{2p^{\mu}_{p_{\text{scat}}} - \not{k}\gamma^{\mu}}{u - m_p^2}\left(\hat{F}_{\text{DW}} - F_u\right)\right] u\left(p_{p_{\text{scat}}}\right)\varepsilon_{\mu}, \tag{A.94}$$

where, $\hat{F}_{\text{DW}}$ is a notation used by R.M. Davidson and R.Workman [96], represented as:

$$\hat{F}_{\text{DW}} = F_s\left(s\right) + F_u\left(u\right) - F_s\left(s\right)F_u\left(u\right). \tag{A.95}$$

Here, the conditions $F_s\left(s = m_p^2\right) = F_u\left(t = m_{\eta'}^2\right) = 1$ and $\hat{F}_{\text{DW}}\left(s = m_p^2, u\right) = \hat{F}_{\text{DW}}\left(s, u = m_{\eta'}^2\right) = 1$ ensure that the contact term M_{contact}, as represented in eq. (A.95), is prevented from reaching the pole.

Appendix B

Fitting

All the fittings of the missing mass spectra for both count base and cross section base methods are shown, under the assumption of two types of background functional forms.

B.1 Count based missing mass spectrum

B.1.1 Background: polynomial

The fittings of the count based missing mass spectra with a polynomial function as the background are shown in Fig. B.1 to Fig. B.5.

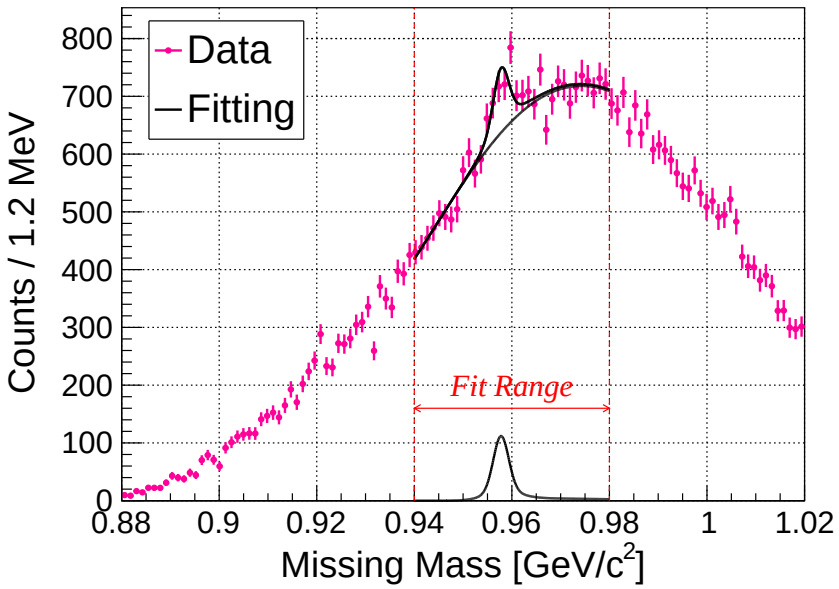

Fig. B.1: Missing mass spectrum (in count) of all data with a fitting using a polynomial function for background (same as Fig. 3.43).

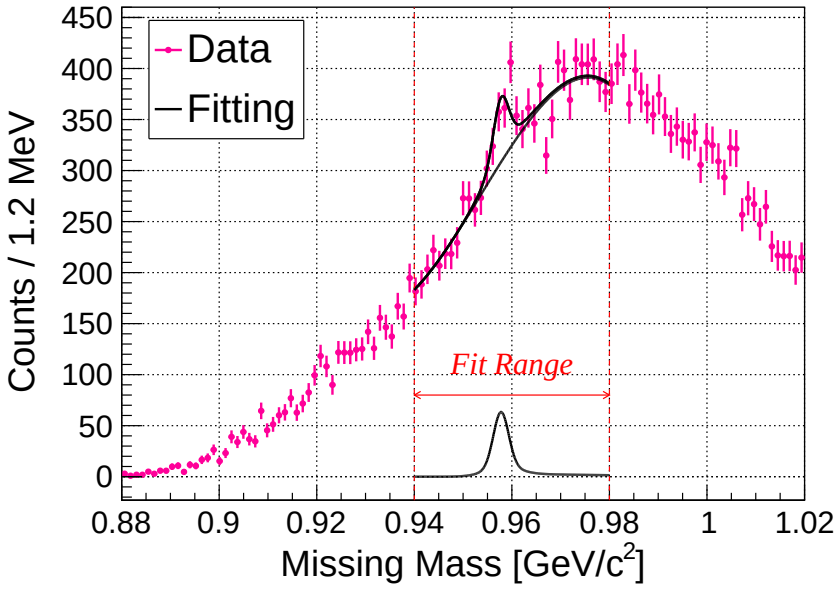

Fig. B.2: Missing mass spectrum (in count) for $Q^2 < (0.47\ \mathrm{GeV}/c)^2$ with a fitting using a polynomial function for background.

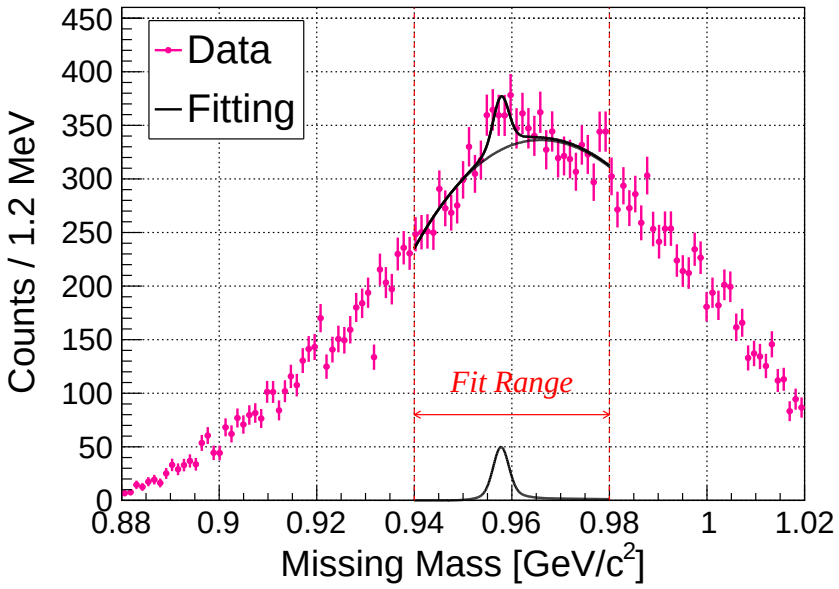

Fig. B.3: Missing mass spectrum (in count) for $Q^2 \geq (0.47\ \mathrm{GeV}/c)^2$ with a fitting using a polynomial function for background.

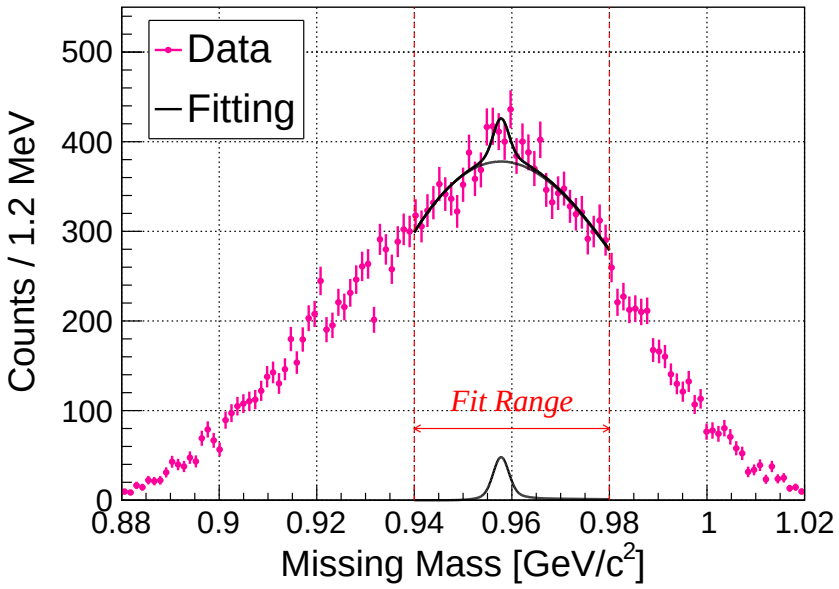

Fig. B.4: Missing mass spectrum (in count) for $W < 2.13$ GeV with a fitting using a polynomial function for background.

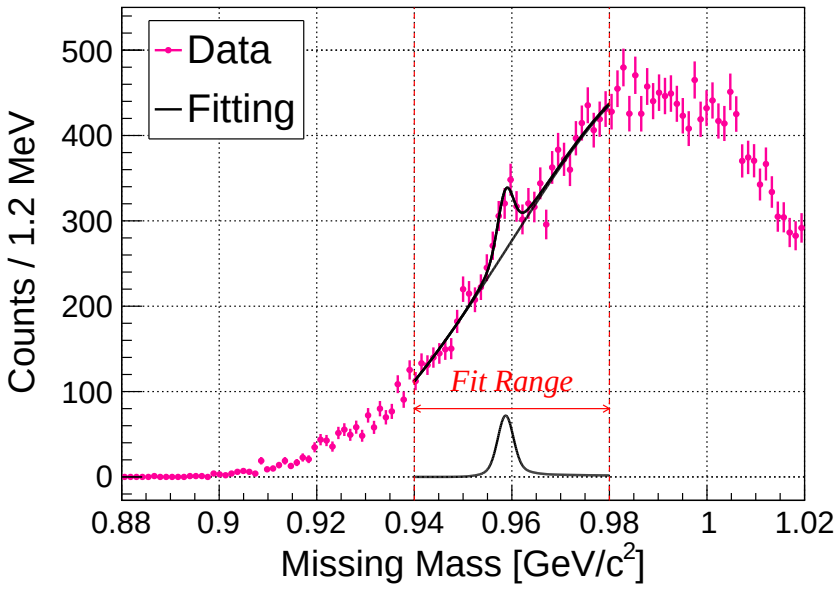

Fig. B.5: Missing mass spectrum (in count) for $W \geq 2.13$ GeV with a fitting using a polynomial function for background.

B.1.2 Background: determined by simulation

The fittings of the count based missing mass spectra with a simulation based function as the background are shown in Fig. B.6 to Fig. B.10.

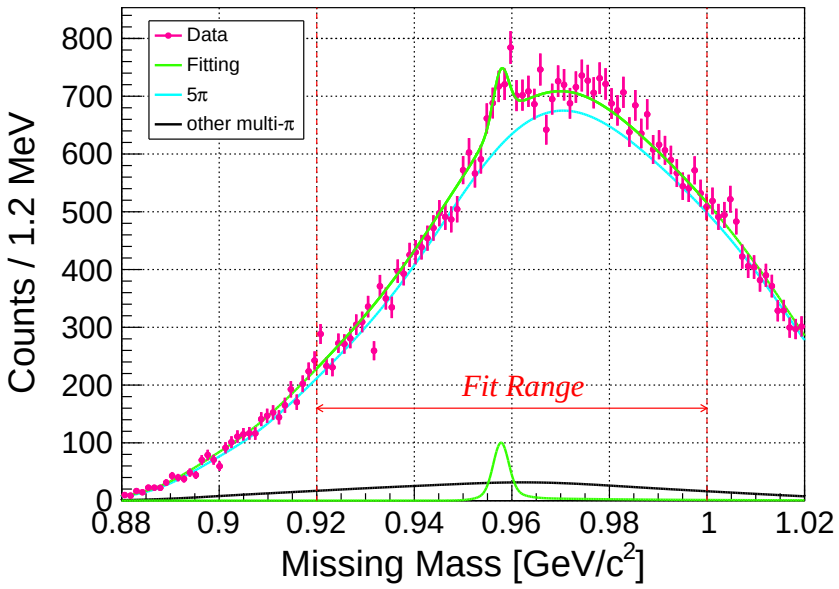

Fig. B.6: Missing mass spectrum (in count) of all data with a fitting using a simulation-based function for background (same as Fig. 3.44).

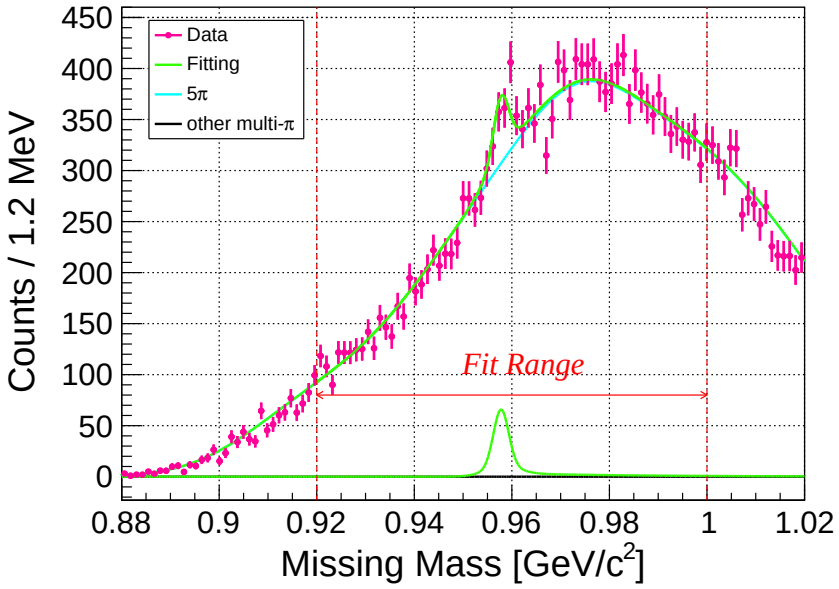

Fig. B.7: Missing mass spectrum (in count) for $Q^2 < (0.47\ \mathrm{GeV}/c)^2$ with a fitting using a simulation-based function for background.

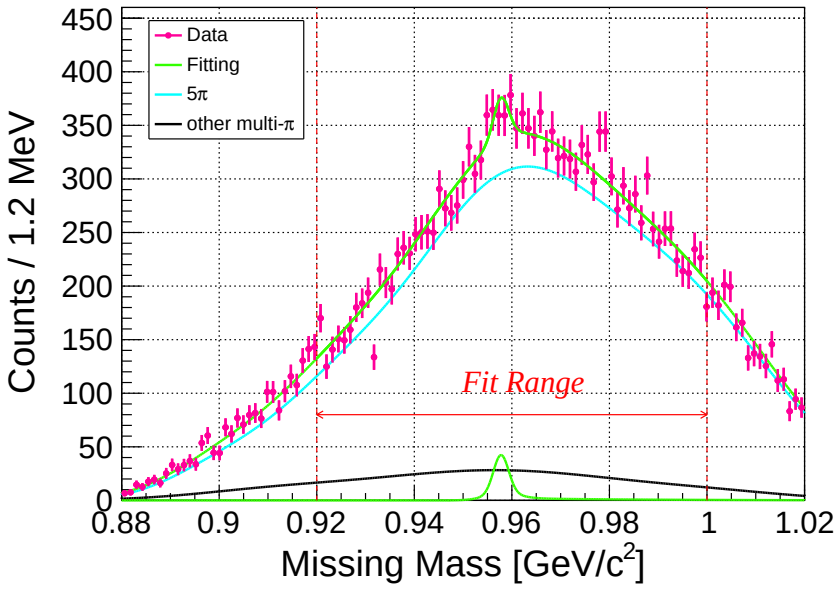

Fig. B.8: Missing mass spectrum (in count) for $Q^2 \geq (0.47\ \mathrm{GeV}/c)^2$ with a fitting using a simulation-based function for background.

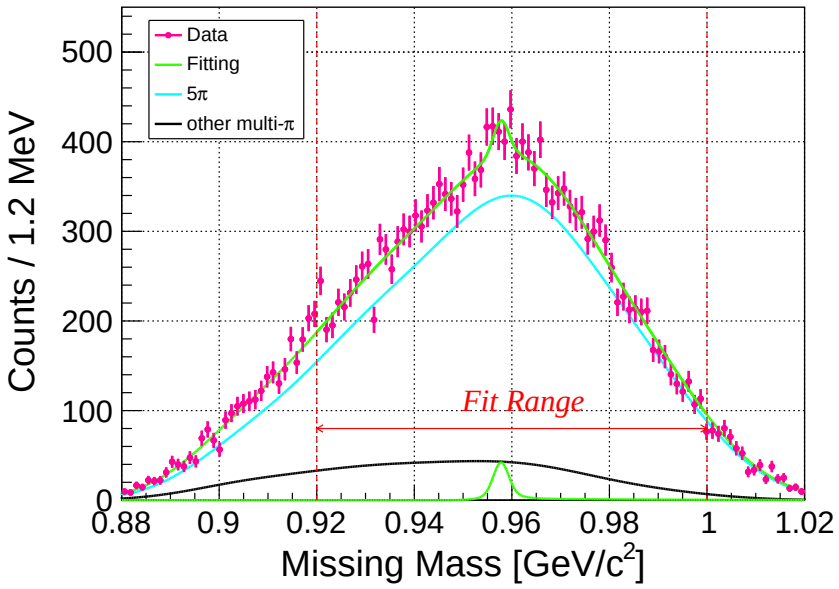

Fig. B.9: Missing mass spectrum (in count) for $W < 2.13$ GeV with a fitting using a simulation-based function for background.

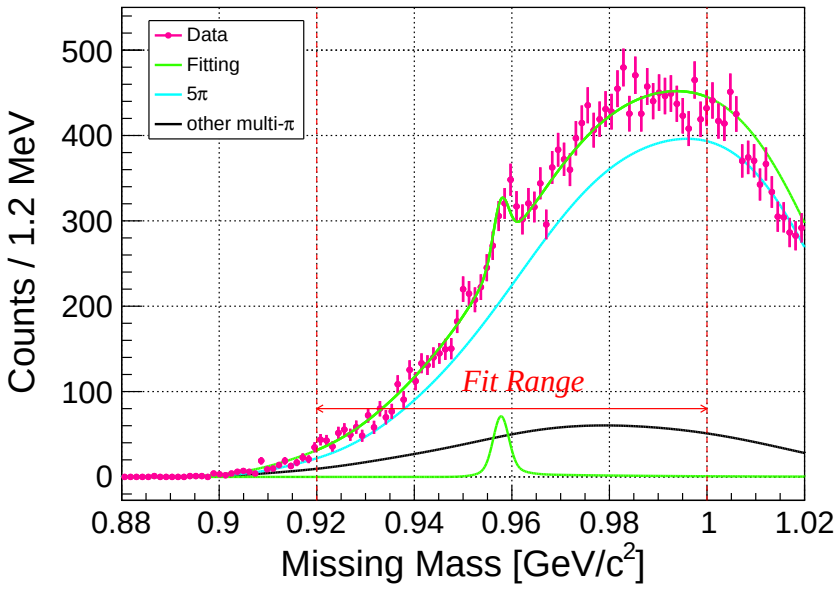

Fig. B.10: Missing mass spectrum (in count) for $W \geq 2.13$ GeV with a fitting using a simulation-based function for background.

B.2 Cross section based missing mass spectrum

B.2.1 Background: polynomial

The fittings of the cross section based missing mass spectra with a polynomial function as the background are shown in Fig. B.11 to Fig. B.15.

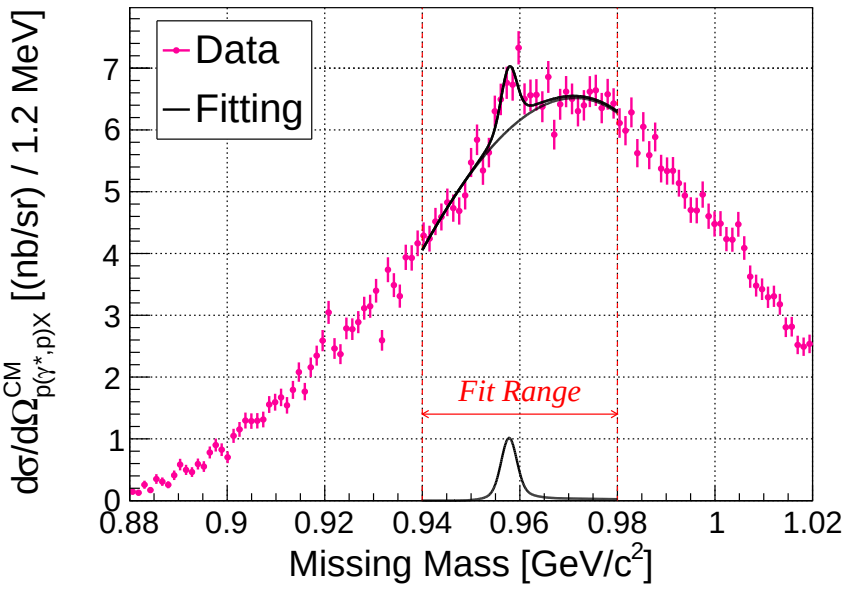

Fig. B.11: Missing mass spectrum (in differential cross section) of all data with a fitting using a polynomial function for background.

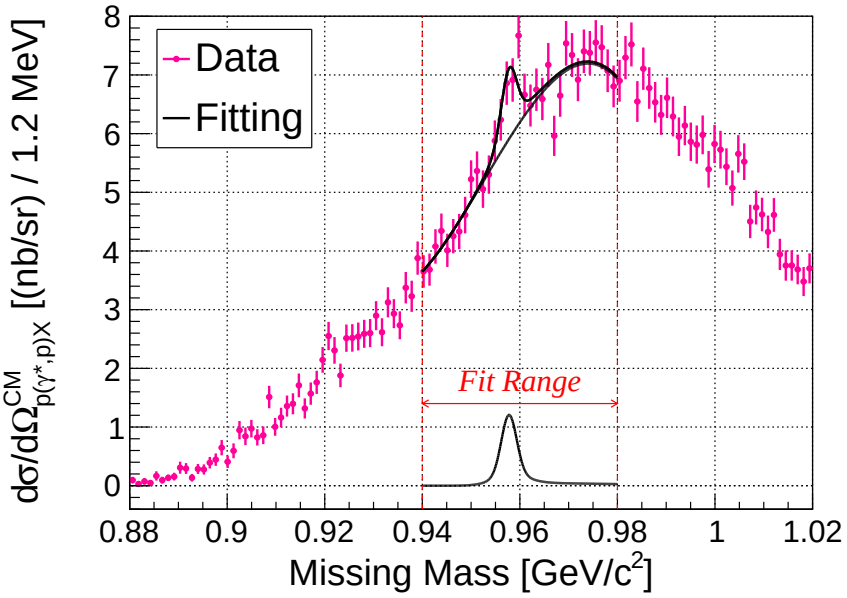

Fig. B.12: Missing mass spectrum (in differential cross section) for $Q^2 < (0.47\ \mathrm{GeV}/c)^2$ with a fitting using a polynomial function for background.

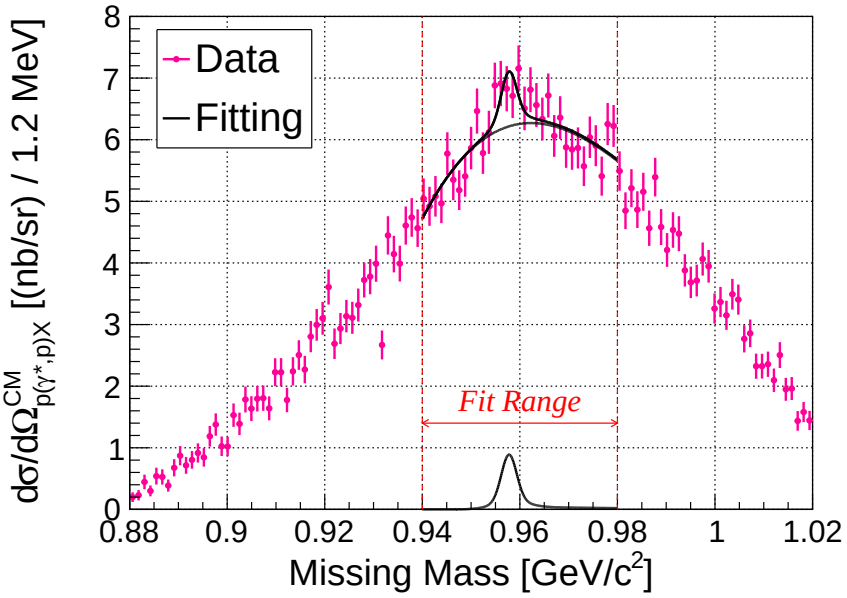

Fig. B.13: Missing mass spectrum (in differential cross section) for $Q^2 \geq (0.47\ \mathrm{GeV}/c)^2$ with a fitting using a polynomial function for background.

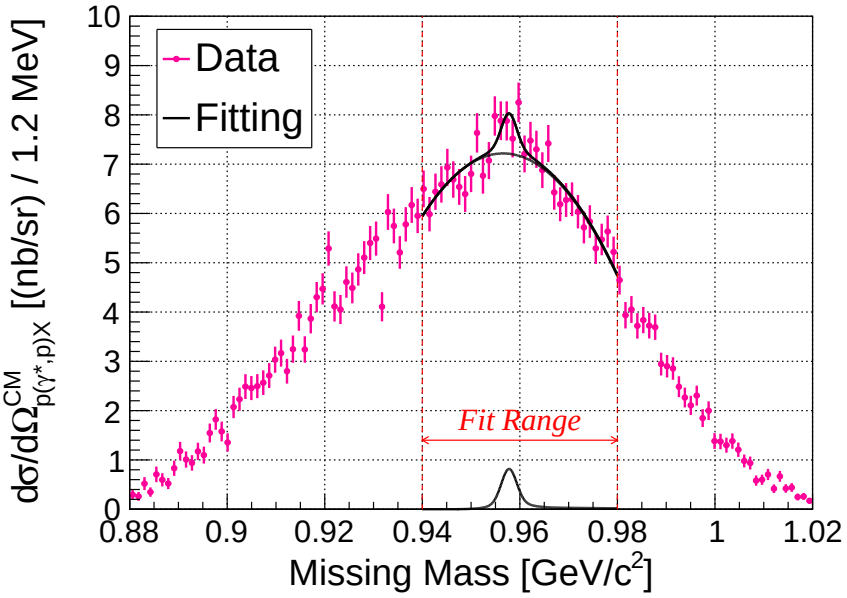

Fig. B.14: Missing mass spectrum (in differential cross section) for $W < 2.13$ GeV with a fitting using a polynomial function for background.

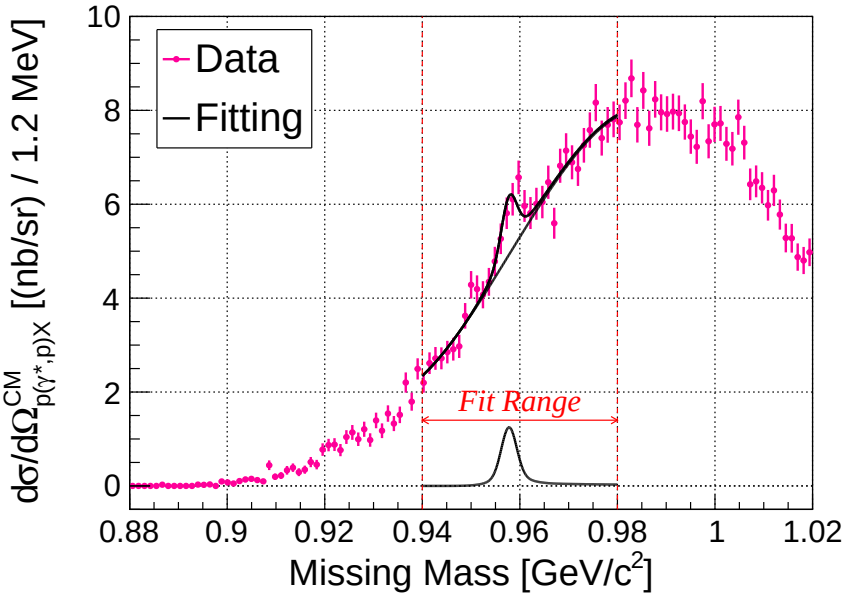

Fig. B.15: Missing mass spectrum (in differential cross section) for $W \geq 2.13$ GeV with a fitting using a polynomial function for background.

B.2.2 Background: determined by simulation, with a free parameter for area

The fittings results of the cross section based missing mass spectra where a simulation based function of multi-pion production is used for the background with the area treated as a free parameter are shown in Fig. B.16 to Fig. B.20.

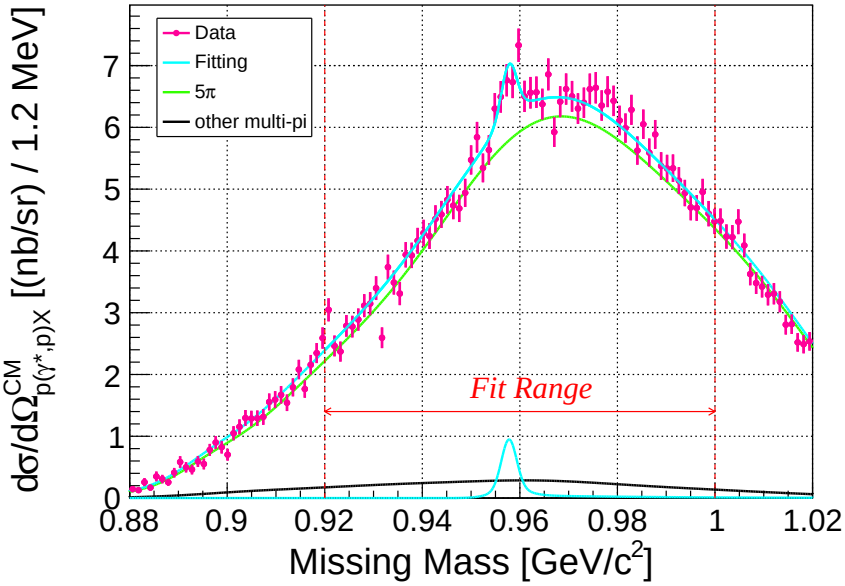

Fig. B.16: Missing mass spectrum (in differential cross section) of all data with a fitting using a simulation-based function for background with the area treated as a free parameter (same as Fig. 3.44).

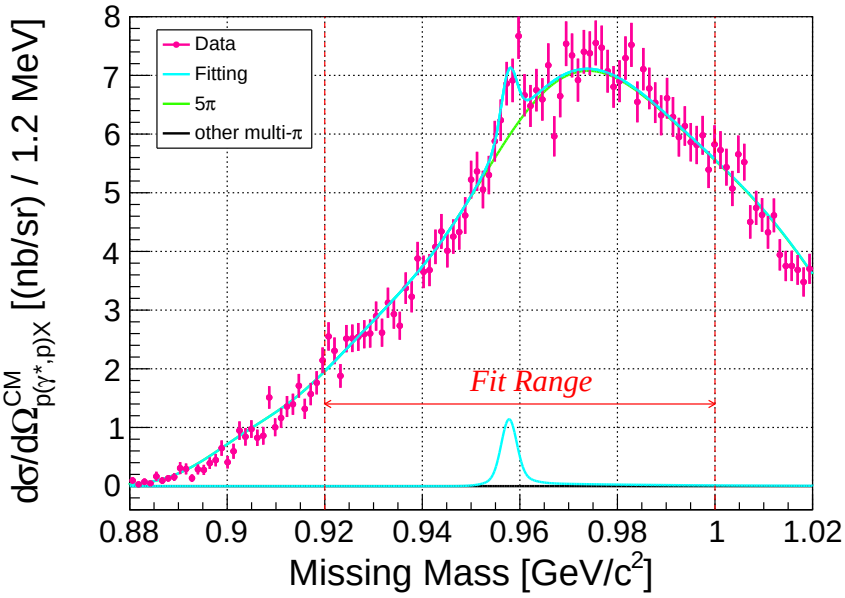

Fig. B.17: Missing mass spectrum (in differential cross section) for $Q^2 < (0.47\ \mathrm{GeV}/c)^2$ with a fitting using a simulation-based function for background with the area treated as a free parameter.

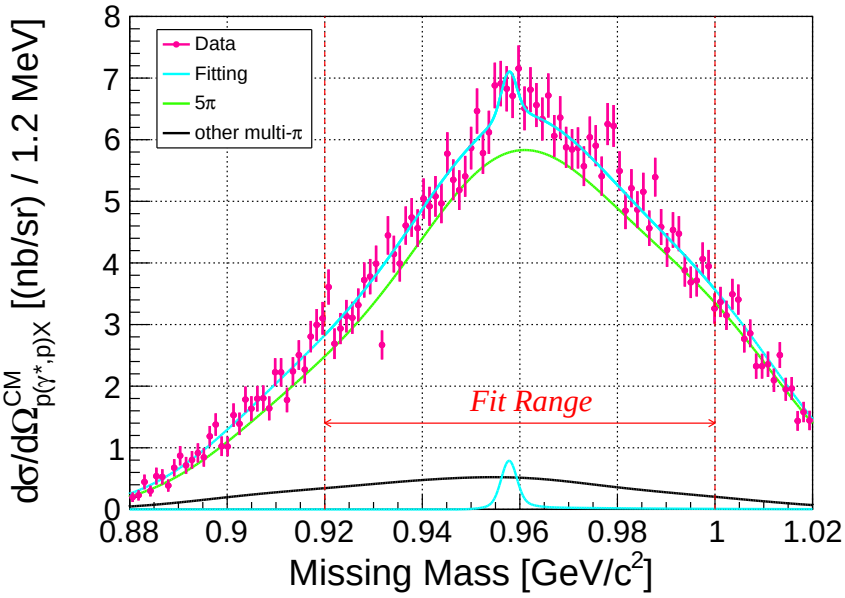

Fig. B.18: Missing mass spectrum (in differential cross section) for $Q^2 \geq (0.47\ \mathrm{GeV}/c)^2$ with a fitting using a simulation-based function for background with the area treated as a free parameter.

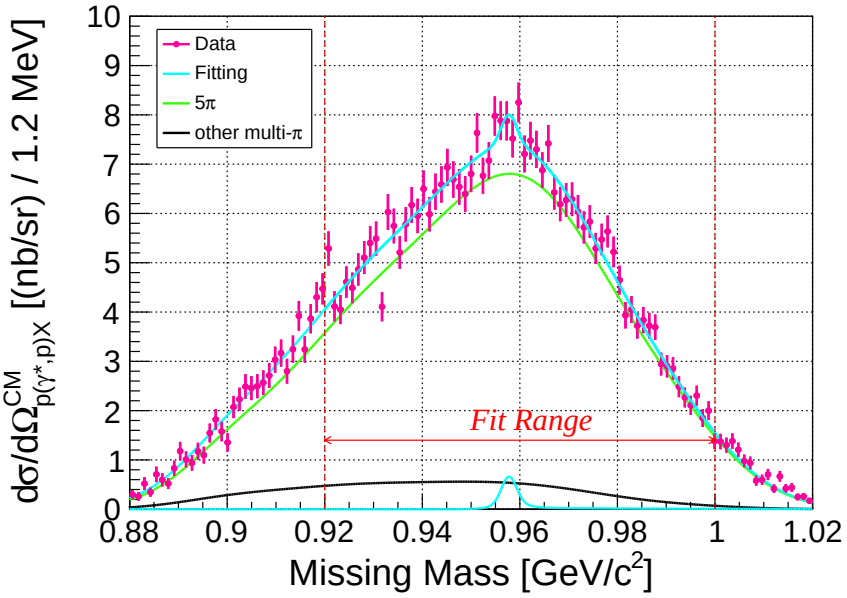

Fig. B.19: Missing mass spectrum (in differential cross section) for $W < 2.13$ GeV with a fitting using a simulation-based function for background with the area treated as a free parameter.

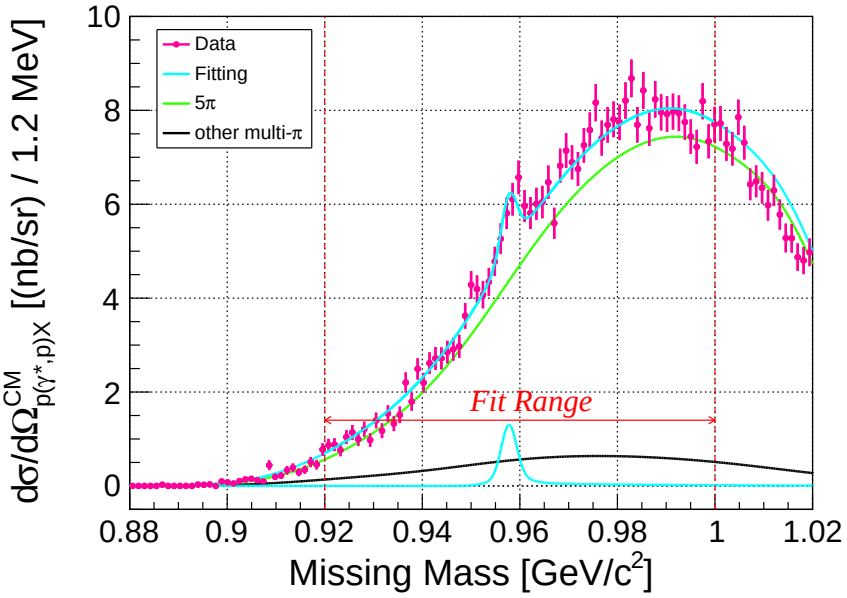

Fig. B.20: Missing mass spectrum (in differential cross section) for $W \geq 2.13$ GeV with a fitting using a simulation-based function for background with the area treated as a free parameter.

B.3 Cross section for different types of momentum cuts

The fittings of the missing mass spectra for looser and tighter momentum cuts are shown in Fig. B.21 to Fig. B.22.

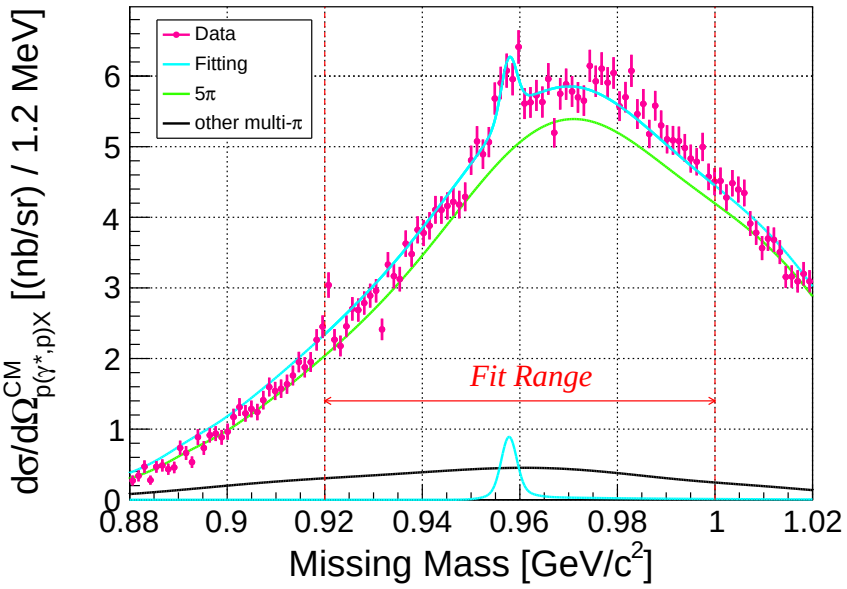

Fig. B.21: Missing mass spectrum (in differential cross section) for looser momentum cut. A fitting using a simulation-based function for background are also presented.

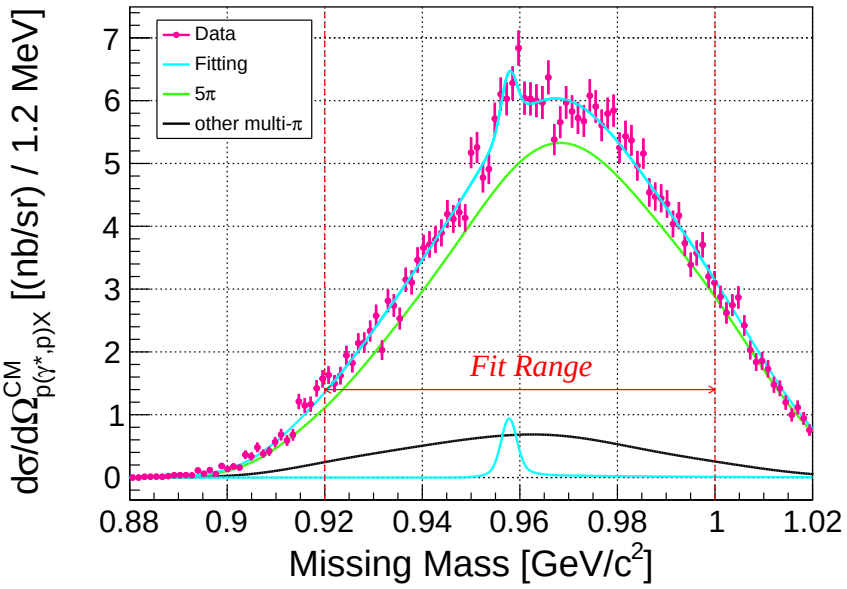

Fig. B.22: Missing mass spectrum (in differential cross section) for tighter momentum cut. A fitting using a simulation-based function for background are also presented.

Bibliography

[1] CMS Collaboration, "Observation of a new boson at a mass of 125 GeV with the CMS experiment at the LHC", Phys. Lett. B **716**, 30–61 (2012).

[2] ATLAS Collaboration, "Observation of a new particle in the search for the Standard Model Higgs boson with the ATLAS detector at the LHC", Phys. Lett. B **716**, 1–29 (2012).

[3] M. Creutz, "Monte carlo study of quantized SU (2) gauge theory", Phys. Rev. D **21**, 2308–2315 (1980).

[4] K. G. Wilson, "Confinement of quarks", Phys. Rev. D **10**, 2445–2459 (1974).

[5] N. Ishii, S. Aoki, and T. Hatsuda, "Nuclear force from lattice qcd", Phys. Rev. Lett. **99**, 022001 (2007).

[6] S. Dürr et al., "Ab Initio Determination of Light Hadron Masses", Science **322**, 1224–1227 (2008).

[7] T. Inoue et al., "Baryon-Baryon Interactions in the Flavor SU(3) Limit from Full QCD Simulations on the Lattice", Progress of Theoretical Physics **124**, 591–603 (2010).

[8] T. Kawanai and S. Sasaki, "Heavy quarkonium potential from bethe-salpeter wave function on the lattice", Phys. Rev. D **89**, 054507 (2014).

[9] Particle Data Group, "Review of particle physics", Phys. Rev. D **110**, 030001 (2024).

[10] M. Gell-Mann, "Isotopic Spin and New Unstable Particles", Phys. Rev. **92**, 833 (1953).

[11] M. Gell-Mann, "Symmetries of Baryons and Mesons", Phys. Rev. **125**, 1067 (1962).

[12] M. Gell-Mann, "A schematic model of baryons and mesons", Phys. Lett. **8**, 214 (1964).

[13] V. E. Barnes et al., "Observation of a Hyperon with Strangeness Minus Three", Phys. Rev. Lett. **12**, 204 (1964).

[14] George R. Kalbfleisch et al., "Observation of a Nonstrange Meson of Mass 959 MeV", Phys. Rev. Lett. **12**, 527 (1964).

[15] M. Goldberg et al., "Existence of a New Meson of Mass 960 MeV", Phys. Rev. Lett. **12**, 546 (1964).

[16] G. 't Hooft, "Computation of the quantum effects due to a four-dimensional pseudoparticle", Phys. Rev. D **14**, 3432 (1976).

[17] E. Witten, "Current algebra theorems for the U(1) "Goldstone boson"", Nuclear Physics B **156**, 269–283 (1979).

[18] G. Veneziano, "U(1) without instantons", Nuclear Physics B **159**, 213–224 (1979).

[19] D. Jido et al., "η' Meson under partial restoration of chiral symmetry in nuclear medium", Nuclear Physics A **914**, 354–359 (2013).

[20] P. Costa et al., "Analysis of $U_A(1)$ symmetry breaking and restoration effects on the scalar-pseudoscalarmeson spectrum", Phys. Rev. D **71**, 116002 (2005).

[21] H. Nagahiro et al., "η- and η'-mesic nuclei and $U_A(1)$ anomaly at finite density", Phys. Rev. C **74**, 045203 (2006).

[22] H. Nagahiro and S. Hirenzaki, "Formation of $\eta'(958)$-Mesic Nuclei and Axial $U_A(1)$ Anomaly at Finite Density", Phys. Rev. Lett. **94**, 232503 (2005).

[23] S. Sakai and D. Jido, "In-medium η' mass and $\eta' N$ interaction based on chiral effective theory", Phys. Rev. C **88**, 064906 (2013).

[24] Y. K. Tanaka et al., "Missing-mass spectroscopy of the ^{12}C(p, d) reaction near the η'-meson production threshold", Phys. Rev. C **97**, 015202 (2018).

[25] N. Tomida et al., "Search for η' bound nuclei in the ^{12}C(γ, p) reaction with simultaneous detection of decay products", Phys. Rev. Lett. **124**, 202501 (2020).

[26] R. Hofstadter et al., "Splitting of the Proton Form Factors and Diffraction in the Proton", Phys. Rev. Lett. **5**, 263–265 (1960).

[27] R. Hofstadter and R. Herman, "Electric and Magnetic Structure of the Proton and Neutron", Phys. Rev. Lett. **6**, 293–296 (1961).

[28] E. D. Bloom et al., "High-Energy Inelastic *e-p* Scattering at 6° and 10°", Phys. Rev. Lett. **23**, 930–934 (1969).

[29] M. Breidenbach et al., "Observed Behavior of Highly Inelastic Electron-Proton Scattering", Phys. Rev. Lett. **23**, 935–939 (1969).

[30] L. Tiator et al., "Eta and etaprime photoproduction on the nucleon with the isobar model EtaMAID2018", Eur. Phys. J. A **54**, 210 (2018).

[31] R. Erbe et al., "Photoproduction of Meson and Baryon Resonances at Energies up to 5.8 GeV", Phys. Rev. **175**, 1669–1696 (1968).

[32] W. Struczinski et al., "STUDY OF PHOTOPRODUCTION ON HYDROGEN IN A STREAMER CHAMBER WITH TAGGED PHOTONS FOR 1.6 GeV $< E_\gamma <$ 6.3 GeV Topological and reaction cross sections", Nuclear Physics B **108**, 45–74 (1976).

[33] R. Plötzke et al., "Photoproduction of η'-mesons with the 4π-detector SAPHIR", Phys. Lett. B **444**, 555–562 (1998).

[34] M. Dugger et al., "η' Photoproduction on the proton for photon energies from 1.527 to 2.227 GeV", Phys. Rev. Lett. **96**, 062001 (2006).

[35] M. Williams et al., "Differential cross sections for the reactions $\gamma p \to p\eta$ and $\gamma p \to p\eta'$", Phys. Rev. C **80**, 045213 (2009).

[36] P. Collins et al., "Photon beam asymmetry Σ for η and η' photoproduction from the proton", Phys. Lett. B **771**, 213–221 (2017).

[37] V. Crede et al., "Photoproduction of η and η' mesons off protons", Phys. Rev. C **80**, 055202 (2009).

[38] I. Jaegle et al., "Photoproduction of η'-mesons off the deuteron", Eur. Phys. J. A **47**, 11 (2011).

[39] V. L. Kashevarov et al., "Study of η and η' Photoproduction at MAMI", Phys. Rev. Lett. **118**, 212001 (2017).

[40] Y. Morino et al., "Backward-angle photoproduction of ω and η' mesons from protons in the photon energy range from 1.5 to 3.0 GeV", Prog. Theor. Exp. Phys. **2015**, 013D01 (2015).

[41] V. Nelyubin et al., "Compton back-scattering of X-photons from 8GeV electrons at SPring-8", Nucl. Instrum. Methods in Phys. Res. A **425**, 65–74 (1999).

[42] N. Muramatsu et al., "Development of high intensity laser-electron photon beams up to 2.9 GeV at the SPring-8 LEPS beamline", Nucl. Instrum. Methods in Phys. Res. A **737**, 184–194 (2014).

[43] F. Huang et al., "Combined analysis of η' production reactions: $\gamma N \to \eta' N$, $NN \to NN\eta'$, and $\pi N \to \eta' N$", Phys. Rev. C **87**, 054004 (2013).

[44] J.-F. Zhang et al., "Photoproduction of the η' mesons as a new tool to probe baryon resonances", Phys. Rev. C **52**, 1134–1137 (1995).

[45] G. Knöchlein et al., "Production of η and η' mesons on nucleons and nuclei", Zeitschrift für Physik A Hadrons and Nuclei **352**, 327–343 (1995).

[46] Qiang Zhao, "η' Photoproduction near threshold", Phys. Rev. C **63**, 035205 (2001).

[47] Xian-Hui Zhong and Qiang Zhao, "η' Photoproduction on the nucleon in the quark model", Phys. Rev. C **84**, 065204 (2011).

[48] W.-T. Chiang et al., "An isobar model for η photo- and electroproduction on the nucleon", Nucl. Phys. A **700**, 429–453 (2002).

[49] A. V. Anisovich et al., "$N^* \to N\eta'$ Decays from photoproduction of η'-mesons off protons", Phys. Lett. B **772**, 247–252 (2017).

[50] A.V. Anisovich et al., "Proton-η' interactions at threshold", Phys. Lett. B **785**, 626–630 (2018).

[51] K. Nakayama and H. Haberzettl, "Analyzing η' photoproduction data on the proton at energies of 1.5–2.3 GeV", Phys. Rev. C **73**, 045211 (2006).

[52] D. Drechsel et al., "A unitary isobar model for pion photo- and electroproduction on the proton up to 1 GeV", Nuclear Physics A **645**, 145–174 (1999).

[53] D. Drechsel et al., "Unitary isobar model—MAID2007", Eur. Phys. J. A **34**, 69–97 (2007).

[54] F.X. Lee et al., "Quasifree kaon photoproduction on nuclei", Nuclear Physics A **695**, 237–272 (2001).

[55] F.X. Lee et al., "Quasifree kaon photoproduction on nuclei", Nuclear Physics A **695**, 237–272 (2001).

[56] P. Bydžovský and D. Skoupil, "Photoproduction of $K^+\Lambda$ within a Regge-plus-resonance model", Phys. Rev. C **100**, 035202 (2019).

[57] D. Skoupil and P. Bydžovský, "Photoproduction of $K\Lambda$ on the proton", Phys. Rev. C **93**, 025204 (2016).

[58] D. Skoupil and P. Bydžovský, "Photo- and electroproduction of $K^+\Lambda$ with a unitarity-restored isobar model", Phys. Rev. C **97**, 025202 (2018).

[59] C. Rappold et al., "Search for evidence of ${}^{3}_{\Lambda}n$ by observing $d+\pi^-$ and $t+\pi^-$ final states in the reaction of ^{6}Li+^{12}C at 2A GeV", Phys. Rev. C **88**, 041001 (2013).

[60] E. Amaldi, S. Fubini, and G Furlan, "Pion-Electroproduction: Electroproduction at Low Energy and Hadron Form Factors", Vol. **83** of Springer Tracts in Modern Physics, Springer-Verlag Berlin Heidelberg (1979).

[61] https://www.google.co.jp/intl/ja/earth/.

[62] S. N. Santiesteban et al., "Precise Beam Energy Determination for Hall A after the CEBAF 12 GeV Upgrade", arXiv:2110.06281.

[63] F. Pilat, "THE 12 GeV ENERGY UPGRADE AT JEFFERSON LABORATORY", Proceedings of LINAC2012, Tel-Aviv, Israel, TH3A02 792–796 (2012).

[64] J. Alcorn et al., "Basic instrumentation for Hall A at Jefferson Lab", Nucl. Instrum. Methods in Phys. Res. A **522**, 294 (2004).

[65] P. Zhu et al., "Beam position reconstruction for the g2p experiment in hall a at jefferson lab", Nucl. Instrum. Methods in Phys. Res. A **808**, 1–10 (2016).

[66] K.B. Unser, "The Parametric Current Transformer, a Beam Current Monitor Developed for LEP", Proceedings of the third Beam Instrumentation Workshop, 1991, CEBAF, Newport News, VA.

[67] J.-C. Denard et al., "HIGH ACCURACY BEAM CURRENT MONITOR SYSTEM FOR CEBAF'S EXPERIMENTAL HALL A", Proceedings of the 2001 Particle Accelerator Conference, 2136.

[68] S. N. Santiesteban et al., "Density changes in low pressure gas targets for electron scattering experiments", Nucl. Instrum. Methods in Phys. Res. A **940**, 351 (2019).

[69] K.G Fissum et al., "Vertical drift chambers for the Hall A high-resolution spectrometers at Jefferson Lab", Nucl. Instrum. Methods in Phys. Res. A **474**, 108 (2001).

[70] https://hallaweb.jlab.org/github/halla-osp/version/Standard-Equipment-Manual.pdf.

[71] D.J. Abbott et al., "CODA performance in the real world", 1999 IEEE Conference on Real-Time Computer Applications in Nuclear Particle and Plasma Physics. 11th IEEE NPSS Real Time Conference. Conference Record (Cat. No.99EX295), 119 (1999).

[72] T. others Miyoshi, "High resolution spectroscopy of the ${}^{12}_{\Lambda}$B hypernucleus produced by the $(e, e' K^+)$ reaction", Phys. Rev. Lett. **90**, 232502 (2003).

[73] S.N. Nakamura et al., "Observation of the ${}^{7}_{\Lambda}$He hypernucleus by the (e, $e' K^+$) reaction", Phys. Rev. Lett. **110**, 012502 (2013).

[74] L. Tang et al., "Experiments with the high resolution kaon spectrometer at jlab hall c and the new spectroscopy of ${}^{12}_{\Lambda}$B hypernuclei", Phys. Rev. C **90**, 034320 (2014).

[75] K.N. Suzuki et al., "The cross-section measurement for the ${}^{3}\mathrm{H}\,(e, e' K^+)\,nn\Lambda$ reaction", Progress of Theoretical and Experimental Physics **2022**, 013D01.

[76] K. Okuyama et al., "Electroproduction of the Λ/Σ^0 hyperons at $Q^2 \simeq 0.5$ $(\mathrm{GeV}/c)^2$ at forward angles", Phys. Rev. C **110**, 025203 (2024).

[77] https://hallcweb.jlab.org/wiki/index.php/SIMC_Monte_Carlo.

[78] A. Uzzle, "Electroproduction of Kaons on Helium-3 and Helium-4," Doctoral thesis, Hampton University (2002).

[79] S. Agostinelli et al., "Geant4—a simulation toolkit", Nucl. Instrum. Methods in Phys. Res. A **506**, 250–303 (2003).

[80] J. Allison et al., "Recent developments in geant4", Nucl. Instrum. Methods in Phys. Res. A **835**, 186–225 (2016).

[81] K. Okuyama, "Study of Λ/Σ^0 electroproduction", Doctoral thesis, Tohoku University (2023).

[82] Y-S Tsai, "Pair production and bremsstrahlung of charged leptons", Rev. Mod. Phys. **46**, 815 (1974).

[83] Y-S Tsai, "RADIATIVE CORRECTION TO ELECTRON SCATTERINGS", Stanford Linear Accelerator Report (1971) No. SLAC – PUB – 848.

[84] M. Vanderhaeghen et al., "QED radiative corrections to virtual Compton scattering", Phys. Rev. C **62**, 025501 (2000).

[85] K.N. Suzuki, "Search for the $nn\Lambda$ state via the ${}^3\mathrm{H}\,(e, e'K^+)\,X$ reaction at JLab", Doctoral thesis, Kyoto University (2021).

[86] V. Pascalutsa, "Quantization of an interacting spin-$\frac{3}{2}$ field and the Δ isobar", Phys. Rev. D **58**, 096002 (1998).

[87] W. Rarita and J. Schwinger, "On a Theory of Particles with Half-Integral Spin", Phys. Rev. **60**, 61–61 (1941).

[88] F. James and M. Roos, "Minuit—a system for function minimization and analysis of the parameter errors and correlations", Computer Physics Communications **10**, 343–367 (1975).

[89] M. F. Gari and W. Krümpelmann, "Vector-meson—nucleon couplings at spacelike momentum transfer", Phys. Rev. D **45**, 1817–1820 (1992).

[90] M. F. Gari and W. Krümpelmann, "Erratum: Vector-meson-nucleon couplings at spacelike momentum transfer", Phys. Rev. D **46**, 484–485 (1992).

[91] R.A. Williams et al., "Hyperon electroproduction in a crossing and duality constrained model", Phys. Rev. C **46**, 1617–1635 (1992).

[92] Earle L. Lomon, "Effect of recent R_p and R_n measurements on extended Gari-Krümpelmann model fits to nucleon electromagnetic form factors", Phys. Rev. C **66**, 045501 (2002).

[93] T. Gogami, "Spectroscopic research of Λ hypernuclei up to medium-heavy mass region with the $(e, e'K^+)$ reaction", Doctoral thesis, Tohoku University (2014).

[94] T. Akiyama, Master's thesis, Tohoku University (2020) (in Japanease).

[95] T. Vrancx et al., "Consistent interactions for high-spin fermion fields", Phys. Rev. C **84**, 045201 (2011).

[96] R. M. Davidson and R. Workman, "Form factors and photoproduction amplitudes", Phys. Rev. C **63**, 025210 (2001).